UNIVERSITE D'AIX-MARSEILLE

ECOLE DOCTORALE DES SCIENCES CHIMIQUES

INSTITUT DES SCIENCES MOLECULAIRES DE MARSEILLE/ UMR 7313

Thèse présentée pour obtenir le grade universitaire de docteur

Discipline : Chimie
Spécialité : Chimie Bioinorganique

Maria-Chrysanthi KAFENTZI

Reactive copper-oxygen species for C-H activation:

Influence of nuclearity and oxygen atom donor

Soutenue le 24/11/2016 devant le jury :

Dr. Carole DUBOC	Université Joseph Fourier	Rapporteur
Dr. Elodie ANXOLABEHERE	Université Paris-Diderot	Rapporteur
Prof. Athanassios G. COUTSOLELOS	Université de Crète	Examinateur
Dr. Wadih GHATTAS	Université Paris-Saclay	Examinateur
Dr. Jalila SIMAAN	Aix-Marseille Université	Directrice de thèse
Dr. Marius REGLIER	Aix-Marseille Université	Directeur de thèse

To my family and friends

"A scientist in his laboratory is not a mere technician: he is also a child confronting natural phenomena that impress him as though they were fairy tales."

Marie Sklodowska Curie

Contents

Acknowledgements

My brothers George, Stelios and my sister-in-law Anna for their care, comprehension and support during those three years. Finally, my biggest love to my nephew, Panos. Only with his smile on skype almost every night, I could forget any tiring day in the lab!

Thank you all!

Merci à vous tous!

Σας ευχαριστώ όλους!

<div align="right">Marianthi</div>

Chapter I

O$_2$ activation by copper-containing monooxygenases and model complexes.

I. Introduction

I.1. Role and characteristics of copper in biological systems

Copper is an essential trace element in living organisms, notably due to its involvement in various biological redox processes existing either in mononuclear or multinuclear configurations.[1,2] One feature of Cu that drives a variation of roles in structure and catalysis is its existence in either a reduced, Cu^+, or oxidized, Cu^{2+}, state, since Cu^{3+} has not been observed in the enzymatic environment due to very high Cu^{III}/Cu^{II} redox potentials.[3]

In contrast to Cu^I which has d^{10} closed shell configuration, Cu^{II} has d^9 configuration allowing its study using several spectroscopic techniques. Electron Paramagnetic Resonance (EPR) spectroscopy and absorption spectroscopy are the basis for studying copper enzymes and the corresponding synthetic models. As the nuclear spin of naturally occurring isotopes, ^{63}Cu and ^{65}Cu is I=3/2, the EPR transitions show hyperfine splitting into four features. In the UV-Vis spectrum, Cu^{II} exhibit weak d-d transitions from the filled d orbitals to the $d_{x^2-y^2}$ orbital. However, ligand-to-metal or metal-to-ligand charge transfer transitions (LMCT and MLCT) can be observed, whose intensities depend on the size of overlap of the ligand's orbitals with the metal's orbitals.

Based on spectroscopic features, the copper(II)-containing active sites have been classified into groups. The blue copper or T1 centers display intense absorption bands at 600 nm and small hyperfine splitting in EPR spectroscopy, and are found in enzymatic systems such as laccases, plastocyanins, ascorbate oxidase etc. The T2 centers which exhibit "normal" signal of Cu^{II} tetragonal system in EPR spectroscopy and low absorption in the UV-Vis region are found in enzymes such as dopamine β-hydroxylase and peptiglycine α-amidating monoxygenase. Finally, the coupled binuclear or the T3 sites which are EPR silent, are found in hemocyanine, tyrosinase and catechol oxidase.[2,4,5]

I.2. Role of copper in copper containing enzymes

Copper-containing enzymes perform a variety of biologically important functions in nature including electron transfer, O_2 binding and transport, O_2 activation or reduction and substrate activation.[4] It has to be mentioned that nuclearity does not correlate with the type of reactivity, since similar active site structures can accommodate different functions.[3]

Dioxygen activation in copper containing enzymes

I.2.1. Hemocyanin and Tyrosinase

Hemocyanin (Hc) is an extracellular oxygen transport in anthropods and mollusks, whereas tyrosinase (Ty) is responsible for the synthesis of melanin in a variety of organisms and catalyzes both the hydroxylation of tyrosine into L-DOPA and its subsequent oxidation into the corresponding quinone (
Scheme 1).
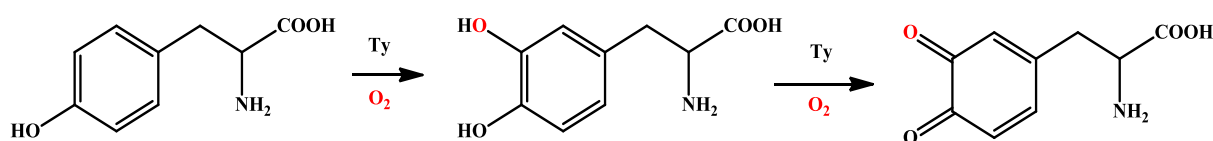
Scheme 1: Hydroxylation of tyrosine into L-DOPA and further oxidation to corresponding quinone.

Hc and Tyr both contain two copper centers in their active sites and each copper ion is coordinated by three histidine imidazoles.

Deoxy-Hc contains a pair of Cu^{I} ions (3.6 Å distance) in a distorted trigonal environment. Upon coordination, dioxygen is reduced by two electrons resulting in a dinuclear side–on $(\mu\text{-}\eta^{2}\text{:}\eta^{2}\text{-peroxo})Cu_2^{II}$ species (oxy-Hc), where the copper ions are arranged in a square planar coordination environment and are bridged by the peroxo moiety (Figure 1).[6] The two coppers are strongly antiferromagnetically coupled.
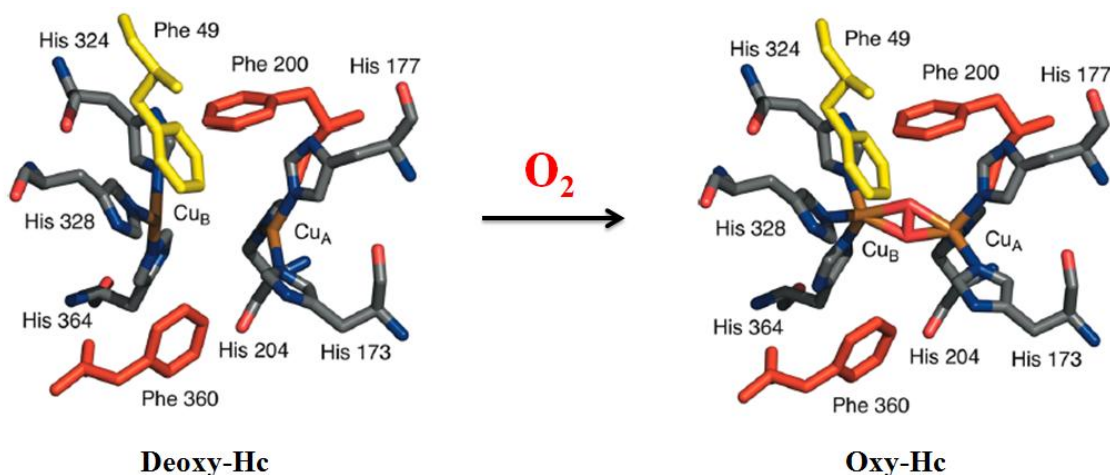
Figure 1 : Active site of Hemocyanin from anthropod *Li. Polyphemus.* Reduced form (Deoxy-Hc), left; oxidized form (Oxy-Hc), right.[4]

The active site of tyrosinase is very similar to that of hemocyanine. Tyrosinase is by far the most well-studied copper-containing oxygenase. The reduced enzyme contains a binuclear Cu^{I} active site which reacts with O_2 to form oxy-Ty, whose characteristics are similar to oxy-Hc and that has been shown to contain a $(\mu\text{-}\eta^{2}\text{:}\eta^{2}\text{-peroxo})Cu_2^{II}$ unit.[7,8] Tyrosinase promotes both the o-hydroxylation of monophenols (phenolase

activity), and the two-electron oxidation of o-diphenols to o-quinones, (catecholase activity). This bridging peroxo species is thought to be the key intermediate in phenol hydroxylation reaction (Scheme 2). The fact that Ty is able to promote C-H bond activation and not Hc, although both form the same intermediate upon dioxygen binding has been rationalized based on structural observations. Indeed, there is a free space for the access and coordination of a substrate to the catalytic core of Tyrosinase active site[9] but not in hemocyanine.
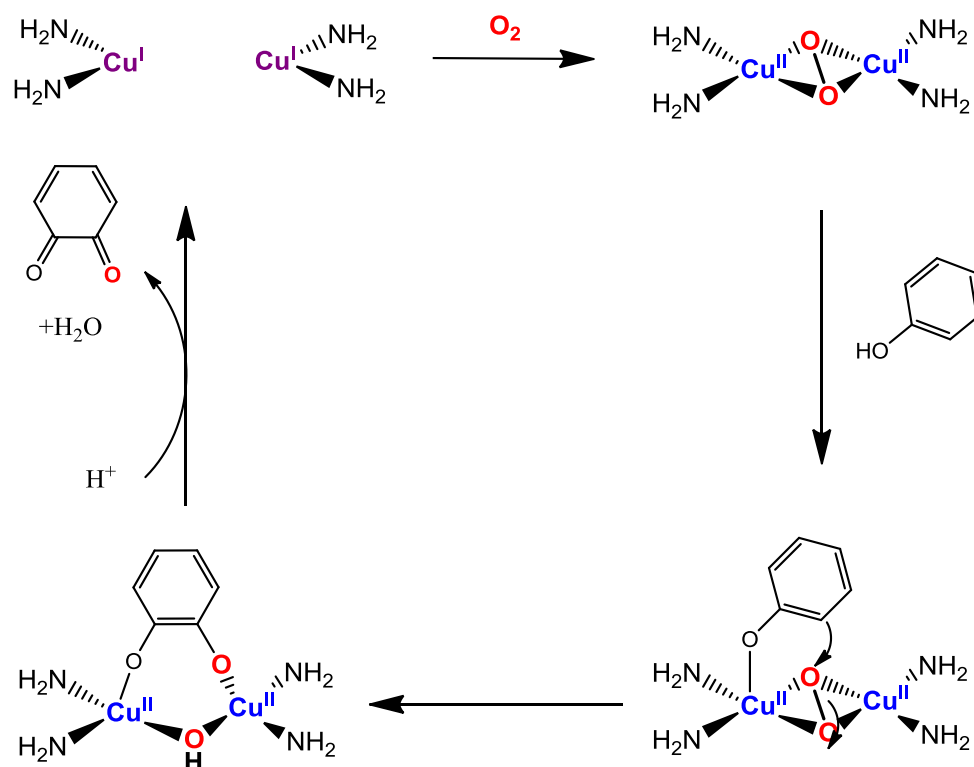
Scheme 2 : Catalytic cycle of tyrosinase.

I.2.2. Dopamine β-monooxygenase (DβM) and peptidylglycine α-hydroxylating monooxygenase (PHM)

Despite their different functions, DβM and PHM exhibit key similarities. Each enzyme catalyzes the stereospecific insertion of an O-atom from dioxygen into a C-H bond. Moreover, these enzymes exhibit 27% sequence homologies and conserved copper ligands at their catalytic active sites that suggest mechanistic similarities as well.[10] Both enzymes are found exclusively in higher eukaryotes and play an important role in the biosynthesis of neurotransmitters and hormones.

DβM is a copper-containing monooxygenase which catalyzes the stereospecific hydroxylation of dopamine to norepinephrine in catecholamine biosynthesis pathway, both substrate and product serving as neurotransmitters in the nervous system (Scheme 3).[11]

Dopamine   **Norepinephrine**
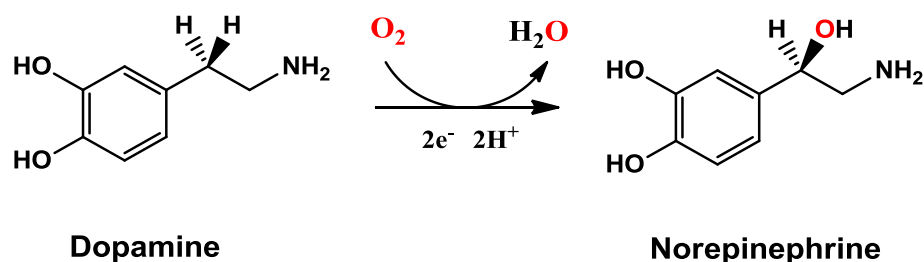
Scheme 3 : Reaction catalysed by dopamine β monoxygenase.

On the other hand, PHM (one component of a multifunctional protein) catalyzes the hydroxylation of C-terminal glycine-extended peptides to their α-hydroxylated products (Scheme 4). Subsequent hydrolysis by a second enzymatic component (peptidyl-*α*-hydroxyglycine amidating lyase or PAL) releases the C-terminal amidated bioactive peptide.
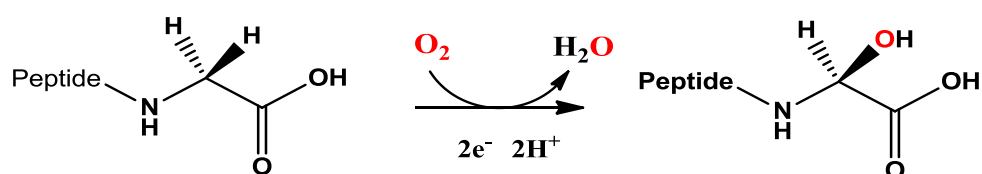
Scheme 4 : Reaction catalysed by peptidylglycine α-hydroxylating monooxygenase.

During the course of dioxygen activation process in DβH and PHM, four electrons are required with two electrons coming from the substrate. The remaining two electrons required for O_2-reduction to water are provided by two molecules of an external one electron donor, such as ascorbate (which is oxidized to unstable free radical semihydroascorbate),[12] or ferrocyanide.[13,14]

In the past, the number of copper ions involved in the catalysis and their roles in the redox events have raised major questions. For a long time, no crystal structure had been reported, leading to attempts to gain information from extensive spectroscopic and kinetic studies that had mainly been conducted on DβH. The coordination chemistry of the two copper atoms in both oxidized and reduced forms was probed by extended X-ray absorption fine structure (EXAFS). DβH requires two copper ions per subunit to be active.[15] By EPR spectroscopy it was not possible to detect any spin coupling between metal sites in oxidized, resting enzyme[16] and in a catalytically generated product complex[17] indicating the presence of rather two distinct copper sites than coupled binuclear copper centers as observed in tyrosinase and hemocyanine. Studies have shown that one CO binds (a competitive inhibitor for O_2) per two coppers providing insight that the two copper sites are chemically inequivalent.[18] Based on those results, it has been suggested that one copper (named Cu_B) is the place where O_2 binds and substrate hydroxylation occurs. Also, ascorbate binds near the other copper ion (named Cu_A) that mediates the electron transfer to Cu_B.

The first structure of this family of enzyme was obtained for the oxidized form of rat PHM (ox-PHMCC).[19,20,21] As illustrated in Figure 2 (left), the structure consists of two nine stranded β-sandwich domains, where the domain 1 binds one copper (Cu_B sometimes named Cu_M) and the domain 2 binds the other copper (Cu_A sometimes named Cu_H). The Cu_A is liganded by three histidines and one water molecule in square pyramidal geometry and Cu_B is liganded by two histidines and one methionine in tetrahedral geometry. The two coppers are separated by ~ 11 Å of a solvent-filled interdomain cleft (Figure 2, right). Moreover, the structure of the O_2-bound enzyme in the presence of a substrate analog was also reported (Figure 2, right).[22] In the latter structure the dioxygen is bound in an end-on fashion on the Cu_B ion (the O-O distance would be compatible with a superoxo redox state of the dioxygen ligand). The substrate analog is also bound close to the Cu_B indicating that, as in DβH, this site would be the substrate's oxidation site.
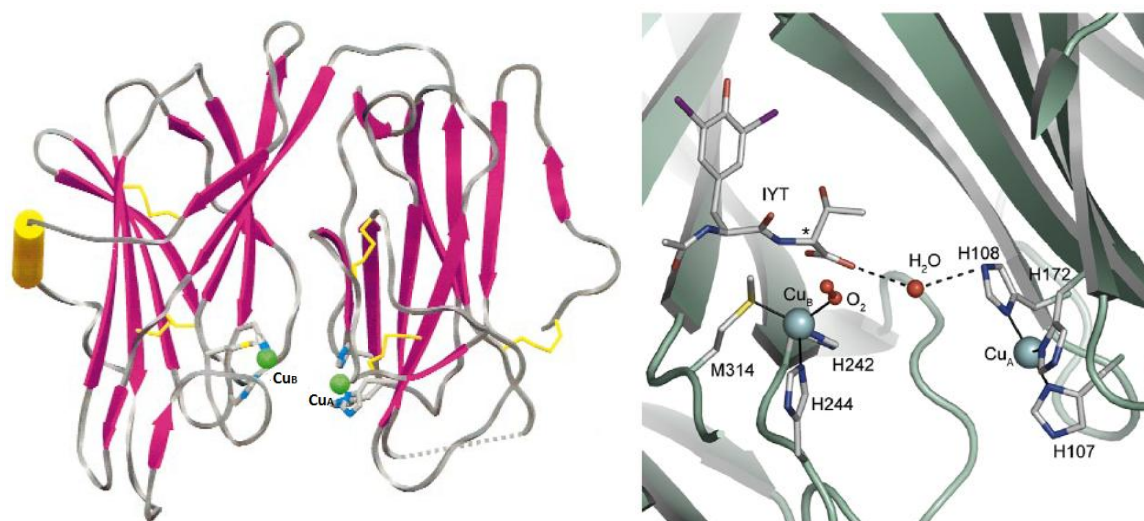
Figure 2 : Left: Crystal structure of PHM. Right: Oxidized active site of PHM. The copper atoms are represented by blue spheres and ligands are colored by atom type. The C_a of substrate IYT (N-acetyl-diiodotyrosyl D-threonine) which is going to be hydroxylated is denoted by an asterisk.[21]

A mechanism proposed by Klinman and co-workers for DβM and PHM is commonly accepted by the scientific community (Scheme 5).[10,23] In this mechanism, the substrate and O_2 bind to the fully reduced enzyme forming a ternary complex, involving the initial dioxygen activation step through electron transfer from Cu_B^I to dioxygen to form the Cu_B^{II}–superoxo species. The abstraction of hydrogen atom from the substrate leads to benzyl radical and Cu_B^{II}–hydroperoxo. Electron transfer from Cu_A^I to Cu_B^{II} is proposed to induce reductive cleavage of the Cu_B^{II}–hydroperoxo intermediate yielding water and a Cu_B^{II}–oxyl species, which recombines with the substrate radical to form an alcohol product.[11] Finally, two molecules of ascorbate bind sequentially to the enzyme, triggering the release of product and the concomitant cyclical reduction of Cu^{II} sites.
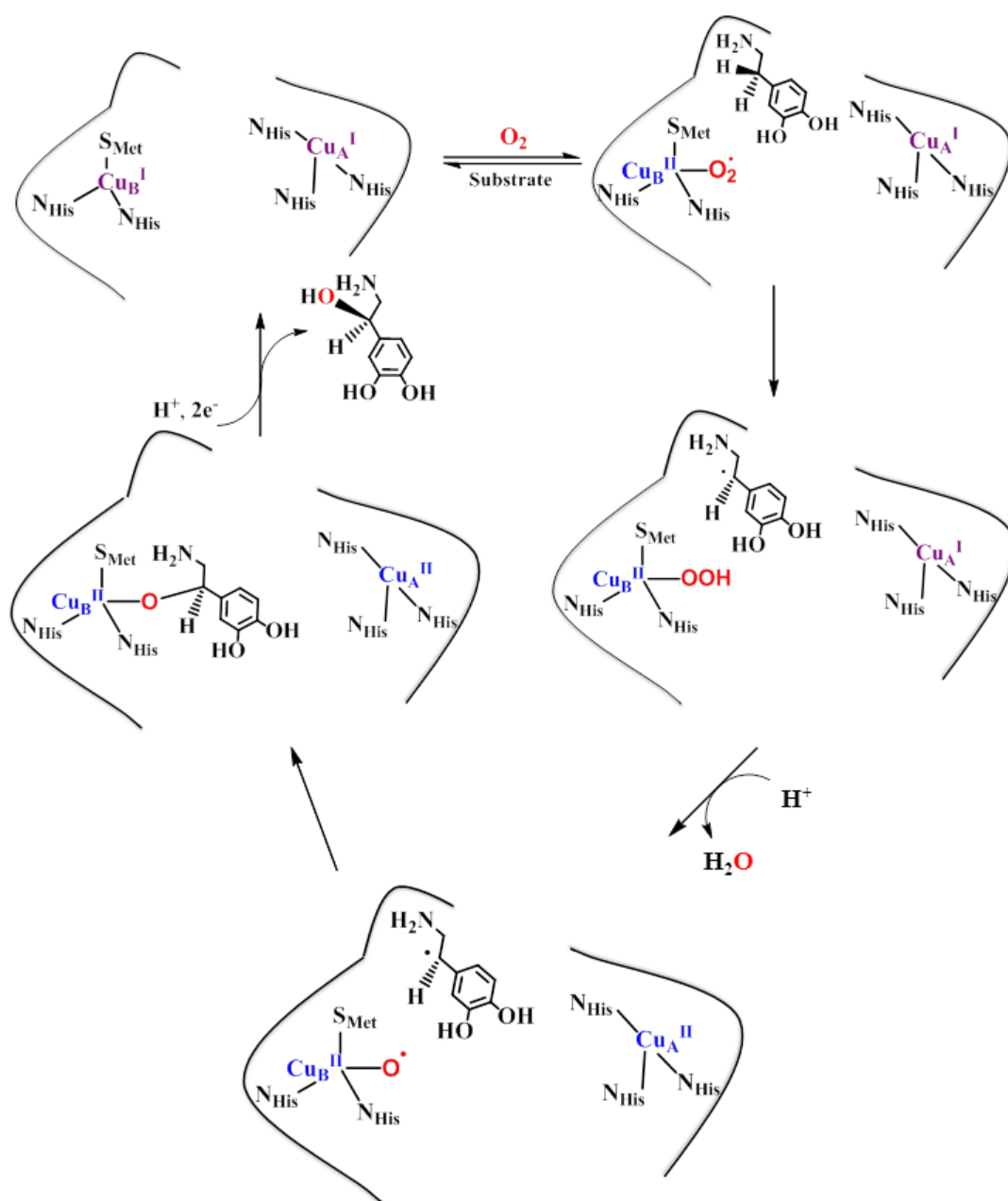
Scheme 5: Proposed mechanism by Klinman.[23]

Recently, the first crystal structure of human DβH was reported by Christensen and coworkers (Figure 3).[24] The enzyme is found dimeric in the crystal structure and each monomer folds into four domains: (i) the DOMON domain (DβM N-terminal domain), (ii) the Cu^A domain (iii) the Cu^B domain and (iv) the C-terminal dimerization domain.

The Cu^A and Cu^B domain constitute the catalytic core where Cu^A and Cu^B bind, respectively. In the dimeric structure, two conformations exist: an opened conformation in which the two copper ions are located at 11-14 Å distance, similar to the conformation found in PHM (Figure 3, left), and a closed conformation, in which

the two copper sites are only 4-5 Å apart (Figure 3, right), a distance compatible with the presence of a coupled binuclear copper site as seen in a number of other proteins, such as tyrosinase and hemocyanine.

On the basis of this structure, an alternative mode of action for this type of enzymes was therefore proposed.[24] In this mechanism, the two different conformations of the DβH catalytic core could alternate, known as a flip-flop mechanism (Figure 3). The opened form would be inactive but would allow substrate binding and product release, whereas the closed conformation would be the catalytically relevant conformation where dioxygen activation and hydroxylation reaction would take place at a binuclear coupled copper center.
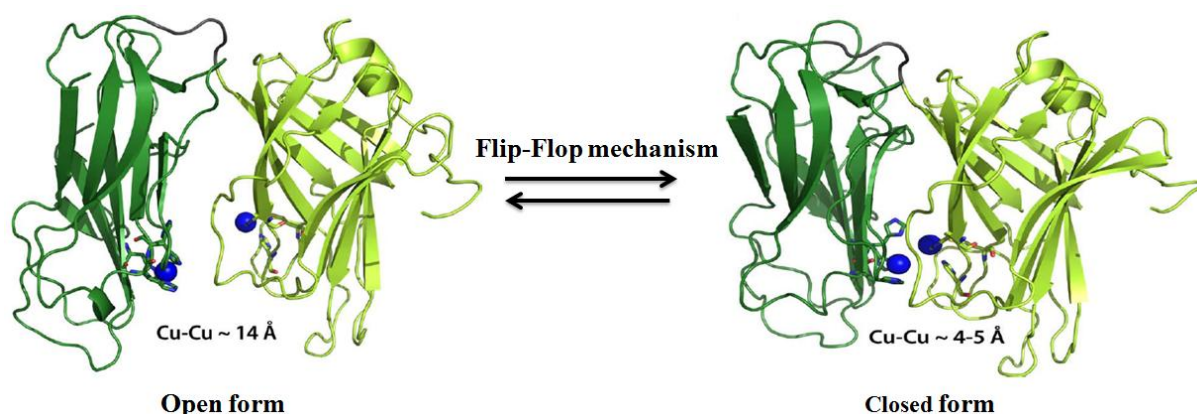
Figure 3 : The two conformations of the DβH catalytic core which reveal an open and a closed form. The copper atoms are represented in blue spheres.

I.2.3. Particulate Methane monooxygenase

Methanotrophic bacteria play an important role in the global carbon cycle by the ability to use methane as a sole carbon and energy source.[25] They catalyze the conversion of methane to methanol at ambient temperature and atmospheric pressure using metalloenzymes called methane monooxygenases, according to the following reaction:[26]

$$CH_4 + NADH + H^+ + O_2 \rightarrow CH_3OH + NAD^+ + H_2O$$
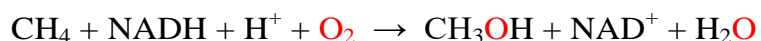
Two enzymatic systems are found: the soluble methane monooxygenase (sMMO) which is expressed by several strains of methanotrophs under copper-limited concentrations[27] (< 0.8 μM) and the particulate methane monooxygenase (pMMO), an integral membrane metalloenzyme produced by all methanotrophs in high copper availability (~4 μM). In addition, the two MMO systems are completely different in sequence, overall structure, substrate selectivity, and active site composition.[28]

sMMO

sMMO has been more extensively studied. The active site of sMMO contains a non-heme diiron cluster and can accommodate a wide variety of hydrocarbon substrates besides methane.[29,30,31] Among them, are saturated and unsaturated, linear, branched, and cyclic hydrocarbons up to C8, as well as aromatic, heterocyclic, and chlorinated compounds.

Inspired by sMMO active site, several diiron model complexes have been reported, providing a better understanding of the mechanism of catalytic methane oxidation by sMMO that involves the formation of high-valent Fe(IV)Fe(IV) intermediate.[32]

pMMO

Compared to sMMO, pMMO can oxidize alkanes and alkenes up to five carbons in length, but cannot oxidize cyclic or aromatic hydrocarbons.[33] The metal composition and the location of pMMO active site has been the object of intense debates unveiled by the low resolution of crystal structures and low copper-stoichiometry.[28,34,36] It has been recently proposed by Culpepper *et al.* that the pMMO activity is dependent on a dinuclear copper site.[35]

In the crystal structure of pMMO from *Bath*, several metal centers are modelled. (Figure 4, left).[36] A first site, a monocopper center, is found in the soluble region of pmoB ~ 25 Å above the membrane. The copper ion is coordinated to His 48 and His 72 (Figure 4B). This mononuclear copper site is not conserved in other pMMO sources. A second copper center has been modeled as a dicopper center located at the N-terminal part of the pmoB subunit ~10 Å above the membrane interface.[36,37] These two coppers are coordinated to the highly conserved residues His 33, His 137 and His 139 consistent with their important role in catalysis (Figure 4A). The Histidine 33 is the pmoB *N*-terminal histidine and is coordinated both by the imidazole function and by the N-terminal amine. This rare coordination motif is called "histidine-brace" and has been observed only in a limited number of metal-containing enzymes.
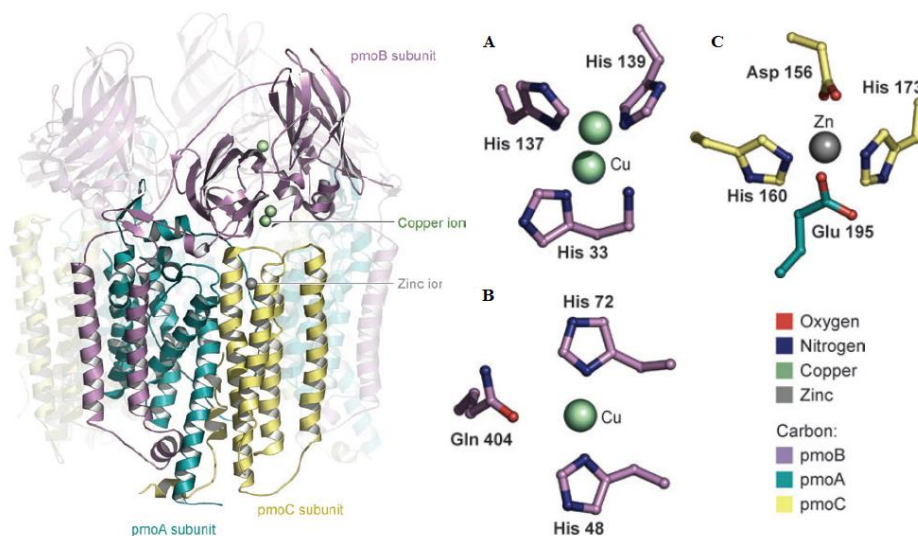
Figure 4: The pMMO trimer from *Methylococcus capsulatus* (Bath) (left). Metal sites located in pMMO (right): (A) The dicopper (B) monocopper and (C) zinc sites modeled in pMMO structure.

A third metal center, occupied by zinc from the crystallization buffer, is located within the membrane and is ligated by Asp 156, His 160 and His 173 from pmoC and possibly Glu 195 from pmoA (Figure 4C). All four of these residues are strictly conserved, strongly suggesting that this site is functionally important. When purified pMMO contains less than 0.2 zinc ions per monomer. There is therefore a possibility that this site is occupied by another metal ion (copper or iron) *in vivo*.[37]

The copper core and the exact mechanism for the oxidation of methane to methanol are still under investigation. However, it is believed that the dicopper center is the active site for several reasons.[36] First, all of the ligands to the dicopper site are highly conserved and secondly, the existence of the dicopper center is clear from both EXAFS data.[35]

However, there is still a question about what type of $[Cu_2O_x]^{y+}$ species are involved for methane hydroxylation in the dicopper site. Cu-loaded zeolites (Cu-ZSM-5) were shown to be able to produce methanol from methane at relatively low temperature ($\sim$100 °C) with high selectivity through the formation of highly reactive Cu^{II}_2(μ-oxo) (Cu_2O) intermediates, making these species relevant for pMMO catalytic cycle (Figure 5).[38] However, synthetic Cu_2O species have been described but their ability to perform C-H bond oxidation has not yet been established.[39]
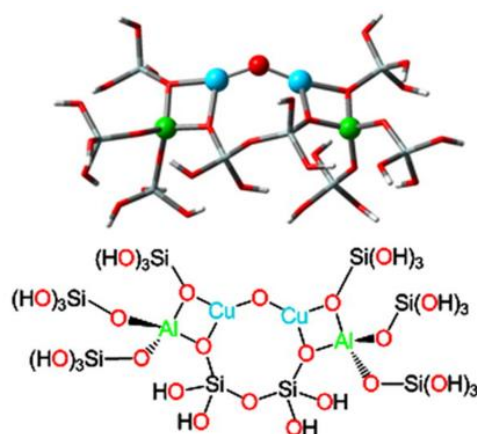
Figure 5 : Methane-oxidizing active site in Cu-ZSM-5.

Recently, using theoretical calculations, Yoshizawa and Shiota demonstrated the ability to form a (μ-η^2:η^2-peroxo)Cu^{II}_2 species at the pMMO active site similar to that found in tyrosinase or hemocyanin.[40] Oxo-bridged high-valent bis(μ-oxo)Cu^{III}_2 species have also been suggested as intermediate which may form at the active site.[39] Using model complexes, Stack and coworkers have shown that primary amine ligation reminiscent of the 'histidine brace' motif, provided greater stabilization to the bis(μ-oxo)Cu^{III}_2 intermediates without attenuation of their oxidizing power and allowing increased substrate accessibility to the core.[41] Finally, using computational analysis, Yoshizawa and coworkers have suggested that mixed-valent $Cu^{II}Cu^{III}$ species such as bis(μ-oxo)$Cu^{II}Cu^{III}$ or (μ-oxo)(μ-hydroxo)$Cu^{II}Cu^{III}$ are more reactive towards oxidative chemistry involving very strong C–H bonds than the bis(μ-oxo)Cu^{III}_2.[40,41] Their newer

calculations have suggested that the reactivity towards methane as substrate in *p*MMO is promoted by (μ-oxo)(μ-hydroxo)Cu^{II}Cu^{III} species that could arise from bis(μ-oxo)Cu^{III} after injection of an electron and a proton from a nearby tyrosine.[42]

Although there is no experimental proof, the species that are postulated as possible intermediates are shown in Scheme 6.
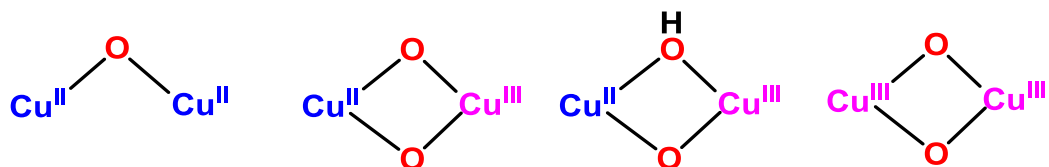
Scheme 6 : Possible dicopper species proposed for oxidation of methane to methanol.

I.2.4. Lytic polysaccharide monooxygenase

Recently, a class of oxygen activating enzymes has been identified. The lytic polysaccharide monooxygenases (LPMOs) have attracted much attention due to their ability to break polysaccharides chains, such as cellulose.[43] So far little is known about the reaction mechanism of these enzymes, however it has been demonstrated by X-ray crystallographic structure that they all display a mononuclear copper-containing active site.[44] This copper is located near the center of an extended flat face, which interacts with the crystalline surface of the substrate, shown in (Figure 6, left). In the active Cu site, two histidines provide three nitrogen ligands. Once more, the N-terminal histidine is coordinated following the histidine brace (Figure 6, right). [44,45]
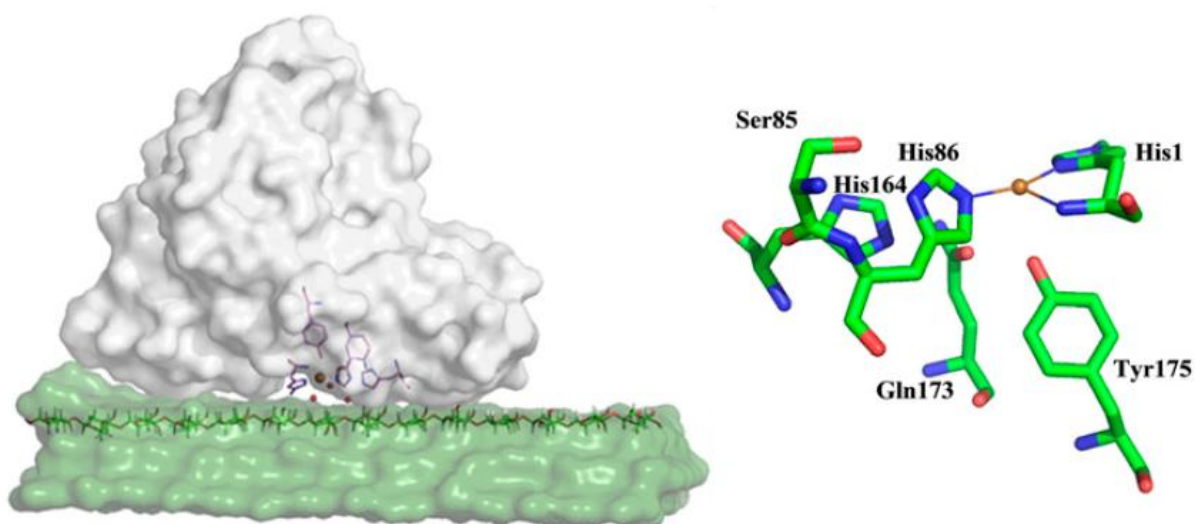
Figure 6 : Illustration of interaction of LPMO (white area) with cellulose (green area) with the copper site shown as an orange sphere (left)[46] and the active site[45] (right) highlighting the six residues around copper.

LPMOs catalyze the oxidation of glycosidic bonds creating new polymer chain breaks, through an oxidative mechanism, which facilitates the action of classical glycoside hydrolases.47,48 LPMOs catalyze the hydroxylation of an inert C-H bond at the glycosidic linkage in the presence of oxygen and electron donors (ascorbate, proteic partner, etc…), shown in

Scheme **7**. This hydroxylation destabilizes the glycosidic bond leading to its subsequent cleavage. Hydroxylation can occur at position C1 and/or C4 of the sugar ring. The C1 oxidation generates oligosaccharides with an aldolic acid at the reducing end, while the product of C4 oxidation is a ketoaldose at the non-reducing end.
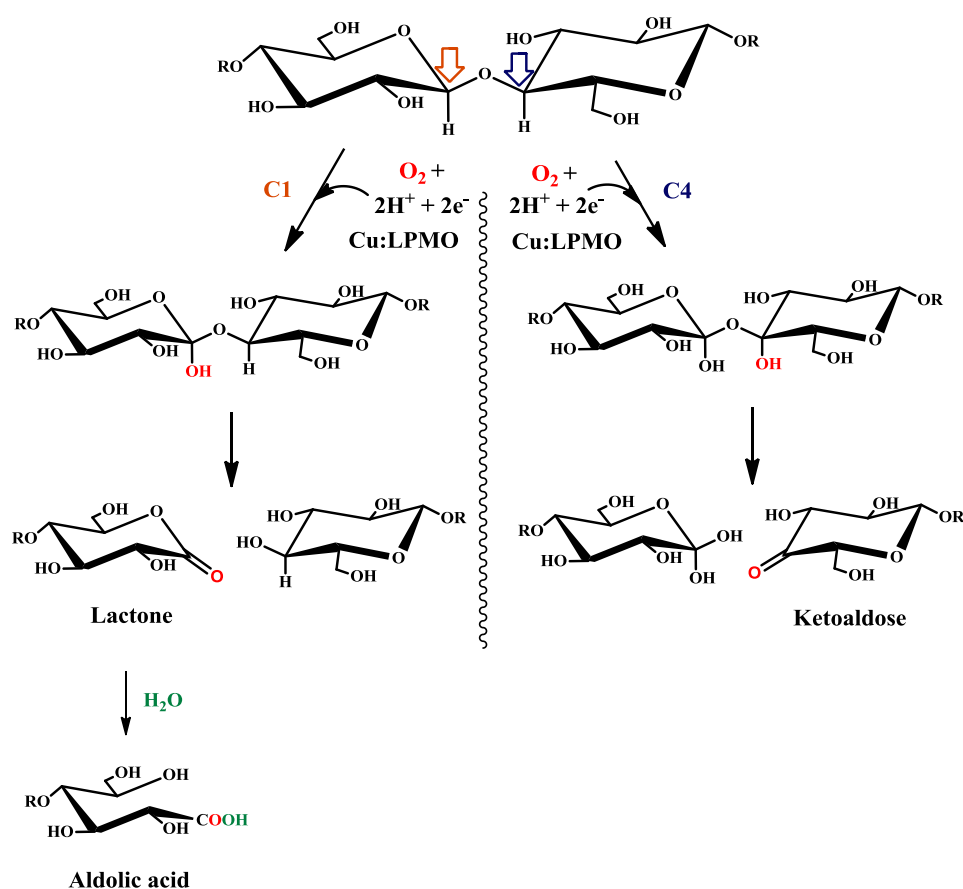
Scheme 7 : Reactivity of LPMO towards polysaccharide chains (here cellobiose) leading to chain cleavage.[48]

Despite some theoretical work, the exact nature of the reactive intermediate in LPMO is not clear. The reduction of the resting Cu(II) state was probed by XAS spectroscopy and a change from four-coordinate Cu(II) center to three-coordinate T-shaped Cu(I) center was observed.[45] Philips and coworkers have proposed a first mechanism (Scheme 8) in which, a copper-superoxo species formed after reaction of the reduced copper center with dioxygen, performs hydrogen atom abstraction on the substrate.[49] This results in the generation of both a copper-hydroperoxo species and a

radical on the substrate. After reduction and O-O bond cleavage, the copper-oxyl species recombines with the substrate radical to form the hydroxylated product.
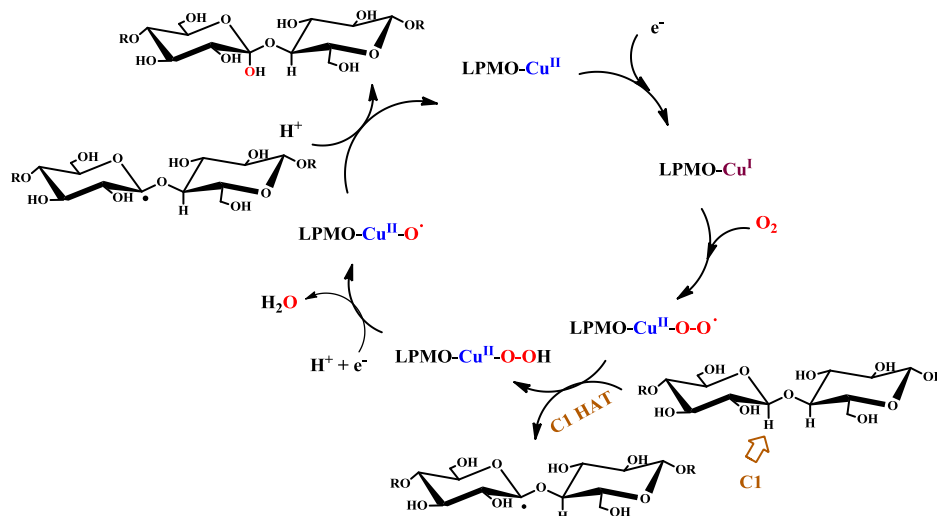
Scheme 8 : Proposed mechanism with copper superoxo as active species for polysaccharide chain cleavage by LPMO.[49]

This mechanism, which proposes an initially formed copper-superoxo species as the active species, has recently been refuted by Kim and coworkers on the basis of the theoretical calculations.[46] The authors propose that the barrier for hydrogen atom abstraction from copper-oxyl species is lower as compared to that from copper-superoxo species. This suggests that the copper-oxyl species is the C-H activating intermediate and that subsequent hydroxylation of the substrate occurs via an oxygen-rebound mechanism (Scheme 9).
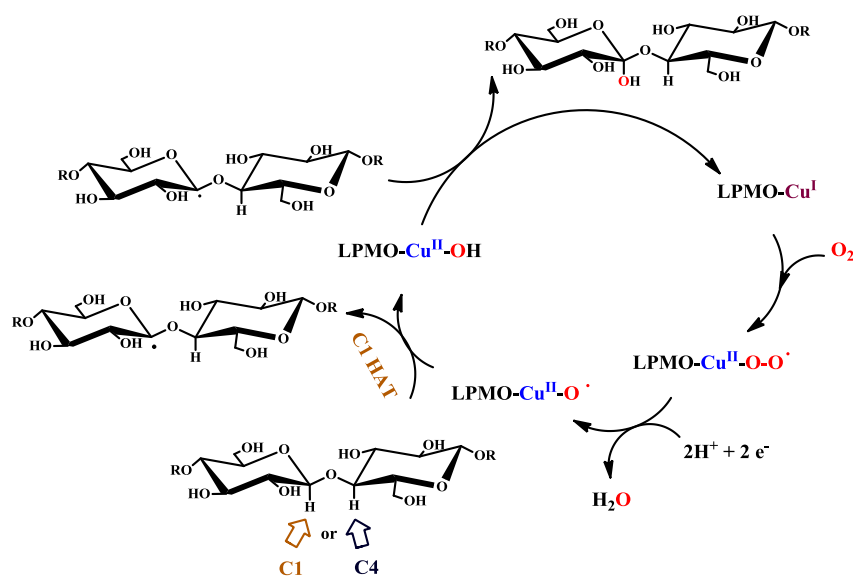
Scheme 9 : Proposed mechanism with copper-oxyl as active species for polysaccharide chain cleavage by LPMO.[46]

I.3. Mimicking enzymes's active sites: synthetic approach

The investigation of structure, function and mechanism of copper containing enzymes's active site is always accompanied by the synthesis and characterization of small molecular copper complexes in order to model the functionality of the enzymes in the laboratory.

I.3.1. Geometric preferences of Cu sites[3]

Cu^I: Geometries of Cu^I complexes are characterized by high lability and flexibility. Cu^I can be coordinated to bidentate, tridentate or tetradentate ligands leading to several geometries, such as tetrahedral or trigonal monopyramidal, T or Y shaped, as well as linear coordination.

Cu^{II}: Cu^{II}, due to significant Jahn-Teller distortion, accommodate square planar or square pyramidal and trigonal bipyramidal geometries.

Cu^{III}: Cu^{III} has d^8 electronic configuration and such complexes are stabilized by strongly basic, anionic ligands. Cu^{III} centers can exist in either high spin (S=1) or low spin state (S=0), most Cu^{III} complexes with oxygen ligation are low spin and diamagnetic.

I.3.2. Copper-dioxygen adducts in synthetic systems

It is very important to highlight the structural and spectroscopic characteristics and the reactivity of Cu-O$_2$ species. Oxygen can bind to the copper ion either in *end-on* (η^1) or *side-on* mode (η^2) and it can be protonated or not and lead to mononuclear or bridged species. The different active copper-oxygen intermediates and possible reaction pathways for their generation are presented in Scheme 10.
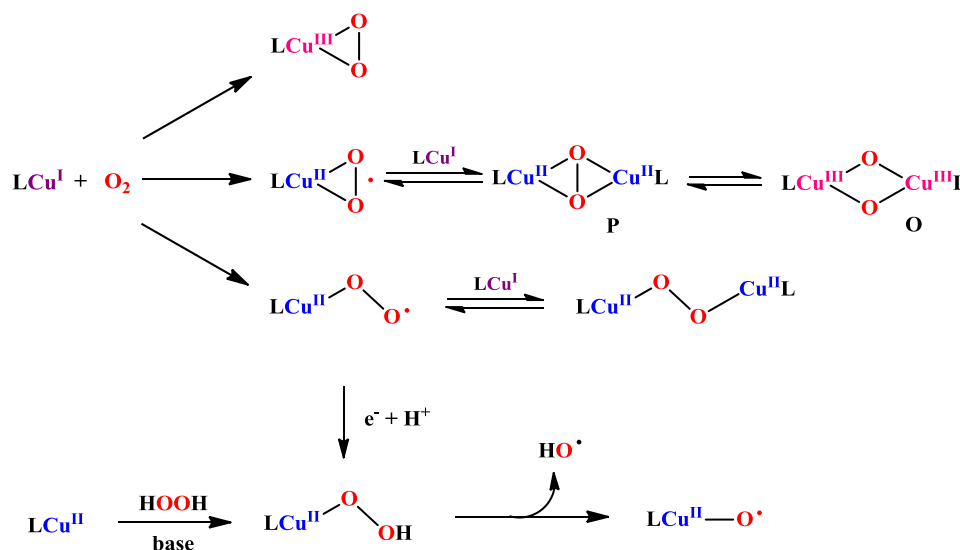
Scheme 10 : O$_2$-derived copper species proposed as reactive intermediates mediating C-H activation.[50]

In the literature, the reaction of a molecule of LCu^{I} complex with one molecule of dioxygen is well documented. It has led to the identification of mononuclear adducts, such as Cu^{II} *superoxide side-on,* Cu^{II} *superoxide end-on* or Cu^{III} *peroxide side-on* complexes, the structure of which depends importantly on the features of the supporting ligand. In many cases, the mononuclear Cu^{II}-dioxygen adducts react rapidly with another LCu^{I} starting complex to give *peroxide* species in which the peroxide is bound in a *side-on* **(P)** or an *end-on* mode. The dinuclear *side-on* Cu^{II} *peroxide* species exist in equilibrium with Cu^{III} *bis-μ-oxido* **(O)** species due to their low isomerization energy barrier.[51] This equilibrium is dependant on the experimental conditions (solvent, temperature) as well as on the nature of the supporting ligands that can favor or disfavor Cu^{III} oxidation state.

Mononuclear Cu^{II}-hydroperoxide complex have also been isolated at low temperature. They can be formed from hydrogen atom transfer to the mononuclear *end-on* superoxo, but have been isolated, in most cases, from addition of hydrogen peroxide (H$_2$O$_2$) on LCu^{II} (or in some cases LCu^{I}) precursors following the *peroxide shunt pathway.*[52]

Finally, copper-oxyl intermediates have only been observed in the gas phase but their reactivity was evaluated through the generation of Cu-alkylperoxide (CuOOR) species that evolve through O-O bond cleavage to yield the corresponding high-valent species.[50]

Low temperature UV-Vis spectroscopy is an important technique to characterize copper-oxygen adducts. Associated with vibrational spectroscopy (mainly rRaman spectroscopy) and the help of oxygen isotope substitution (^{18}O$_2$), it has been used to monitor and identify the various types of Cu/O$_2$ species (Table 1).

I.3.3. Characteristics of the ligands

A large amount of data exist in the literature[3,53] concerning the reactions of Cu^{I} complexes with dioxygen which have been spectroscopically and/or structurally characterized. Subtle variations of ligands and experimental conditions (solvent, temperature) have been used in order to stabilize different types of Cu/O$_2$ species.[54,55]

The Cu/O$_2$ structure, redox properties, nuclearity (mono- *vs.* dinuclear), stability and reactivity vary depending on the nature of the ligand and in particular depending on (i) the geometry and environment around the copper ions, (ii) the nature of donor atoms (alkyl *vs.* pyridyl) (iii) the steric hindrance[56] and (iv) the chelate size of the ligands. Conditions such as temperature, concentration, solvation and counter anions of copper salts can play an important role as well.

In biomimetic studies, most of ligands are designed to mimic the coordination sphere of biological copper active sites, and in general contain amines functions and/or aromatic nitrogen-containing moieties (pyrazole, pyridine, amide or imidazole).

Table 1 : Main spectroscopic features of characterized Cu_x/O_2 species [3,4,57]

Cu/O$_2$ species	UV-Vis ε (mM^{-1} cm^{-1})	rR Vibrations ($\Delta^{18}O_2$)/ cm^{-1}
Cu^{III} (O)(O) Cu^{III}	*ca.* **300 nm (20)** *ca.* **400 nm (24)**	**ν (Cu-O) = 606 (23)**
Cu^{II} (O)(O) Cu^{II}	*ca.* **360 nm (24)** *ca.* **530 nm (1)**	**ν (Cu-Cu) = 284 (0)** **ν (O-O) = 763 (40)**
Cu^{II} O-O •	*ca.* **500 nm (2)** *ca.* **650 nm (sh)**	**ν (Cu-O) = 742 (20)** **ν (O-O) = 1121 (63)**
Cu^{II} (O)(O) •	*ca.* **380-420 nm**	**ν (Cu-O) = 554 (20)** **ν (O-O) = 1043 (59)**
Cu^{III} (O)(O)	*ca.* **400 nm (2)**	**ν (O-O) = 965 (50)**
LCu^{II} O-O-OH	*ca.* **350-400 nm (1)**	**ν (Cu-O) = 332 (10)** **ν (O-O) = 892 (52)**
Cu^{II} O-O Cu^{II}	*ca.* **530 nm (6-11)** *ca.* **600 (sh)**	**ν (Cu-O) = 561 (26)** **ν (O-O) = 832 (44)**
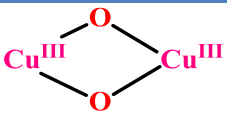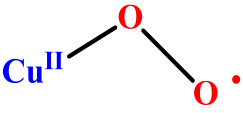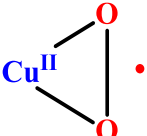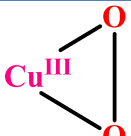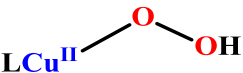
Neutral ligands are the most commonly used, however, Cu^{I} complexes supported by monoanionic ligands are more reducing and upon oxygenation form more stable copper-dioxygen intermediates that can be isolated (but that are in consequence less oxidizing).

The number of nitrogen atoms that are coordinated to copper, the so-called denticity, influences also the reactivity of Cu^{I} complexes with dioxygen. Cu^{I} complexes containing bi- and tridentate ligands allow the *side–on* coordination of dioxygen to copper, while complexes containing tetradentate ligands allow the *end-on* mode.

The mixture of those factors determines whether the reaction between copper complex and dioxygen is facilitated or if the copper-oxygen adduct is stable or isolable.

I.4. Bioinspired Cu/O$_2$ complexes and their reactivity towards external substrates

I.4.1. First model: an hemocyanin model

In 1992, Kitajima and coworkers were the pioneers and reported the first μ-η^2:η^2 peroxo structure supported by bulky tris(pyrazolyl)borate ligand [Cu[HB(3,5-iPrpz)$_3$]]$_2$(O$_2$)]. The spectroscopic parameters were found highly to those of oxy-hemocyanin (Figure 7).[3,6]

Cu---Cu	3.56	Cu–N$_{eq\ avg}$	2.00
O–O	1.41	Cu–N$_{ax\ avg}$	2.26
Cu–O$_{avg}$	1.91		
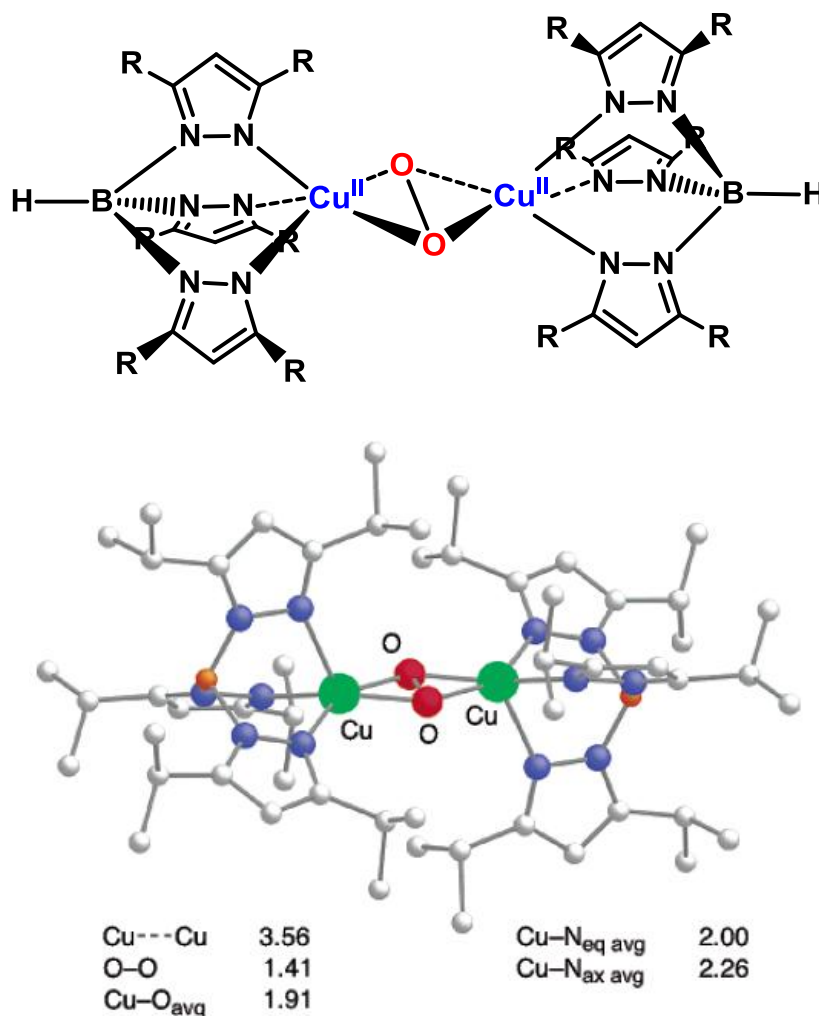
Figure 7 : Schematic representation of [Cu[HB(3,5-iPrpz)$_3$]]$_2$(O$_2$)] (R=iPr) and crystallographic structure.

UV-Vis spectrum of the intermediate is dominated by characteristic absorption bands at 350 nm and 550 nm and the species is diamagnetic due to strong antiferromagnetic coupling between the two copper atoms.

I.4.2. RPY₂ type ligands

In the laboratory, the group of Dr. Marius Réglier has developed an expertise in the study of the reaction of dioxygen with copper complexes based on tridentate ligand systems RPY_2 (where RPY_2 = (N,N-bis-[2-(2-pyridyl)ethyl] alkylamines), presented in Scheme 11. This type of ligands has also greatly contributed to the clarification of the structure and reactivity of various copper-oxygen species. Therefore, a special attention will be dedicated to this family of ligands in this bibliographic section.
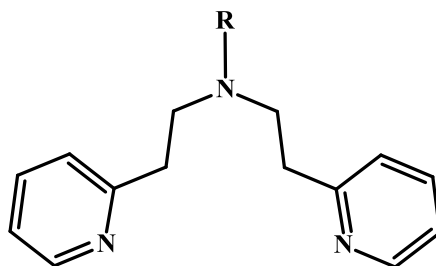
Scheme 11 : General representation of tridentate ligand RPY_2 systems (where RPY_2 = (N,N-bis-[2-(2-pyridyl)ethyl] alkylamines)

Generally, RPY_2 ligands coordinate copper (II) mostly in square pyramidal geometry with either the pyridine or the amine positioned in the axial position. On the contrary, copper(I) is generally coordinated in *mer* fashion in a T-shaped or trigonal planal geometry.[3,58] X-ray structures of representative Cu(I) complexes obtained with this family of ligands are displayed in Figure 8 $[(PhPY_2)Cu^I](PF_6)$[58] in trigonal planar geometry and $[(NMe_2-MePY_2)Cu^I](BArF)$[59] in distorted three coordinate geometry.

$$[(PhPY_2)Cu^I]^+ \qquad [(NMe_2-MePY_2)Cu^I]^+$$
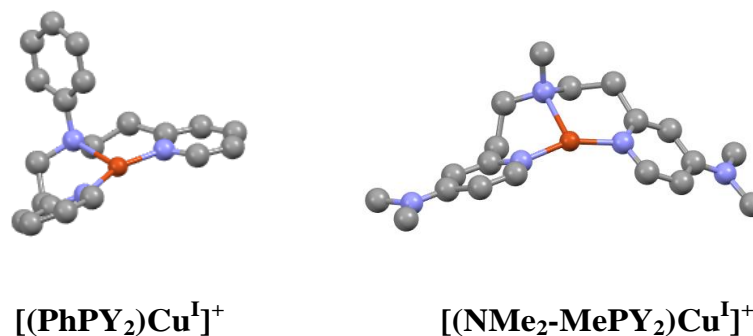
Figure 8 : X-ray structures of $[(PhPY_2)Cu^I]^+$ and $[(NMe_2-CH_3PY_2)Cu^I]^+$ complexes. Counterions and hydrogens are removed for clarity.

Oxygenation at -80°C of $[PhPY_2Cu^I]^+$ yielded mainly peroxo ^{SP} $[(PhPY_2)_2Cu^{II}_2(O_2)]^{2+}$, while $[MePY_2Cu^I]^+$ species form primarily ^{SP} $[(MePY_2)_2Cu^{II}_2(O_2)]^{2+}$ but a small amount of **O** $[(MePY_2)_2Cu^{III}_2(O_2)]^{2+}$ is also present in aprotic solvents such as CH_2Cl_2, THF and acetone.[3] In addition, reaction of $[MePY_2Cu^I]^+$ complex with O_2 requires 45 min to fully develop the maximum intensity

at 360 nm, while the reaction with $[PhPY_2Cu^I]^+$ needs 90 min. This is consistent with the electron donating capacities of the substituent (CH_3>Ph) highlighting the importance of electronic effects on the formation and stability of Cu/O_2 adducts.[58,60]

The influence of electronic factors on the **P/O** equilibrium has also been extensively studied using the $MePY_2$-based systems and varying the substituent at the 4-pyridine position from H to MeO ($R-MePY_2$).[59,62,63] The electronic donating capacity of the ligand shifts the equilibrium towards the formation of **O** species which is attributed to a better stabilization of Cu^{III} oxidation state (Table 2).

Table 2 : Spectroscopic features of ^SP and O intermediates in the case of $R-MePY_2$ based systems.[3,62]

R	^SP:O	solvent	anion	UV-Vis (ε , M^{-1} cm^{-1})		rR: ν, cm^{-1} (Δ [^{18}O])	
				^SP	O	^SP	O
H	90:10	CH_2Cl_2	BArF⁻	356 (14800)	410 (2 900) 530 (570)	729 (40)	587 (26)
MeO	88:12	CH_2Cl_2	BArF⁻	356 (20000)	410 (3 500) 535 (1 000) 650 (750)	728 (39)	585 (26)
Me₂N	86:14	CH_2Cl_2	BArF⁻	360 (21000)	410 (sh) 515 (1 400) 650 (730)	729 (40)	548 (26)

I.4.3. Reactivity vs. exogenous substrates

The **O** or **P** adducts formed are rather stable at low temperature in the absence of the exogenous substrate (decomposition rates < 10^{-7} s^{-1}), but upon warming, O-O bond cleavage occurs and Cu^{II}-O-Cu^{II} complexes are formed. If the oxygenation of Cu^I complexes is carried out in a wet solvent or if water is added to the copper intermediates, decomposition into dihydroxo bridged dicopper(II) species is observed (Scheme 12).[58,60]

The same dihydroxo bridged dicopper(II) species is obtained after addition of the external substrates on the **P** or **O** intermediates.

A wide range of reactions with exogenous substrates have been studied,[59,61] such as conversion of tetrahydrofuran to 2-hydroxytetrahydrofuran, alcohols to aldehydes or ketones, phenols oxidation, 9,10-dihydroanthracene to anthracene, 1,4 cyclohexadiene to benzene and N,N-dimethylaniline to methylaniline and formaldehyde. After the reaction of the mixture of Cu^{II} peroxo complex and the Cu^{III} bis(μ-oxo) complex with the added substrate, the Cu_2-bis(μ-hydroxo) complex and the oxidized substrate are formed (Scheme 13).
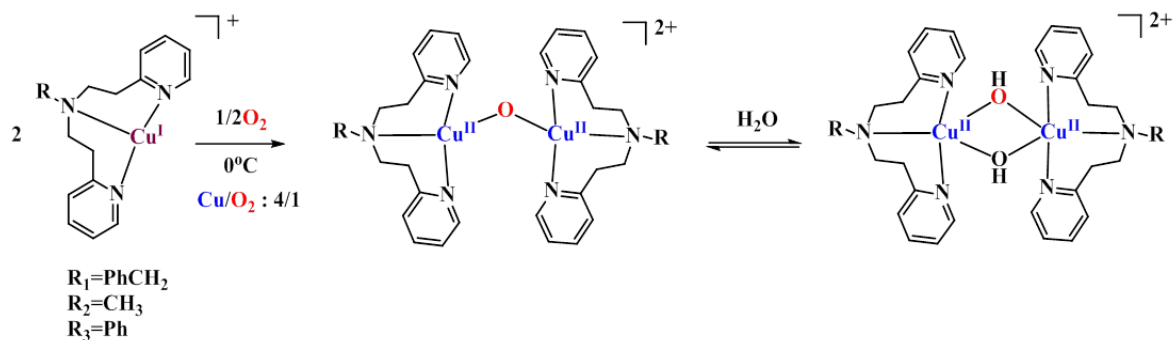
Scheme 12 : Schematic representation of dinuclear Cu^{II}-O-Cu^{II} species produced after the reaction of Cu^{I} species with dioxygen at 0°C. Addition of water led to the formation of dinuclear Cu_2(bis-µ-hydroxo) species.

Those results showed the ability of those oxidants to react with exogenous hydrocarbon substrates, owing to the electrophilicity of their oxygen atoms. Yields and reaction rates increased when more electron donating supporting ligands (e.g. Me_2N-$MePY_2$) were used, but the origin of this enhanced reactivity has not been fully determined.[59]
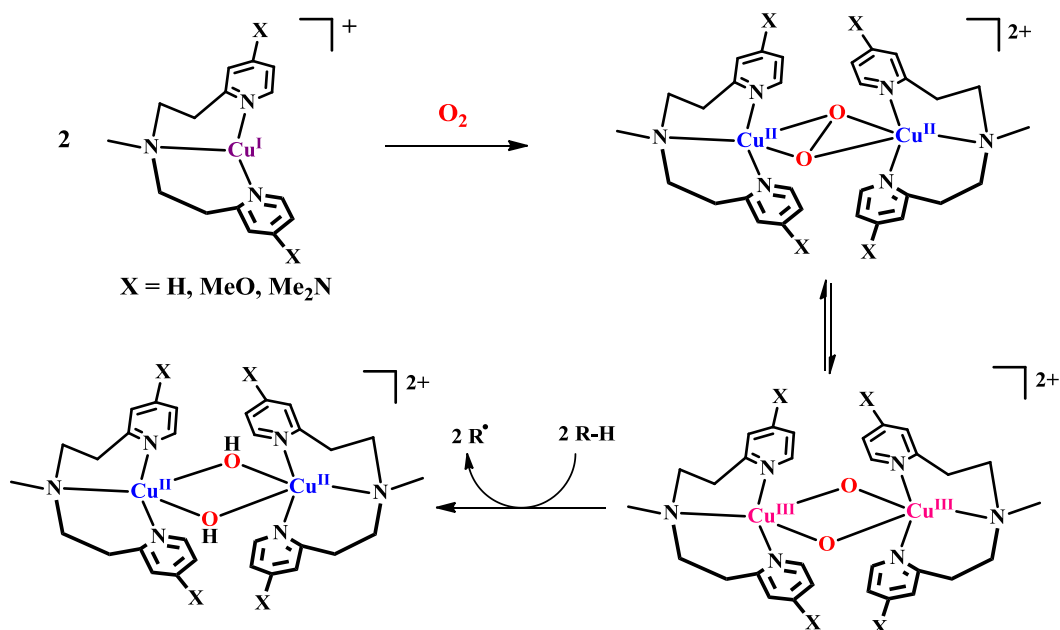
Scheme 13 : Schematic representation of the reaction of Cu/O_2 adducts supported by X-$MePY_2$ ligands with external substrates in C-H bond activation (substrates = DHA, THF etc.).[59]

I.5. Intramolecular reaction of Copper-Dioxygen complexes

In some cases, ligands bearing an internal substrate (the so called "substrate-binding ligand approach") were used to monitor the intramolecular C-H bond activation.[3,64] A diversity of ligands were used to monitor several hydroxylation positions. Such systems are of particular interest to investigate alkane or aromatic hydroxylation reactions as performed by pMMO, Tyrosinase etc.

I.5.1 Aromatic hydroxylation of the ligand

Karlin *et al.* described the first example of "aromatic hydroxylation of the ligand" after the reaction of a binuclear Cu^I complex with dioxygen, opening the current research field of Cu/O_2 bioinorganic chemistry. Using a bridging ligand with a m-xylene spacer, the reaction of the Cu^I precursor with O_2 resulted in the generation of dicopper μ-η^2:η^2-peroxo that was characterized at low temperature. After warming at room temperature, the m-xylene spacer of the ligand was hydroxylated in the 2-position resulting from electrophilic attack of the side on peroxo dicopper unit **P** on the π system of the aromatic ring (Scheme 14).[65] This reaction is relevant to the activity of tyrosinase in which a coupled dinuclear copper complex converts phenols to catechols probably through a peroxo **P** intermediate.
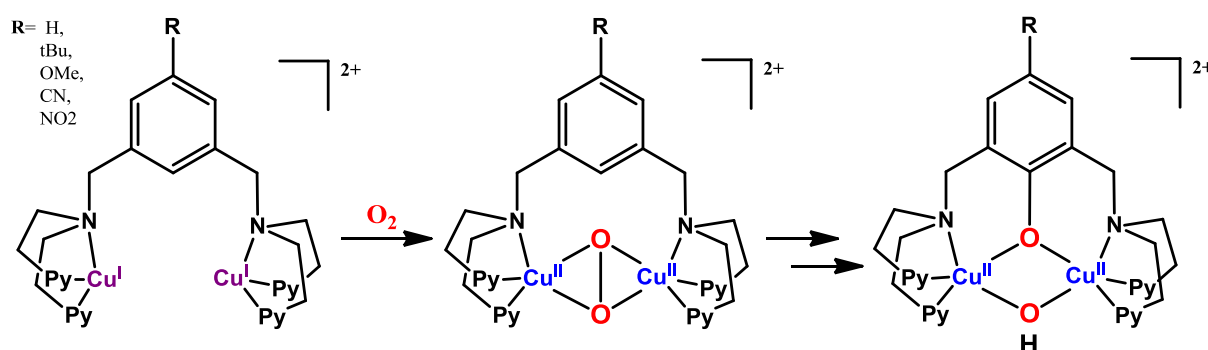
Scheme 14 : Schematic representation of aromatic hydroxylation of the ligand by a dinuclear copper peroxo **P** complex.

In addition, the ability of the dicopper bis(μ-oxo) **O** species to transfer an oxygen atom to an internal aromatic substrate has been also established.[66] Using a simple phenyl-substituted ligand, the formation of the **O** species after exposure to dioxygen was monitored by its characteristic absorption features. The absence of O-O vibration mode in rRaman spectrum is consistent with the presence of **O** species and only a small amount of peroxo **P** species. After ligand extraction using ammonia solutions, analysis revealed that intramolecular hydroxylation occurred on the aromatic ring suggesting that the **O** species are also capable of arene hydroxylation reactions (Scheme 15).
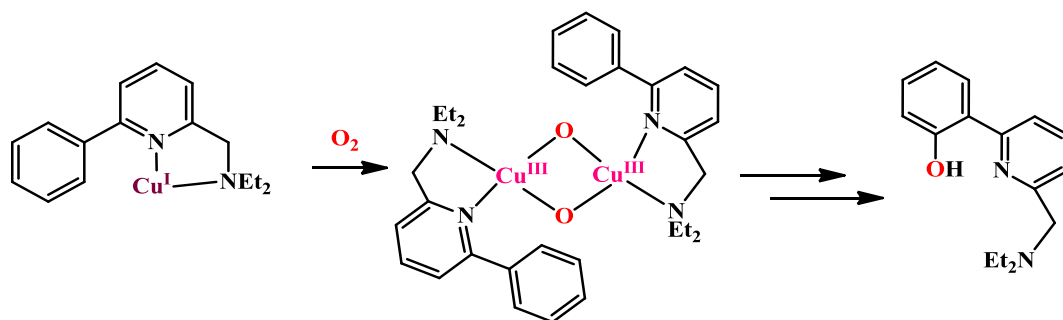
Scheme 15 : Schematic representation of aromatic hydroxylation of the ligand by a dinuclear copper bis-μ-oxo **O** species.

I.5.2. Aliphatic hydroxylation of the ligand

In contrast to the *aromatic ligand hydroxylation*, Tolman and coworkers described *aliphatic ligand hydroxylation*. They have described the reaction of Cu^I complex $[(LiPr3)Cu^I(CH_3CN)]^+$ (L = 1,4,7-tri-isopropyl-1,4,7-triazacyclononane) with O_2 in CH_2Cl_2 at -80°C that resulted in the formation of $μ-η^2:η^2$-peroxo dicopper species (Scheme 16), followed by hydrogen atom abstraction from a methyl of the isopropyl group.[67] Interestingly, interconversion between ^SP and **O** species is observed by changing the solvent. Both species are EPR silent but they can be distinguishable by UV-Vis and rRaman parameters.
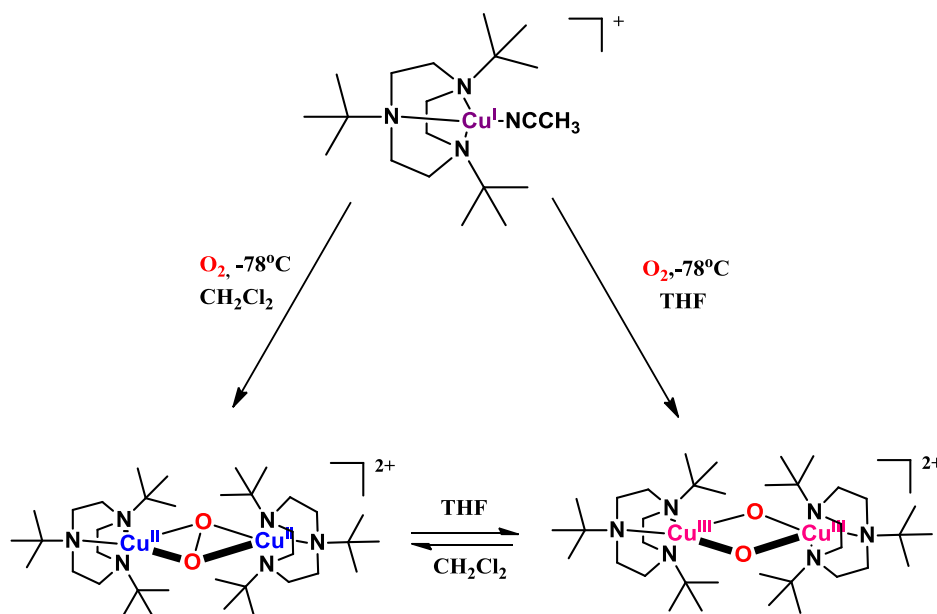
Scheme 16 : Synthesis and interconversion of $[(LiPr3)Cu^I(CH_3CN)]^+$

Itoh and co-workers have reported the aliphatic hydroxylation using the RPY_2 family of ligands.[68] After ligand extraction using ammonia solutions, intramolecular hydroxylation occurred selectively at the β-position of the tertiary amine of the "substrate" moiety of the ligand (Scheme 17). Interconversion was not observed in this case by changing the solvent, however the authors proposed the bis(μ-oxo) **O** species as active species for the aliphatic hydroxylation of the ligand.

X= H, CH$_3$,Cl, NO$_2$
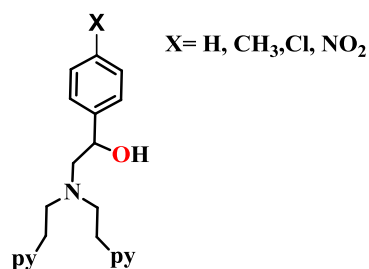
Scheme 17 : Selective ligand hydroxylation on the β-position of the ligand.

Réglier and coworkers reported the reactions with dioxygen of new RPY$_2$ ligands in which different internal substrate moieties (R) were used including: propyl (*n*Pr) or cyclopentyl (*c*Pt) groups.[69] Aminoindane was also used as internal substrate in order to study the stereochemistry and stereoselectivity of oxygen atom transfer.[70] Indeed, 2-aminoindane has two pro-chiral centers and each one bear two hydrogen atoms. At the end, hydroxylation can yield to two pairs of stereo-isomers with the OH group either in *cis* or in *trans* from the C-N bond (Scheme 18).
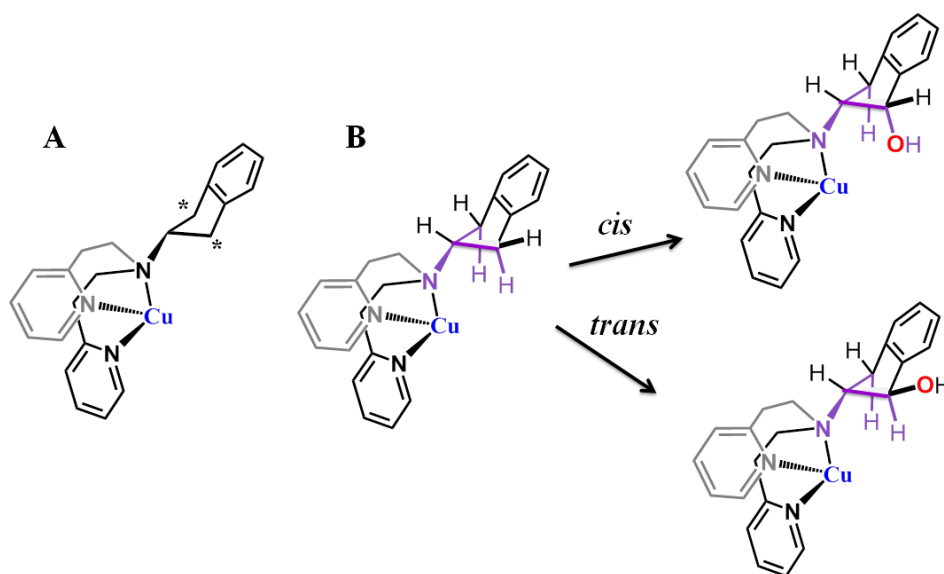
Scheme 18 : A. Schematic representation of the pro-chiral centers (positions with asterisks) of the IndanePY$_2$ ligand **B.** the stereochemistry of O-atom insertion (*cis* or *trans*) regarding to the tertiary amine N group.

After reaction with dioxygen, selective *cis*-hydroxylation of the ligand was obtained. This was rationalized by intramolecular H-abstraction from a copper-oxygen intermediate (possibly binuclear peroxo or oxo species) and rebound mechanism with retention of configuration as presented on Figure 9 and rebound mechanism with retention of configuration.
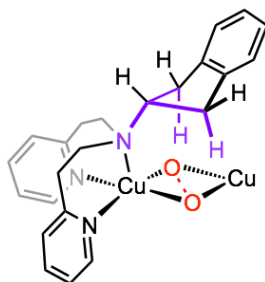
Figure 9 : Formation of copper-oxygen intermediate, dinuclear peroxo or bis-μ-oxo, for intramolecular H-atom abstraction of the indane moiety.

I.6. Hydrogen Atom Abstraction by [CuOH]$^{2+}$ core

A series of Cu^{III} complexes supported by alkoxide-polyanionic ligands, which are very powerful donors for stabilizing high oxidation states, were reported in the literature.[71] Using an electron donating N,N′-bis(2,6-diisopropylphenyl)-2,6-pyridinedicarboxamide ligand, Tolman and coworkers have recently investigated the formation of a Cu^{III}-OH species generated by one-electron oxidation of the Cu^{II}-OH precursor (Scheme 19).[72,73,74] The one electron-oxidation of Cu^{II} to Cu^{III} is reversible ($E_{1/2}$= -0.0076V *vs.* Fc/Fc$^+$). The Cu^{III}-OH was extensively characterized by Cu K-edge absorption edge energies and DFT calculations. Importantly, those species are capable of attacking C-H bonds of various substrates such as dihydroanthracene, resulting to the formation of Cu^{II}-OH$_2$ complexes and anthracene. The rapid reaction and the large kinetic isotope effect (k_H/k_D = 44 at −70 °C) is consistent with a rate-determining hydrogen atom abstraction (HAT) mechanism. Varying the electron-donating capabilities of the supporting ligands affects the redox potentials of the Cu^{III}/Cu^{II} couple and consequently the kinetics of the HAT reactions.[72]
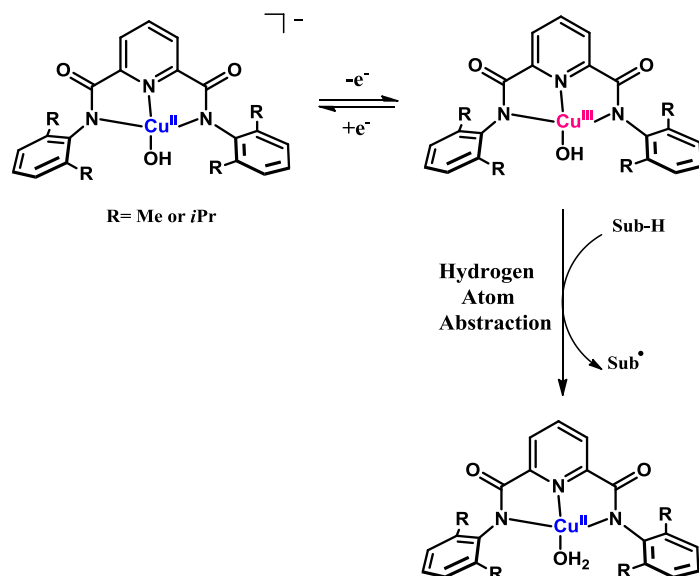
Scheme 19 : Synthesis of Cu^{III}-OH complex and reactivity towards external substrate. Sub-H is a hydrocarbon (DHA, THF, cyclohexane).

The characterization of those Cu(III)-OH species is of importance since it provides experimental support of their ability to perform C-H bond activation, and thus it highlights their possible involvement in biological copper-based oxidation catalysis.

I.7. Mixed valent Cu^{II}Cu^{III} intermediates

Interestingly, from theoretical studies it has been postulated that mixed-valent Cu^{II}Cu^{III} species could be the oxidizing intermediate in the catalytic cycle in pMMO enzyme.[75] Tolman and coworkers have isolated the first Cu^{II}Cu^{III} species at low temperature.[76] Using a macrocyclic ligand containing electron donating pyridinedicarboxamide moieties, they performed the one-electron chemical oxidation of the Cu^{II}$_2$(µ-hydroxo) precursor at low temperature (Scheme 20). The EPR spectrum of the oxidized species reveals an axial signal with hyperfine splitting of Cu^{II} complex consistent with the description of a localized Cu^{II}Cu^{III} mixed-valent species.

Cu^{II}Cu^{II} (µ-OH)   Cu^{II}Cu^{III} (µ-OH)   Cu^{III}Cu^{III} (µ-OH)
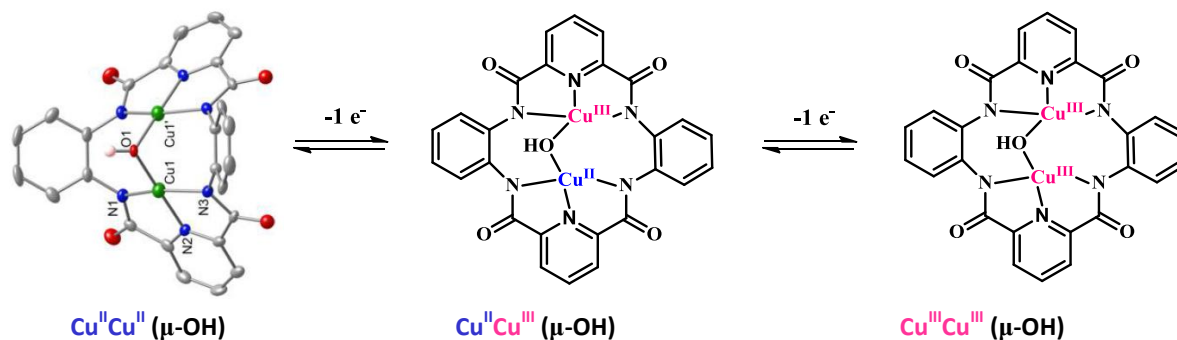
Scheme 20 : Proposed oxidized products of Cu^{II}Cu^{II} (µ-OH).

Recently, Belle and coworkers reported the second example of such intermediate starting from the bis(μ-hydroxo)Cu$^{II}_2$ complex with the DPMN= 2,7-bis(dipyridyl)methyl)-1,8-naphthyridine ligand (Figure 10).[77] After one electron oxidation of the dicopper(II) complex, a new mixed valent Cu^{II}Cu^{III} species has been characterized. This mixed-valent species is relatively stable at room temperature. After electrolysis at low temperature, UV-Vis spectra revealed the appearance of an absorption band at 424 nm (LMCT py→Cu^{III}) and EPR spectra consistent with a localized valence as previously described by Tolman.[76] Further DFT calculations indicated, in agreement with the experimental data, that no deprotonation occurs during the oxidation process. No reactivity of this complex has been reported yet.
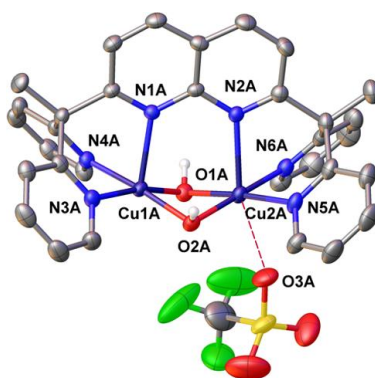
Figure 10 : Molecular structure of the Cu^{II}Cu^{II} (bis-μ-hydroxo) complex.

II. Objectives

Model complexes for copper-containing monooxygenases have therefore provided valuable information on the structure and reactivity of several copper-dioxygen adducts. However, mechanistic features are still unclear. In addition, the recent discovery of two new enzymatic systems (LPMO and pMMO) able to perform activation of very strong C-H bonds has re-opened the debate on the catalytically relevant copper-dioxygen species. The use of model systems that mimic an enzyme is a simple approach to obtain a better knowledge of how nature works.

In the present work, we aimed at re-investigating the copper-mediated dioxygen activation pathways using simple copper complexes based on RPY_2-type ligands (Scheme 21). We chose ligands bearing indane, cyclopentyl or propyl groups as internal substrates, as previously developed in our laboratory. Our choice aimed at following the stereo-selectivity of the reaction towards activated and non-activated C-H bonds and therefore monitor metal-centered mechanism.[69,70] We have also selected the $MePY_2$ ligand to provide a similar system without internal substrate for comparison when needed.

IndanePY$_2$ **CyclopentylPY$_2$** **$n$propylPY$_2$** **MePY$_2$**
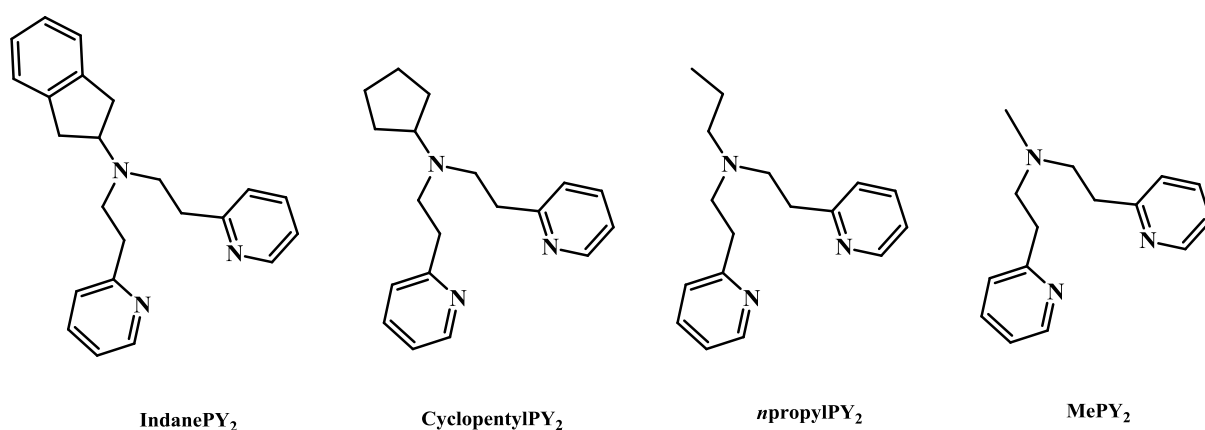
Scheme 21 : RPY2 ligands used in the present work. R= Indane, cyclopentyl, $n$propyl, and methyl group.

Armed with these simple systems:
- In the first part of the dissertation (Chapter II), we have studied the effect of O-atom donors (O$_2$, PhIO, H$_2$O$_2$ etc.) on the type of copper-oxygen adducts formed and provided data on their comparative O-atom transfer reactivity.
- In the second part (Chapter III), we have explored the ability to use water as an alternative O-atom donor for O-atom transfer reactions.
- In the third part of the dissertation (Chapter IV), we have focused on the modulation of the electronic properties of high-valent bis(μ-oxo) cores by preparing heterobimetallic Cu-Ni intermediates. We have synthesized new

heterobimetallic Cu-Ni complexes and investigated their electronic properties and their reactivity towards internal and external substrates.

Chapter II

Intramolecular O-atom transfer: Effect of the oxidant.

I. Introduction and context

I.1. Previous results using substrate-bound ligands

As already mentioned in the **Chapter I**, the use of substrate-bound containing ligands have provided valuable information on the reaction of copper-oxygen species in O-atom transfer reactions. In particular, a few years ago, the group of Marius Réglier has extensively studied the reaction using several RPY_2 ligands in which R contains a substrate moiety (Scheme 22).[69,70,78] Starting from mononuclear Cu^I complexes ligated to IndanePY$_2$ ligand, the *cis*-2-amino-1-indol ligand product was obtained in 50% yield. Kinetic isotopic effects of k_H/k_D =7.6 revealed that C-H cleavage is the rate determining step producing the hydroxylated products with retention of configuration. On the contrary, when using ligands such as nPrPY$_2$ and cPtPY$_2$, no hydroxylation was observed on the internal substrate moieties resulting in the quantitative recovery of the initial ligand after extraction at the end of the reaction.
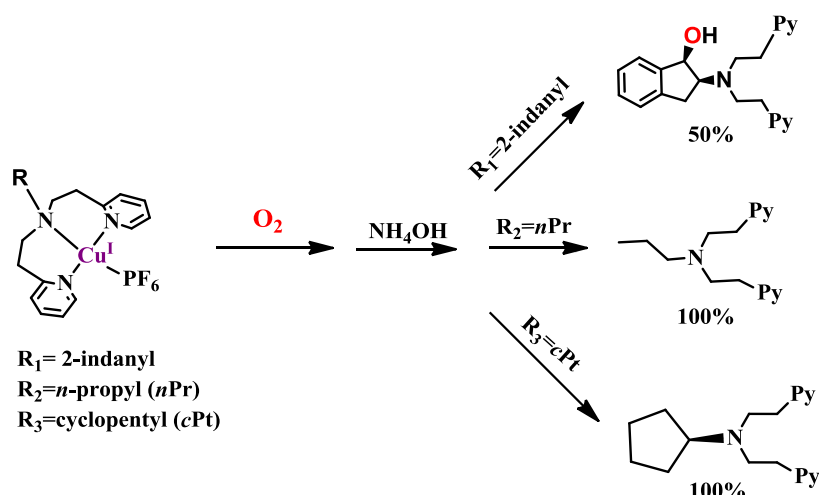
Scheme 22 : Schematic representation of reaction of Cu^I complexes with dioxygen and the products formed. Only when R=indane, the *cis*-hydroxylated products were observed. In the other two cases, the initial ligand was recovered.

Starting from IndanePY$_2$Cu^{II} precursor and in the presence of excess of reductant (benzoin/triethylamine system) the aminoindane substrate was quantitatively hydroxylated with a *cis* stereochemistry, *i.e.* higher than the hydroxylation yield of 50% obtained in the case of the Cu^I + O_2 reaction. A symmetric dicopper (II) complex was crystallized at the end of the reaction displaying the hydroxylated alkoxide functions of the ligand bridging the two copper ions (Scheme 23). Kinetic isotopic effects under those conditions were estimated to k_H/k_D =11.
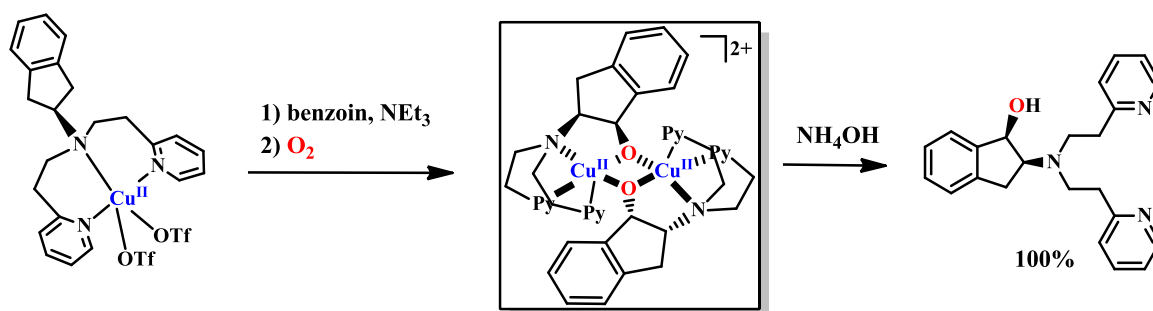
Scheme 23 : Schematic representation of the formation of *cis*-(OH)-IndanePY$_2$ product after the reaction of IndanePY$_2$Cu^{II} complex with O$_2$ in presence of benzoin/Et$_3$N system.

Interestingly, exposure of [*n*PrPY$_2$]Cu^{II}(OTf)$_2$ to dioxygen after treatment with benzoin and triethylamine, led to hydroxylation at β-position of the pyridine groups as the main product and a small amount of the compound hydroxylated at the β-position of the *n*-propyl group. In addition, when [*c*PtPY$_2$]Cu^{II}(OTf)$_2$ was reacted with dioxygen in the same conditions, β-*cis* hydroxylation of the cyclopentane ring was obtained (Scheme 24).
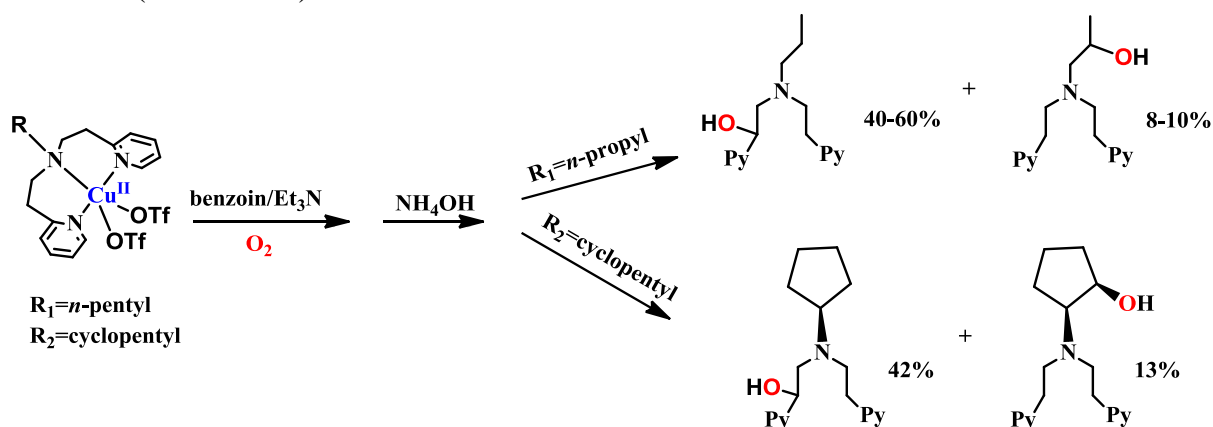
Scheme 24 : Schematic representation of the hydroxylated products formed after the reaction of RPY$_2$Cu^{II} complexes with O$_2$ in the presence of benzoin/Et$_3$N system.

The hydroxylation of the inactive C-H bond of *n*PrPY$_2$ and *c*PtPY$_2$ ligands only occurred in the presence of benzoin (as reductant). This may be related to the involvement of different copper-oxygen species of different oxidizing power. It has been well established in the literature that the reaction of Cu^{I} with dioxygen using RPY$_2$-type ligands leads to **O** or **P** intermediates (see **Chapter I**).[3] In the presence of excess reductant, it is possible that these species are further reduced to yield Cu^{II}Cu^{III} mixed-valent species that would be stronger oxidizing intermediates, able to transfer an oxygen atom at non-activated positions. These types of mixed-valent species were proposed to be key intermediates for the hydroxylation of the strong C-H bond of methane to methanol in pMMO,[75] shedding light on their possible involvement in the present reactivities.

Also, differencies in the kinetic isotopic effects observed in the Cu^I/O_2 system and Cu^{II}/O_2/benzoin/triethylamine system, (7.6 *vs.* 11) indicates the possibility of different "copper-oxygen" intermediates involved in those conditions.

The possible involvement of different copper-oxygen species (as compared to **P** and **O**) in the catalytic cycles of copper-containing monooxygenases has led us to re-investigate the reactivity of RPY_2-based systems in different conditions. We have selected the indane and the cyclopentyl substrate as the stereoselectivity of the reaction allows us to rule out any non-centered reactive species. For comparison, a complex without bound substrate ($MePY_2$) was also prepared. The reactivity was then monitored in presence of dioxygen with or without a reductant, as well as in the presence of other oxidants such as hydrogen peroxide, iodosylbenzene and sodium hypochlorite. The experiments were performed starting from either Cu^I or Cu^{II} precursors and in different solvents. The oxygen atom source was further investigated by isotopic labeling.

II.   Synthesis and characterization of the copper complexes

II.1. Synthesis or Cu^I and Cu^{II} complexes liganded to $IndanePY_2$

II.1.1. Synthesis and structural characterization

The ligand $IndanePY_2$ was obtained by Michael-type addition of 2-aminoindane with 2-vinylpyridine freshly distilled in a MeOH/acetic acid mixture (reflux 5 days, yield: 30%). The $[IndanePY_2Cu^I]^+$ complex **1a** was prepared *in situ* inside the glove box by mixing the ligand and 1 eq. of $[(CH_3CN)_4Cu^I]PF_6$ in degassed dichloromethane.

The corresponding copper(II) complex **2a** was prepared by mixing $Cu(OTf)_2$ with 1 eq. of $IndanePY_2$ ligand in methanol. The recrystallization of the complex in dichloromethane with diffusion of ether gave blue crystals suitable for X-ray diffraction. The structure that has been previously reported is displayed (Figure 11).[70] The complex has two triflate ions coordinated to the copper ion.
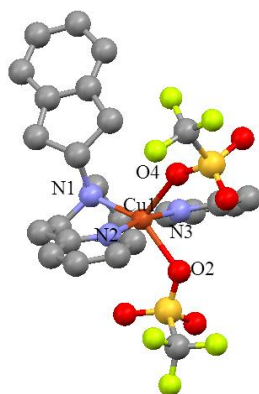
Figure 11 : Crystal structure of [Cu(CF$_3$SO$_3$)$_2$(IndanePY$_2$)] (**2a**). Hydrogen atoms were removed for clarity.

II.1.2. EPR spectroscopy of [IndanePY$_2$Cu^{II}(OTf)$_2$]

EPR spectrum of **2a** was recorded at 120K in propylene carbonate giving a typical axial signal of Cu^{II} complex. The EPR parameters were extracted after simulation of the experimental spectrum (g$_{//}$=2.252 and g⊥=2.065 and A$_{//}$=145G). The EPR spetrum is characteristic of S=1/2 axial system. The fact that g// > g⊥ > 2.023 suggests that d$_x{}^2{}_{-y}{}^2$ is the highest energy half-occupied orbital of copper ion. The experimental and simulated spectra are shown in Figure 12. A highly similar EPR spectrum is obtained in other organic solvents (acetone / CH$_2$Cl$_2$).
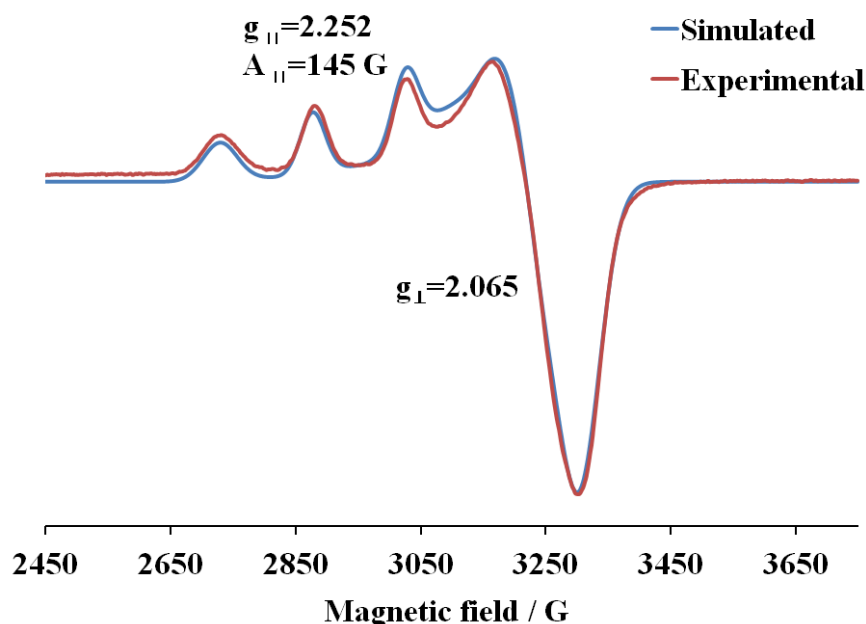
Figure 12 : Experimental and simulated EPR spectra of **2a** in propylene carbonate at 120K.

^{19}F NMR spectra have indicated that triflate counter-anions remain coordinated in CH$_2$Cl$_2$ and probably in most non-coordinating organic solvents (see **Chapter III**).

Furthermore, DFT calculations have been carried out and the Singly Occupied Molecular Orbitals (SOMO) of **2a** (Figure 13) confirmed that the $d_{x^2-y^2}$ is the highest energy half-occupied orbital, consistent with the EPR spectrum.
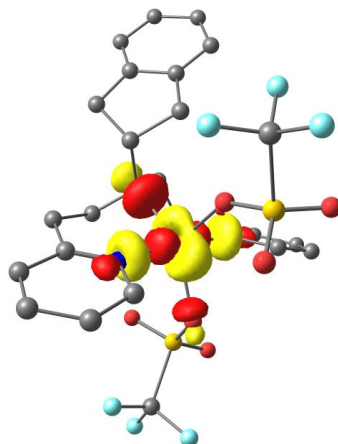
Figure 13 : Singly occupied molecular orbital (SOMO) of copper ion in **2a**.

II.1.3. *Cyclic voltammetry of [IndanePY$_2$Cu^{II}(OTf)$_2$]*

Cyclic voltammetry (CV) of **2a** was performed in propylene carbonate with NaOTf as a supporting electrolyte by using a graphite electrode, a platinum counter electrode and an Ag pseudo-reference electrode. As shown in Figure 14, CV of **2a** in propylene carbonate at 100 mV/s, exhibits a quasi-reversible wave at $E_{1/2}$=-0.1V *vs.* Fc$^+$/Fc assigned to the quasi-reversible redox process of Cu$^{II/I}$ couple. Further oxidation peak of Cu$^{III/II}$ was not observed. This is very similar to the previously reported redox properties in CH$_2$Cl$_2$.[70]
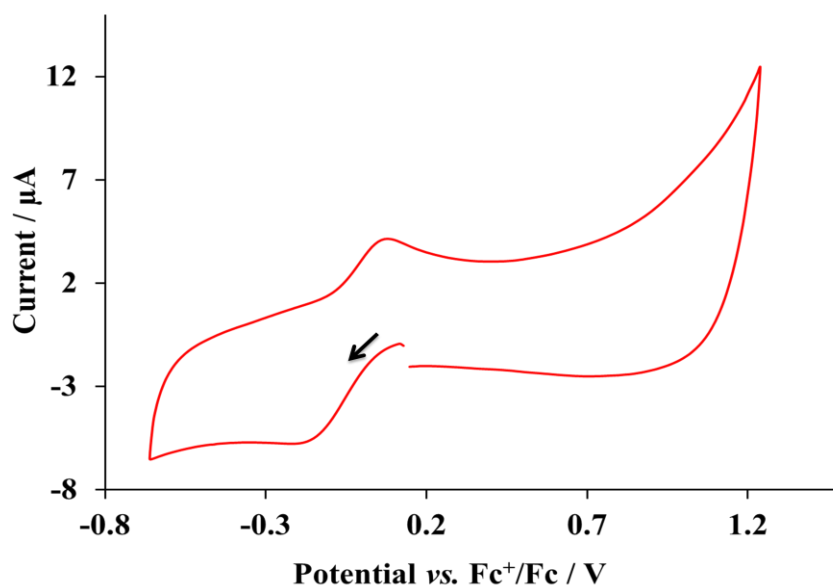
Figure 14 : Cyclovoltamogram of **2a** under inert atmosphere (1mM) in propylene carbonate (0.1M NaOTf), 100 mV/s, Working electrode: Graphite, Pseudo-reference Electrode: 50µM AgNO$_3$/Ag in 0.1 M tBu$_4$NPF$_6$ in acetonitrile. The arrow shows the direction of the scan.

II.2. Cu^I and Cu^{II} complexes liganded to MePY$_2$

II.2.1. Synthesis and structural characterization

MePY$_2$ was prepared following the same procedure as described above for IndanePY$_2$ and 2-(2-methylaminoethyl) pyridine was refluxed in a solution of 2-vinylpyridine/MeOH/acetic acid (30% yield).

The [MePY$_2$Cu^I] complex **1b** was prepared *in situ* inside the glove box by mixing the ligand and 1 eq. of [(CH$_3$CN)$_4$Cu^I]OTf in degassed dichloromethane.

The corresponding copper(II) complex **2b** was prepared by mixing copper(II) triflate salt with 1 eq. of MePY$_2$ ligand in methanol. The recrystallization of the complex in methanol with diffusion of ether gave blue crystals suitable for X-ray diffraction (Figure 15). The triflate anions are not coordinated and two water molecules are bound to copper.
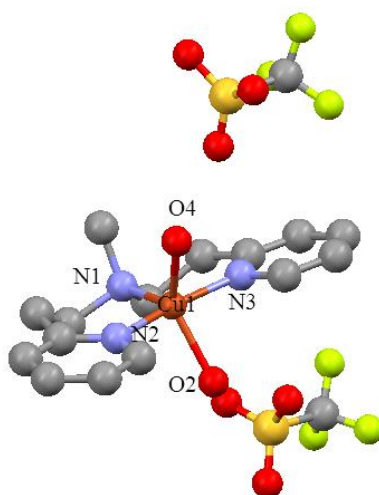
Figure 15 : Crystal structure of [(MePY$_2$)Cu(H$_2$O)$_2$] (**2b**). Hydrogen atoms were removed for clarity.

The global structure of **2b** is very similar to that of **2a**. Selected bond lengths and angles for **2b** are displayed in **Table 3** and compared to the similar parameters in **2a**. The structural parameter τ was calculated as defined by Addison *et al.*[79] This parameter is defined as follow:

$$\tau = \frac{(\alpha - \beta)}{60}$$, where α and β are defined as the greatest angles between adjacent ligands. τ = 0 indicates a perfect square-pyramidal geometry although τ = 1 is found for trigonal bipyramidal geometry.

The value τ = 0.25 indicates that **2b** is in a distorted square-pyramidal geometry and the value τ = 0.57 indicates that **2a** is in an intermediate geometry between square-pyramidal geometry and trigonal bipyramidal geometry.

Table 3 : Bond lengths and Angles based on crystallographic data of **2a** and **2b**.

	2a	2b
Bond lengths (Å)		
Cu1–N1	2.019(7)	2.022(5)
Cu1–N2	2.043(7)	1.978(4)
Cu1–N3	1.977(8)	1.960(4)
Cu1–O2	2.109(8)	2.136(3)
Cu1–O4	2.211(7)	2.105(3)
Angles (deg)		
N1–Cu1–N3	95.9(3)	97.5(2)
N2–Cu1–N3	171.2(3)	166.0(2)
N2–Cu1–N1	92.1(3)	96.3(2)
N1–Cu1–O2	148.4(3)	112.1(2)
N1–Cu1–O4	114.1(3)	120.9(2)
N2–Cu1–O2	86.3(3)	87.6(2)
N2–Cu1–O4	88.7(3)	87.2(2)
N3–Cu1–O2	85.0(3)	85.4(2)
N3–Cu1–O4	91.5(3)	87.4(1)
O2-Cu-O4	97.5(3)	127.0(1)
Structural index		
τ	0.57	0.25

II.2.2. EPR spectroscopy

EPR spectrum of **2b** was recorded at 120K in propylene carbonate giving a typical axial signal of Cu^{II} complex. The EPR parameters were extracted after simulation of the experimental spectrum (g$_{//}$=2.247 and g⊥=2.060 and A$_{//}$=154G), shown in Figure 16.
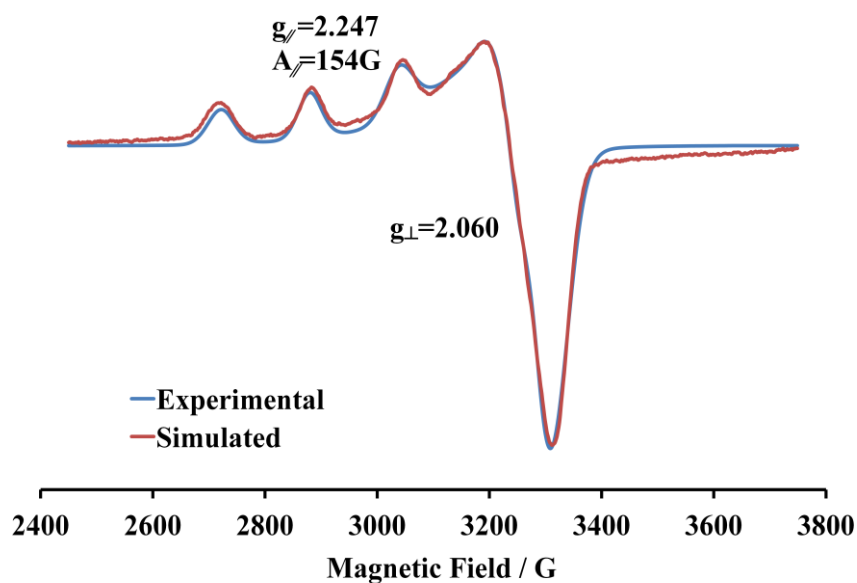
Figure 16 : Experimental and simulated EPR spectra of **2a** in propylene carbonate at 120K.

II.2.3. *Cyclic voltammetry*

CV measurement of **2b** was performed in propylene carbonate with NaOTf as a supporting electrolyte (Figure 17). The CV of **2b** in propylene carbonate at 100 mV/s, exhibits a quasi-reversible wave at $E_{1/2}$= -0.067V *vs.* Fc$^+$/Fc assigned to the quasi-reversible redox process of Cu$^{II/I}$ couple. Further oxidation peak of Cu$^{III/II}$ was not observed as well.
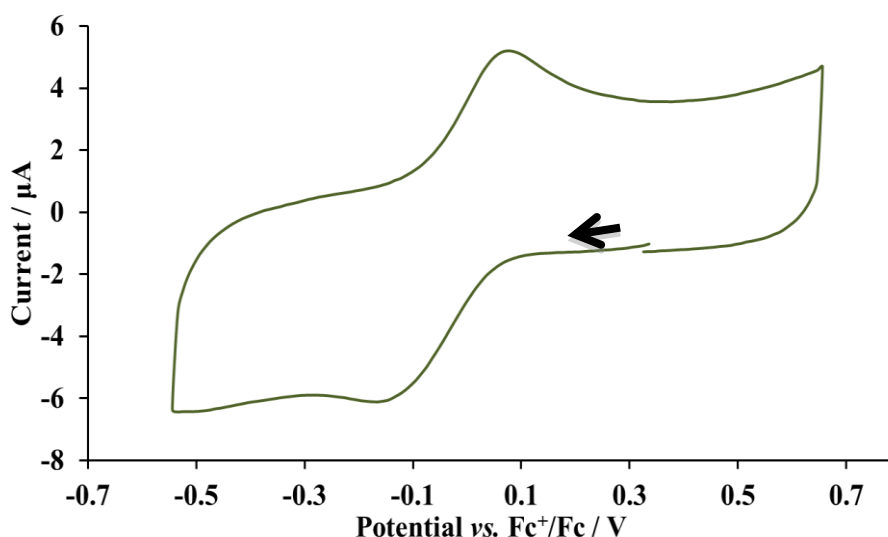
Figure 17 : Cyclic voltammogram of **2b** (1mM) in propylene carbonate (0.1M NaOTf), 100 mV/s Working electrode: Graphite, Pseudo-reference Electrode: 50µM AgNO$_3$/Ag in 0.1 M tBu$_4$NPF$_6$ in acetonitrile. The arrow shows the direction of the scan.

III. Reactions with dioxygen

III.1. General Procedure for the study of O-atom transfer reactions

In the following chapter, after the reaction of Cu^{II} or Cu^{I} complexes with an oxidant or oxygen atom donor, the solution is treated with concentrated ammonia solution followed by extractions with dichloromethane, resulting in the recovery of the crude mixture containing both the un-reacted ligand and the oxidized products. The determination of the products after the reaction and their quantification analysis is performed on the crude mixture by ^{1}H NMR spectroscopy using well-known NMR spectra of each of the possible oxidation products that have been previously reported in the group.[70] The conversion yield is measured by integration of well resolved signals.

In the ^{1}H NMR spectrum of the initial IndanePY$_2$ ligand (Figure 18, bottom), the characteristic quintet peak (at 3.76 ppm) corresponds to the proton of the tertiary carbon (C-N) of the indane moiety (Figure 18, bottom).

On the other hand, it is well established that in the spectrum of the final product *cis*-2-amino-1-indol (or called for clarity *cis*-(OH)-IndanePY$_2$) (Figure 18, top), a doublet peak (at 4.99 ppm) corresponds to the proton of the secondary carbon of the indane moiety, presented in Figure 18 (top), when it is hydroxylated as *cis* stereoisomer.

Integration of those two characteristic peaks allows the estimation of the conversion yield. The ^{18}O isotopic labeling yield was determined, when applicable, by mass spectrometry.
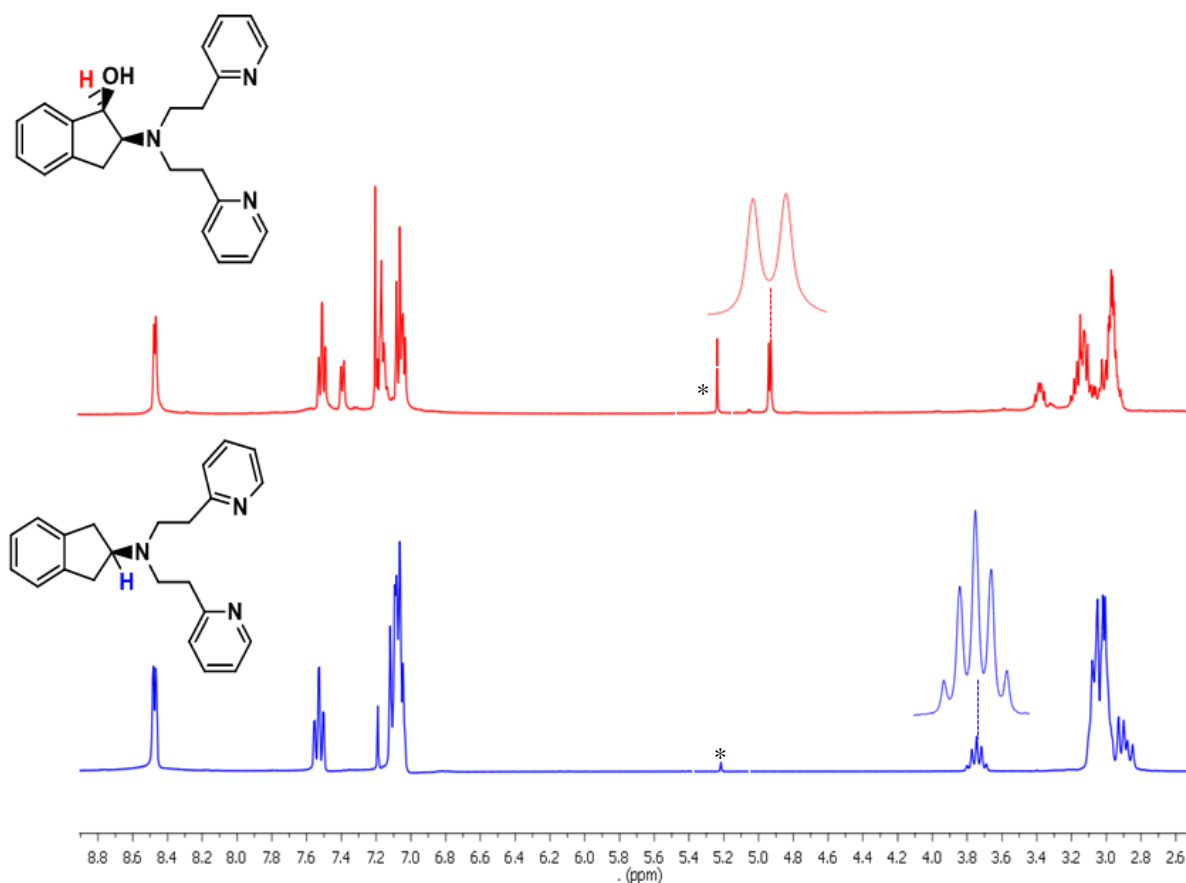
Figure 18 : ^{1}H NMR spectra of the initial ligand IndanePY$_2$ (bottom, blue line) and the *cis*-(OH)-IndanePY$_2$ (top, red line). Peaks originated from the solvent (CH$_2$Cl$_2$) are marked by asterisks.

III.2. Reaction of Cu^I complex with O$_2$

We performed the reaction of [(IndanePY$_2$)Cu^I]PF$_6$ (**1a**) complex with dioxygen in CH$_2$Cl$_2$ as already reported.[70] However, no mechanistic insight, neither labeling experiments had been reported. This reaction was therefore re-investigated here. The Cu^I precursor was prepared *in situ* inside the glove box. After exposure to dioxygen, the pale yellow color changed rapidly to green. Decomplexation with 35% ammonia solution and ^{1}H NMR analysis of the organic products indicated the presence of *cis*-(OH)-IndanePY$_2$ derivative at 50% yield as already reported (Scheme 25).
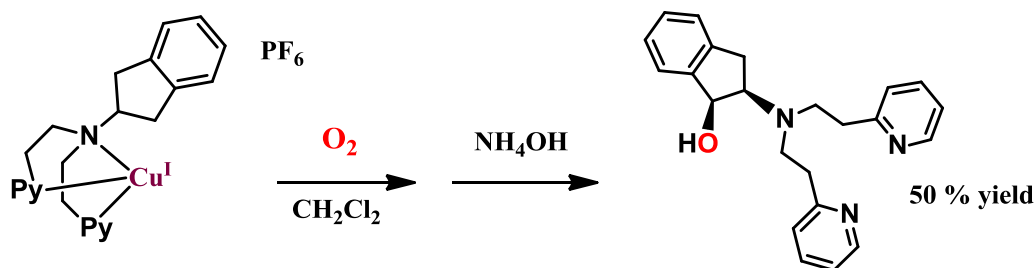
Scheme 25 : Schematic representation of oxidation of **1a** with O_2 in CH_2Cl_2.

The UV-Vis spectrum of $[(IndanePY_2)Cu^I]PF_6$ complex **1a** recorded immediately after exposure to O_2 at room temperature exhibits a transition at 380 nm ($\varepsilon\sim891$ M^{-1} cm^{-1}) and a d-d band at 650 nm ($\varepsilon\sim133$ M^{-1} cm^{-1}) (Figure 19). This is compatible with the presence of a stable Cu^{II} complex at the end of the reaction. Reactions at low temperature (-80°C) did not allow us to trap any intermediate probably because of the intramolecular hydroxylation reaction.
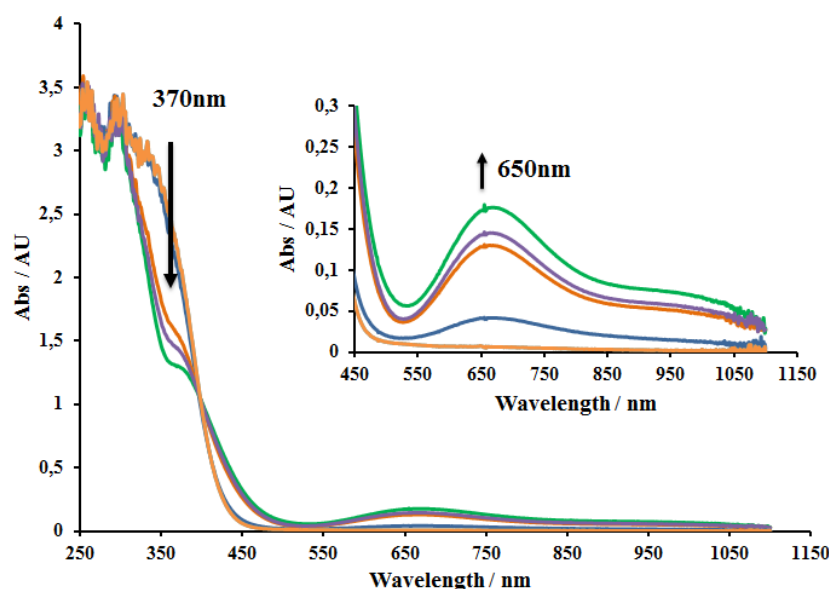
Figure 19 : Spectral changes within 20 min illustrating the reaction of **1a** (1.5mM) with O_2 in CH_2Cl_2 at room temperature.

For the investigation of the oxygen atom source, labeled $^{18}O_2$ was used. Mass spectrometry analysis of the oxidized ligand obtained using $^{18}O_2$ (99%) allowed us to determine that a quasi-quantitative ^{18}O incorporation in the product occurs (>97%). This clearly indicates that the oxygen atom of the OH group comes from molecular dioxygen (Figure 20).
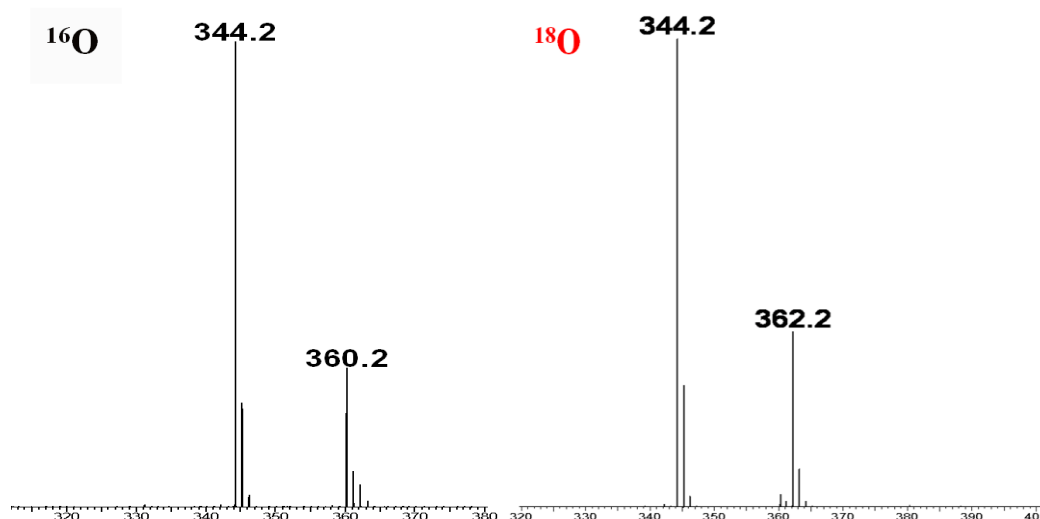
Figure 20 : ESI-MS spectrum of *cis*-(OH)-IndanePY$_2$ (^{16}O) left and *cis*-(OH)-IndanePY$_2$ (^{18}O) right. The peak at m/z=344.2 corresponds to the initial ligand IndanePY$_2$.

III.3. Reaction of Cu^{II} complex with reductant/O$_2$ system

The blue solution of **2a** in degassed dichloromethane turned to yellow within 10 min after the addition of excess benzoin and triethylamine. After exposure to dioxygen, the pale yellow color changed rapidly to green. The final green dinuclear complex (which was mentioned in the introduction) was isolated by the addition of ether. This final dinuclear species was found EPR silent.

Decomplexation with 35% ammonia solution and ^{1}H NMR analysis of the organic products indicated the presence of *cis*-(OH)-IndanePY$_2$ derivative formed in a quantitative yield.

For the investigation of the oxygen atom source, labeled ^{18}O$_2$ was used. The mass spectroscopic analysis of the oxidized product obtained using ^{18}O$_2$ gave at least 90% of ^{18}O incorporation in the *cis*-(OH)-IndanePY$_2$ product (Figure 21) which clearly shows that the oxygen atom of the OH group comes from molecular dioxygen.
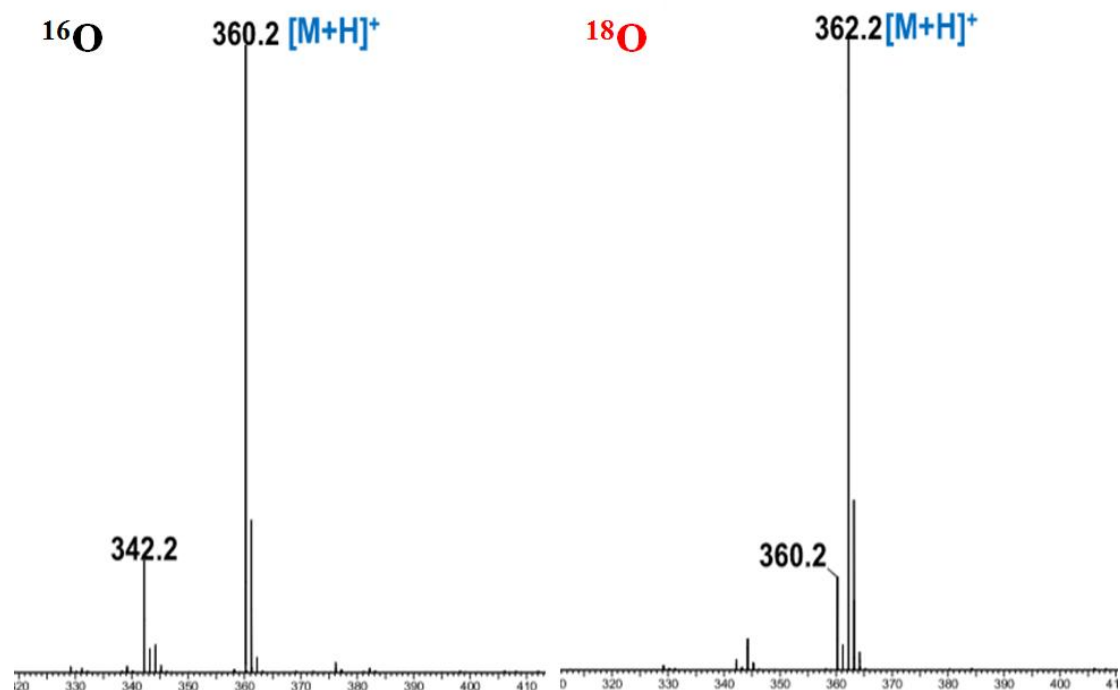
Figure 21 : ESI-MS spectrum of *cis*-OH-IndanePY$_2$ (^{16}O) on the left and *cis*-^{18}OH-IndanePY$_2$ (^{18}O) on the right. M is referred to *cis*-OH-IndanePY$_2$ product. The peak at m/z=344.2 corresponds to the initial ligand IndanePY$_2$.

IV. Reaction with Hydrogen peroxide (H$_2$O$_2$)

IV.1. Context

Another oxygen atom donor that has been widely used for oxidation reaction using transition metal complexes is hydrogen peroxide. H$_2$O$_2$ is considered as a clean oxidant because it forms water as sole by-product. Most of the times, some equivalents of base (triethylamine) are added in order to facilitate the deprotonation of the hydrogen peroxide.

Depending on the steric hindrance of the ligand, the reactions of Cu^{II} complexes with H$_2$O$_2$ provided either mononuclear or dinuclear copper-peroxo species. Cu^{II}-hydroperoxo complexes have indeed been isolated.[80,81] In addition, (μ-η^2:η^2-peroxo)dicopper(II) and bis(μ-oxo)dicopper(III) complexes have also been generated from the reactions of Cu^{II} complexes with H$_2$O$_2$.[82–84] Itoh and coworkers have observed that Cu^{II} complexes, supported by tridentate RPY$_2$ ligands, react with H$_2$O$_2$ to form the Cu^{II}-OOH.[85] Interestingly, at high concentrations of the initial copper complex, the hydroperoxo species decayed to provide the (μ-η^2:η^2-peroxo)dicopper(II) complexes.

Considerable efforts have been devoted to the characterization of Cu/O$_2$ species in the presence of H$_2$O$_2$ as well as their reactivity, but most of the experiments have been performed in organic solvents. Karlin and coworkers have published the first example of stable bridged Cu^{II}$_2$-peroxo intermediate in aqueous solution (neutral pH) after the

48

addition of H_2O_2 starting from either binuclear $[Cu^{II}_2R(PY)_2]^{2+}$ with R= bridging $(CH_2)_n$, n=3-5 or mononuclear $[Cu^{II}(MePY_2)(CH_3CN)(ClO_4)]^+$ complexes at room temperature.[84] The same type of peroxo intermediates have been reported when $[Cu^I_2R(PY)_2]^{2+}$ complex were reacted with O_2 at -80°C in CH_2Cl_2.[58] These intermediates were not very reactive towards a series of electron or hydrogen atom donors. However they decayed producing hydroxyl radicals identified using chemical trapping technique, which were probably responsible for the observed DNA cleavage reactivity.

Herein, we intended to investigate the formation of copper-oxygen species starting from **2a** or **2b** upon addition of hydrogen peroxide in organic solvent and H_2O as well as their reactivity towards internal or external substrates.

IV.2. Reaction with Hydrogen peroxide (H_2O_2)

IV.2.1. Reaction of Cu(I) complexes

Reaction of a yellow solution of $[IndanePY_2Cu^I]PF_6$ (**1a**) in degassed methanol with 10 eq. of H_2O_2 under inert atmosphere provided 90% yield of cis-1,3-$(OH)_2$-$IndanePY_2$ and 10% yield of cis-(OH)-$IndanePY_2$ (Scheme 26). This is attributed to the fact that H_2O_2 coordinates to copper resulting to hydroxylated complex on the one position of indane group and the excess of H_2O_2 oxidizes the produced complex leading to the second hydroxylation on the second position of the indane group.
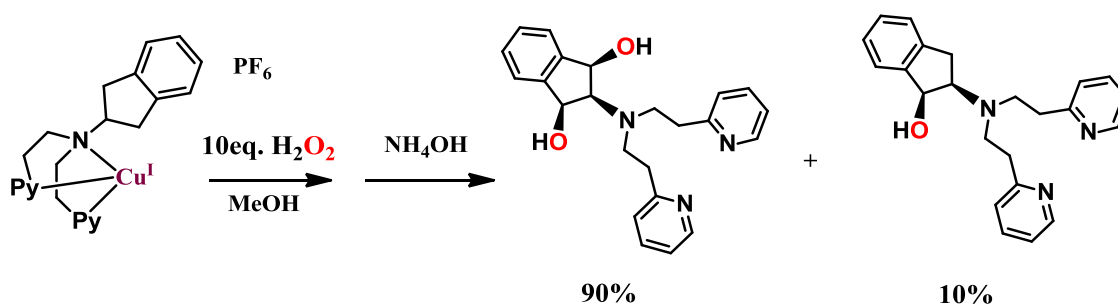
Scheme 26 : Schematic representation of $[IndanePY_2Cu^I]^+$ (**1a**) with 10 eq. H_2O_2 in methanol [**1a**]=11mM.

In the same solvent (MeOH), reaction of $[IndanePY_2Cu^I]$ with O_2 provided 90% of cis-(OH)-$IndanePY_2$ and 10% of the cis-1,3-$(OH)_2$-$IndanePY_2$. Excess of H_2O_2 probably favors over-oxidation of the substrate. In addition, kinetic isotopic effect in methanol using H_2O_2 was estimated as 8.8, a value comparable to the KIE=7.6 obtained when reacting Cu^I with O_2 in dichloromethane.

Interestingly, reaction of a yellow solution of $[cyclopentylPY_2Cu^I]PF_6$ or $[npropylPY_2Cu^I]PF_6$ in degassed methanol with 10 eq. of H_2O_2 under inert atmosphere

did not provide any hydroxylated products. These compared reactivity results are also similar to that obtained when reacting Cu(I) + O_2, which suggested the similar copper-oxygen species involved in the presence of O_2 and H_2O_2.

IV.2.2. Reaction of Cu(II) complexes

IV.2.2.1 Reaction of IndanePY$_2$Cu^{II} complex with H$_2$O$_2$ in methanol

Then we evaluated the O-atom transfer to indane moiety starting from Cu^{II} complexes. Reaction of blue solution [IndanePY$_2$Cu^{II}](OTf)$_2$ **2a** in degassed methanol with 10 eq. of H_2O_2 under inert atmosphere gave almost quantitative yield of *cis*-1,3-(OH)$_2$-IndanePY$_2$. Also, when [cyclopentylPY$_2$Cu^{II}](OTf)$_2$ or [*n*propylPY$_2$Cu^{II}](OTf)$_2$ was used, no hydroxylated products were detected.

IV.2.2.2 Reaction of IndanePY$_2$Cu^{II} complex with H$_2$O$_2$ in H$_2$O

Intramolecular reaction

In order to investigate the influence of the solvent on the O-atom transfer towards an internal substrate, H_2O was used as solvent (set at pH 8.10 facilitating the deprotonation of hydrogen peroxide). 1 eq. of H_2O_2 was added to the aqueous solution of **2a** at pH 8.10 and after overnight stirring, extractions and NMR analysis revealed the presence of two products. The *cis*-(OH)-IndanePY$_2$ and *cis*-1,3-(OH)$_2$-IndanePY$_2$ were present in solution at 66% and 33% yield, respectively.

^{18}O labeling

The oxygen source of the OH group in IndanePY$_2$ was confirmed by isotope labeling experiment using $H_2^{18}O_2$ (90% ^{18}O) in natural H_2O. ESI-MS mass spectra revealed the presence of almost quantitative ^{18}O incorporation from hydrogen peroxide both in *cis*-(OH)-IndanePY$_2$ and *cis*-1,3-(OH)$_2$-IndanePY$_2$ (Figure 22). Interestingly, hydroxylated products were not detected when [*c*PtPY$_2$Cu^{I}]$^+$ and [*n*PrPY$_2$Cu^{I}]$^+$ were reacted with excess H_2O_2. These compared reactivity results are similar to that obtained when reacting Cu(I) + O_2.
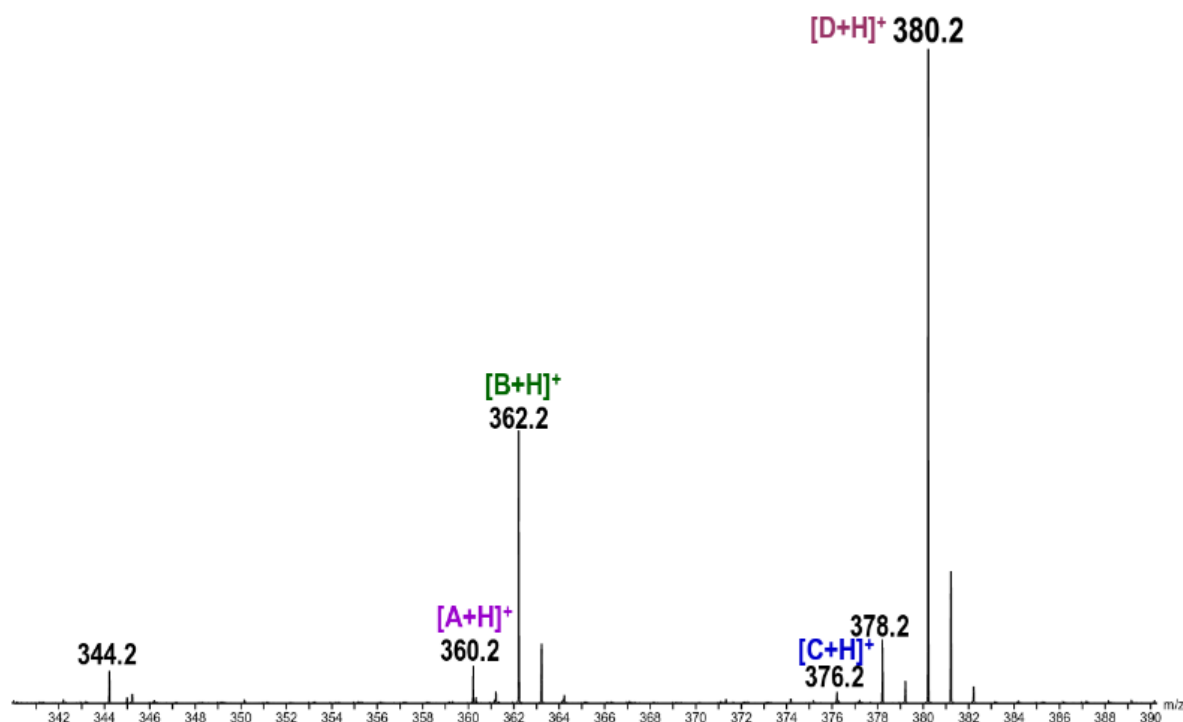
Figure 22 : ESI-MS mass spectrum of the extracted ligands (IndanePY$_2$, *cis*-(OH)-IndanePY$_2$, *cis*-1,3-(OH)$_2$-IndanePY$_2$) after reaction of **2a** with H$_2$^{18}O$_2$ (90%). **A** corresponds to non-labeled *cis*-(OH)-IndanePY$_2$, **B** corresponds to labeled *cis*-(^{18}OH)-IndanePY$_2$and **C** corresponds to the *cis*-1,3-(OH)$_2$-IndanePY$_2$ and **D** is referred to *cis*-1,3-(^{18}OH)$_2$-IndanePY$_2$. The peak at m/z 344.2 corresponds to the initial ligand IndanePY$_2$.

IV.2.2.3 Reaction of [MePY$_2$Cu^{II}] complex with H$_2$O$_2$ in H$_2$O

In order to get further insights on the copper-oxygen species formed upon addition of H$_2$O$_2$, we studied the reactivity of **2b** with H$_2$O$_2$. Using a similar complex, Karlin *et al.* have observed the formation of dinuclear Cu^{II} peroxo species in aqueous solutions.[84]

At basic pH= 8.4

The reactions of **2b** with H$_2$O$_2$ were studied in H$_2$O and the formation of copper-oxygen species was followed by UV-Vis spectroscopy. The UV-Vis spectral changes upon reaction of **2b** (0.8mM) dissolved in H$_2$O pH 8.40 (set with 1M NaOH) in the presence of 45 eq. H$_2$O$_2$ (2mM) are displayed on Figure 23. A band centered at 370 nm increased and reached the maximum absorption within 3 minutes. Also, the intermediate still displays d-d transitions around 650nm which suggests the maintenance of Cu(II) redox state. The intermediate then decayed slowly with t$_{1/2}$=55 min to a product that displays different spectral features from the initial ones (Figure 24).
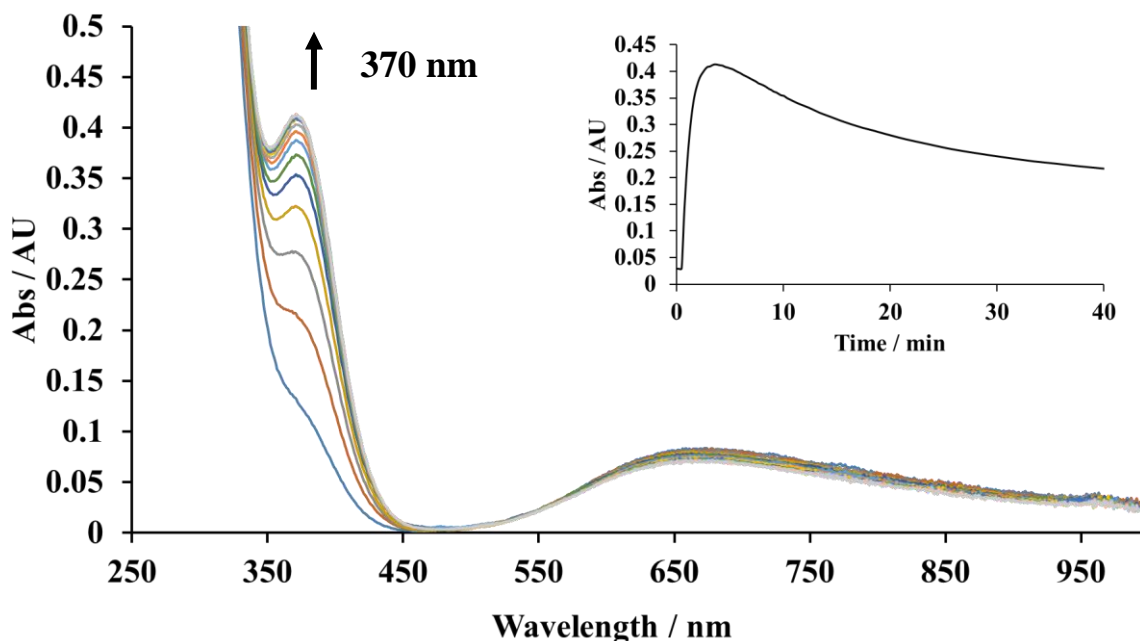
Figure 23 : Spectral changes of **2b** upon addition of 45 eq. H_2O_2 (2mM) in H_2O pH 8.40 at room temperature. Formation of an intermediate (grey) over three minutes reaction time. Inset: Time trace of the formation of the species. [**2b**]=0.8mM.
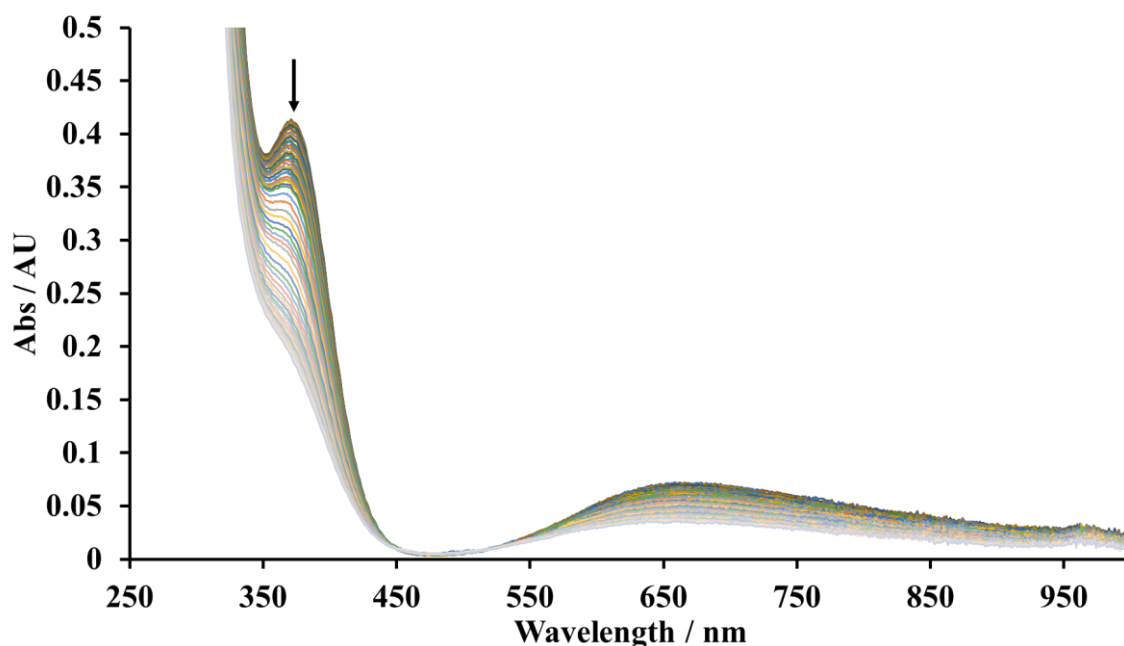
Figure 24 : Decay of copper-oxygen species formed of **2b** upon addition of 45 eq. H_2O_2 (2mM) in H_2O pH 8.40. [**2b**]=0.8mM.

Similar spectroscopic features (*e.g.* absorption at *ca.* 360 nm) have been described in the literature for the reaction of $[Cu^{II}(PhCH_2PY_2)(ClO_4)_2]$ with H_2O_2 in methanol at -90°C,[83] and of $[Cu^{II}(MePY_2)(CH_3CN)(ClO_4)]^+$ with H_2O_2 in H_2O at room temperature.[84] These spectral features were attributed to bridged peroxo species (usually displaying intense absorption bands at 320-380 nm).[3] Here, the absorption intensity at 370 nm is significantly lower than that of the reported dinuclear Cu^{II}-

peroxo complexes.[3,7,86] On the other hand, reaction of Cu^{II} complexes with H_2O_2 can yield mononuclear copper(II)-hydroperoxo complexes LCu^{II}-OOH exhibiting intense absorption bands around 325-387 nm assigned to $HOO^- \rightarrow Cu^{II}$ ligand-to-metal charge transfer (LMCT) transitions.[57,85]

In order to probe the nature of the species (mononuclear or dinuclear), we recorded the EPR spectra in frozen solutions in the absence and presence of H_2O_2. The addition of 1 eq. H_2O_2 in aqueous solution of **2b** set at pH 8.40 (+10% glycerol) led to partial loss of the signal intensity (45% loss of signal) indicating that the formed species is EPR silent, consistent with the formation of bridged peroxo adduct (Figure 25) and in agreement with the results of Karlin and co-workers.[84]
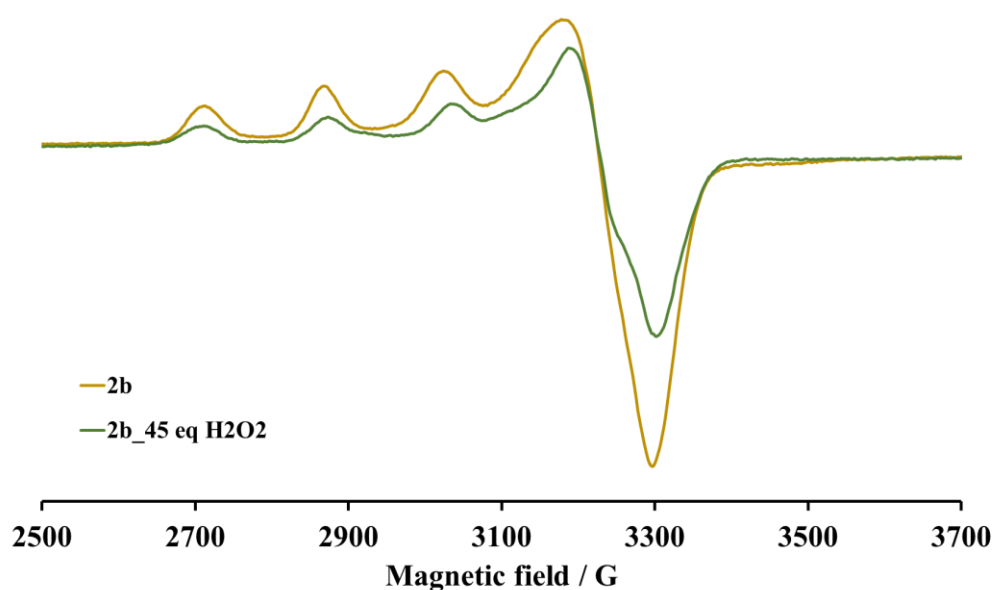
Figure 25 : EPR spectra of **2b** (0.8mM) in the absence (yellow) and in the presence (green) of 45 eq. H_2O_2 in H_2O pH 8.4 recorded at 120K.

At acidic pH= 6.5

The value of the pH slightly influenced the amount of the intermediate formed in solution but not the formation rate. At pH 6.50, a band also appeared at 370 nm with lower intensity.

EPR spectra of **2b** in H_2O set at pH 6.50 (10% glycerol) were recorded before and after addition of 45 eq. H_2O_2. Only 20% of the initial intensity was lost after reaction with hydrogen peroxide, in contrast to the disappearance of 45% of intensity at pH 8.50.

Those results suggested the formation of dinuclear Cu^{II} peroxo species in H_2O at different pHs.

Reactivity towards an external substrate

Using similar ligands (Scheme 27) Alda-Lisa Concia, postdoctoral researcher in our laboratory, has prepared mononuclear copper complexes as models for LPMO.
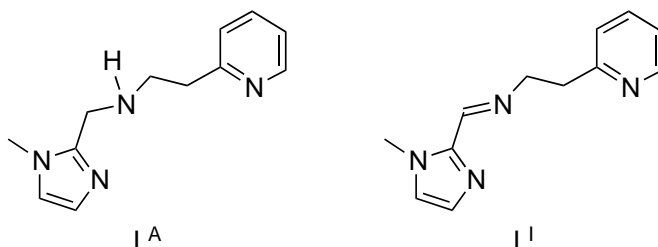
Scheme 27: Ligands for the preparation of mononuclear copper complexes as models for LPMO.

These complexes were found active towards a model substrate for glycosidic substrates (*p*-nitrophenyl-β-D-glucopyranoside) in the presence of hydrogen peroxide (Scheme 28).

Scheme 28 : Reaction used to model LPMO-like reactivity.

We were therefore interested in evaluating the activity of our complex **2b** in the same reaction. The assay was performed in basic conditions (carbonate buffer pH 10.5) and the formation of *p*-nitrophenolate was monitored by spectrophotometry (λ_{max} = 400 nm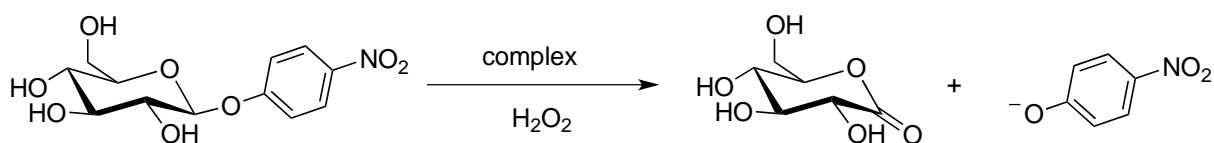, ε = 18500 mol^{-1}.L.cm^{-1}). When the substrate is placed in the presence of complex **2b** and 20 mM H$_2$O$_2$, *p*-nitrophenolate is produced as attested by the increase of the absorption at 400 nm. The assay was performed in the presence or absence of H$_2$O$_2$ in carbonate buffer pH 10.5 using different concentrations of the complex **2b.**

The initial velocities are dependent on the concentrations of complexes (0-0.1mM) (Figure 26, left) reaching a plateau above 0.06 mM of complex. In the absence of either hydrogen peroxide or complex, very low amount of *p*-nitrophenolate is detected (2-3μM) suggesting that oxidative processes are involved rather than hydrolysis (Figure 26, right).

Those results are consistent with the fact that reactive species are formed by the addition of hydrogen peroxide in aqueous solution of **2b** detected by UV-Vis. EPR spectra revealed that those reactive species are silent consistent with dinuclear Cu$^{II}_2$-peroxo species that are capable of catalyzing the oxidative cleavage of glycosidic bonds.
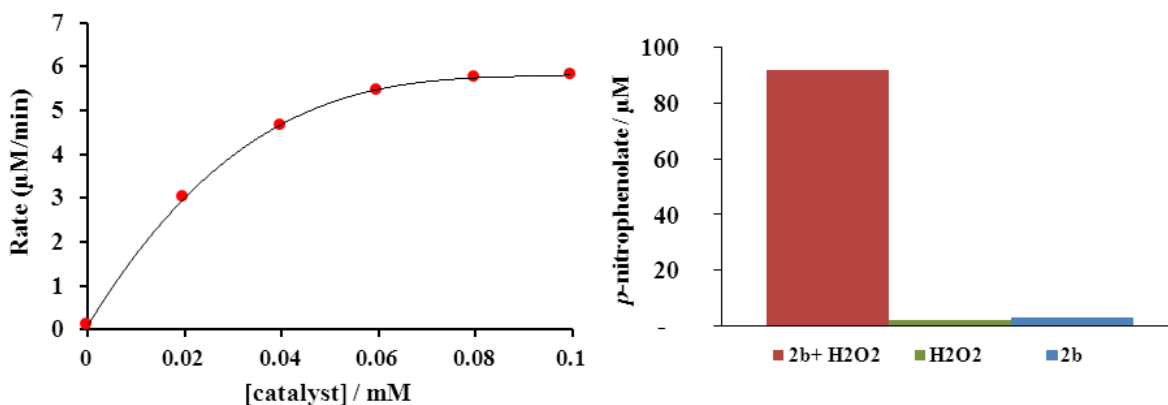
Figure 26 : Reaction of p-nitrophenyl-β-D-glucopyranoside with **2b** and H_2O_2 in carbonate buffer 100 mM pH 10.5 and at 30°C with $[H_2O_2]$= 20 mM and $[S]$ =20 mM. Left: initial velocities as a function of complex concentration for complex **2b** Right: concentration of p-nitrophenolate obtained after 15 min of reaction with $[2b]$=0.10 mM.

IV.3. Conclusion on H_2O_2 as O-atom donor

From the above-mentioned experiments, we have observed that products are similar when H_2O_2 is added on either Cu(I) or Cu(II) complexes (Figure 27). This indicates that initial redox state of the complex (either Cu^{II} or Cu^{I}) does not influence the O-atom transfer reactions induced by hydrogen peroxide when used in the same solvent. This can be due to the fact that, in the presence of excess H_2O_2, oxidation of Cu(I) to Cu(II) by hydrogen peroxide first occurs and is followed by coordination of peroxide. This has already been observed in the case of iron complexes.[94]

Figure 27 : Formation of same dinuclear peroxo complexes after reaction of hydrogen peroxide either with Cu^{I} or Cu^{II} complexes.

V. Oxidation with Iodosylbenzene

V.1. Context

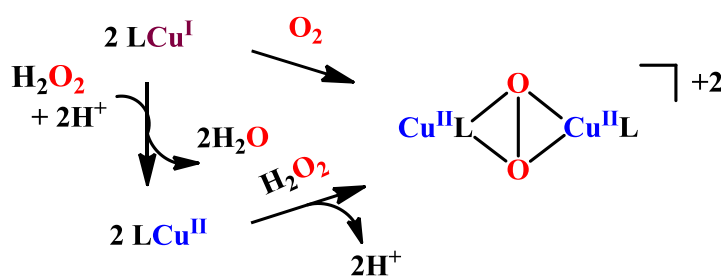Iodosylbenzene (PhIO) was initially used as a single oxygen atom donor in alkane hydroxylation and olefin epoxidation reactions catalyzed by cytochrome P450 or synthetic iron porphyrins.[88] It has also been extensively used to generate Fe(IV)=O intermediates using either porphyrines or non-heme ligands.[89]

Karlin *et al.* have reported that the reaction of two equivalents of $[MePY_2Cu^I(CH_3CN)]^+$ complex with PhIO yielded an intermediate that was formulated as the oxo bridged Cu^{II}-O-Cu^{II} species (Scheme 29).[58,60] The $\nu_{(O-H)}$ vibration was absent confirming the deprotonation of the bridging oxygen. EXAFS spectroscopy allowed to measure Cu-O (oxo) distance of 1.906 Å, shorter than that found in Cu^{II}_2(bis-μ-hydroxo) and longer than that found in Cu^{II}_2-peroxo and Cu^{III}_2(bis-μ-oxo) species.[61] The same dinuclear Cu-O-Cu complex is also formed when $[PhCH_2Cu^I]^+$ is reacted with O_2 at higher temperatures (0^oC).[58]
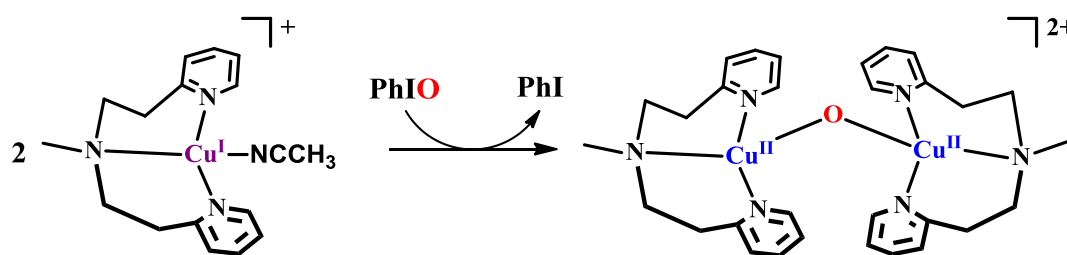
Scheme 29: Synthesis of $[(MePY_2)_2Cu_2(O)]^{2+}$ after the reaction of $[MePY_2Cu^I]^+$ complex with iodosylbenzene.

Such Cu-O-Cu species and their reactivity have been recently reviewed by Haack and Limberg (Scheme 30).[39] Interestingly, it has been reported that Cu-loaded zeolites (Cu-ZSM-5), are able to perform selective functionalization of methane to methanol after reaction with dioxygen. This type of Cu_2 (μ-oxo) species have been described as the key intermediates in methane oxidation reaction.[38]
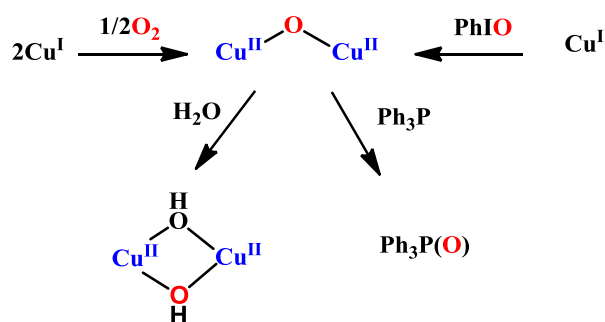
Scheme 30 : General formation and reactivity of Cu^{II}-O-Cu^{II} species.[39]

In 1989, Réglier *et al.* reported the first example of an intramolecular copper-mediated *ortho* hydroxylation of a pyridine after reaction of Cu^I complexes (e.g. $[(PhCH_2CH_2PY_2)Cu^I(CH_3CN)]^+$ or $[(PhCH_2PY_2)Cu^I(CH_3CN)]^+$) with PhIO in acetonitrile.[90] It has to be mentioned that no hydroxylated product was obtained when the reaction was carried out in dichloromethane highlighting the importance of the solvent in the formation of copper-oxygen species and therefore in oxygen atom transfer reactions. The nature of the oxidizing species was not clear but the authors proposed the involvement of strongly oxidizing $Cu^{III}=O$ (or Cu^{II}-oxyl) species.

In 2008, Karlin and coworkers have reported intramolecular methyl hydroxylation from the reaction of $[(TMG_3tren)Cu^I]^+$ and PhIO (TMGtren=tris(2-(*N*-tetramethylguanidyl)ethyl)amine).[80] This reaction led to the corresponding alkoxo product which was detected by electrospray ionization mass spectrometry ESI-MS (Scheme 31). Using another ligand (derived from TMPA), low temperature mass spectrometry allowed the detection of a cupryl species ($Cu^{III}=O$ or Cu^{II}-O· radical) prior to ligand oxidation. Interestingly, further mass experiments with labeled iodosylbenzene (PhI^{18}O) did not produce the corresponding labeled copper-oxygen species. Therefore, the labeled product was not obtained and no further explanation was provided.
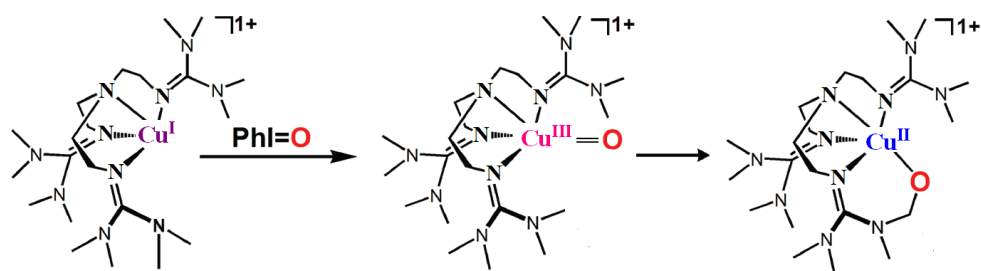
Scheme 31 : Proposed reaction of $[(TMG_3tren)Cu^I]^{1+}$ complex with PhIO, *via* the formation of cupryl intermediates.

Herein, we investigated the regio- and stereo- selectivity of O-atom transfer when $[IndanePY_2Cu^I]$ **1a** reacts with PhIO as well as the influence of the solvent.

V.2. Preparation of PhIO and ^{18}O-labeled PhIO

Iodosylbenzene is described as a polymer linked by I-O-I bonds, rather than a monomer, $PhI=O$ or PhI^+O^- as it is sometimes written. This polymeric formulation explains its very low solubility in most solvents.[91]

PhIO was prepared by addition of iodobenzene diacetate in 3N aqueous solution of $NaOH_{(aq)}$ following an already described procedure.[92] ^{18}O labeled iodosylbenzene was prepared using the same procedure but starting from $H_2^{18}O$ in the presence of NaH.

The resulting products were first analyzed by FT-IR spectroscopy (Figure 28). The IR spectrum of PhIO displays two intense bands at 488 cm^{-1} and 435 cm^{-1} that are assigned to the principal I-O-I group vibrations.[91] These bands are O-sensitive and shift

to 483 cm^{-1} and 414 cm^{-1} respectively upon ^{18}O labeling. Another ^{18}O sensitive frequency, assigned as the (I-O-I) antisymmetric vibration is found at 588 cm^{-1} band and shifts at 559 cm^{-1} upon ^{18}O substitution. FT-IR spectroscopy thus confirmed the presence of labeled product.
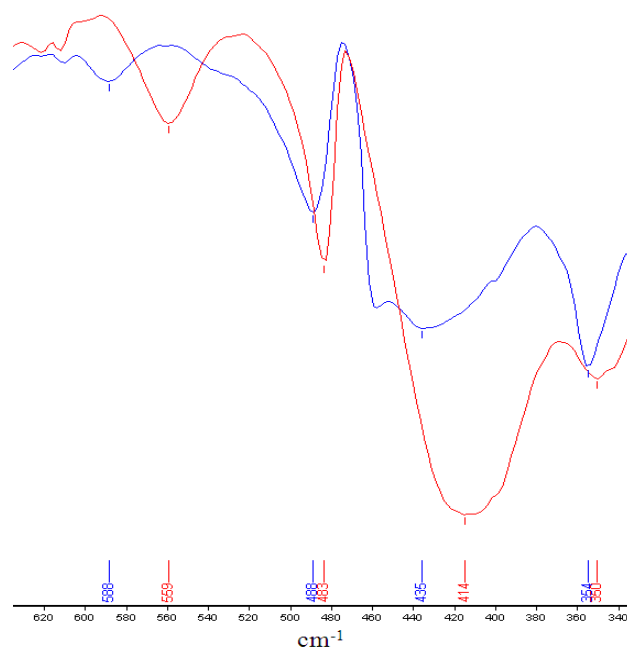
Figure 28 : Infrared spectra (IR) of PhIO (blue) and PhI^{18}O (red).

^{18}O content of the labeled PhIO was determined after reaction with triphenylphosphine. Reaction of labeled iodosylbenzene with triphenylphosphine was performed in degassed dichloromethane inside the glove box and the product, triphenylphosphine oxide was analyzed by MS spectrometry (Figure 29). The ^{18}O content of labeled iodosylbenzene was estimated to be *ca.* 50%.
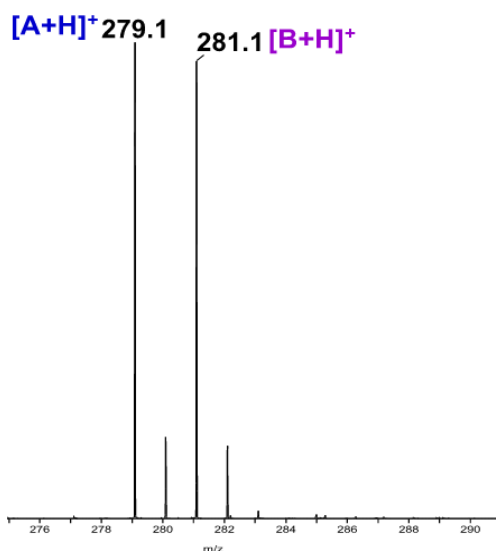
Figure 29 : Mass spectra of triphenylphosphine oxide after reaction of triphenylphosphine with PhI^{18}O. **A** corresponds to Ph$_3$P=^{16}O and **B** corresponds to labeled Ph$_3$P=^{18}O.

V.3. Reaction of Cu^I complexes with PhIO

V.3.1. Reaction of [(IndanePY$_2$)Cu^I] complex

2 eq. of PhIO were added on a yellow solution of **1a** in degassed dichloromethane inside the glove box. The solution immediately turned green. NMR analysis of after ammonia extraction clearly shows that the oxygen atom transfer occurs in the benzylic position of the indane group in 20%-30% yield (Scheme 32, left) and no other hydroxylated products were observed. The reaction was also performed in CH$_3$CN after addition of 2 eq. of PhIO. Under those conditions, a mixture of products was observed containing 30% of *cis*-(OH)-IndanePY$_2$ and 26% of product hydroxylated on the *ortho*-position of pyridine group (Scheme 32, right). Therefore, the reactivity of **1a** with PhIO is different depending on the solvent (CH$_2$Cl$_2$ *vs.* CH$_3$CN).
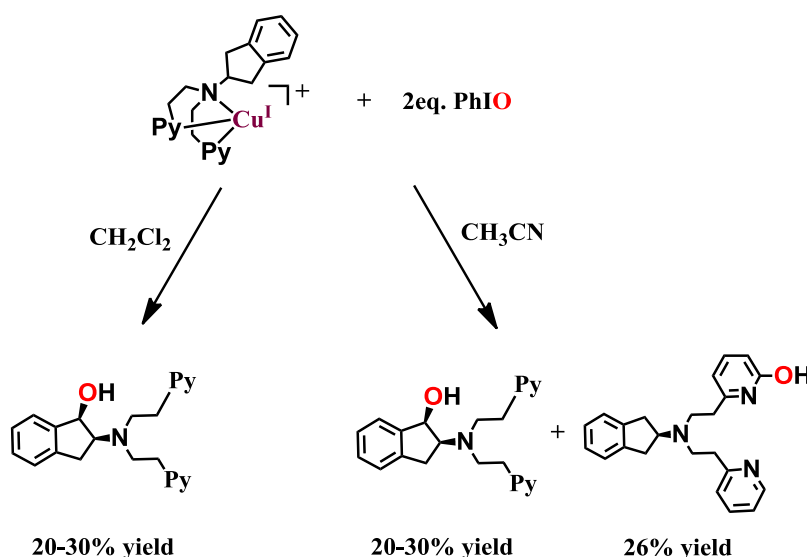
Scheme 32 : Schematic representation of [(IndanePY$_2$Cu^I]$^+$ (1a) with iodosylbenzene in dichloromethane (left) and in acetonitrile (right).

The reaction of complex **1a** with 2 eq. PhI^{18}O in degassed dichloromethane was stirred overnight at room temperature inside the glove box. By NMR analysis after ammonia treatment, 20% yield of *cis*-hydroxylated product was estimated. Further analysis of the product by ESI-MS spectrometry gave an ^{18}O incorporation yield of only 15% over 50% maximum theoretical labeled product (Figure 30).

This result was puzzling. The low ^{18}O content in *cis*-(^{18}OH)-IndanePY$_2$ suggested that either (i) not all of the oxygen atoms incorporated in the indane moiety come from iodosylbenzene or (ii) that an exchange occurs during the reaction with another oxygen source in the medium. The oxygen atom source from atmospheric dioxygen was excluded since the reaction was performed inside the glove box in degassed dichloromethane and since in absence of PhIO, no hydroxylation was detected. A

similar result was described by Nam and co-workers using iron porphyrins and PhIO. The authors have observed that the intermediates formed readily exchange their oxygen atoms with water.[93] In our case, the addition of $H_2^{18}O$ in the reaction medium (10 μL in 3 mL) of **1a** with $Ph^{18}O$ in dichloromethane caused significant increase of ^{18}O incorporation (*ca.* 40%) to the ligand (Figure 31).
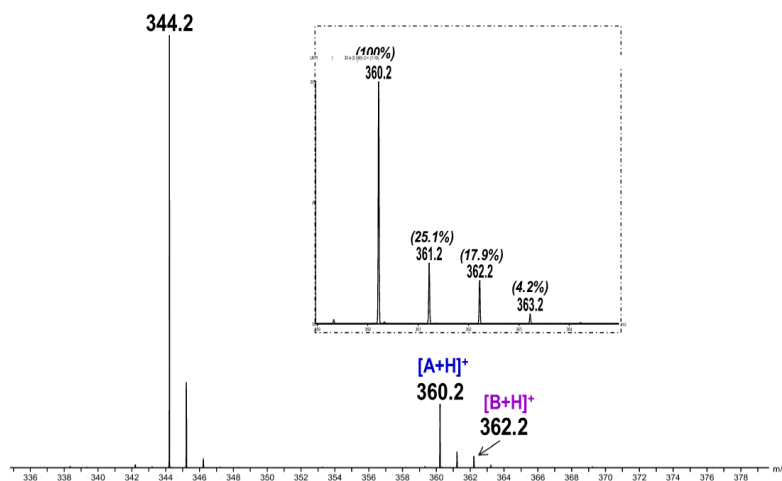
Figure 30 : ESI-MS spectrum of the extracted ligands (IndanePY$_2$ and *cis*-(OH)-IndanePY$_2$) after reaction of **1a** with $PhI^{18}O$. **A** corresponds to non-labeled *cis*-(^{16}OH)-IndanePY$_2$ and **B** corresponds to labeled *cis*-(^{18}OH)-IndanePY$_2$. The peak at *m/z* 344.2 corresponds to the initial ligand IndanePY$_2$.

It has been suggested that the exchange of oxygen atom is greatly facilitated by the coordination of iodosylbenzene to a Lewis acidic metal center.[86] This therefore suggests that, as observed in the case of other metal ions, PhIO coordinates to the copper ion and that [LCu^I-O-IPh]$^+$ species are intermediately formed.
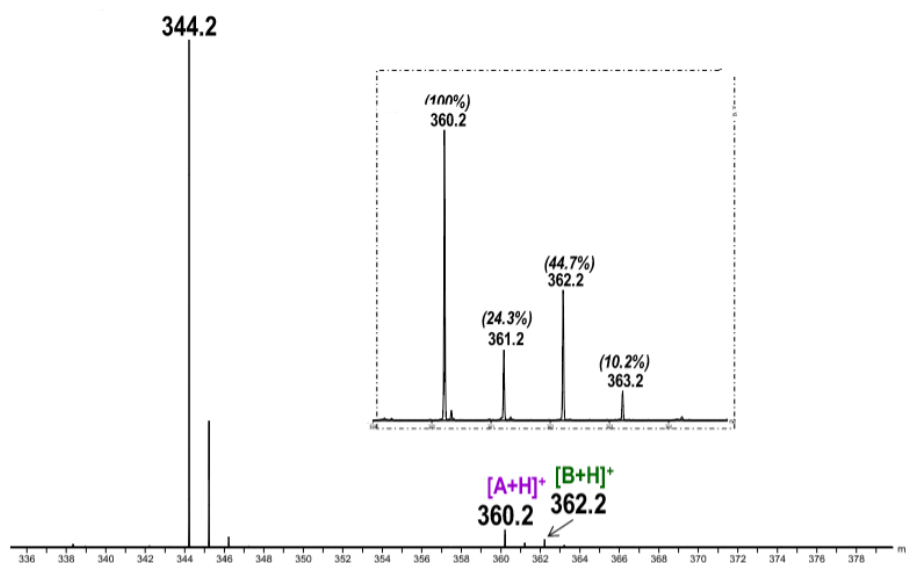

Figure 31 : Mass spectrum of the extracted ligands (IndanePY$_2$ and *cis*-(OH)-IndanePY$_2$) after reaction of **1a** with $PhI^{18}O/H_2^{18}O$. **A** corresponds to non-labeled *cis*-(^{16}OH)-IndanePY$_2$and **B**

corresponds to labeled *cis*-(^{18}OH)-IndanePY$_2$. The peak at m/z 344.2 corresponds to the initial ligand IndanePY$_2$.

V.3.2. Reaction of other RPY$_2$Cu^I complexes

The reaction was also evaluated using RPY$_2$ containing complexes, [*c*PtPY$_2$Cu^I]$^+$ and [*n*PrPY$_2$Cu^I]$^+$, which contain non-activated C-H bonds. The reaction with PhIO in dichloromethane yielded only to 1-2% of hydroxylated products and only the *ortho* position of the pyridine was oxidized (Scheme 33).
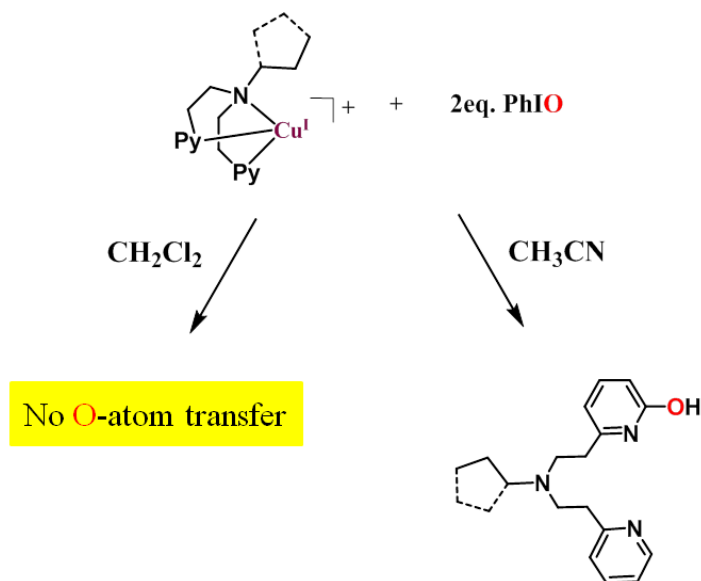
Scheme 33 : Schematic representation of [(cyclopentylPY$_2$Cu^I]$^+$ or [(*n*propylPY$_2$Cu^I]$^+$ with iodosylbenzene in dichloromethane (left) and in acetonitrile (right). In dichloromethane no hydroxylated products were obtained, while in acetonitrile only the only the *ortho* position of the pyridine was oxidized.

So far, hydroxylation on the *c*PtPY$_2$ and *n*PrPY$_2$ ligands has only been observed upon addition of benzoin/triethylamine on solutions of [*c*PtPY$_2$Cu^{II}]$^{2+}$ and [*n*PrPY$_2$Cu^{II}]$^{2+}$ respectively and no pyridine hydroxylation has ever been detected. Those results showed that so far, non-activated C-H bonds are hydroxylated through benzoin/Et$_3$N/O$_2$ system, suggesting that under those conditions different species are involved.

V.3.3. Conclusion on PhIO as O-atom donor

The reaction of PhIO with copper complexes is far less documented than that with other metal ions including iron. In the literature, there are only few examples on copper-oxygen species formed after the reaction of Cu^I complexes with PhIO, and either mononuclear copper-oxyl or binuclear Cu^{II}-O-Cu^{II} species have been proposed.[80,94]

Using very similar types of ligands (RPY$_2$), Karlin has observed the formation of binuclear Cu^{II}-O-Cu^{II} species. In addition, Réglier and coworkers have reported that *ortho*-hydroxylation of pyridine groups occur when the Cu^I complexes are reacted with PhIO in a coordinating solvent such as acetonitrile. Here, in dichloromethane, no pyridine hydroxylation is observed but only aliphatic C-H bond hydroxylation. A non-coordinating solvent such as CH$_2$Cl$_2$ could favor the formation of dinuclear species whereas a coordinating one as CH$_3$CN could favor the formation of mononuclear species (Figure 32).
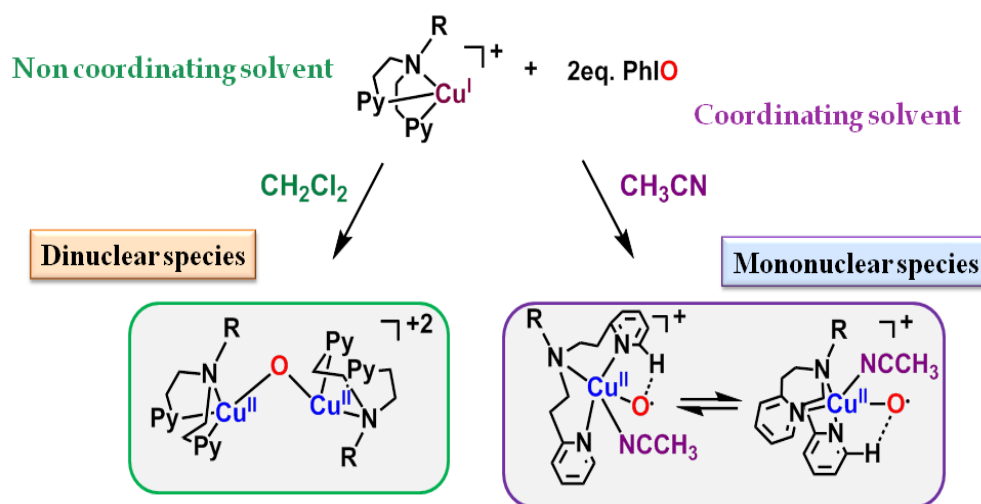

Figure 32 : Formation of Cu/O species upon reaction of RPY$_2$Cu^I complexes with PhIO in dichloromethane (left) and in acetonitrile (right).

However, the exact nature of copper-oxygen active species formed after the reaction of Cu^I complexes with PhIO is not clear and it is still under investigation.

V.4. Reaction of Cu^{II} complexes with PhIO

Valentine *et al.* have reported the catalytic epoxidation of olefins by Cu^{II} complexes upon addition of iodosylbenzene.[95] Interestingly, it has been described that after reaction of PhIO with dinuclear Cu^{II} complex containing an m-xylene linker, the internal ligand was not hydroxylated. This internal linker is hydroxylated in the case of Cu$^I_2$ + O$_2$.

In our case, 2 eq. of PhIO were added to a blue solution of [IndanePY$_2$Cu^{II}(OTf)$_2$] (**2a**) complex in dichloromethane or water and the color turned immediately to green. No hydroxylation was observed in any of those solvents.

# VI. Reaction with Sodium hypochlorite (NaOCl)

VI.1. Introduction

Sodium hypochlorite is a cheap single-oxygen donor. NaOCl is known as an oxidant (OCl⁻), which works well in basic medium. By decreasing the pH value of hypochlorite solution, the hypochlorous acid, HOCl, gradually becomes the main species and is usually a source of radical species. So the pH values of hypochlorite solution largely influence its chemical properties.

NaOCl was used for Mn^{III} porphyrins[96] and Fe^{III} complexes[97] in order to catalyze the highly selective epoxidation of olefins from NaOCl as an oxygen atom donor through high-valent metal-oxo species. Moreover, sodium hypochlorite has been also used to study the water oxidation mechanism of photosystem II model complexes such as a dinuclear Mn-containing dinuclear complex producing dioxygen.[98]

In the literature, there are no examples of oxygen atom transfer to substrates mediated by copper complexes using NaOCl as an oxidant. Herein, we investigated the oxygen atom transfer to indane moiety using NaOCl as an oxygen atom donor.

VI.2. Reaction of Cu^I with NaOCl

Addition of 2 or 10 eq. of NaOCl to a solution of **1a** in methanol gave 10 or 20% of stereo-selective *cis*-(OH)-IndanePY₂, respectively (Scheme 34). No other hydroxylated products were observed by ¹H NMR spectroscopy.
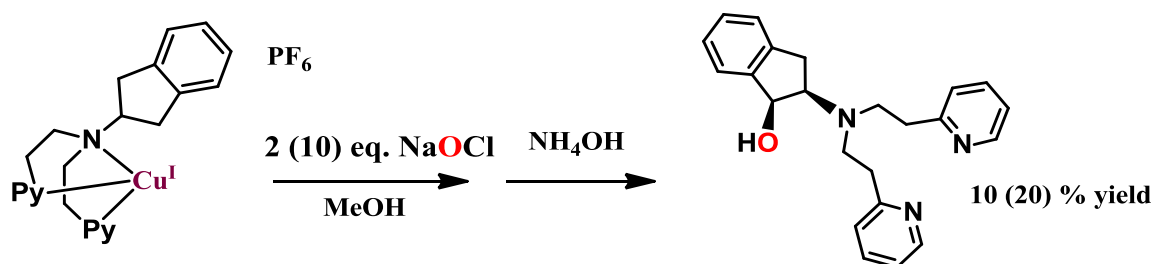
Scheme 34 : Schematic representation of [IndanePY₂Cu^I]⁺ (**1a**) with NaOCl in methanol.

In this case, it is possible that highly reactive species such as Cu^{II}-O° or Cu^{II}-O-Cu^{II} are formed (as formed in the case of Fe with NaOCl)[97] where the oxygen atom originates from OCl-. Possible formation pathway for those species is displayed on Scheme 35.

$$LCu^{I} + ClO^{-} \longrightarrow LCu^{I}\text{-}OCl \longrightarrow LCu^{III}{=}O + Cl^{-}$$

Scheme 35 : General pathways for the formation of different possible intermediates after reaction of Cu^{I} precursors with NaOCl.

Investigating the influence of the solvent, the same reaction was performed in dichloromethane yielding no hydroxylated products. This can be rationalized by the fact that H_2O/NaOCl is not miscible with organic solvents.

VI.3. Reaction of Cu^{II} with NaOCl

Addition of 2 or 10 eq. of NaOCl to a solution of **2a** in methanol didn't lead to the formation of any hydroxylated products. Interestingly, addition of 2 eq. of NaOCl to a solution of **2a** in H_2O set at pH 6.5 led to the formation of 80% *cis*-(OH)-IndanePY$_2$ product. Increasing the pH from 6.5 to 8.5 lowered the conversion yield from 80% to 30%.

Following the reaction scheme proposed in the case of Cu^{I} precursors, the reaction of Cu^{II} with hypochlorite is likely to yield high-valent copper-oxo species such as Cu(IV)=O or Cu(III)-O° (Scheme 36).

$$LCu^{II} + ClO^{-} \longrightarrow LCu^{II}\text{-}OCl \longrightarrow LCu^{IV}{=}O + Cl^{-}$$
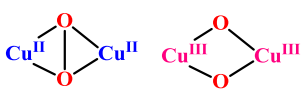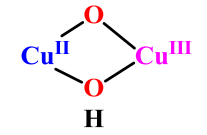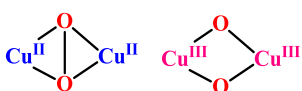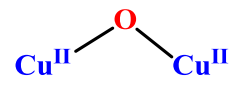
Scheme 36 : General pathways for the formation of different possible intermediates after reaction of Cu^{II} precursors with NaOCl.

Further experiments to investigate the oxygen atom source are undergoing in the laboratory.

VII. Summary and conclusions

In summary, we have investigated the O-atom transfer mediated either by Cu^I or Cu^{II} complexes using different types of oxidants probably leading to different reactive intermediates. This approach allowed us to monitor the reactivity of several copper-oxygen species towards activated (indane) or non-activated C-H bonds (cyclopentyl and $n$propyl). The results are summarized in Table 4. From these results, it appears that only two types of intermediates are able to oxidize non activated C-H bonds: (i) mixed-valent species and (ii) Cu^{II}-O° oxyl species. The reactivity of putative Cu(III)-O° that may be formed upon reaction of Cu(II) with NaOCl has yet to be evaluated on non activated C-H bonds.

Table 4 : Reactivity of species formed in the presence of oxidants towards activated and non-activated C-H bonds.

	Conditions	Proposed species	Activated	Non-Activated	Pyridine group
O_2	$Cu^I + O_2$	$Cu^{II}(\mu\text{-}O)_2Cu^{II}$ / $Cu^{III}(\mu\text{-}O)_2Cu^{III}$	✓	✗	✗
	Cu^{II}/reductant/ O_2	$Cu^{II}(\mu\text{-}O)(\mu\text{-}OH)Cu^{III}$ (**H**)	✓	✓	✗
H_2O_2	Cu^I/H_2O_2/MeOH	$Cu^{II}(\mu\text{-}O)_2Cu^{II}$ / $Cu^{III}(\mu\text{-}O)_2Cu^{III}$	✓	✗	✗
	Cu^{II}/H_2O_2/MeOH		✓	✗	✗
PhIO	Cu^I/PhIO/CH_2Cl_2	$Cu^{II}(\mu\text{-}O)Cu^{II}$	✓	✗	✗
	Cu^I/PhIO/CH_3CN	$Cu^{II}\text{-}O° \leftrightarrow Cu^{III}=O$	✓	✓	✓
NaOCl	Cu^I/NaOCl/MeOH	$Cu^{II}\text{-}O° \leftrightarrow Cu^{III}=O$	✓	nd	nd
	Cu^{II}/NaOCl/H_2O	$Cu^{III}\text{-}O° \leftrightarrow Cu^{IV}=O$	✓	nd	nd

nd: not determined

Chapter III

Electrochemical C-H bond activation mediated by Cu^{II} complexes and water

I. Introduction

I.1. Photosystem II: a source of inspiration

The 21% of oxygen in the atmosphere comes from the procedure of photosynthesis. O_2 production is catalyzed by the oxygen evolving center (OEC) of photosystem II, found in plants and cyanobacteria. The X-ray structure of OEC has been solved and it shows four manganese atoms and a calcium atom arranged as shown in Figure 33 with μ-oxo bridges between Mn ions.[99,100]

In OEC the energy required to produce dioxygen is provided by visible photons producing high valent metal oxo species as key intermediates through proton coupled electron transfer (PCET).
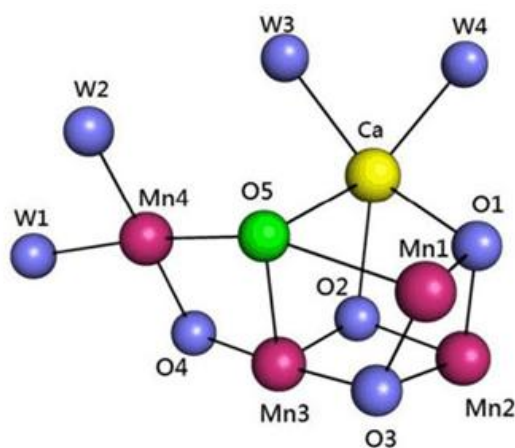

Figure 33 : Oxygen evolving centre of photosystem II[100]

The Mn ions are oxidized within the course of the Kok cycle, and high oxidation states of Mn ions are involved in the mechanism. Moreover, $Mn^V=O$ is considered as possible intermediate which is capable of reacting with water to form O_2.[101,102] In biomimetic studies, the formation of high valent metal-oxo complexes (M=Mn, Fe, Ru, Ir, Co) has been established for water oxidation and mechanistic insights have been reported.[103,104,105,106,107]

I.2. Possible mechanisms for water oxidation (WO)

Two basic mechanisms have been proposed for WO to O_2 (Scheme 37).[108,109] In the first mechanism **A**, called water nucleophilic attack (WNA), highly oxidized metal oxo species is attacked by solvent water of hydroxide under alkaline conditions, resulting in a two-electron oxidation process to form a hydroperoxo intermediate, which can then be further oxidized to release O_2. The second mechanism **B** and **C** by which WO can be catalyzed is radical coupling mechanism (RC). In RC, two one- or two-electron oxidized oxyl containing species couple to form an O-O bond in either a two- or four-

electron process. Commonly, ORC occurs between identical oxyl species (symmetric ORC) or between two distinct oxyl species (asymmetric ORC).
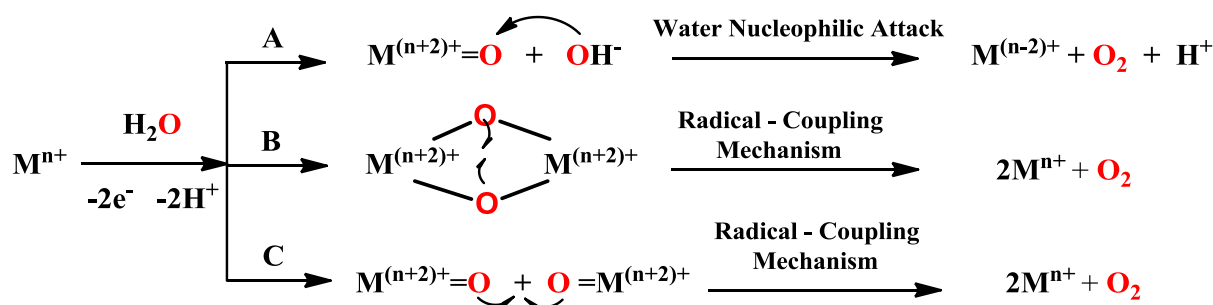
Scheme 37 : Possible pathways for metal oxo mediated reactions for O-O formation.

I.3. Oxidation modes

In order to activate water, transfer of protons and electrons are needed to form sufficient oxidative species. Those species can be generated *(i)* by chemical oxidants, *(ii)* by applying an external potential or *(iii)* by light energy.[110]

III.3.1. Chemically Induced water activation

Sacrificial oxidants must have an oxidation potential sufficient to oxidize the metal complex. Common used oxidants[111] are:

- *CAN* (the so-called cerium (IV) ammonium nitrate) is a powerful one electron oxidant (1.75V *vs.* NHE) that has been widely used.[103] However, it is stable only at low pH and begins to form insoluble cerium oxide nanoparticles above *ca.* pH 3.0. This means that there is a limitation for metal complexes that are designed to work at neutral or alkaline pH.

- *Sodium periodate* is a two electron oxidant (1.6V *vs.* NHE) that has been used for characterizing water oxidation catalysts.[112,113] However, it is stable until *ca.* pH 7.5 and can potentially serve as an oxo transfer reagent.

- *Sodium hypochlorite*, a two electron oxidant, has been investigated thanks to its stability at basic pH. This can also serve as an oxygen atom transfer reagent producing oxygen from hypochlorite and not from water.

I.3.2. Electrochemically induced water activation

Electrochemical reactions require the use of a potentiostat as the electron source in order to apply a specific potential at the desired pH. Cyclic voltammetry is a useful technique for homogeneous catalysis in order to determine the potential where the catalytic process occurs as well as its catalytic efficiency.[114]

Copper complexes have been shown to act as homogeneous or heterogeneous catalysts depending on the ligand environment, pH scale and reaction conditions.[115] In the past years several copper-based coordination complexes have been reported as electrocatalysts for water oxidation.

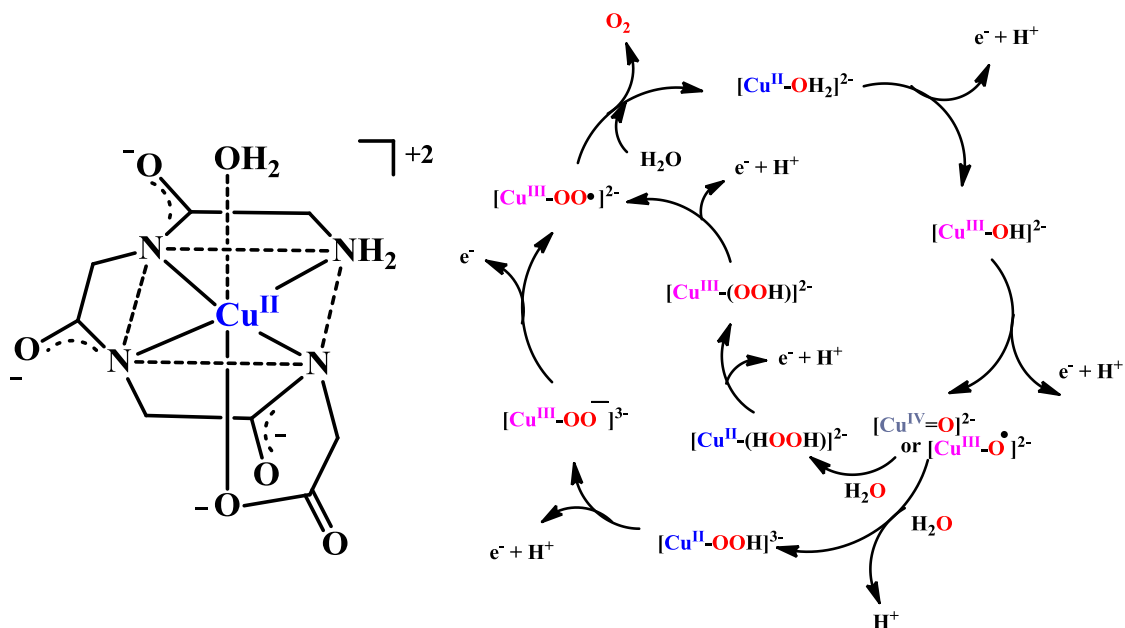## I.3.2.1 Mononuclear copper-based water oxidation catalysts

The first electrocatalytic water oxidation by a copper-based system was reported in 2012 by Mayer and coworkers using 2,2 bipyridine (bpy) ligand. Spectroscopic studies and cyclic voltammetry have shown that upon raising pH between 8-12, the dimeric $Cu_2(bpy)_2(\mu\text{-}OH)_2$ complexes are formed, while at pH > 12 monomers of $Cu_2(bpy)_2(OH)_2$ are the main species in solution (Scheme 38). These species are proposed to be responsible for electrocatalytic water oxidation with a TOF of 100 s^{-1}.[129]
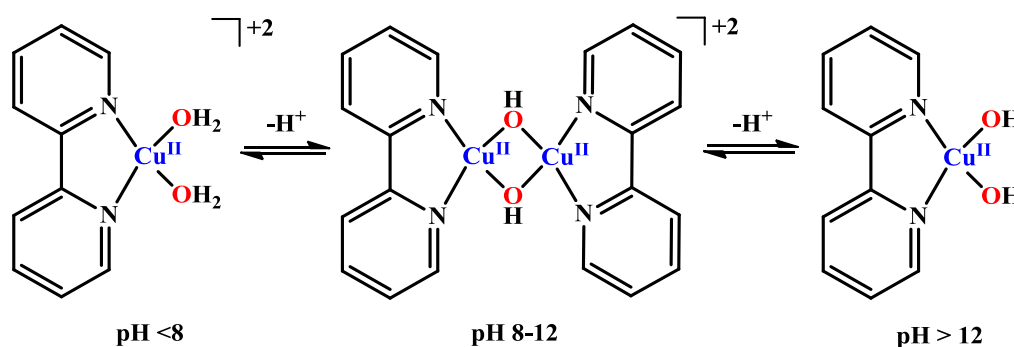
Scheme 38 : Schemetic representation of speciation of 1:1 (bpy):Cu^{2+} in aqueous solution at different pH values

The bpy ligand and its substituted derivatives have played an important role in the study of copper-based water oxidation catalysts. A modified version of [Cu(bpy)(OH)$_2$] with hydroxyl groups on the 6 and 6' positions of bpy, [Cu(bpyOH)(OH)$_2$], was recently reported by Lin and co-workers.[117] In this WOC, the ligand is redox active and able to serve as an internal base for proton transfer.

Later on, Meyer and coworkers reported an electrocatalytic water oxidation catalyst based on triglycylglycine ligand (Scheme 39, left).[118] Catalysis was performed at basic pH (pH=11) and kinetic studies agree with a single-site catalysis and a Cu^{IV}=O was proposed as the active species (Scheme 39, right). Nucleophilic water attack on the oxo group in presence of base or proton acceptor may give a hydroperoxide intermediate which can be further oxidized producing dioxygen.

O_2

$e^- + H^+$

$[Cu^{II}\text{-}OH_2]^{2-}$

H_2O $e^- + H^+$

$[Cu^{III}\text{-}OO\bullet]^{2-}$

$[Cu^{III}\text{-}OH]^{2-}$

$[Cu^{III}\text{-}(OOH)]^{2-}$

e^-

$e^- + H^+$

$e^- + H^+$

$[Cu^{III}\text{-}OO^-]^{3-}$

$[Cu^{II}\text{-}(HOOH)]^{2-}$

$[Cu^{IV}{=}O]^{2-}$ or $[Cu^{III}\text{-}O^\bullet]^{2-}$

H_2O

H_2O

$e^- + H^+$ $[Cu^{II}\text{-}OOH]^{3-}$

H^+

Scheme 39 : Cu^{II} triglycylglycine complex (left). Proposed mechanism for water oxidation by Cu^{II} triglycylglycine complex (right).

The formation of Cu^{II}-peroxide intermediate was also proposed using other Cu^{II}/peptide systems or other Cu^{II} complexes.[119,120,121,135]

Llobet and coworkers have reported a family of Cu^{II} complexes containing an amidate ligand (Figure 34).[121] The nature of the species involved was investigated by DFT calculations and water nucleophilic attack was also proposed as the key step for the O-O bond formation.
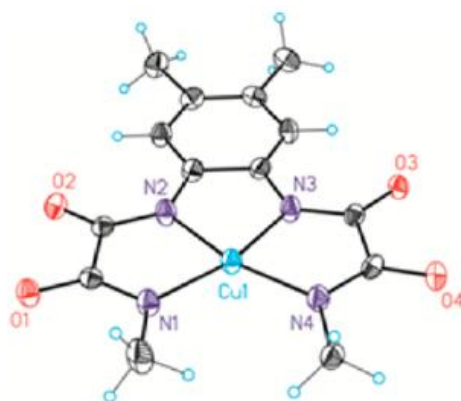
Figure 34 : ORTEP representation of Cu^{II} complex coordinated to the amidate ligand L^{4-} with two methyl groups on the aromatic ring.

Interestingly, a monomeric Cu^{II}-(Py$_3$P) (where Py$_3$P is N,N-bis(2-(2-pyridyl)ethyl)pyridine-2,6-dicarboxamidate) is a stable water oxidation electrocatalyst working in basic $H_2PO_4^-/HPO_4^{2-}$ buffered solution.[123] It has been reported the $H_2PO_4^-/HPO_4^{2-}$

buffer solution plays a role in the mechanism in catalysis, possibly in a proton transfer step. The mechanism is not clear yet. [124]

Finally, copper salts have been described as efficient water oxidation catalysts.[125] For instance, free Cu^{II} salts in concentrated carbonate have been shown to be water oxidation catalysts. The mechanism and the nature of the metal intermediates were found to be dependent on the conditions (concentration and pH) and mononuclear or dinuclear species were involved.[126] At high concentration of Cu^{II} salts, water oxidation catalysis is due to deposition of electroactive CuO surface on ITO electrodes.

I.3.2.2. Dinuclear water oxidation catalysis

Most of the copper-based molecular water oxidation catalysts are proposed to act as "single-site" catalysts. However, a dinuclear copper complex, $[Cu_2(BPMAN)(\mu\text{-}OH)]^{3+}$ using 2,7-[bis(2-pyridylmethyl) aminomethyl]-1,8-naphthyridine ligand (BPMAN) was found to perform water oxidation in neutral conditions. [140] DFT calculations suggested the oxidation of the precursor into $Cu^{II}Cu^{III}$ then $Cu^{III}Cu^{III}$ complexes through consecutive proton coupled electron transfer steps (PCET). Proton transfers are proposed to be assisted by a de-coordinated pyridyl nitrogen. The O-O bond is formed. After proton release and an additional oxidation step, the $Cu^{II}Cu^{II}$ superoxide intermediate is further oxidized to release dioxygen and start the next catalytic cycle.

The formation of dinuclear active species was also postulated by DFT calculations on mononuclear Cu^{II}-azo (L=3-(pyridine-2yldiazenyl)naphthalene-2-ol) complex where the coupling of two formed $Cu^{III}=O$ species leads to Cu peroxide (Cu^{III}-OO-Cu^{III}) which is further oxidized to superoxyl Cu^{II}-O·O-Cu^{II} releasing dioxygen through a reductive elimination step.[128]

I.3. Photochemically induced water activation

Inspired by the photosystem II, several models have been developed in order to photo-oxidize water to dioxygen. In the homogeneous phase, those systems contain a photosensitizer such as porphyrins or $[Ru(bpy)_3]^{2+}$ which harvest sunlight, a water oxidation catalyst and a sacrificial electron acceptor (SEA). Following the excitation of the photosensitizer, electrons are injected to the sacrificial electron donor. The latter oxidizes the metal complex to form high valent metal oxo species (probably), which oxidizes water to dioxygen (Figure 35).
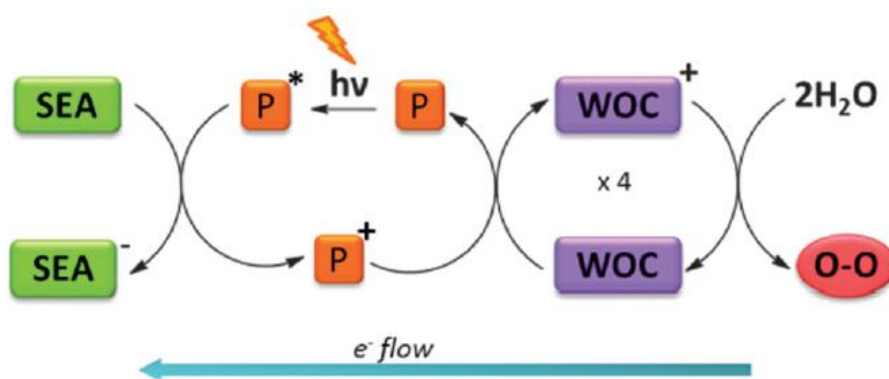
Figure 35 : Light induced water oxidation mechanism.

The water oxidation catalysis of Cu^{II} complex coordinated to α-fluorinated tris(2-pyridylmethyl)amine (F_3TPA) is the only example of a copper catalyst for photochemical dioxygen production.[129]

I.4. Oxidation of various hydrocarbons

High-valent metal-oxo species are key intermediates in biological oxidations by metalloenzymes. Interestingly, the synthetic high valent metal-oxo (M=Fe, Ru, Ir) complexes have been found to be reactive toward substrates containing unreactive C–H bonds transferring an oxygen atom from water.[130,131]

In the field of redox catalysis, such high valent metal – oxo species (M=Mn, Fe, Ru) formed by light source also oxidize a variety of substrates such as alkanes, alkenes sulfides or triphenylphosphine with water as an oxygen atom source.[132,133,134] No examples using copper has been reported yet.

II. Objectives

To the best of our knowledge, no intermediate has been directly detected during water oxidation catalysis using copper complexes. Also, there is no report on oxygenation reactions mediated by copper (II) complexes using water as an oxygen atom source. More importantly, the question of heterogeneous catalysis *versus* homogeneous catalysis is a matter of debate in the scientific community. [115] In very alkaline pH, metal ions form copper oxides that have been shown to be effective in water oxidation for dioxygen evolution.[136]

The main advantage of manipulating homogeneous catalysts over heterogeneous ones is the ability to examine the reaction mechanisms and the identification of the reactive intermediates.

Based on the well-known chemistry of Cu^I with dioxygen, we were interested in investigating the "reverse way" i.e. performing water oxidation or activation to generate similar intermediates possibly leading to the release of dioxygen (Scheme 40). We were interested in starting from a copper-water complex or a Cu_2(bis-µ-hydroxo) complex to perform an O-atom transfer reaction and investigate the mechanism.
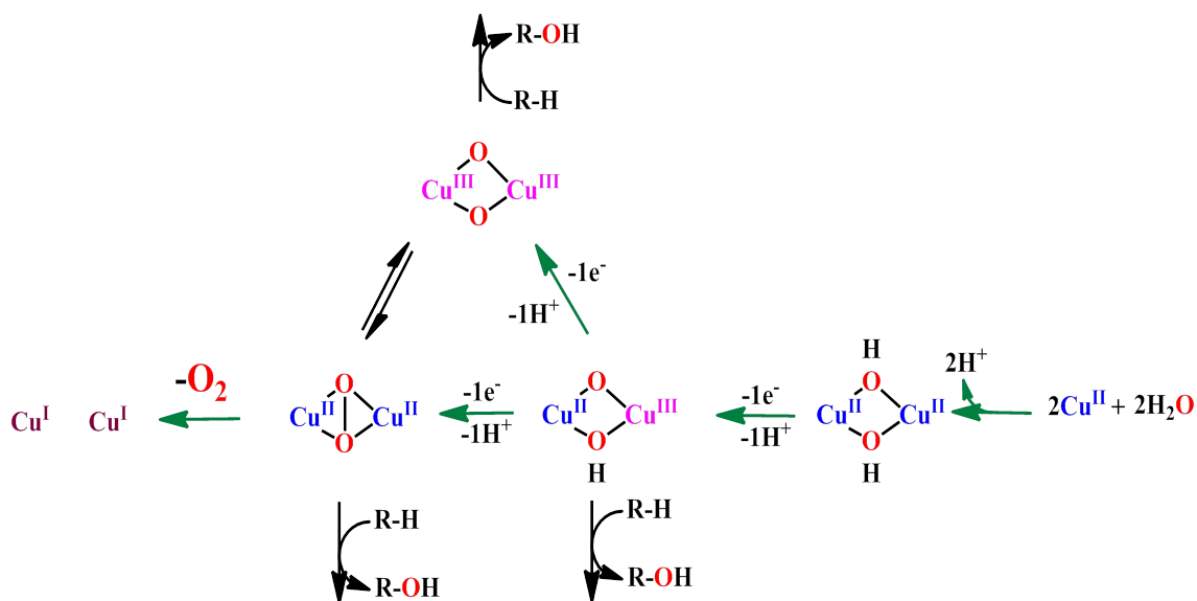
Scheme 40 : Schematic representation of possible intermediates starting from Cu^{II} complex and H_2O.

Our approach is the "substrate binding ligand approach" described in the **Chapter II**. Herein, we have investigated the selective oxygen-insertion into the indane moiety of $IndanePY_2$ by electrochemically oxidizing copper(II) precursors in water.

III. Results and Discussion

III.1. Characterization of 2a in aqueous solution

III.1.1. NMR spectroscopy

In order to investigate the exchange of triflate anions (which are bound to copper) with water in aqueous solution, ^{19}F paramagnetic NMR was recorded. The ^{19}F NMR spectrum in $CDCl_3$ showed a broad peak shifted to lower ppm (-67 ppm) due to a strong interaction of fluoride of triflate anion with the paramagnetic copper center and therefore indicating that triflate counter-anions remain coordinated under those conditions (Figure 36, top). On the contrary, in D_2O the peak is sharp and found at -78 ppm, a value close to the ^{19}F NMR peak of free triflate anions in D_2O (Figure 36, bottom).
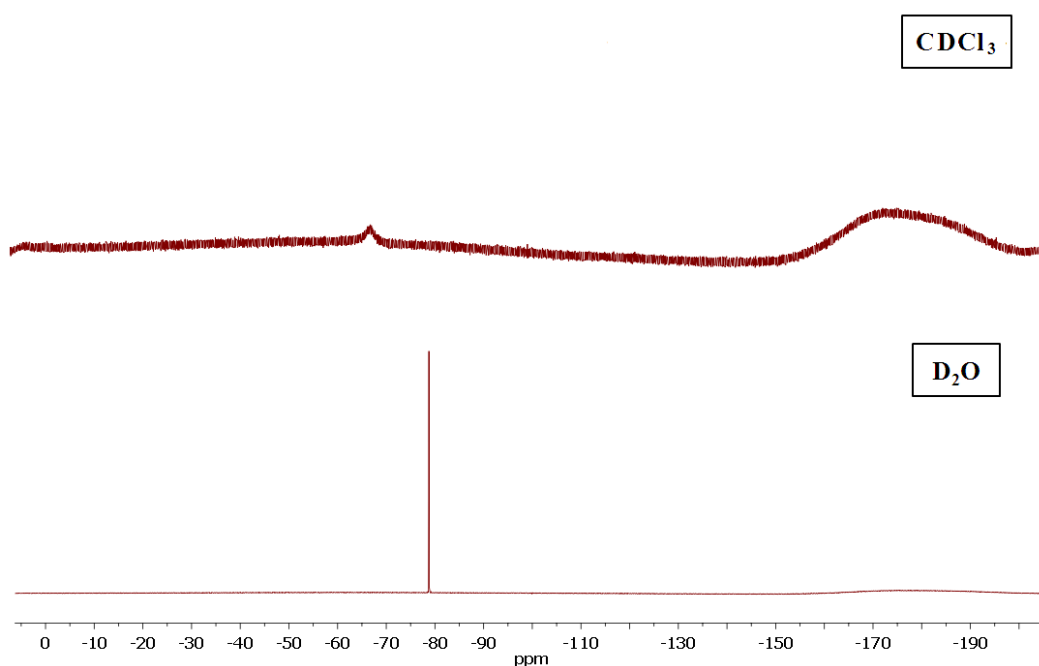
Figure 36 : ^{19}F NMR spectra of **2a** in $CDCl_3$ (top) and D_2O (bottom).

So, this suggests that the triflate counter-anions are not coordinated to copper(II) in aqueous solutions and that they are replaced by water molecules (Scheme 41).
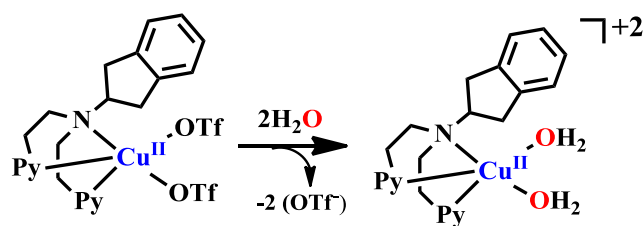
Scheme 41 : Triflate substitution by water molecules in aqueous solutions.

III.1.2. Redox properties

Electrochemical properties of **2a** in organic solvents are described **Chapter II**. The quasireversible redox process of Cu^{II}/Cu^{I} was observed but further oxidation of Cu^{II} to Cu^{III} was not observed.

Electrochemical properties of **2a** were then recorded in deoxygenated aqueous solutions at pH 6.5 with $NaNO_3$ as supporting electrolyte. As shown in Figure 37, the CV of **2a**, exhibits a quasi-reversible wave at $E_{1/2}$=0.32V *vs.* NHE assigned to $Cu^{II/I}$ couple. In addition, a large irreversible anodic (oxidation) peak at 1.3V *vs.* NHE, which was absent in organic solvent, can be attributed to the oxidation of Cu^{II} to Cu^{III}. However, the intensity of this peak is larger than the 1e⁻ reduction peak suggesting that an electrocatalytic process occurs (possibly water oxidation).
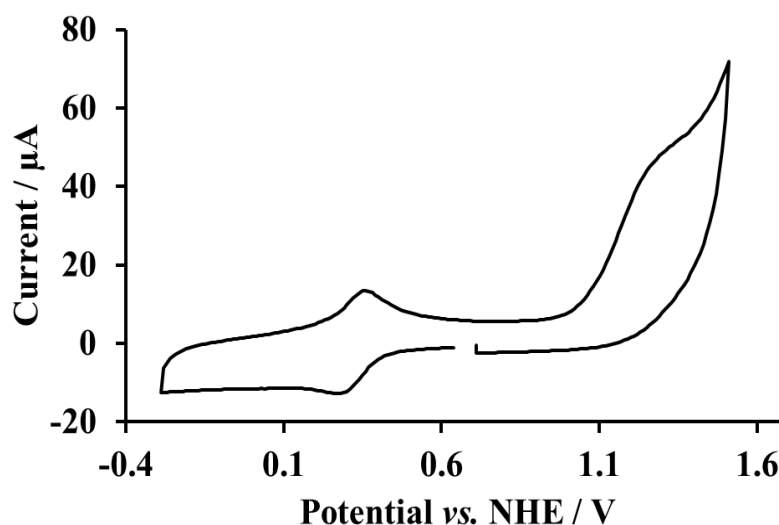
Figure 37 : Cyclovoltamogram of **2a** in H_2O pH 6.5 (0.7mM, $NaNO_3$). Three electrode set-up with glassy carbon working electrode, platinum counter electrode and AgCl/Ag reference electrode (0.210 *vs.* NHE). 100 mV/s

III.2. Influence of the pH

III.2.1. Influence of the pH on the redox properties

Increasing the pH, the $Cu^{II/I}$ wave is shifted to lower potentials (Figure 38). Interestingly, from pH 7.9 to 8.9 the cathodic and anodic peak become broader and several peaks can be distinguished. This kind of electrochemical behavior can be rationalized by the presence of species in equilibrium with different protonation states that affect the redox potentials.
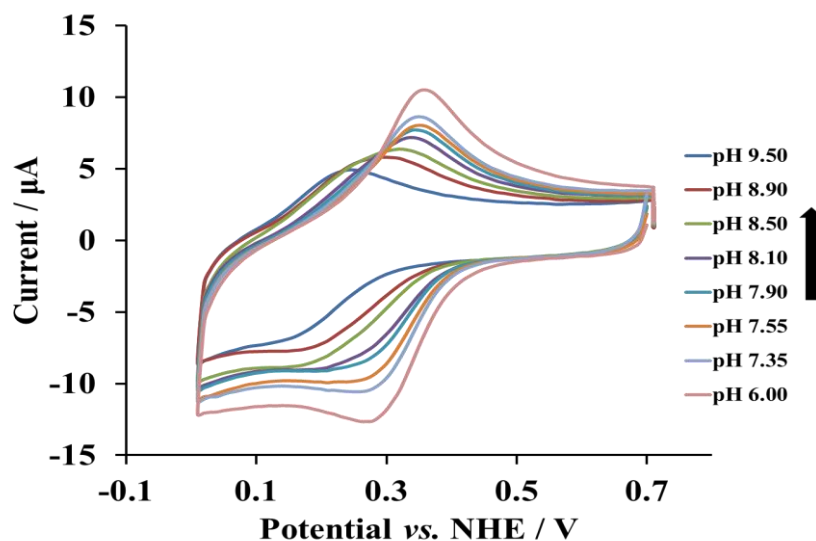

Figure 38 : Influence of the pH on the Cu^{II}/Cu^{I} peak of **2a** recorded at 100 mV/s. [**2a**]=0.7mM in NaNO$_3$/H$_2$O, WE= Glassy carbon, Reference electrode: AgCl/Ag (0.210 *vs*. NHE).

On the other hand, the oxidation peak at 1.3V *vs*. NHE is not significantly affected by the pH (Figure 39) until pH 8.10. Above that pH, the intensity of the peak decreases and a new oxidation process appears around 1 V *vs*. NHE.
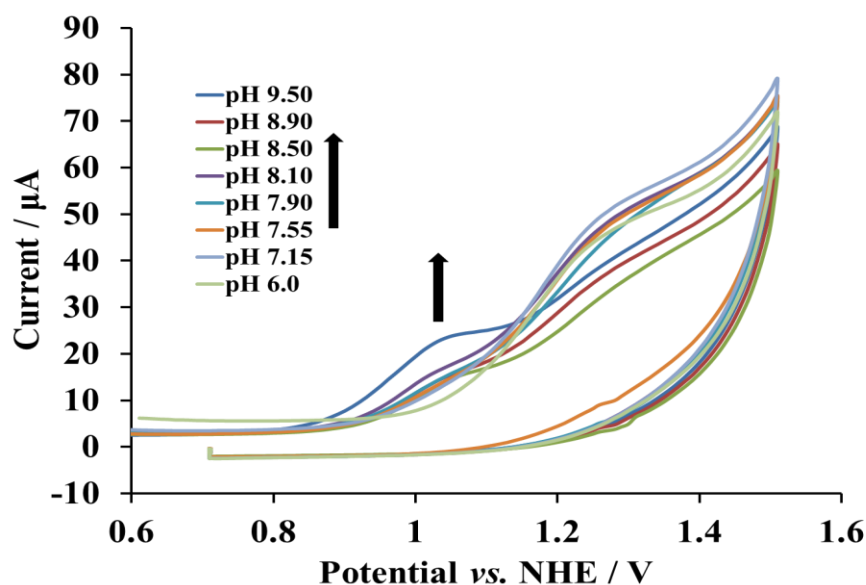
Figure 39 : Influence of the pH on the oxidation peak of **2a** recorded at 100 mV/s. [**2a**]=0.7mM in NaNO$_3$/H$_2$O, WE= Glassy carbon, Reference electrode: AgCl/Ag (0.210 *vs.* NHE)

III.2.2. Potentiometric Titrations and speciation diagrams

III.2.2.a. Protonation constants of the ligand IndanePY$_2$

   The potentiometric titration experiments were performed and analyzed in collaboration with Dr. Olga Iranzo in the laboratory. The protonation constants of the IndanePY$_2$ were determined at 25°C in the presence of 0.1 M NaNO$_3$. The titration curve was fitted using HYPERQUARD.[137] From the titration of the ligand, three protonation states were determined in the 3-7.5 pH range. The two first protonation constants at 2.81 and 3.9 were assigned to the protonation of the pyridine N groups and the subsequent one protonation constant at 7.74 to the protonation of the tertiary amine group. Those values, which are shown in Table 5, are in agreement with already reported protonation constants of RPY$_2$ ligands.[138] At pH higher than 7.8 the ligand IndanePY$_2$ is neutral resulting in precipitation in aqueous solution. Therefore after this point we stopped recording.

Table 5 : Overall (β_i^H) and stepwise (logK_i^H) protonation constants of the ligand in aqueous solution at 25°C and ionic strength 0.1M NaNO$_3$.

Equilibrium reaction	Log β	Equilibrium reaction	logK_i^H
$L_{ind} + H^+ \leftrightarrow HL_{ind}^+$	7.74	$L_{ind} + H^+ \leftrightarrow HL_{ind}^+$	7.74
$L_{ind} + 2H^+ \leftrightarrow H_2L_{ind}^{2+}$	11.64	$HL_{ind}^+ + H^+ \leftrightarrow H_2L_{ind}^{2+}$	3.9
$L_{ind} + 3H^+ \leftrightarrow H_3L_{ind}^{3+}$	14.45	$H_2L_{ind}^+ + H^+ \leftrightarrow H_3L_{ind}^{3+}$	2.81

Where L_{ind} refers to IndanePY$_2$

III.2.2.b. Speciation diagrams for the copper (II) complexes of the ligand IndanePY$_2$

The stability constants of the formation of the copper(II) complexes with the IndanePY$_2$ were also determined by potentiometric titrations (Figure 40) under the same experimental conditions as those described above by using different C_{Cu}/C_{ligand} ratios, namely, 0.5:1, 1:1, and 1.5:1.
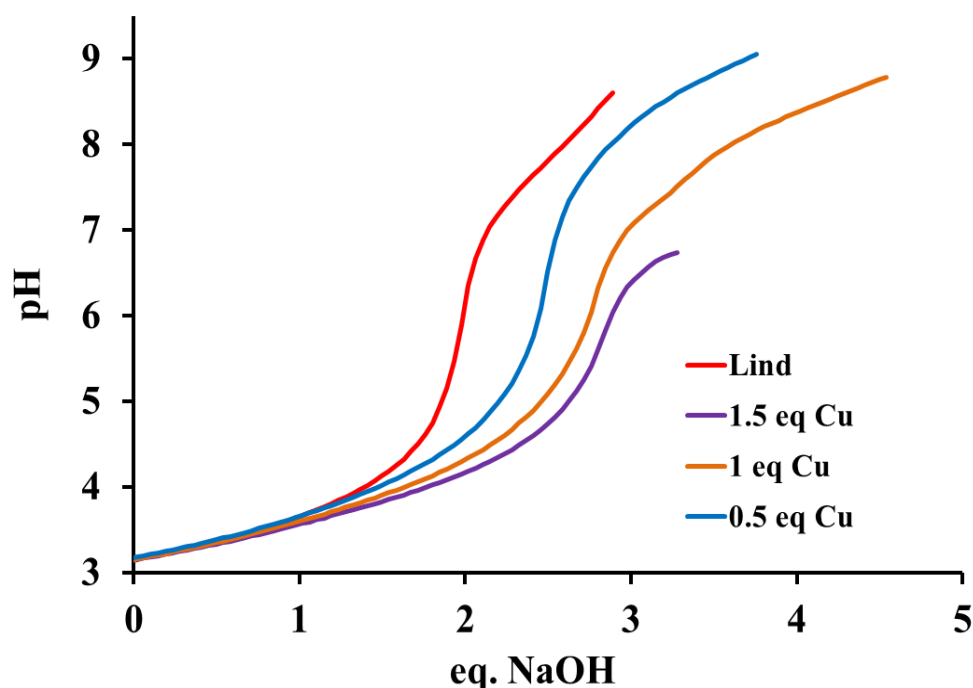

Figure 40 : Potentiometric curve of IndanePY$_2$ at 0.9 mM (red) and in the presence of 0.5 eq. (blue), 1.2 eq. (orange) and 1.5 eq. (purple) of Cu^{II}(NO$_3$)$_2$ (0.1M NaNO$_3$).

The species considered in the final model were obtained by taking into account the total set of data of all titrations. In addition to the ligand's deprotonation steps, we considered: several formation constants for complexes formed with the ligand in different protonation states. Two additional deprotonation states had to be included, probably accounting for the deprotonation of water molecules bound to the copper ions. The values determined for the overall formation constants (logβ) and the calculated stepwise formation constants (logK_i^H) are summarized in Table 6.

Table 6 : Overall (β_i^H) and stepwise (logK_i^H) protonation constants of the copper (II) complexes of IndanePY$_2$ in aqueous solution at 25°C and ionic strength 0.1M NaNO$_3$.

Equilibrium reaction	Log β	Equilibrium reaction	logK_i^H
$Cu^{2+} + H^+ + L_{ind} \leftrightarrow [CuHL_{ind}]^{3+}$	10.81	$[CuL_{ind}]^{2+} + H^+ \leftrightarrow [CuHL_{ind}]^{3+}$	3.95
$Cu^{2+} + L_{ind} \leftrightarrow [CuL_{ind}]^{2+}$	6.86	$Cu^{2+} + L_{ind} \leftrightarrow [CuL_{ind}]^{2+}$	6.86
$Cu^{2+} + L_{ind} \leftrightarrow [CuL_{ind}H_{-1}]^+ + H^+$	-0.96	$[CuH_{-1}L_{ind}]^+ + H^+ \leftrightarrow [CuL_{ind}]^{2+}$	7.8
$Cu^{2+} + L_{ind} \leftrightarrow [CuL_{ind}H_{-2}]^0 + 2H^+$	-9.43	$[CuH_{-2}L_{ind}]^0 + H^+ \leftrightarrow [CuH_{-1}L_{ind}]^+$	8.47

From those constants, a speciation diagram can be drawn (see Figure 41 for the $[L_{ind}]:[Cu^{2+}]$ 1:1 system at 0.7 mM concentration). At pH 3.0, a "Cu((L$_{ind}$)H)" complex

is predominant (80%). It is highly probable that the amine group of the ligand remains protonated and that copper ions are only coordinated to the pyridine groups of the ligand. When pH > 4, the ligand gets fully deprotonated and the Cu^{II} ions are probably bound to the three N groups of the ligand providing a blue solution. The major species corresponds to a $[L_{ind}Cu]^{2+}$ complex with log β= 6.86. At pH > 6.0, $[CuH_{-1}L_{ind}]$ species are formed and reach a maximum (50%) at pH *ca.* 8.2. These species are formed after losing one proton from an external source. In our case, we assume that a water molecule bound to copper is deprotonated. Interestingly above pH=8.0-8.5, $[CuH_{-2}L_{ind}]$ species are formed after a second deprotonation of external source, i.e. probably another copper-bound water molecule. At pH > 9.0, precipitation was observed, consistent with the formation of neutral $LCu(OH)_2$ species.

Changing the supporting electrolyte in the aqueous solution (NaOTf *vs.* $NaNO_3$) or the copper salt ($Cu(OTf)_2$ *vs.* $Cu(NO_3)_2$) did not change significantly the titration curves and therefore the protonation and formation constants determined herein.
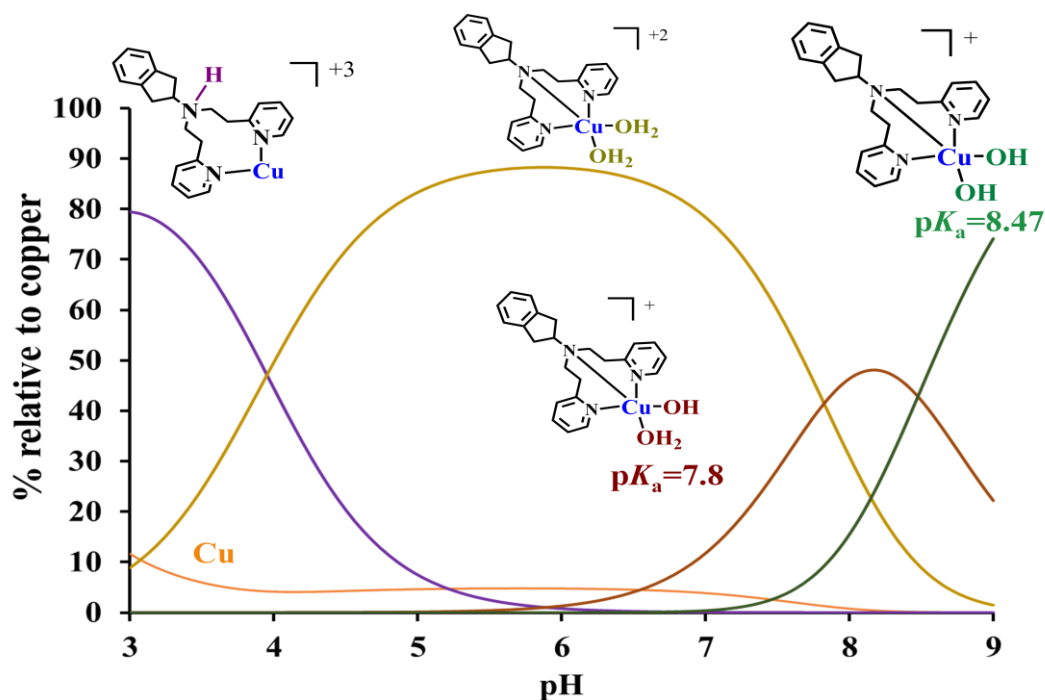
Figure 41 : Species distribution diagram for the copper(II) complex of 0.7 mM IndanePY$_2$ with $Cu(NO_3)_2$ (1 equiv) at 25^oC and 0.1 M $NaNO_3$. Charges are omitted for simplicity.

From these data, three copper-containing predominant species exist above pH 6.0. Those species are summarized in Table 7.

Table 7 : Speciation of IndanePY$_2$: Cu^{2+} 1:1 in solution

Species		$\log K_i^H$
$[CuL_{ind}]^{2+}$	$[L_{ind}Cu(OH_2)_2]^{2+}$	6.86
$[CuL_{ind}H_{-1}]^+$	$[L_{ind}Cu(OH)(OH_2)]^+$	7.8
$[CuL_{ind}H_{-2}]$	$[L_{ind}Cu(OH)_2]$	8.47

III.2.3. Spectroscopic studies vs. pH

III.2.3.a. UV-Vis spectroscopy

The complex **2a** dissolved in water pH 6.0 exhibits one d-d band at 690 nm (Figure 42). In the pH range 6.5-8.5, an increase of absorbance is observed at 307 nm. This absorbance is often observed in dinuclear hydroxo-bridged copper(II) complexes with RPY_2 ligands. Above pH 8.50 this band decreases and precipitation occurs. The change of the salt ($NaNO_3$ or NaOTf) in the solution does not affect the spectroscopic features and their pH dependance.
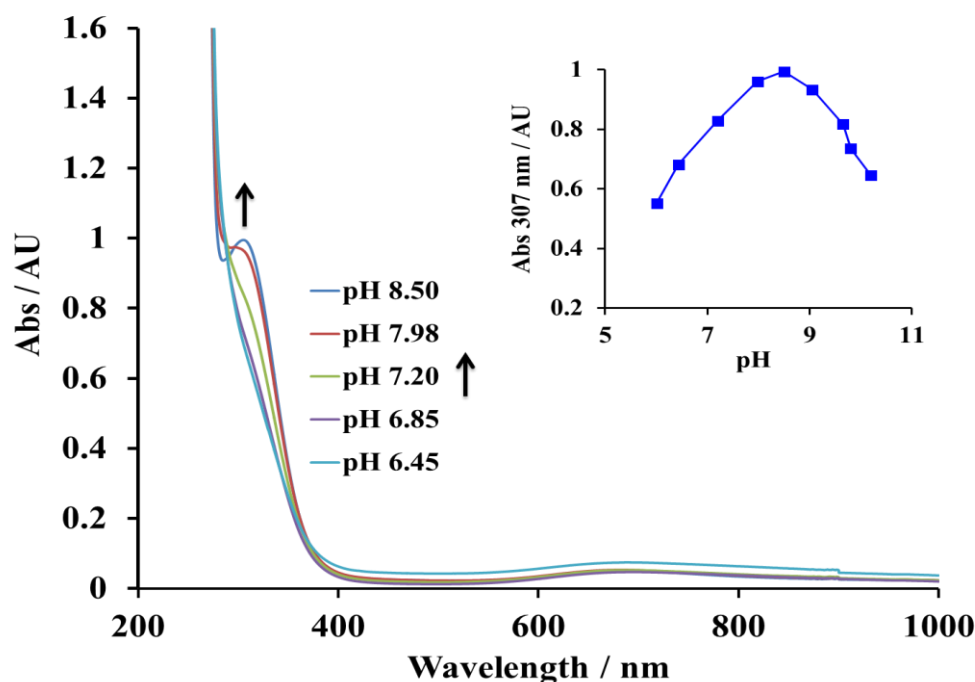
Figure 42 : UV-Vis spectra of complex **2a** in aqueous solution in different pH values [**2a**]=0.4mM

III.2.3.b. EPR spectroscopy

To probe the nature of the species in solution as a function of pH (mononuclear or binuclear), electron paramagnetic resonance (EPR) spectra were recorded at different pHs. EPR spectra were recorded at 120K using calibrated tubes in the presence of 10% glycerol (Figure 43). At pH 6.0 the EPR spectra is typical for mononuclear Cu^{II} ions and is consistent with the presence of a monomeric $L_{ind}Cu^{II}(H_2O)_2$ complex. Another signal, probably arising from "$CuL_{ind}H$" species as determined in the potentiometric titrations, is also detected at this pH.

The overall intensity of the signal of the mononuclear species decreases as the pH increases indicating the formation of X-band EPR silent species at higher pHs. As suggested by UV-visible spectroscopy, hydroxo-bridged dinuclear species can be

formed such as $[((L_{ind})Cu^{II})_2(\mu\text{-}OH)_2]$ (Scheme 42). The copper ions of this dinuclear species would either be ferromagnetically or anti-ferromagnetically coupled, leading to the decrease of EPR intensity. Increasing the pH above 8.5 led to precipitation.
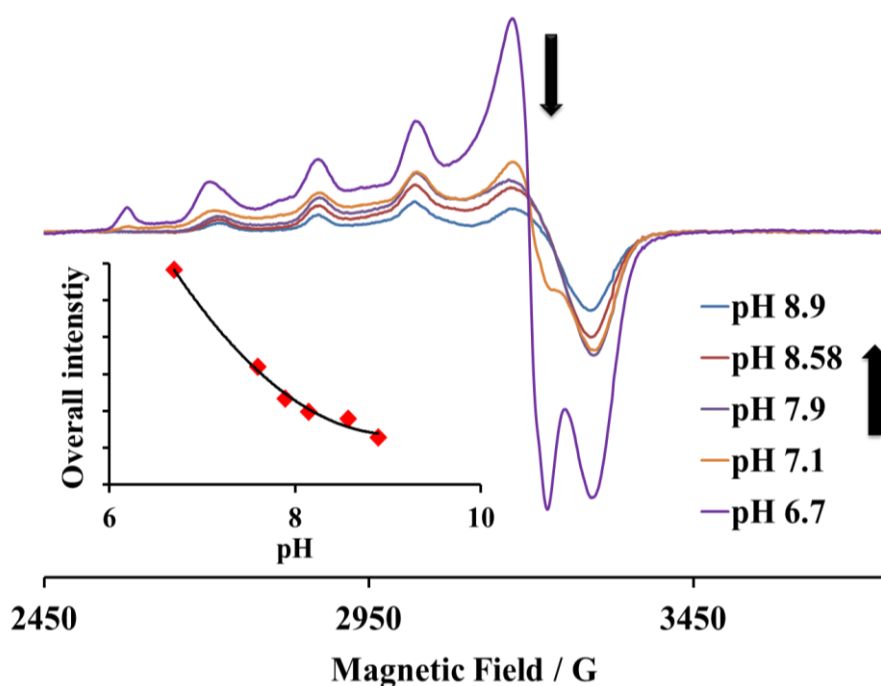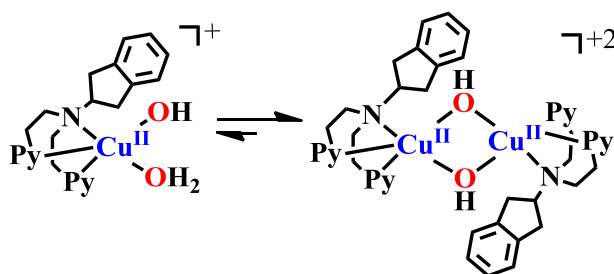

Figure 43 : EPR spectra of **2a** recorded at 120K Conditions: [**2a**]=0.7mM, 0.1M NaNO$_3$/H$_2$O, 10% glycerol.

Scheme 42 : Formation of dinuclear species, either ferromagnetically or anti-ferromagnetically coupling, proposed by the decrease of EPR intensity.

At pH 3.0, only one species is predominatly formed in aqueous solution. The measured EPR intensity in this pH corresponds to "CuL$_{ind}$H" species, as determined in the potentiometric titrations. The parameters derived from simulation at pH 3.0 (data not shown) are the following: $g_{//}$ = 2.41 $A_{//}$ = 115 G (388 MHz) and $g\perp$ = 2.083. At pH 4.0 – 6.0, two species exist in equilibrium. The measured EPR intensity arises from the signal of the "CuL$_{ind}$H" species along with the monomeric $[L_{ind}Cu(H_2O)_2]^{2+}$. At pH 6.0 only the $[L_{ind}Cu^{II}(H_2O)_2]^{2+}$ species exist in aqueous solution. The EPR parameters derived from simulation at pH 6.0 are: $g_{//}$ = 2.25 $A_{//}$ =142 G (447 MHz) and $g\perp$ = 2.067. These EPR parameters are similar to that obtained for complex **2a** in organic solvents (See **Chapter II**).

At pH 6.0 – 8.0, two major species exist in solution, according to potentiometric titrations. The decrease of the EPR signal as the pH increases, indicates the formation of dinuclear

81

species. Therefore, the remaining EPR signal arises from the remaining mononuclear $L_{ind}Cu^{II}(H_2O)_2$ complex. After simulation and integration, 40-60% loss of intensity was calculated at pH 8.0 depending on the conditions (concentration/supporting electrolyte etc.)

III.2.3.c. Spectroscopic studies vs. pH: comparison

After comparison of the intensity trends followed by UV-Vis and EPR spectroscopy as a function of pH (Figure 44), it is evident that the species with characteristic absorption at 307 nm is EPR silent.
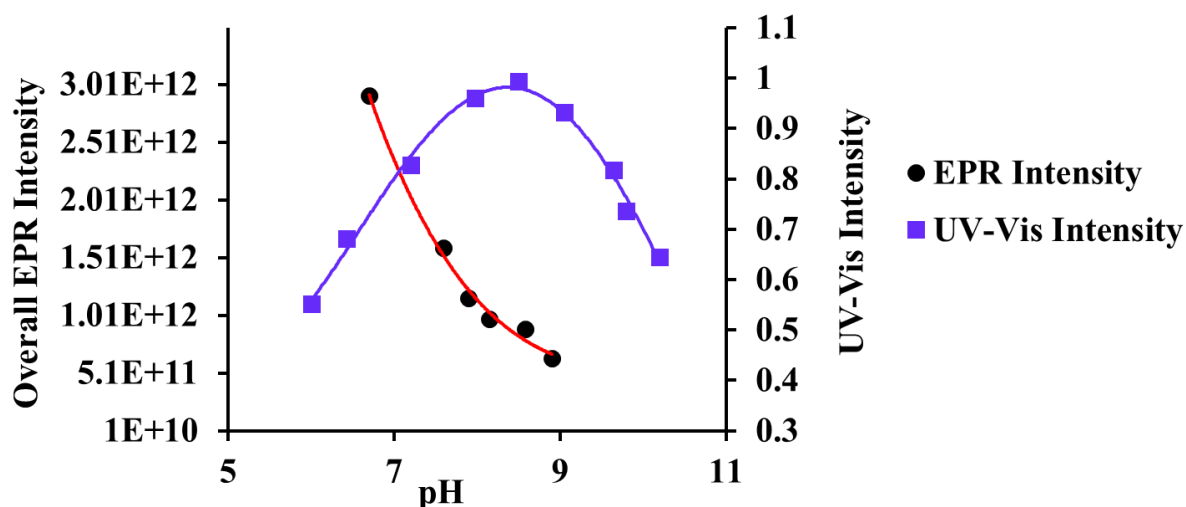
Figure 44 : Comparison of intensity by UV-Vis spectroscopy (at 307 nm) and overall intensity by EPR spectroscopy (after baseline correction and double integration).

III.3. DFT calculations

In the absence of X-ray structure of the different species, DFT calculations were undertaken in collaboration with Dr. Amélie Kochem in our group in order to investigate the structures of the species. DFT geometry optimizations were performed at the B3LYP level of theory. All calculations have been performed with the ORCA program package.[139] Full geometry optimizations have been calculated with the hybrid functional B3LYP in conjunction with the Def2-TZV/P basis set for all atoms.[140] According to the experimental conditions, solvent effects were accounted for property calculations, energy calculations and geometry optimizations. For that purpose, we used the water ($\varepsilon = 80.4$) solvent within the framework of the conductor like screening (COSMO) dielectric continuum approach.[141]

^{19}F-NMR studies showed that in aqueous solution the triflate counterions are presumably replaced by one or two water molecules. Potentiometric titrations have indicated that two bound water molecules are deprotonated therefore, calculations were

performed considering the most probable structure: $[L_{ind}Cu(H_2O)_2]^{2+}$. DFT calculations were nevertheless performed on other putative species including (i) with one water molecule ($[L_{ind}Cu(H_2O)]^{2+}$) and (ii) one or two hydroxyl groups ($[L_{ind}Cu(OH)]^+$ and $[L_{ind}Cu(OH)_2]$, respectively), that could coexist in solution at different pH based on the results of potentiometric titrations. In each case, we considered two possible conformations with either two pyridines bound in the equatorial positions (*conf1*) or one pyridine equatorial and the other in axial position (*conf2*). The first conformation (*conf1*) was found to be energetically favored over the other one for each species considered (Figure 45-Figure 48).

(H₂O)₂
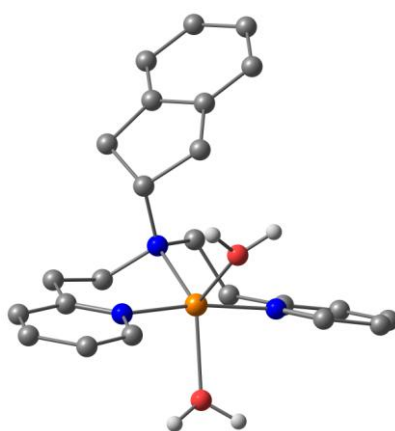
Conformer 1

Figure 45 : Geometry optimized structure of $[L_{ind}Cu(H_2O)_2$-*conf1*$]^{2+}$ (doublet state). ($[L_{ind}Cu(H_2O)_2$-*conf2*$]^{2+}$) does not converge.

(H₂O)

Conformer 1   **Conformer 2**
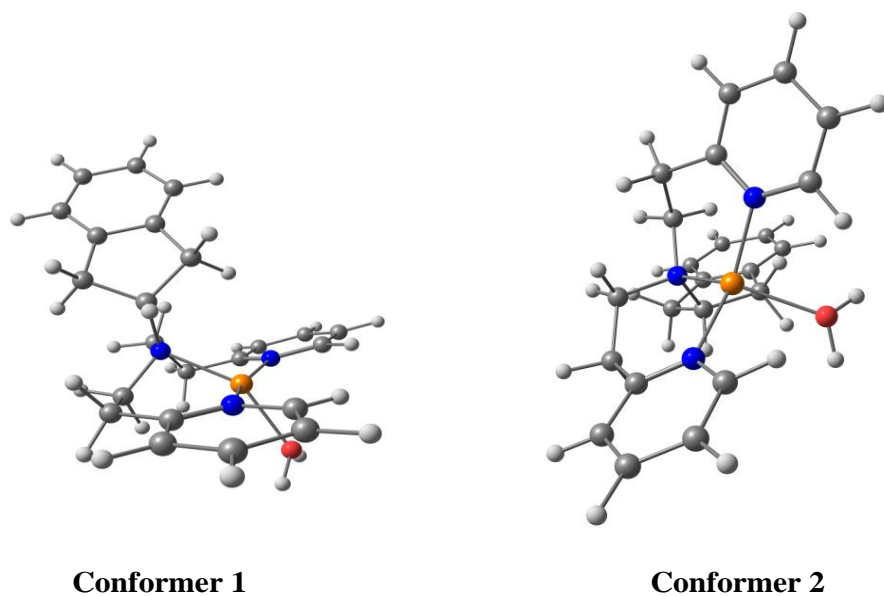
Figure 46 : Geometry optimized structure of [L$_{ind}$Cu(H$_2$O)-*conf1*]$^{2+}$ (left) and [L$_{ind}$Cu(H$_2$O)-*conf2*]$^{2+}$ (right). [L$_{ind}$Cu(H$_2$O)-*conf1*]$^{2+}$ was found to be isoenergetic as compared to [L$_{ind}$Cu(H$_2$O)-*conf2*]$^{2+}$ (favored by only 0.3 kcal/mol).

(OH)₂

Conformer 1   **Conformer 2**
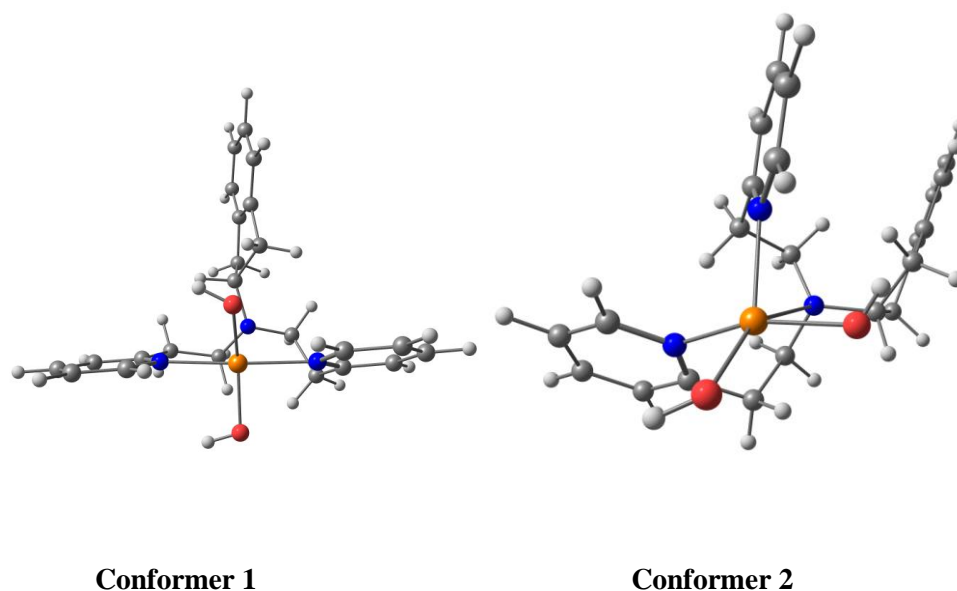
Figure 47 : Geometry optimized structure of [L$_{ind}$Cu(OH)$_2$-*conf1*] (left) and [L$_{ind}$Cu(OH)$_2$-*conf2*] (right). [L$_{ind}$Cu(OH)$_2$-*conf1*] is found to be favored by 4.18 kcal/mol over [L$_{ind}$Cu(OH)$_2$-*conf2*].

(OH)

<div align="center">

Conformer 1   **Conformer 2**

</div>
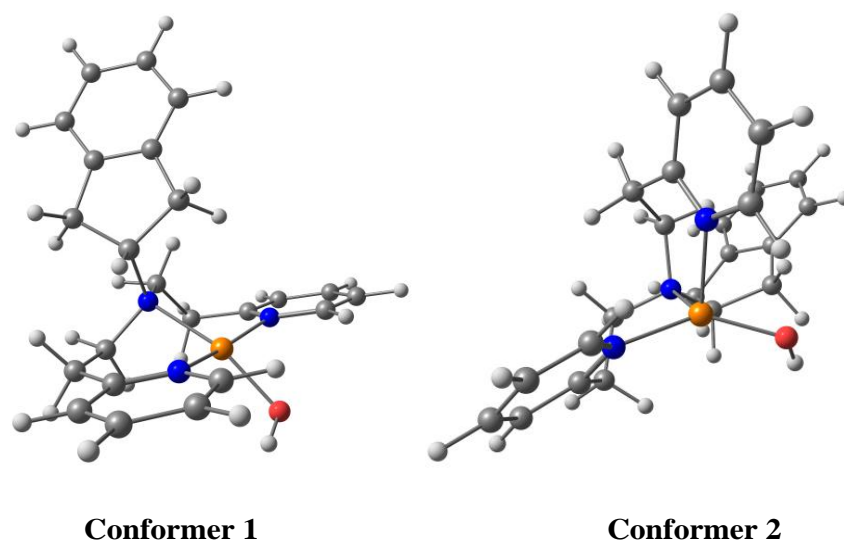
Figure 48 : Geometry optimized structure of [L_{ind}Cu(OH)-*conf1*]$^+$ (left) and [L_{ind}Cu(OH)-*conf2*]$^+$ (right). [L_{ind}Cu(OH)-*conf1*]$^+$ was found to be favored by 4.81 kcal/mol over [L_{ind}Cu(OH)-*conf2*]$^+$.

EPR calculations on the optimized structures of each species mentioned above have been performed. The calculated g-tensors and hyperfine coupling constants are given in Table 8. The calculated g-tensors for most of the different species are rather similar and are in good agreement with the experimental data except for [L_{ind}Cu(OH)-*conf2*]$^+$ that could clearly be ruled out since it points to a dz^2 SOMO with EPR parameters far from the experimental ones. Comparing the calculated A-values lead us to the conclusion that two calculated structures could account for the observed experimental data: [L_{ind}Cu(H$_2$O)$_2$]$^{2+}$-*conf1*] and [L_{ind}Cu(OH)$_2$-*conf1*]. Given the potentiometric titration data, our calculations therefore support the formation of [L_{ind}Cu(H$_2$O)$_2$]$^{2+}$ species at pH 6-8 range.

Table 8 : Calculated EPR parameters of the mononuclear complexes considered in this study.

Complex	Calculated g_1, g_2, g_3 [A_1, A_2, A_3] [a]	g_{iso} [A_{iso}]	Experimental $g_{\perp}, g_{//}$ [$A_{//}$] [a]
$L_{ind}Cu$-$(H_2O)_2$-*conf1*	2.025, 2.092, 2.171 [-66, 199, -460]	[2.096, -109]	
$L_{ind}Cu$-$(H_2O)_2$-*conf2*	//doesn't converge	[,]	
$L_{ind}Cu$-(H_2O)-*conf1*	2.039, 2.051, 2.153 [23, -45, -547]	[2.081, -198]	
$L_{ind}Cu$-(H_2O)-*conf2*	2.046, 2.069, 2.178 [-13, 19, -522]	[2.097, -172]	
$L_{ind}Cu$-$(OH)_2$-*conf1*	2.041, 2.068, 2.185 [71, 145, -481]	[2.098, -88]	2.067, 2.25 [447]
$L_{ind}Cu$-$(OH)_2$-*conf2*	2.045, 2.067, 2.192 [7, -89, -604]	[2.101, -229]	
$L_{ind}Cu$-(OH)-*conf1*	2.036, 2.047, 2.146 [-84, -137, -680]	[2.077, -300]	
$L_{ind}Cu$-(OH)-*conf2*	2.004, 2.176, 2.190 [-17, -171, 365]	[2.123, 59]	

[a] Hyperfine coupling constant A: values given in MHz. DFT calculations were performed by using the B3LYP functional.

Spectroscopic studies suggest that a dinuclear EPR silent $Cu_2(\mu$-hydroxo) species is the predominant species in water at pH 8-9. Therefore, DFT geometry optimization was performed for the dinuclear $([(L_{ind}Cu)_2(\mu$-$OH)_2])^{2+}$ complex by considering a triplet state (Figure 49). Again, we computed several putative conformations of the dinuclear Cu(II) complex with two hydroxo bridges.
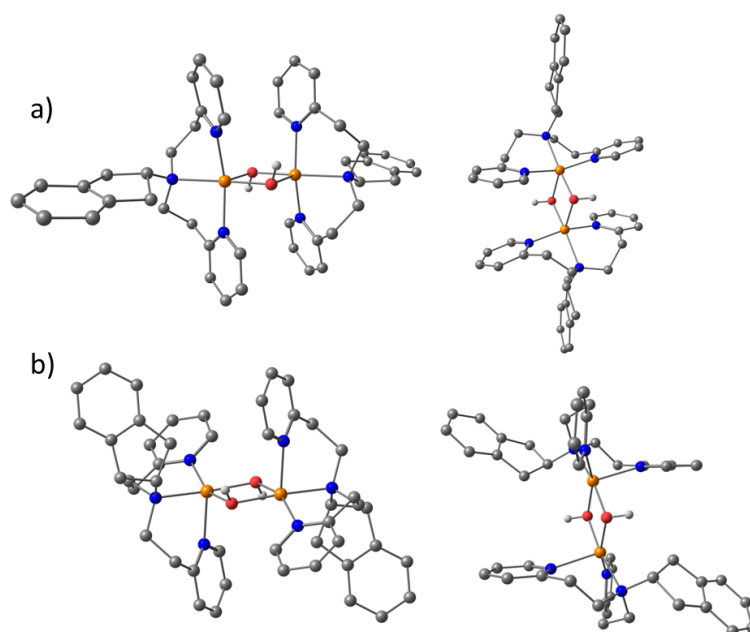

Figure 49 : Different views of the geometry optimized structures of a) $[(L_{ind}Cu)_2$-$(OH)_2$-*conf1*$]^{2+}$ and b) $[(L_{ind}Cu)_2$-$(OH)_2$-*conf2*$]^{2+}$ (triplet states). $[(L_{ind}Cu)_2$-$(OH)_2$-*conf2*$]^{2+}$ is found to be favored by 3.34 kcal/mol over $[(L_{ind}Cu)_2$-$(OH)_2$-*conf1*$]^{2+}$. H atoms except for OH bridging groups are omitted for clarity.

The broken-symmetry (BS) singlet state of of $[(L_{ind}Cu)_2(OH)_2$-*conf2*$]^{2+}$ (obtained from a BS(1,1) calculation) is found to be energetically favored by 0.27 kcal.mol^{-1} over

the triplet state and magnetic coupling constant of 93.5 cm^{-1} was computed by using the Yamaguchi formula[142,143] to estimate the exchange coupling constants J based on the Heisenberg–Dirac–van Vleck Hamiltonian.[144–147] This value corresponds to a moderate antiferromagnetic coupling and is consistent with the formation of an X-band EPR silent species at pH 8-9.

The exact nature of the orbitals involved in the UV-vis transitions of $[L_{ind}Cu(H_2O)_2]^{2+}$ (doublet state) and $[(L_{ind}Cu)_2(OH)_2\text{-}conf2]^{2+}$ (BS singlet state) was investigated by time-dependent density functional theory (TD-DFT) calculations. In the case of $[L_{ind}Cu(H_2O)_2]^{2+}$, the principal electronic excitations are LMCT transitions which are computed at λ_{calc} = 293 nm (f =0.15) and λ_{calc} = 322 nm (f = 0.08) (

Figure 50). In both cases, the acceptor orbital has a significant d_{xy} character, and the donor orbital is principally developed on pyridine for the band computed at 293 nm and on the aminoindane fragment for the band computed at 322 nm (Figure 51). In addition, several transitions of low intensity contribute to the absorption experimentally observed at 690 nm and that are predicted at 661 nm and 633 nm (d-d transitions, f = 0.002 in both case). In the case of $[(L_{ind}Cu)_2(OH)_2\text{-}conf2]^{2+}$, the principal electronic excitations are predicted at 310 nm (f = 0.092) and 345 nm (f = 0.061) (Figure 52). The appearance of the second transition (calculated at 345 nm) is consistent with the experimental appearance of a transition at 310 nm. Interestingly, calculations also predict the appearance of a new transition of significant intensity at lower energy (368 nm, f = 0.062), in agreement with experimental UV titration upon going at basic pH. This absorbance is often observed in dinuclear hydroxo-bridged copper(II) complexes with RPY$_2$ ligands. The component transitions of the excited state calculated at 368 nm are numerous, and none of them is decisively dominant as is it also the case for the excited states predicted at 310 nm and 345 nm. However, for each of these excited states, the acceptor fragment has a significant $d_{x^2-y^2}$ character from both copper ions with a contribution of both hydroxyl bridging groups and other coordinated atoms while the donor fragment is mainly developed on the ligand and on the Cu$_2$(OH)$_2$ core with a contribution of the coordinated atoms.

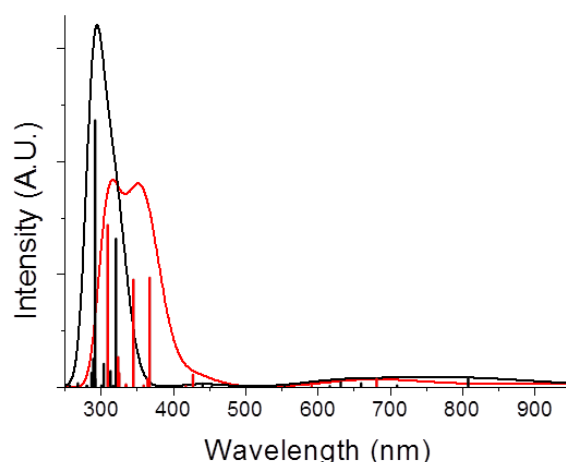**Figure 50 :** TDDFT-predicted UV-vis spectra of $[L_{ind}Cu(H_2O)_2]^{2+}$ (black line, doublet state), and $[(L_{ind}Cu)_2(OH)_2\text{-}conf_2]^{2+}$ (red line, BS singlet state).
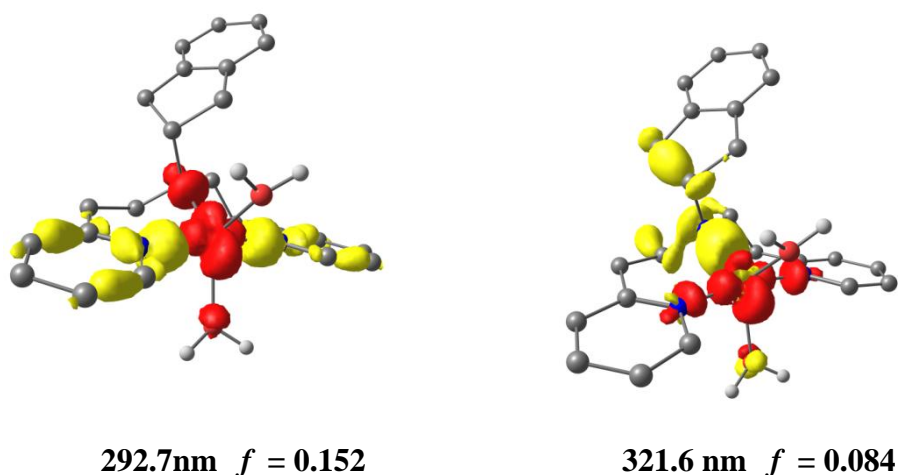
292.7nm $f = 0.152$ **321.6 nm** $f = 0.084$

Figure 51: TD-DFT assignment of the electronic transitions of $[L_{ind}Cu(H_2O)_2]^{2+}$ (doublet state). The diagrams give difference electron densities where red corresponds to positive density and yellow to negative density.
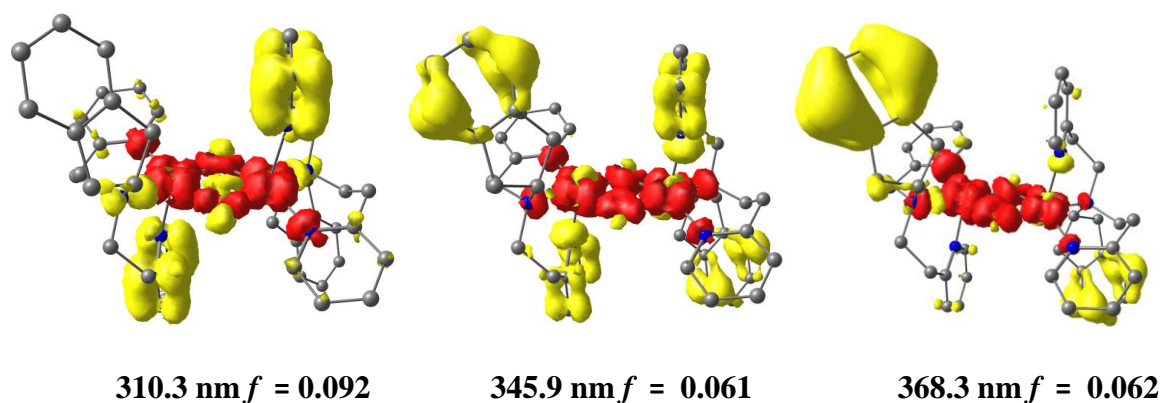

310.3 nm $f = 0.092$ **345.9 nm** $f = 0.061$ **368.3 nm** $f = 0.062$

Figure 52 : TD-DFT assignment of the electronic transitions of $[(L_{ind}Cu)_2(OH)_2\text{-}conf2]^{2+}$ (BS singlet state). The diagrams give difference electron densities where red corresponds to positive density and yellow to negative density.

Finally, we attempted to evaluate the relative stability of the dinuclear complex in respect to the corresponding mononuclear complex with one hydroxo ligand coordinated taken into account the most energetically favored conformation in each cases $[(L_{ind}Cu)_2(OH)_2\text{-}conf2]^{2+}$ in respect to $[L_{ind}Cu(OH)\text{-}conf1]^+$. For energetic analysis, the basis set superposition error was accounted for in the calculation of the final energies of the complexes. The calculated energies predict $[(L_{ind}Cu)_2(OH)_2\text{-}conf2]^{2+}$ to be favored by 15.03 kcal/mol over the monomer $[L_{ind}Cu(OH)\text{-}conf1]^+$ in the triplet state (Figure 53). These results therefore support the fact that the predominant species in solution after the first "external" deprotonation is the binuclear complex.
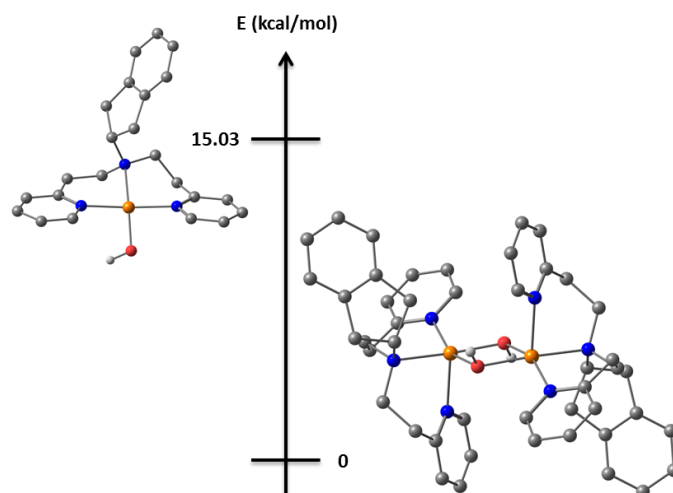
Figure 53 : Calculated relative energies for $[(L_{ind}Cu)_2(OH)_2\text{-}conf2]^{2+}$ (triplet state) and $[L_{ind}Cu(OH)\text{-}conf1]^+$ (doublet state). H atoms except for OH bridging groups are omitted for clarity.

III.4. Summary of the species in solution vs. pH

Taken all together, this investigation supports the assignment of relevant species in solution in the pH range 6-9. These results therefore strongly support the formation of an EPR silent dinuclear antiferromagnetically coupled species. Taken together all those results allow us to propose the following speciation of species (Figure 54).
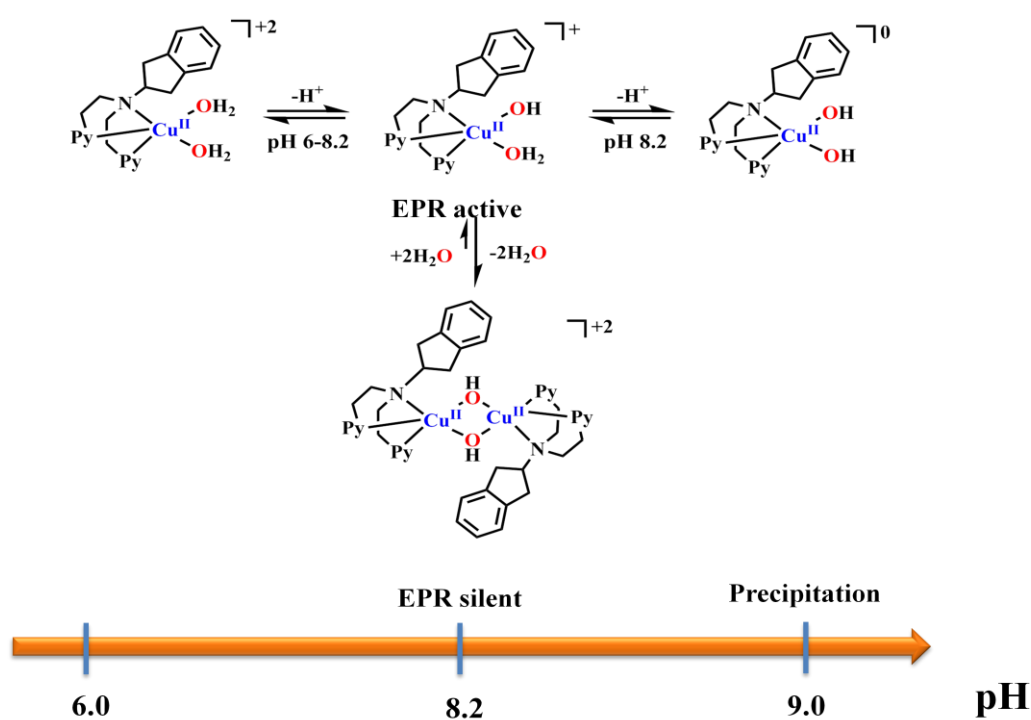
Figure 54 : Proposed species formed in aqueous solution as a function of pH.

III.5. O-atom transfer and dioxygen evolution

III.5.1. O-atom transfer reaction (electrochemically)

III.5.1.a. General Procedure

In order to investigate the O-atom transfer to internal aminoindane substrate, **2a** was placed in aqueous solutions and the pH was adjusted by adding concentrated $NaOH_{(aq)}$ solution. In some cases, when the concentration of the complex was too high, a co-solvent (acetone or methanol) was used to increase solubility. Different supporting electrolytes were used and bulk electrolysis was performed using either a platinium electrode or a graphite rod as working electrodes, a platinum counter electrode and an Ag/AgCl reference electrode (0.210 *vs.* NHE). 2h electrolyses were in general performed at 1.3 V *vs.* NHE after the major oxidation peak observed in the cyclovoltammograms. Experiments were performed either inside the glove box ($O_2 < 2ppm$) or under a flux of argon. Analysis of the products was performed by NMR spectroscopy after demetallation (using ammonia solution) and extraction of the organic part with CH_2Cl_2. The general strategy followed is depicted in Scheme 43.
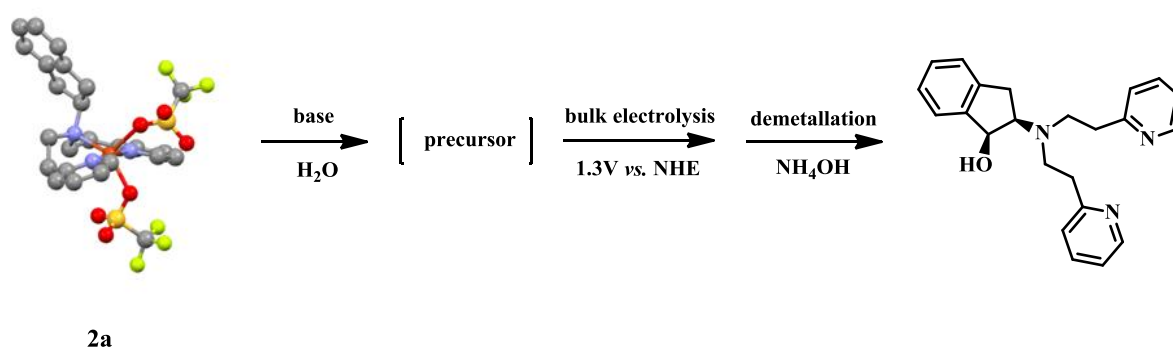
Scheme 43 : General strategy followed in the present work.

III.5.1.b. O-atom transfer after electrolysis at 1.3 V vs. NHE

NMR analysis revealed in most cases the presence of the initial ligand together with one major product after electrolysis. The NMR features indicate that this oxidation product is the *cis*-2-amino-1-indol (namely *cis*-(OH)-IndanePY$_2$). The conversion yield is measured on extracted ligands by NMR spectroscopy using the same methodology as discussed in **Chapter II.** A typical NMR analysis after electrolysis is presented on Figure 55.
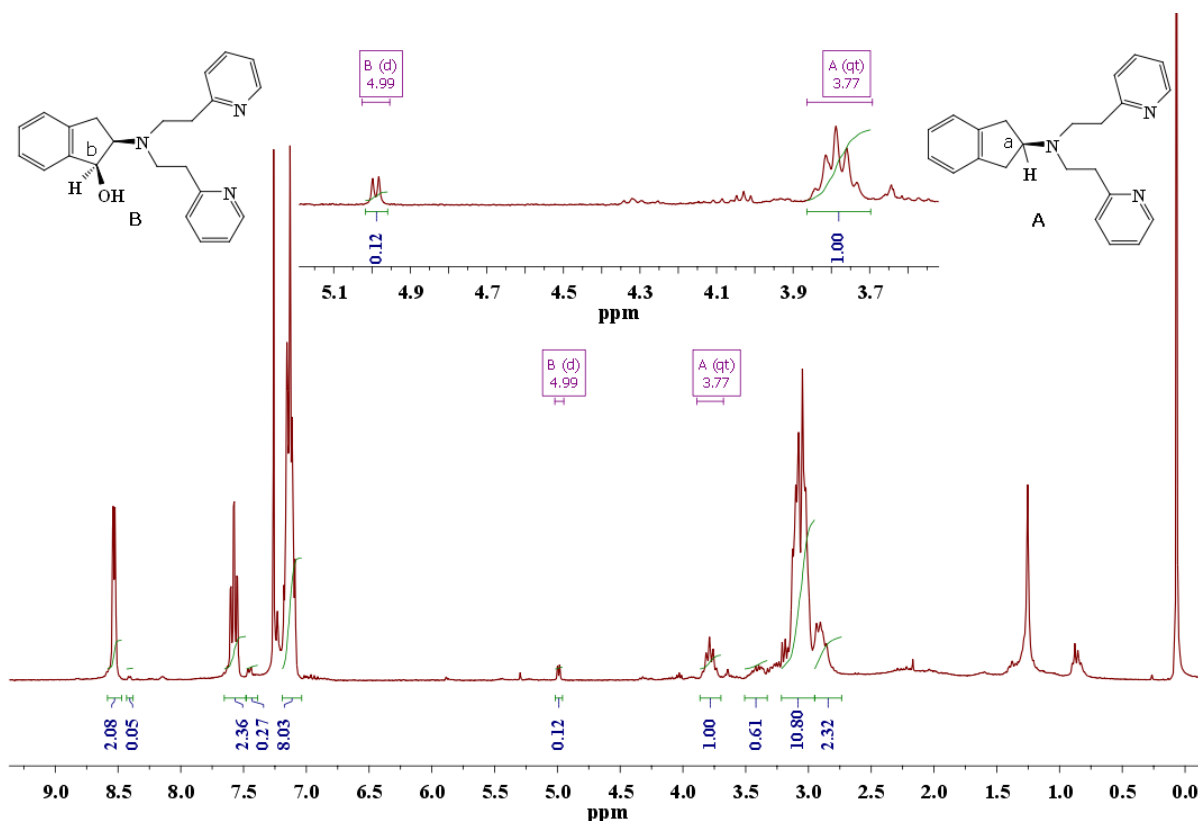
Figure 55 : Typical NMR analysis obtained in the case of electrolysis of **2a** in NaOTf/H_2O pH 8.5.

In order to investigate the influence of the pH on the conversion yields, bulk electrolysis was performed at different pH values. The conversion yield increases as the pH increases until pH 8.9 and then drops (Figure 56). In the case of **2a** placed at 0.7 mM, the conversion yield reaches a maximal value of 13 % at pH 8.5.
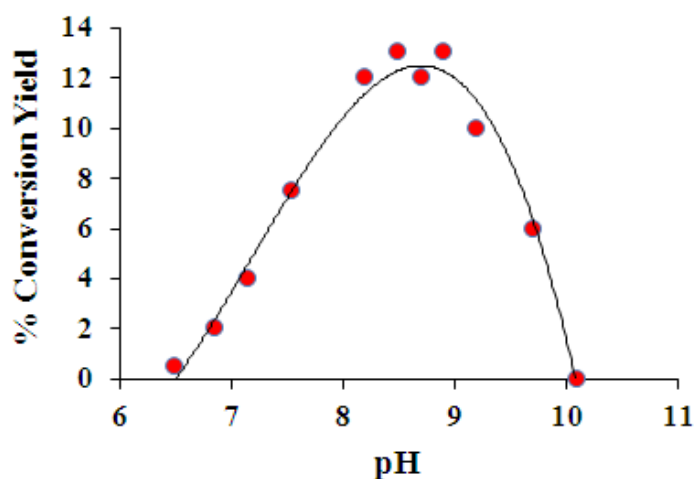

Figure 56 : Effect of the pH on hydroxylation obtained after electrolysis of **2a** (0.7 mM) at 1.3 V vs. NHE in aqueous solution containing 0.1 M NaOTf (conversion yield regarding the formation of $L_{ind}OH$). Every point is an average of at least two measurements.

III.5.1.c. Electrolysis at *ca.* 1 V *vs.* NHE

Above pH 8.5, an additional oxidation peak around 1 V *vs.* NHE is detected in the electrochemical studies (Figure 39). In order to investigate the O-atom transfer ability of the species that is getting oxidized at this potential (possibly the $L_{ind}Cu(OH)_2$ complex) electrolysis was also performed at 1 V at pH=8.5. No hydroxylation was detected.

III.5.1.d. Copper mediated O-atom transfer: control experiments

Different control experiments were performed:
- ✓ Electrolysis of pure ligand in (90% DMF + 10% water mixture, due to low solubility of the ligand in basic water) at 1.3V vs. NHE in presence of base did not result into the hydroxylation of the ligand.
- ✓ Exchange of copper center with a redox inactive metal, such as zinc did not lead to the oxidized ligand neither. This supports that the stereo-selective hydroxylation of the indane moiety is mediated by the redox active copper ion.
- ✓ Extractions of an aqueous solution of **2a** set at pH 8.5 with ammonia solution and without electrolysis, did not yield the hydroxylation product.

Taken together, those results strongly suggest that stereoselective O-atom transfer is mediated by the copper.

III.5.2. O₂ production reaction

III.5.2.a. Electrolysis at 1.3 V vs. NHE

As observed in the electrochemical studies, the intensity of the oxidation peak at *ca.* 1.3 V *vs.* NHE is higher than that of the quasi-reversible peak attributed to the Cu^{II}/Cu^{I} couple. This suggests that an electro-catalytic process is going on. We have therefore investigated dioxygen production upon electrolysis at 1.3 V *vs.* NHE. The O_2 production was followed using a calibrated FOXY probe namely an Oxygen monitoring Kit with a NEOFOX-KIT Probe. 2h electrolysis experiments were performed under inert atmosphere in a hermetically closed cell after degassing with argon. The probe was immersed inside the electrochemical cell before starting the electrolysis.
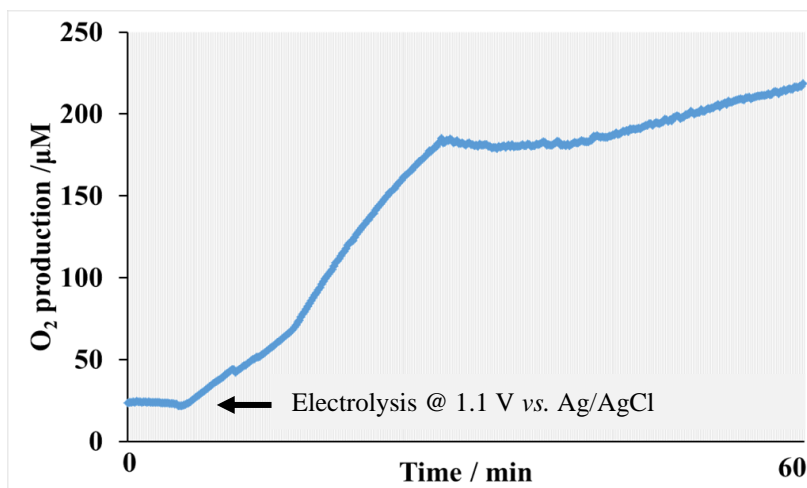
Figure 57: O_2 production during *ca.* 1h electrolysis measured by FOXY Probe every 10 sec. Conditions: [**2a**]=0.7mM, 0.1 M NaOTf pH 8.5.

During electrolysis, dioxygen is indeed produced (Figure 57). Nevertheless, the concentration of dioxygen produced was not easy to estimate due to some leak as well as a partition of O_2 between the solution and the gas phase. Control experiments were however performed in the absence of complex and significantly lower amount of dioxygen is detected under those conditions.

III.5.2.b. O_2-production from hydroxylated complex

The present complex **2a** therefore undergoes two different reactivities when placed at 1.3 V *vs.* NHE: O-atom transfer and O_2 production. We investigated the ability of the hydroxylated complex to perform O_2 production. We therefore performed the following experiments:

✓ The *cis*-hydroxylated ligand was placed in electrolyte solution at pH 8.5 in the presence of a copper salt. No oxidation peak at 1.3 V was detected.

✓ The hydroxylated dinuclear complex $[(L_{ind}Cu)_2(OH)_2]^{2+}$ isolated after reaction of IndanePY$_2$Cu^{II} with O_2 in the presence of benzoin/Et$_3$N was placed in the electrolyte solution. No oxidation peak at 1.3 V was detected (Figure 58).

93
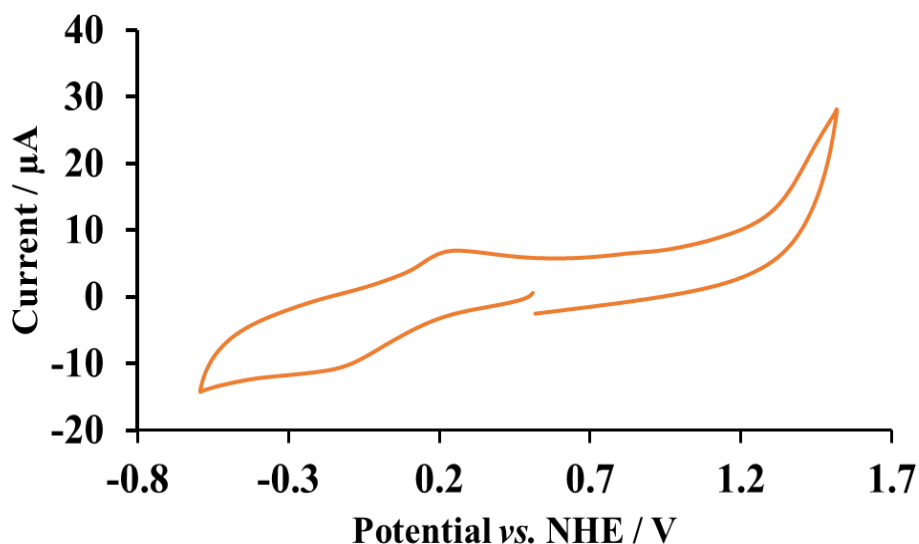
Figure 58 : Cyclovoltamogram of 0.4mM dinuclear complex isolated after reaction of IndanePY$_2$Cu^{II} with O$_2$ in the presence of benzoin/triethylamine in NaNO$_3$/H$_2$O set at pH 8.6. Working electrode: Glassy carbon. Reference Electrode: AgCl/Ag (0.210 V *vs.* NHE, 100mV/s)

Therefore, the complex bearing a hydroxylated ligand appears more difficult to oxidize to Cu^{III} and does not display any O$_2$-evolution ability. This implicates that during the course of the electrolysis, the catalyst is being modified (ligand hydroxylation) and progressively loses the ability to perform water oxidation.

III.5.2.c. Homogeneous *vs.* heterogeneous complex

Among the reported Cu(II) complexes, only a few Cu(II) complexes have been reported as molecular catalysts to enable electrocatalytic water oxidation and the ability of electrodeposited heterogeneous CuO materials to perform water oxidation has been established.[136] Thus, it is important to recognize if the metal complex remain molecular (homogeneous catalyst) or act as precursor of an active species (heterogeneous catalyst) during electrolysis. In order to get insight into the nature of the O$_2$-producing species, a graphite electrode was used to perform bulk electrolysis at 1.3V vs. NHE during 10 minutes in a deoxygenated NaOTf (0.1 M, pH 8.5) containing 0.7 mM of complex **2a**. The electrode was removed from the solution, it was rinsed but not polished and then it was placed in a fresh, complex-free electrolyte. No catalytic current was observed (Figure 59) which is consistent with fact that molecular precursors are performing water oxidation.
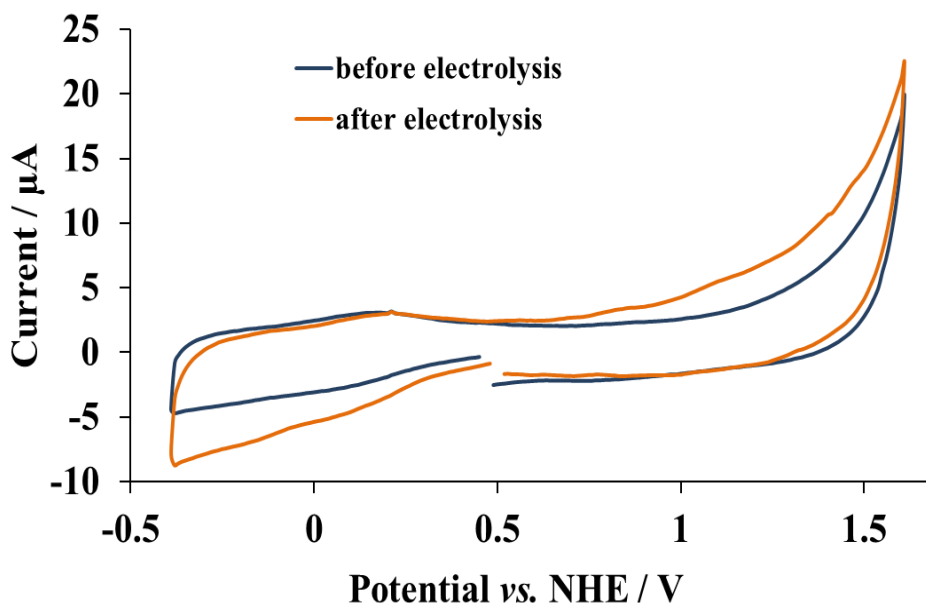
Figure 59 : Cyclovoltammograms of 0.1M NaOTf before (blue) and after (orange) electrolysis of **2a** in aqueous solution (0.7mM, pH 8.5) for 15 minutes, without polishing the electrode. Working electrode: Carbon Graphite, Reference electrode: Ag/AgCl (0.210 *vs.* NHE)

III.6 Investigation of precursor species

As previously mentioned, two reactions take place upon electrolysis rendering the quantitative analysis of the electrochemical data difficult. In addition, quantitative analysis of O_2 production is difficult and the nature of the species performing water oxidation (homogeneous *vs.* heterogeneous) is not fully clear. We therefore mainly focused on the O-atom transfer reaction in the following studies.

III.6.1. pH dependence

The pH dependence of the hydroxylation yield (bell-shaped) was first compared to the speciation curves obtained from potentiometric titrations in the 6-10 pH range (Figure 60). The tendency suggests that the best activity is obtained when the mono-deprotonated species i.e. $[L_{ind}Cu^{II}(OH)(H_2O)]^+$ is formed. Our spectroscopic and theoretical studies have indicated that after deprotonating a coordinated water molecule, the mononuclear $[L_{ind}Cu^{II}(OH)(H_2O)]^+$ complex is in equilibrium with the dinuclear form $[(L_{ind}Cu)_2(\mu\text{-}OH)_2]^{2+}$ that is the major species in solution. This therefore suggests that the dinuclear $[(L_{ind}Cu)_2(\mu\text{-}OH)_2]^{2+}$ species is the precursor that is getting oxidized at 1.3 V resulting in ligand oxidation. It has to be noted that from this study, intramolecular oxidation from the mononuclear $[L_{ind}Cu(OH)_2]$ cannot be completely ruled out since precipitation interferes with the determination of the reactivity of this species.
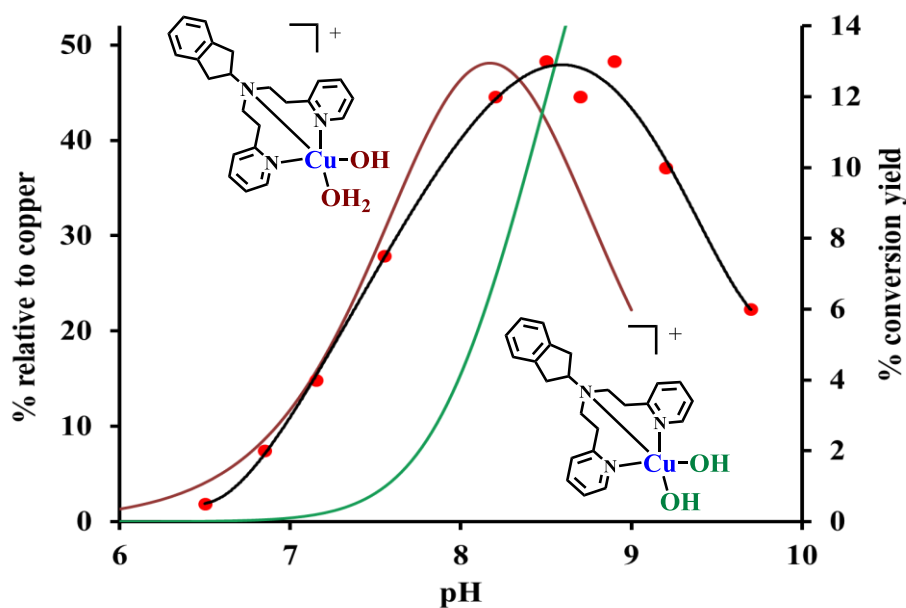
Figure 60 : Influence of the pH on the ligand's hydroxylation yield and the speciation of species derived from potentiometric titrations.

The pH dependence of the hydroxylation yield was then compared to that of the characteristic 307 nm band in UV-visible spectroscopy in the 6-10 pH range (Figure 61). It clearly appears that the O-atom transfer activity is correlated to the formation of the species absorbing at 307 nm, i.e. the dinuclear $[(L_{ind}Cu)_2(\mu-OH)_2]^{2+}$ species.
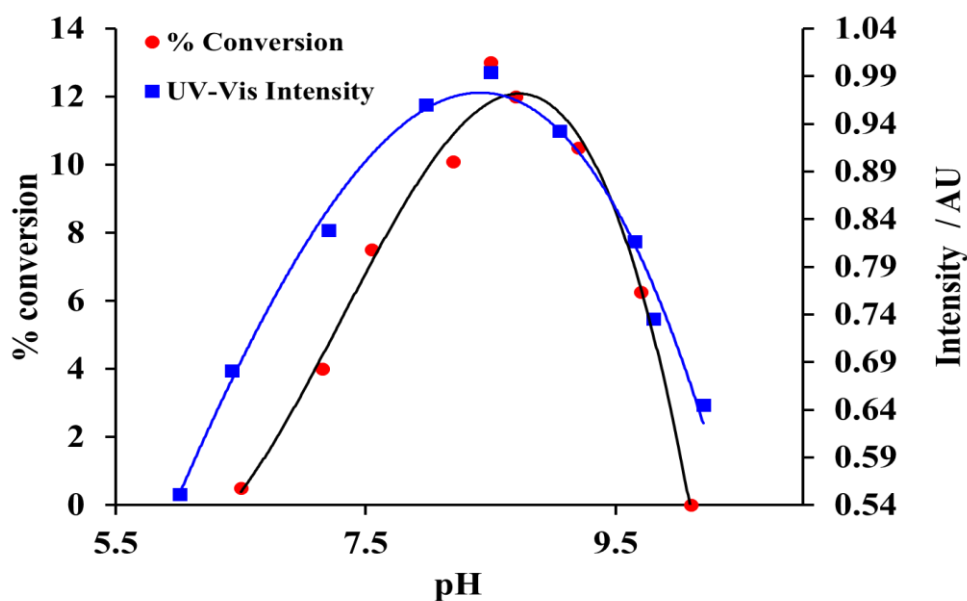

Figure 61 : pH dependence of hydroxylation yield and of the intensity of the UV-Vis absorbance at 307 nm.

III.6.2. Concentration effect

In order to further investigate the involvement of binuclear precursor, we measured the CVs of **2a** at pH 8.5 at different concentrations. When the concentration increased, the intensity of the electrocatalytic peak increased linearly (Figure 62), consistent with a homogeneous water oxidation catalysis.
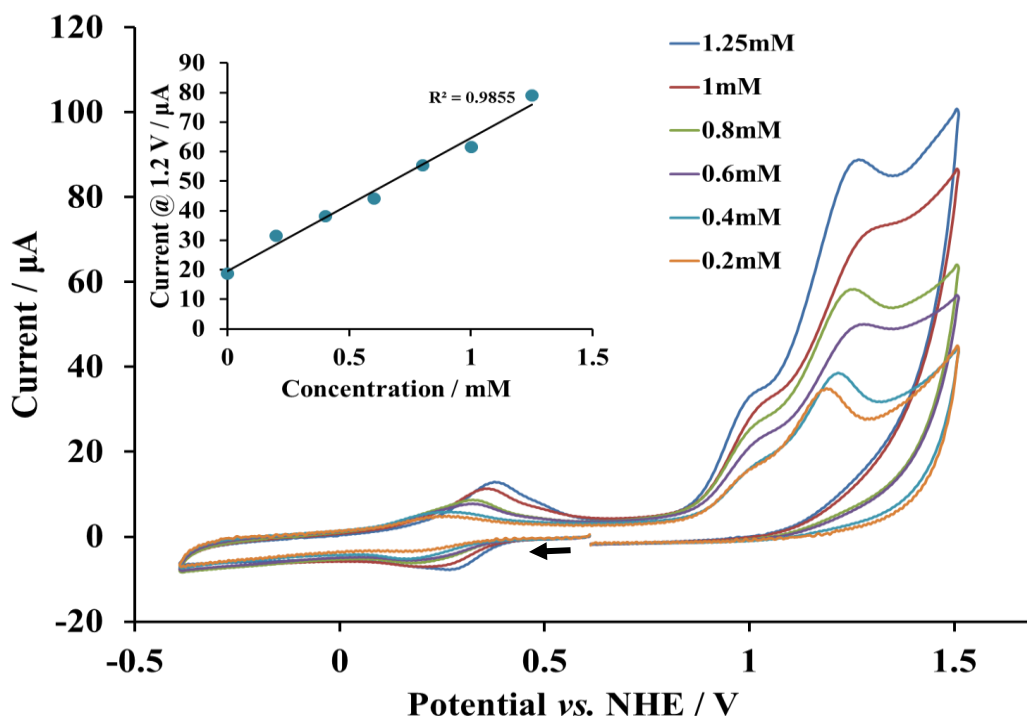
Figure 62 : CVs of **2a** at different concentrations. Conditions: NaOTf/H$_2$O 0.1 M, pH 8.5, 100 mV/s, Working electrode: Graphite, Reference Electrode: AgCl/Ag (0.210 *vs.* NHE). Inset: Plot of catalytic peak current (@ 1.2V *vs.* NHE) *vs.* the concentration of the catalyst. Background is not substracted. The arrow shows the start of scan.

Due to low solubility of complex **2a** in water at concentrations higher than 1.25mM, 5% of acetone as a co-solvent was added. Bulk electrolysis of **2a** at two different concentrations (2.5 mM and 0.6 mM) was performed at different pHs in the presence of 5% of acetone as a co-solvent. The results are presented in Figure 63. As previously observed, the hydroxylation yield increases when the pH increases. No precipitation occurs at pH 9. However, potentiometric titrations were not performed in the presence of a co-solvent so it is difficult to directly transpose the results to the present experiments. More importantly, increasing the concentration increases the hydroxylation yields that reach *ca*. 18% in the case of the most concentrated solution at pH 9. This effect is consistent with the involvement of dinuclear precursors since at higher concentrations, the formation of the dinuclear species is favored.
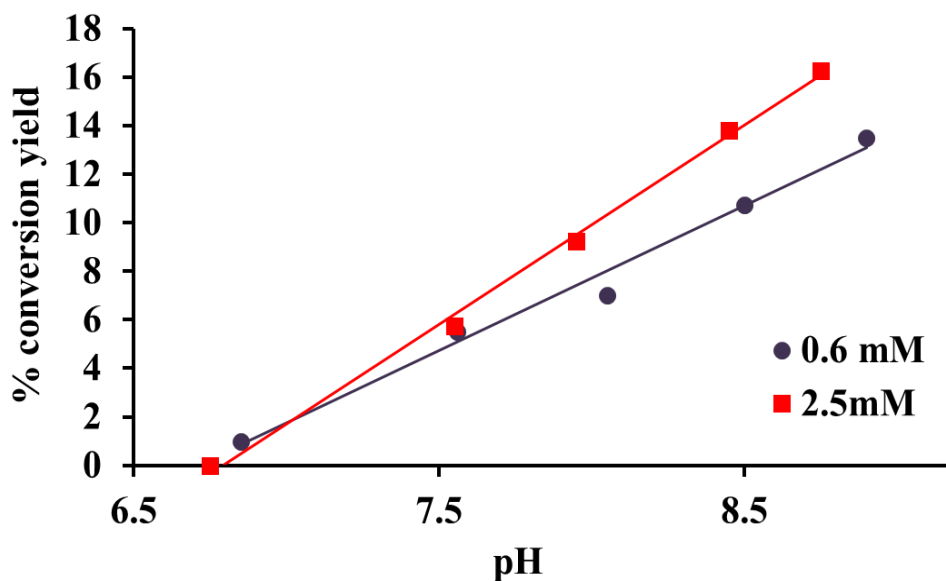
Figure 63 : % conversion yield as a function of pH at [**2a**]=2.5mM (red line) or 0.6mM (purple line) Conditions: 0.1M NaNO$_3$/H$_2$O, pH set with 2,6 lutidine.

III.6.3. pH drop and readjustment

The pH of the solution after 2h of electrolysis (initial value of 8.5) was reduced by 4 units, probably due to the release of protons following water oxidation reaction ($2H_2O \rightarrow O_2 + 4H^+ + 4e^-$). In addition, UV-Vis spectrum recorded after electrolysis showed the absence of the d-d band at 690 nm of the characteristic LMCT the band at 307 nm. This result indicated the complete degradation of the complex during electrolysis. However, upon re-adjustment of pH at 8.5 inside the glove box, allowed partial reappearance of the initial spectroscopic features (Figure 64). This can be explained by the fact that, as indicated by the potentiometric titrations, the major species at pH = 4 (not considering the hydroxylated complex) is a complex in which the ligand is partially protonated and the copper ions are only coordinated to the pyridine groups of the ligand. Upon pH readjustment, the dinuclear species can be formed again.
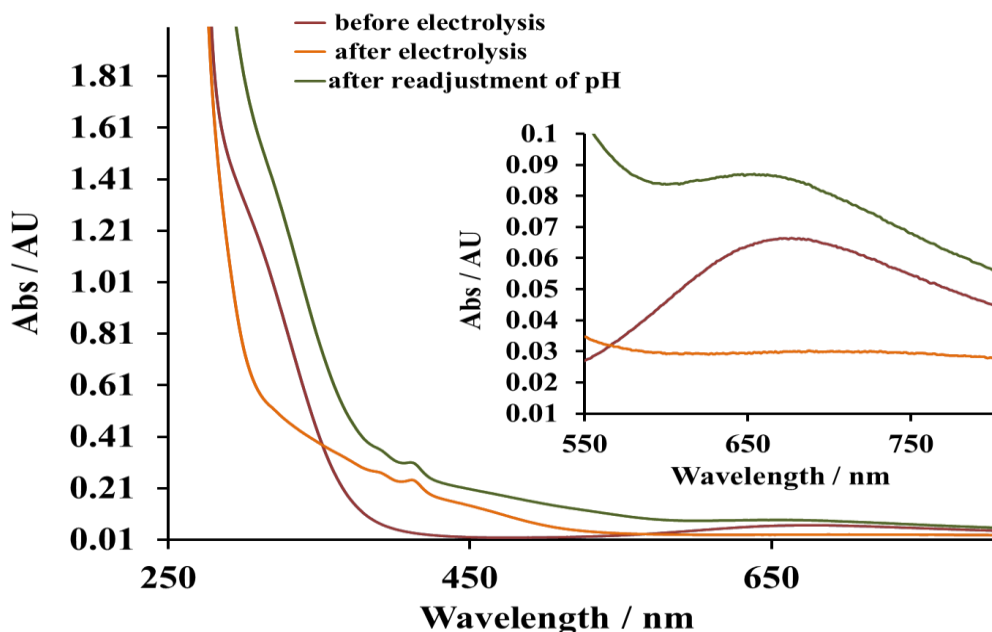
Figure 64 : UV-Vis absorption of **2a** before electrolysis pH 8.50 (red), after electrolysis pH 4.0 (orange) and after readjustment of pH at 8.5 (green) Conditions: 0.1 M NaOTf/H_2O

This pH drop during electrolysis is therefore probably limiting the hydroxylation yield. After electrolysis, we therefore readjusted the pH back to the initial value of 8.5. This was performed 6 times and the yield of the hydroxylated product increased from 12 to 30%. This supports that the pH is critical for the formation of the precursor species for the oxygenation reaction. This also indicates that the complex is not degraded by the pH drop and that restoring the initial species by adding base, restores the reactivity.

III.6.4. Buffered solutions

In order to avoid this drop of pH we evaluated different buffers for the electrolytic experiments at pH 8.5 including phosphate, TRIS-HCl and borate buffers. Unfortunately, neither oxygenation, nor O_2-production reactivities occured upon electrolysis. Interestingly, UV-Vis spectra of complex **2a** recorded in those buffers (See Figure 65 for 0.1M phosphate buffer pH 8.5) indicated that the dinuclear species with the characteristic band at 307 nm were not formed (Figure 65). All those buffers can probably interact with copper and change the species formed in solution.
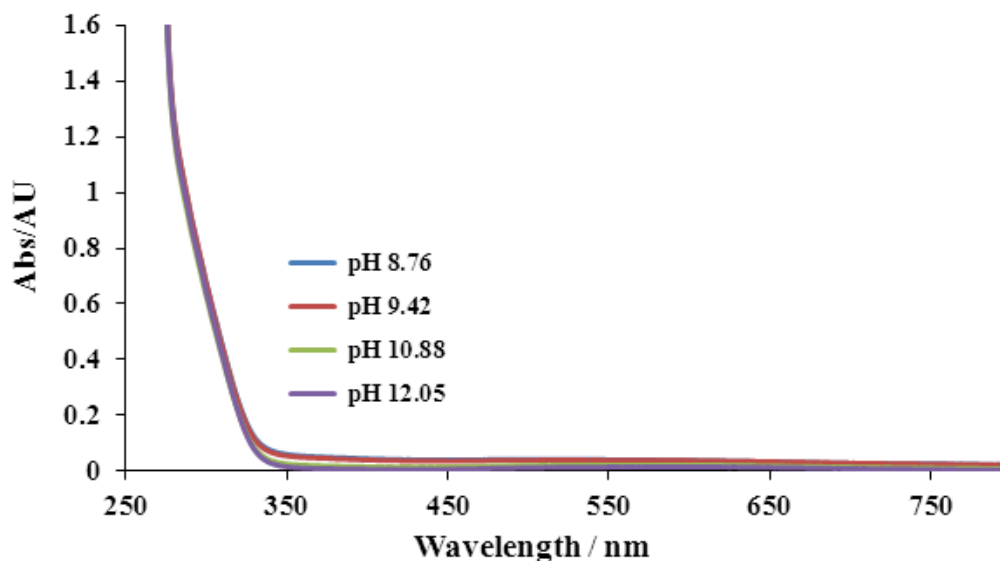
Figure 65 : UV-Vis spectra of **2a** in phosphate buffer pH 8.5 [**2a**]=0.4mM.

III.7. Where does the oxygen come from?

III.7.1. ^{18}O Labeling experiment

In order to investigate the origin of oxygen atom of the cis-hydroxylated ligand, electrolysis of **2a** was performed in labeled water $H_2^{18}O$. In order to obtain high amount of product for mass analysis, the electrolysis of **2a** was first performed at [**2a**] = 2.5mM in 0.1M $NaNO_3/H_2O$ set at pH 8.95 in the presence of acetone. After extractions of the products with ammonia solution, the conversion yield was found to be 9%, a yield significantly lower as compared to the one obtained in $H_2^{16}O$ (19%). By ESI-MS spectroscopy, the hydroxylated ligand and the initial ligand were both detected (Figure 66). The protonated hydroxylated ligand is detected at m/z = 360 with ^{16}O and is shifted to m/z=362 when incorporating ^{18}O. The isotopic profile of the IndanePY$_2$-OH product suggests that only 3-5% corresponds to IndanePY$_2$-^{18}OH, although the experiment contained more than 85% ^{18}O-enriched water.
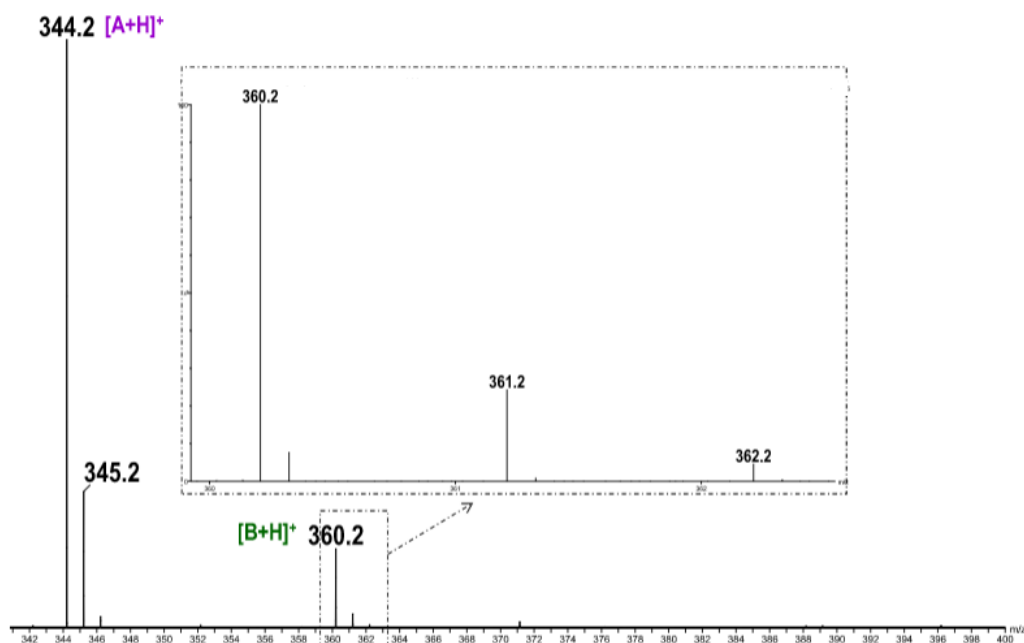
Figure 66 : Mass spectra of crude product after electrolysis in labeled $H_2{}^{18}O$, 0.1M NaNO$_3$ pH 8.5 set with 1M NaOH$_{(aq)}$, [**2a**]=2.5 mM, 5% acetone. **A** corresponds to IndanePY$_2$ and **B** corresponds to *cis-*^{16}OH-IndanePY$_2$. Inset: Magnification of the isotopic profile of [B+H]$^+$.

III.7.2. Other O-atom sources

This result was puzzling. Several problems could be listed: (i) a leak occured from the electrodes compartments (reference and counter electrodes) that were not filled with labeled water or (ii) there is another source of oxygen atoms. In the latter case, other oxygen-containing constituents of the solution were considered. The only O-atom containing species that are present in solution are *(i)* dioxygen, although the solution was constantly degassed or placed inside the glove box *(ii)* the co-solvent (acetone), *(iii)* the counter-anion of copper salt (triflates) and *(iv)* the supporting electrolyte (NaNO$_3$ here).

III.7.2.a The case of dioxygen

As previously mentioned, in normal experiments, the solution was constantly degassed or placed inside the glove box (O$_2$<2ppm). Two control experiments were performed:
- ✓ An electrolysis of **2a** (0.7mM) was performed in the presence of air (bubbling O$_2$ in the solution before electrolysis and flux of oxygen on the top of the solution during electrolysis) in 0.1M NaOTf/H$_2$O set at pH 8.5. The hydroxylation yield obtained after electrolysis was similar in the presence and in the absence of dioxygen.
- ✓ De-metallation and extraction of the ligand were performed inside the glove-box without affecting the hydroxylation yield.

101

III.7.2.b Investigation of the co-solvent

The experiment was reproduced without co-solvent. As a result of the low solubility of **2a** in water, the concentration of **2a** was lowered at *ca.* 1 mM. The bulk electrolysis was performed in 0.1M NaOTf/H$_2$O pH 8.5 set with 1M NaOH$_{(aq)}$ inside the glove box to remove all traces of oxygen in solution. After extractions of the products with ammonia solution, the conversion yield was estimated by NMR spectroscopy to 12%. This conversion yield is similar to that obtained using similar conditions and in the presence of co-solvent (0.6 mM, 5% acetone). The absence of co-solvent therefore does not affect the hydroxylation yield. In addition, experiments performed in ^{18}O labeled water in the absence of co-solvent did not lead to more than 5% incorporation of oxygen from water. Interestingly, upon use of labeled water, hydroxylation yield was affected and dropped to 0-5% although it was found of 12% in non-labeled conditions (H$_2$^{16}O).

III.7.2.c Counter-anions of the copper salt

Although by NMR spectroscopy it was observed that the triflate counteranions in aqueous solution are exchanged with water, a new Cu^{II} complex (**2c**) with perchlorates as counteranions was synthesized. The blue powder of complex **2c** [(L$_{ind}$Cu^{II}(ClO$_4$)$_2$](MeOH)(H$_2$O) was prepared by mixing the Cu^{II}(ClO$_4$)$_2$·6H$_2$O with 1 eq. of IndanePY$_2$ in MeOH/H$_2$O. The complex was precipitated by the addition of ether and its purity was confirmed by elemental analysis. In addition, the experiments were also performed by preparing a complex *in situ* by mixing the ligand and Cu(NO$_3$)$_2$.

Cyclic voltammetry experiments were performed to compare the different complexes using various supporting electrolytes. In all the conditions tested, the intensity and the potential of the oxidation peak was not significantly affected at pH 6.5 (Figure 67) as well as in basic pH.
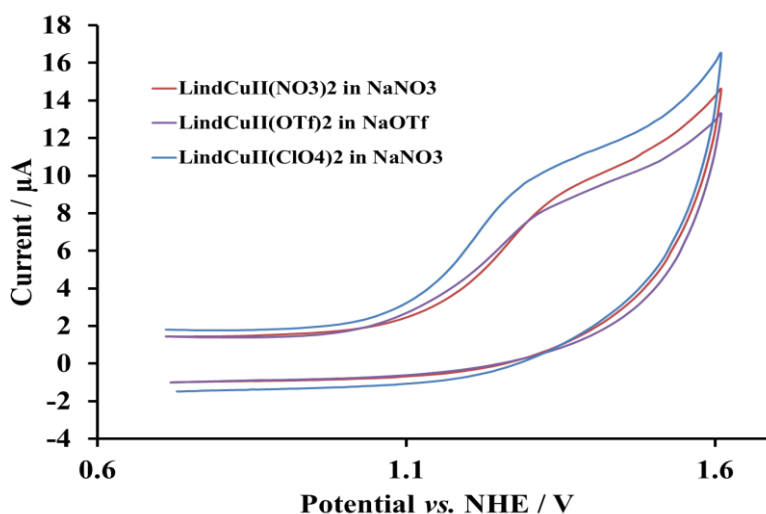
Figure 67 : Cyclic voltammetry of anodic part of Cu^{II} complexes at pH 6.5 (set with NaOH$_{(aq)}$). Working electrode: Glassy carbon. Reference electrode: AgCl/Ag (0.210 *vs.* NHE), 100 mV/s.

UV-Vis spectra of aqueous solutions of **2c** at different pHs confirmed that the species that are formed in solution are the same as observed in the case of **2a** (Figure 68).
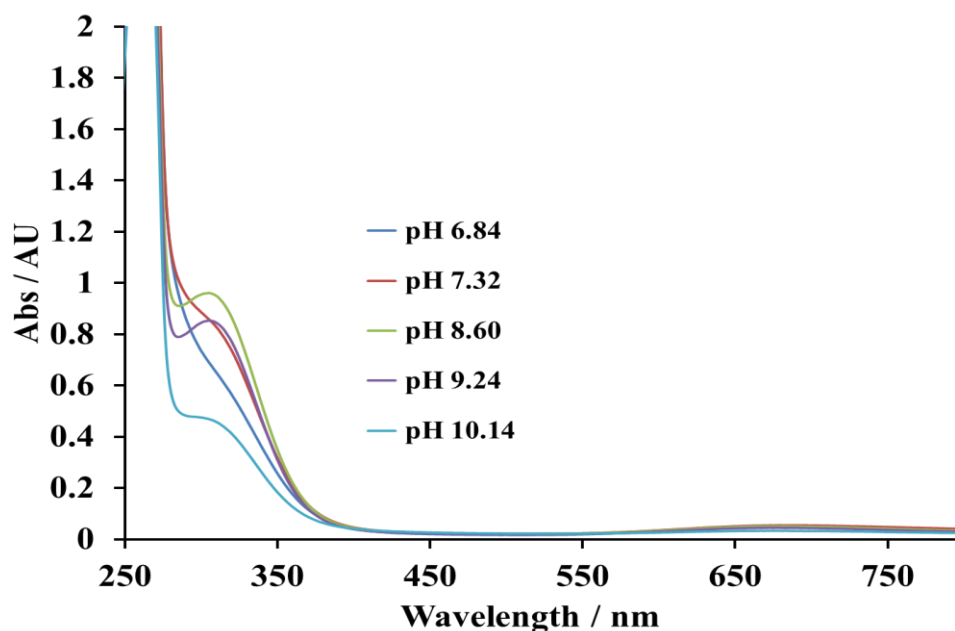
Figure 68 : UV-Vis spectra of **2c** (0.3mM) in 0.1M $NaNO_3/H_2O$ at different pH values set with $NaOH_{(aq)}$.

The complex **2c** (0.7mM) was then electrolyzed in 0.1M $NaNO_3/H_2O$ at pH 8.5 under argon. The hydroxylation yield was 12% as obtained in the case of **2a** in the same conditions. These results suggest that the counter-anion does not influence the formation of the dinuclear species with characteristic absorption at 307 nm and does not interfere with the reactivity. This also indicates that the counter-anion is probably not the source of oxygen atom.

III.7.2.d. Investigation of the supporting electrolyte

Another source of oxygen in solution was the supporting electrolyte. Instead of $NaNO_3$, NaOAc and NaOTf were used. The hydroxylation yield (around 12-13%) was not affected after electrolysis by the nature of the supporting electrolyte.

The only labeled supporting electrolyte that was available commercially was the $Na^{18}OAc$. The complex **2a** (0.7mM) was placed in 0.1 M $Na^{18}OAc/H_2O$ at pH 8.2 and was electrolyzed at 1.3 V vs. NHE inside the glove box. After extraction of the products with concentrated ammonia solution, the conversion yield was estimated to be 14%. Further analysis by ESI-MS spectroscopy indicated the absence of labeled product ^{18}OH-IndanePY$_2$. So, the change of supporting electrolyte did not result in a drastic increase of the ^{18}O content of hydroxylated ^{18}OH-IndanePY$_2$. Although some oxygen atoms from the supporting electrolyte could be incorporated, this result indicates that the electrolyte is not the major oxygen atom source for the hydroxylation of aminoindane moiety.

III.7.2.e The electrode as O-atom source?

It is known that in alkaline solutions, Pt=O species can be formed on the surface of the electrode.[107] Those species might be the oxygen atom source in the present experiments. Bulk electrolyses were performed either using graphite rod or platinum as working electrode and the oxygenation yield was not affected by the nature of the electrode. In addition, the output of ^{18}O labeling experiments were the same results in both cases.

In Summary:

In total, up to 4 different experiments were performed using labeled water. In all cases, bulk electrolyses in labeled water ($H_2^{18}O$) led to significantly lower conversion yields as compared to the ones in natural water ($H_2^{16}O$) (Table 9).

Table 9 : Comparison of conversion yields in labeled water ($H_2^{18}O$) and in natural water ($H_2^{16}O$). ^{18}O incorporation is also shown in various conditions. SE refers to supporting electrolyte and WE refers to working electrode.

Conditions pH range 8.2-8.9			% conversion yield in $H_2^{16}O$	% conversion yield in $H_2^{18}O$	^{18}O incorporation (when $H_2^{18}O$ was used)
SE	WE	Co-solvent			
NaNO$_3$	Pt	acetone	19%	9%	5-7%
NaOTf	C$_{Graph}$	-	12%	0-5%	0-3.5%
NaOAc	C$_{Graph}$	-	12%	-	-
Na^{18}OAc	C$_{Graph}$	-	-	14%	0%

Different hypotheses can be raised to explain this lack of labeling product. One hypothesis is that we are facing analytical problems. Indeed, ESI-MS ionization of polar molecules is more difficult than that of apolar ones. The hydroxylated product is present in very low quantities in the reaction mixtures, especially in labeling conditions. The analysis of traces of product (ca. 5%) is therefore more difficult. In particular, an iso-mass molecule is sometimes detected at m/z = 360 in the ESI-MS spectrum of the initial IndanePY$_2$ ligand. This product is however not detectable in the NMR spectrum. The presence of traces of this product would therefore lower our sensitivity and accuracy in the determination of labeling ratios of the oxidation product. A second hypothesis, which is not in contradiction with the previous one, is that an isotopic effect occurs. Indeed, global hydroxylation yield was significantly lowered upon use of labeled water (but not in the case of labeled acetate). So, taken all together, this could indicate high oxygen kinetic isotopic effect (KIE). This hypothesis is currently under investigation.

IV. Conclusion

In the literature, examples on stereo-selective intramolecular O-atom transfer mediated by Cu^{II} complex and water have not been reported yet. Herein, it was described the first example of intramolecular O-atom transfer for C-H bond activation (indane) in moderate yields (30% maximum) *via* the electrolysis of Cu^{II} precursors in water. The fact that the hydroxylated ligand is likely produced through a stereo-controlled reaction and a metal centered mechanism, strongly supports that complex **2a** is a molecular catalyst toward water oxidation and water activation. Although the oxygen atom source is not clear yet, our extensive studies limited the possibility that other oxygen atom sources are capable of transferring an oxygen atom to the substrate. Therefore, the oxygen atom on the indane moiety should come from water. The ^{18}O labelling experiments are still under investigation.

Chapter IV

Activation of O_2-Synthesis of heterobimerallic complexes, electronic structure and reactivity

---

I. Heterobimetallic systems

I.1. Intoduction and context

In contrast to the homobimetallic systems, the properties of mixed-metal dioxygen species have been relatively less explored. These types of intermediates are probably involved in various catalytic processes in metalloenzymes. In nature, for example, in cytochrome c oxidase, a Cu^I ion cooperates with an Fe^{II}(heme) to activate dioxygen[148] (Figure 69, left) or in Cu-Zn superoxide dismutase (Figure 69, right), in which the superoxido ligand disproportionation to molecular dioxygen and hydrogen peroxide is mediated through a mixed Cu-Zn metal site.[149]
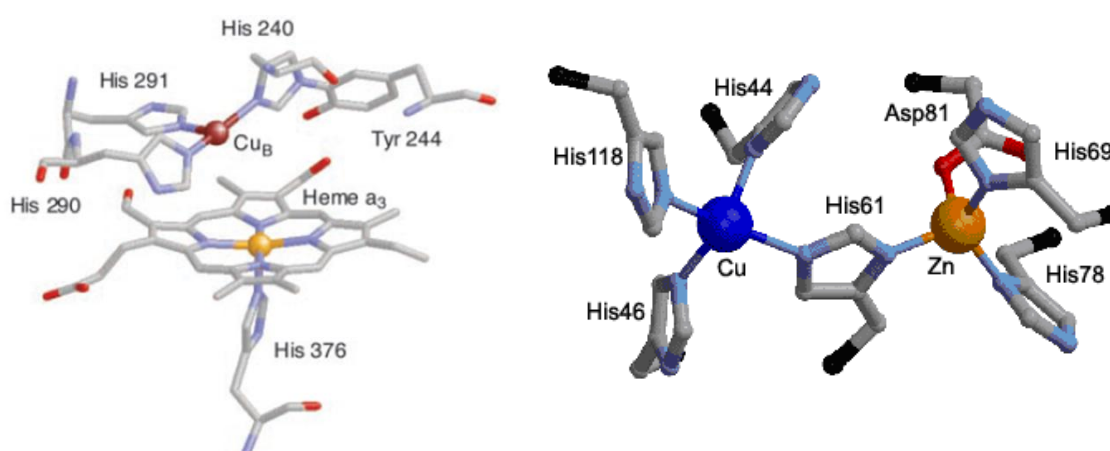
Figure 69: Active sites of cytochrome c oxidase (left) and Cu-Zn superoxide dismutase (right).

The generation and the study of such mixed metal species are therefore of significant interest due to the unique properties obtained by the combination of two different metal ions.

The typical procedure for preparing the homometallic analogues where a monomeric precursor is reacting with O_2 cannot be used for the synthesis of the heterobimetallic complexes. The synthesis of heterodinuclear complexes, presents a special challenge because of the possibility of disproportionation and selectivity problems resulting in the formation of mixtures of homo- and heterodinuclear complexes, as well as metal-site isomers.[150] In order to overcome these problems two main strategies were previously used in the literature (Scheme 44). The first one involves the synthesis of ligands providing different coordination environments that are specific for each of the two metal ions. An alternative route is the reaction of a well-defined dioxygen metal subunit L_nM-O_2 with a low-valent metal complex fragment L'_mM'.
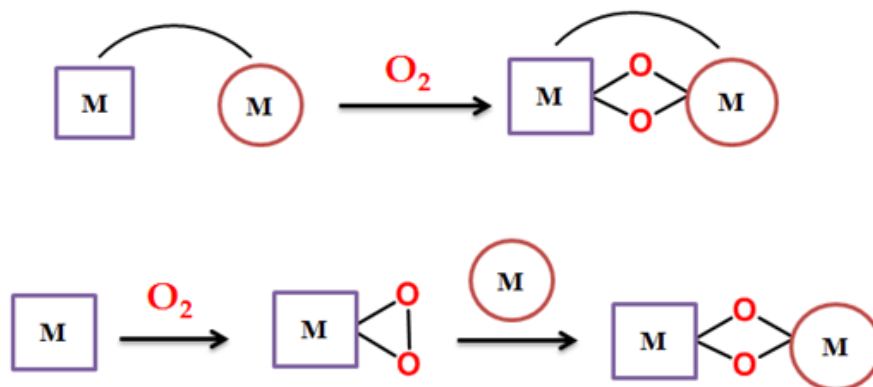
Scheme 44 : Two main strategies used in the development of unsymmetric complexes for the dioxygen activation.

This last strategy has been successfully used to generate heterobimetallic oxygen-containing species with PdMo,[151] NiCu,[152] CuGe,[153] PtCu[154] and PdCu[154] combinations, starting from well-defined dioxygen metal precursors.

I.2. Ni^{II} superoxo radical: precursor for preparation of Ni-M complexes

Driess, Limberg and co-workers contributed in the field generating a new family of NiO$_2$M complexes by using a mononuclear *side-on* LNi^{II} superoxo precursor bearing a β-diketiminate (Nacnac) ligand (L= [HC-(CMeNC$_6$H$_3$(*i*Pr)$_2$)$_2$]) system (Scheme 45).[155]
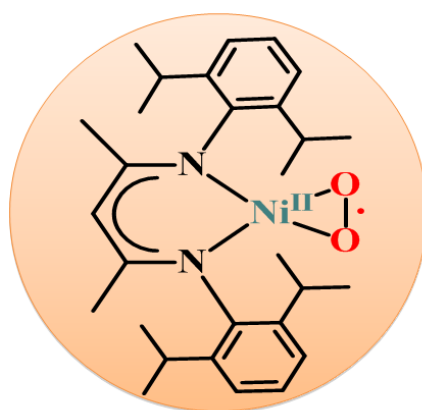
Scheme 45 : Ni^{II} superoxide complex with the β-diketiminate ligand (Nacnac).

This precursor is easily prepared by reaction of Ni^{I} complex with dioxygen. It bears the sterically bulky β-diketiminate ligand preventing the formation of homometallic and symmetric Ni-Ni dioxygen complexes. Characterized by X-ray structure and other spectroscopic methods, it accommodates a square planar geometry and has an unpaired electron localized on the superoxo ligand, suggesting the presence of a low spin Ni^{II} configuration.[155] Moreover, its redox potential is -0.98V *vs.* Fc$^+$/Fc which indicates that

it may be easily reduced by one electron. Notably, it is remarkably stable and can be handled at room temperature, which makes it a suitable precursor for the synthesis of heterobimetallic Ni-M dioxygen complexes.

I.3. Heterobimetallic Ni-M complexes: past

Driess, Limberg and co-workers have reported the one electron reduction of Ni^{II} precursor by elemental potassium resulting to the formation of heterobimetallic peroxo $Ni^{II}(\mu-\eta^2:\eta^2-O_2)K^I$(solvent) species, where K^+ ion is coordinated strongly to the peroxo moiety.[156]

Attempts to substitute the potassium center by a redox-inactive zinc (II), led to the O-O scission and generated the formation of diamagnetic bis-μ-hydroxo $Ni^{II}(OH)_2Zn^{II}$ (Scheme 46). The X-ray structure revealed a square planar Ni^{II} site and a tetrahedral Zn^{II} site, which are bridged by two hydroxo ligands. DFT calculations showed that substitution of K^+ ion by Zn^{2+} ion leads to the formation of highly reactive $Ni(\mu-O)_2Zn$ postulated as a biradical that is performing H-atom abstraction from surrounding molecules (i.e. solvent).

solv = THF, [18]crown-6
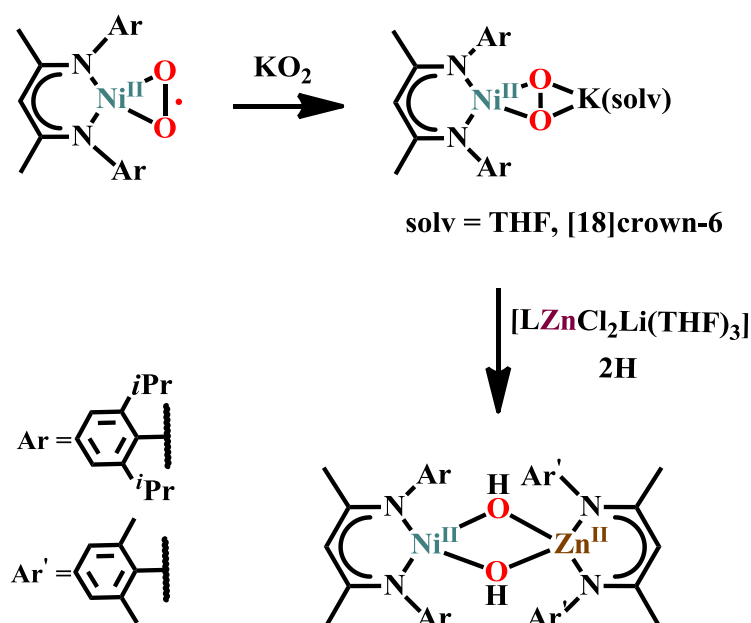
Scheme 46 : Synthetic pathway of the heterobimetallic Ni^{II} (bis-μ-hydroxo)Zn^{II} complex.

One year later, the same authors have reported the reaction of superoxo Ni^{II} complex with an Fe^I precursor resulting in the generation of a Ni^{II}-Fe^{II} complex.[157] The X-ray structure revealed a square planar and a tetrahedral coordination for nickel(II) and iron(II), respectively. The metal atoms are bridged by a hydroxide ligand and a μ-alkoxide moiety derived from the intramolecular ligand oxidation of a *i*Pr group from the β-diketiminate ligand coordinated to nickel center (Scheme 47).

R = Me, tBu
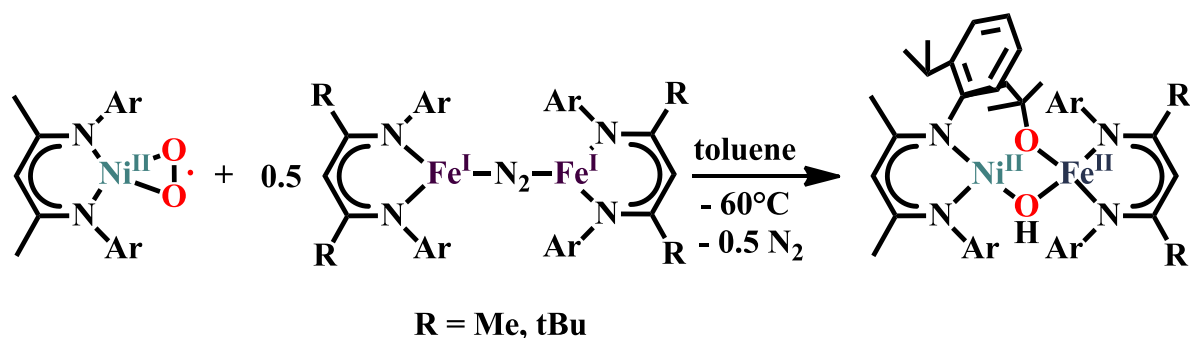
<center>**Scheme 47** : Development of Ni-(bis-μ-hydroxo)-Fe complexes.</center>

However, the identification of the intermediate species was not possible. Low temperature (-70°C) UV-Vis spectra revealed the presence of a short-lived species which decays within seconds. DFT calculations have suggested the stepwise formation of peroxo $Ni^{II}O_2Fe^{II}$ and bis(μ-oxo) $Ni^{III}(\mu$-O$)_2Fe^{III}$ intermediates. Those species are postulated to be highly reactive intermediate species responsible for the hydroxylation of the unreactive C-H bond and the generation of the final product presented on Scheme 48.

Although, the fleeting [LNiO$_2$ML] (M= Fe, Zn) could not be isolated, in a subsequent study, a related heterodinuclear [LNiO$_2$Cu(MeAN)]$^+$ species[158] could be stabilized at low temperature by reacting the aforementioned [LNi^{II}O$_2$] precursor with a copper triamine [Cu(MeAN)]$^+$ reductant (Scheme 48).
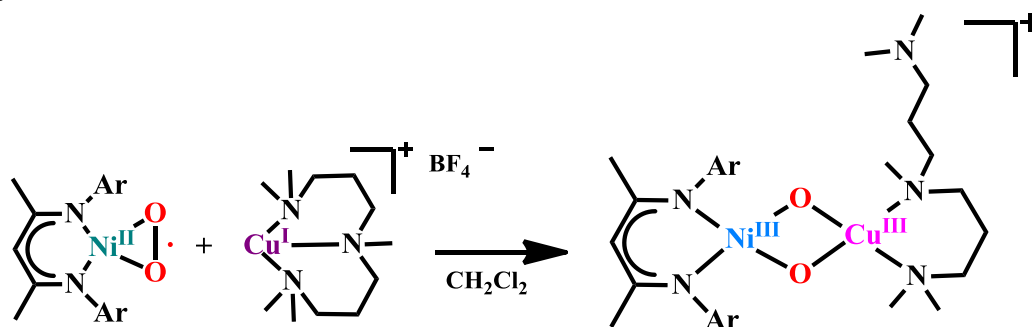
Scheme 48 : Generation of Ni^{III}bis-μ-oxoCu^{III} complex after reaction of Ni^{II} superoxide and [(MEAN)Cu^I]$^+$.

Treatment of nickel superoxido with copper complex resulted in the immediate generation of Ni^{III}(bis-μ-oxo)Cu^{III} species, which exhibits a characteristic absorption band at 895 nm. XAS studies showed the 1e$^-$ oxidation of Cu^{II} to Cu^{III} and Ni^{II} to Ni^{III}. Moreover, the X-band EPR spectrum is assigned to a typical S=1/2 Ni^{III} rhombic signal with no interaction of electron spin with nuclear spin of copper. Therefore, the absence of copper hyperfine splitting is in agreement with low-spin Cu(III) ion. In the absence of X-ray structure of the intermediate, DFT calculations were performed and showed that both nickel and copper sites have four-coordinate planar geometries, where MeAN acts as a bidentate ligand with one of the nitrogen atoms remaining out of the coordination sphere of copper.

Interestingly, the presence of Cu in the second metal binding site resulted in nucleophilic oxo groups in the high-valent bis-μ-oxo Ni-Cu species, and the intermediate was able to react towards electrophilic substrates in contrast to the reported electrophilic properties of the homobimetallic NiO_2Ni,[159,160] CuO_2Cu[3] counterparts as well as of the heterobimetallic NiO_2Fe complex.

II. Objectives

For previous results in the literature, the electronic structure of heterodinuclear $[NiO_2M]^{n+}$ cores starting from Nacnac-based Ni-precursors were found to be dependent on the nature of the second metal ion, M. We were therefore interested in investigating how the nature of the copper ancillary ligand can modulate the formation, structure, electronic properties and reactivity of such high-valent heterobimetallic dioxygen species.

For this purpose, the triamine MeAN ligand at Cu was replaced by the RPY_2 (R = methyl or Indane) ligand systems. As previously discussed (**Chapter II**), homometallic CuO_2Cu counterparts with RPY_2 (R=internal substrate) as ancillary ligands, dispay electrophilic oxo cores capable of transferring an O-atom to internal substrate in a stereo- and regio- selective way. We therefore intended to explore how the electronic structure of the new high-valent heterobimetallic Ni-Cu dioxygen species bearing an RPY_2 ligand around the coordination sphere of copper can affect the reactivity towards internal (indane) and external substrates.

This part of my thesis was carried out in collaboration with Prof. Matthias Driess (Technical University, Berlin) and Prof Kallol Ray (Humboldt University, Berlin) thanks to the support of the COST action ECOSTBIO (CM1305). I therefore had the opportunity to travel twice in Berlin to perform experiments. The results were recently published (Kafentzi *et al.* Dalton Trans, DOI: 10.1039/C6DT02391F, see Annex).

III. Results and Discussion

III.1. Synthesis and characterization of heterobimetallic complexes

III.1.1. Synthesis of heterobimetallic complexes 3a and 3b

The complexes **1a** and **1b** were prepared by mixing one molar eq. of $Cu^I(CH_3CN)_4(OTf)$ with one molar eq. of ligand in dichloromethane in absence of dioxygen. Equimolar amounts of **1a** or **1b** and **2** were then mixed at -90°C in dry dichloromethane leading to the immediate formation (within 20 sec) of the brownish intermediates **3a** and **3b**, respectively (Scheme 49).

1a R= indane
1b R= methyl

2

3a R=indane
3b R=methyl
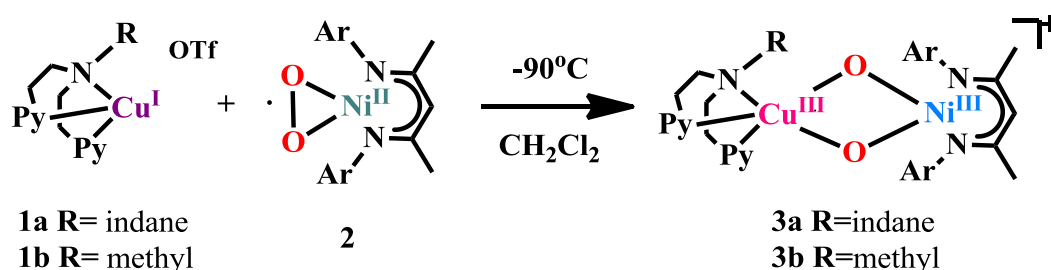
Scheme 49 : Generation of $[LNi^{III}O_2Cu^{III}(RPY_2)]^+$ species **3a** (**3b**) upon mixing a solution of the LNi^{II} superoxo complex **2** with the $(RPY_2)Cu^I$ complexes **1a** (or **1b**). L=NacNac.

III.1.2. UV-Vis spectroscopy

The generation of these species was monitored by UV-Vis spectroscopy following the appearance of a characteristic absorption band centered at 885 nm for **3a** and 870 nm for **3b** with $\varepsilon \sim 6000$ L.mol^{-1}.cm^{-1} (Figure 70).
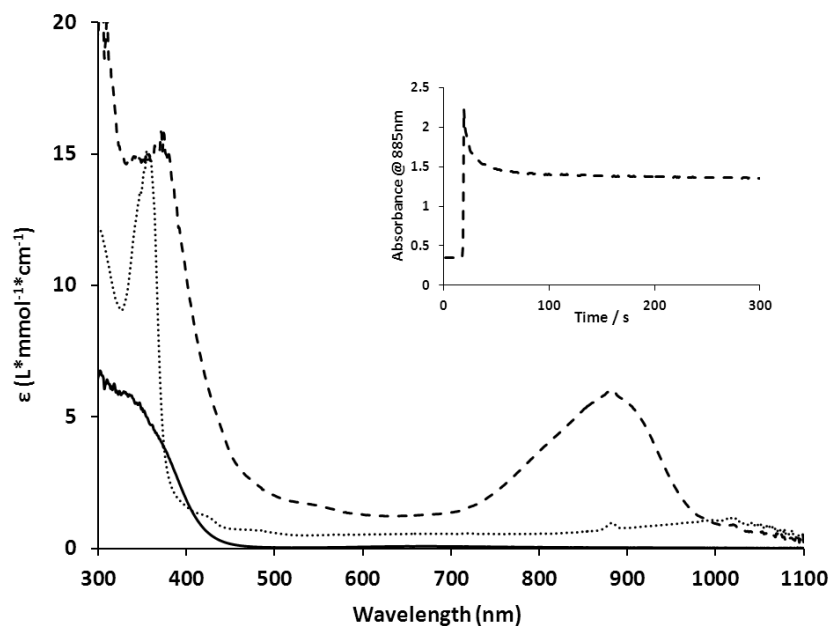
Figure 70 : Absorption spectra of Cu^{I} complex (solid trace) **1a**, Ni^{II} superoxo complex **2** (dotted trace) and the 0.15 mM [Ni^{III}(μ-O$_2$)Cu^{III}]$^{+}$ species **3a** (dashed trace) in dichloromethane at -90°C. Inset: Time trace of the absorption at 885 nm characteristic of the [Ni^{III}(μ-O$_2$)Cu^{III}]$^{+}$ species **3a**.

The intermediates are stable at -90°C, but they are thermally sensitive, as indicated by bleaching of their UV-Vis absorption features upon warming to higher temperatures ($t_{1/2}$ = 2000 s at -60°C) (Figure 71).
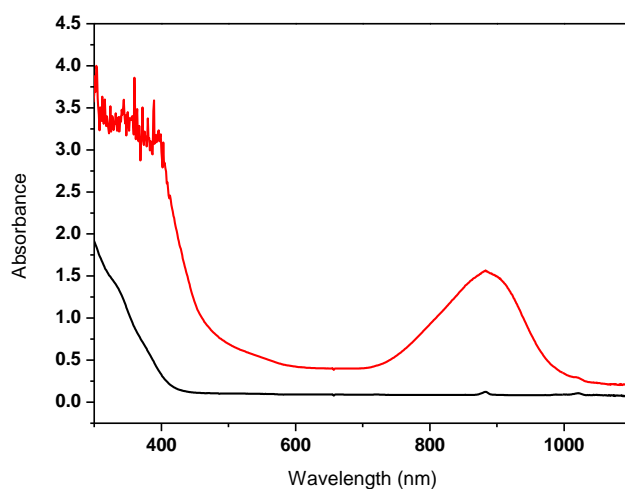
Figure 71 : Absorption spectra of **3a** at -90°C (red) and decomposition upon warming at -30°C (black) in dichloromethane (0.15 mM).

III.1.3. EPR spectroscopy

The EPR spectra were recorded in frozen CH_2Cl_2 solutions (77 K) for **3a** and **3b** and are very similar for both complexes. The EPR spectrum obtained in the case of **3a** is presented in Figure 72. The spectra are composed of typical S = 1/2 rhombic signals with g_1= 2.39, g_2= 2.13, g_3= 2.005 for **3a** and g_1=2.39, g_2=2.13, g_3= 2.006 for **3b**. These EPR signals are very similar to the one reported previously for the $[LNiO_2Cu(MeAN)]^+$ complex (g_1=2.41, g_2=2.14, g_3=2.006).[158] Notably, no Cu-related hyperfine splittings are observed for both **3a** or **3b**, consistent with the $Ni^{III}(\mu-O)_2Cu^{III}$ assignment, in agreement with the data previously reported in the literature for the Cu-Ni analog.
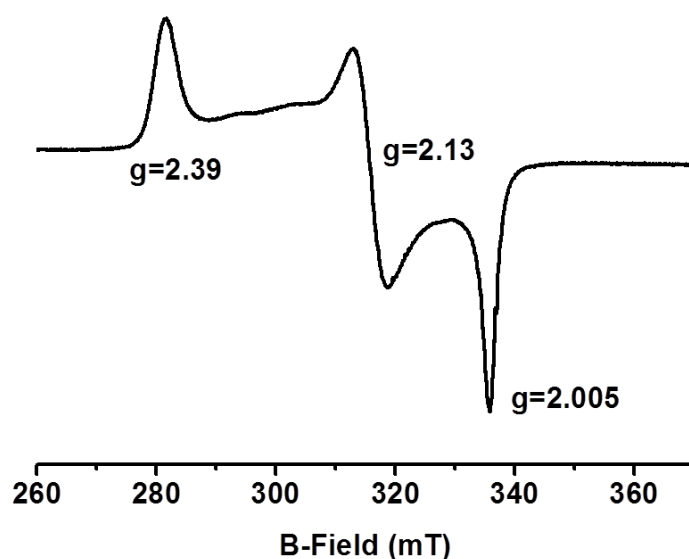
Figure 72 : X-band EPR spectrum of **3a** recorded at 77K in CH_2Cl_2.

III.1.4. Mass spectrometry

The electrospray mass spectra of **3a** and **3b** exhibit peaks at mass–charge ratios (m/z) of 915.30 and 815.25 respectively, with a mass and isotope distribution pattern assigned to the presence of the decay product $[LNi^{II}(OH)_2Cu^{II}(IndanePY_2)]^+$ and $[LNi^{II}(OH)_2Cu^{II}(MePY_2)]^+$, respectively (Figure 73-Figure 74). It seems that the experimental conditions for the ionization and detection of the intermediate **3a** and **3b** are not appropriate resulting to the detection of the decay bis(μ-hydroxo) product.
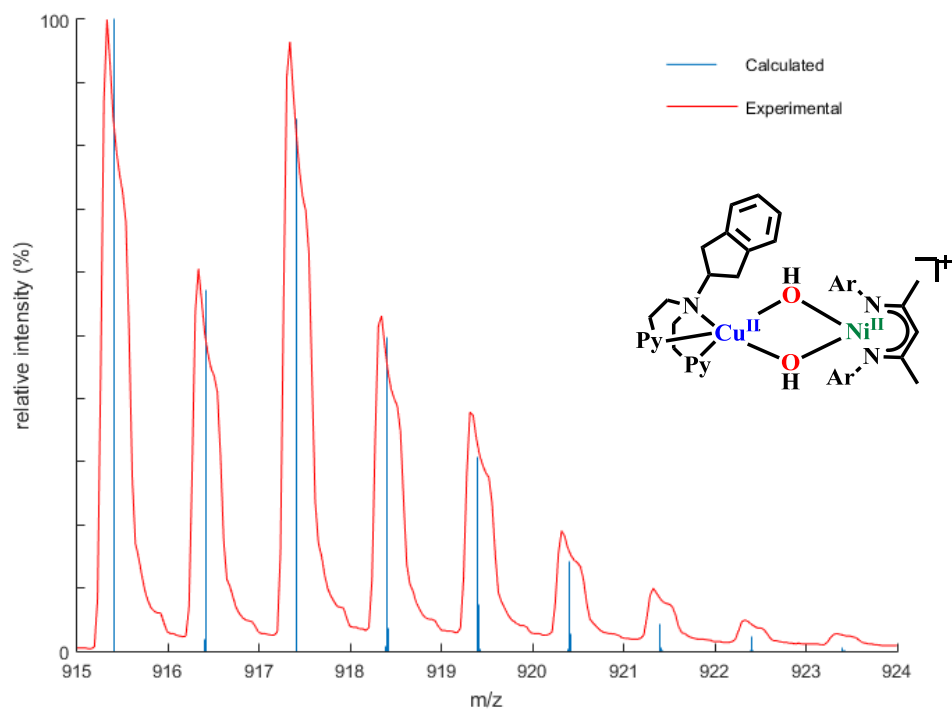
Figure 73 : Calculated and experimental mass spectrum of the decay bis(μ-hydroxo) product of **3a**.
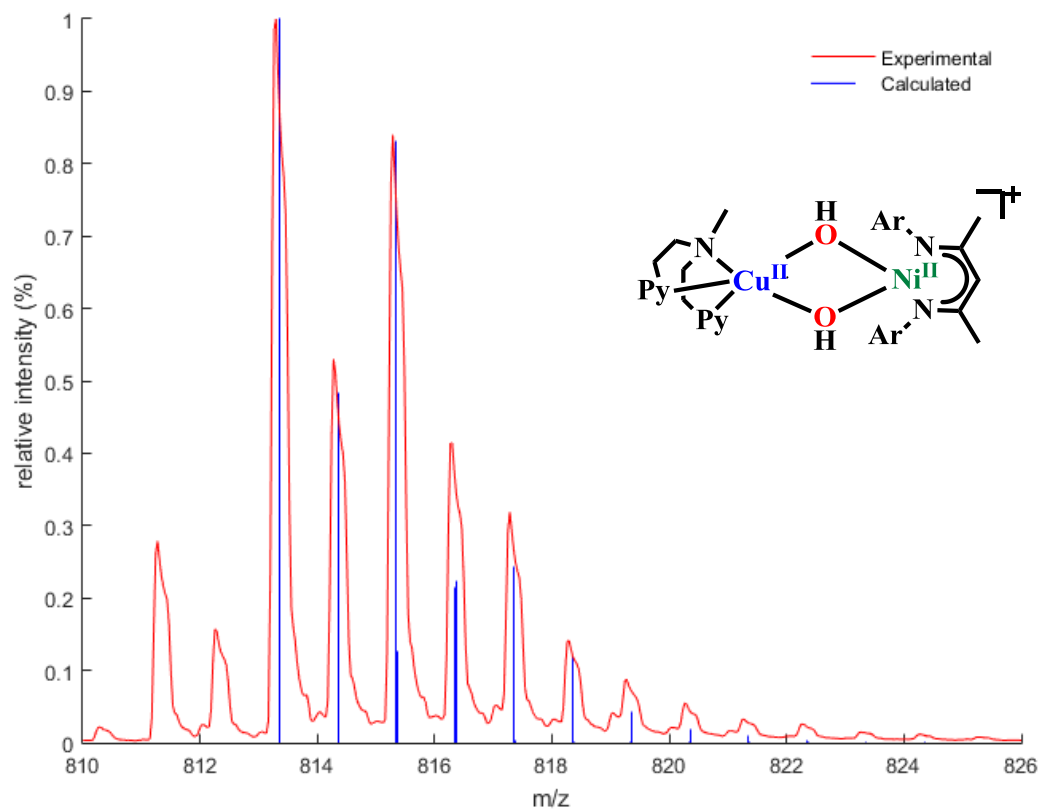
Figure 74 : Calculated mass spectrum and experimental of the decay bis(μ-hydroxo) product of **3b**.

III.1.5. rRaman spectroscopy

The Resonance Raman (rRaman) spectra of **3a** and **3b** were recorded using a 413-nm laser excitation in collaboration with the group of Prof. Peter Hildebrandt (TU, Berlin). rRaman bands are detected at 605 cm^{-1} and 612 cm^{-1} for **3a** and **3b**, respectively (Figure 75-Figure 76), which are sensitive to ^{18}O substitution (performed by using Ni^{18}O$_2$ as a starting reagent) and downshift (Δ^{18}O) by 31 cm^{-1} and 29 cm^{-1}, respectively. Notably, these bands are shifted to lower energies relative to the tetra-atomic vibrational mode of the [LNi(μ-O$_2$)Cu(MeAN)]$^+$ complex observed at 625 cm^{-1}. Furthermore, as previously observed, the absence of any isotope sensitive bands in the 700-1200 cm^{-1} region, excludes the possibility of the presence of peroxo or superoxo units in **3a** or **3b**. Interestingly, a second ^{18}O sensitive band is also detected at 556 cm^{-1} (Δ^{18}O =-21 cm^{-1}) and 579 cm^{-1} (Δ^{18}O =-19 cm^{-1}) for **3a** and **3b** respectively, which was not observed in the previously reported spectrum of the [LNiO$_2$Cu(MeAN)]$^+$ complex. The attribution of these bands to core vibrations of Cu(III)(μ-O)$_2$Ni(III) was performed with the aid of DFT calculations (see after) confirming the nature of the intermediate.
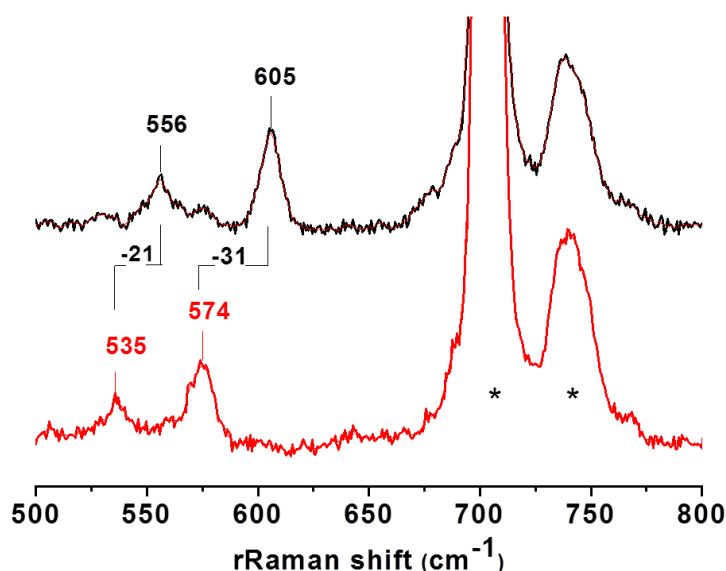
Figure 75 : Raman shifts obtained at -90°C in dichloromethane using a 413-excitation laser for **3a** involving ^{16}O (top) and ^{18}O (bottom) atoms.([**3a**]=7-10mM) Bands originated from the solvent are marked by asterisks.
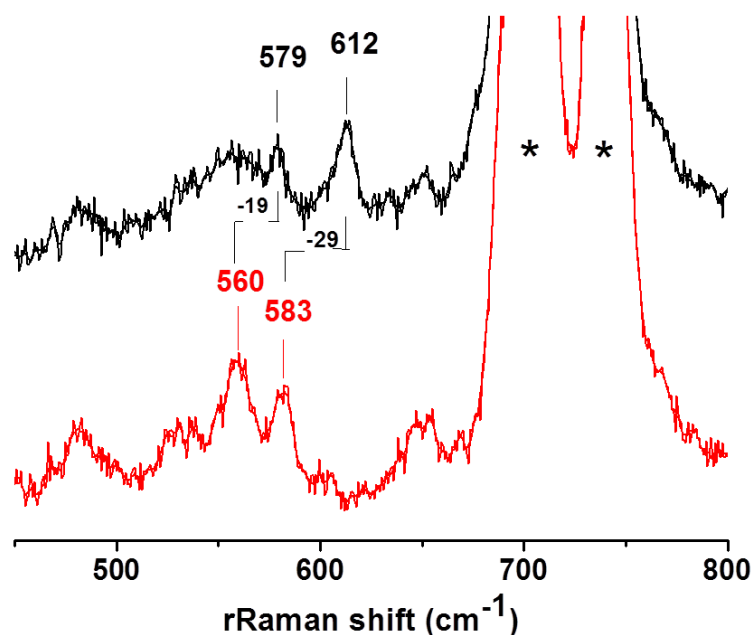
Figure 76 : Raman shifts obtained at -90°C in dichloromethane using a 413 excitation laser for **3b** involving ^{16}O (top) and ^{18}O (bottom) atoms. ([**3b**]=7-10mM) Bands originated from the solvent are marked by asterisks.

III.2. DFT calculations

III.2.1. Geometry optimization

DFT calculations were performed on **3a** and **3b** in collaboration with Dr. Maylis Orio in our group, in an effort to understand their structural and electronic properties. Full geometry optimizations were carried out revealing two conformations around the copper ion for each system (conformers A and B). In all cases, the copper site is in a five-coordinate square pyramidal geometry but with either the amine group (conformer A) or one pyridine group (conformer B) weakly bonded to the metal ion in axial position (Figure 77 and Figure 78).
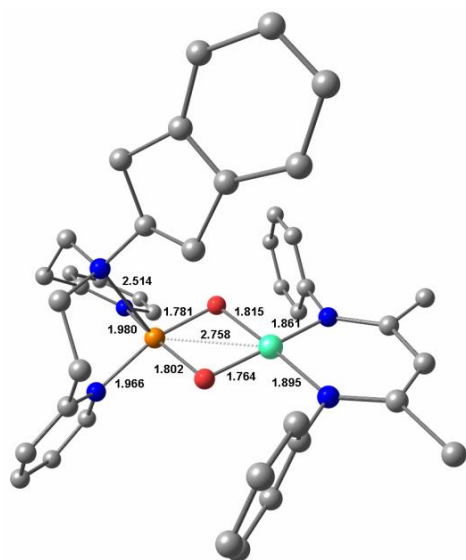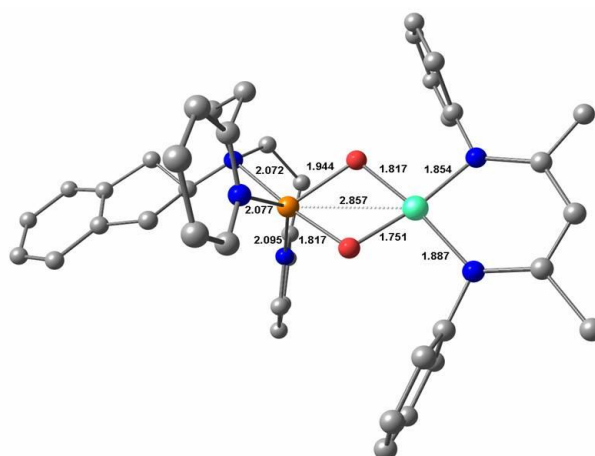
Conformer A   Conformer B

Figure 77 : Optimized molecular structures for **3a**; Conformers A (left) and B (right)
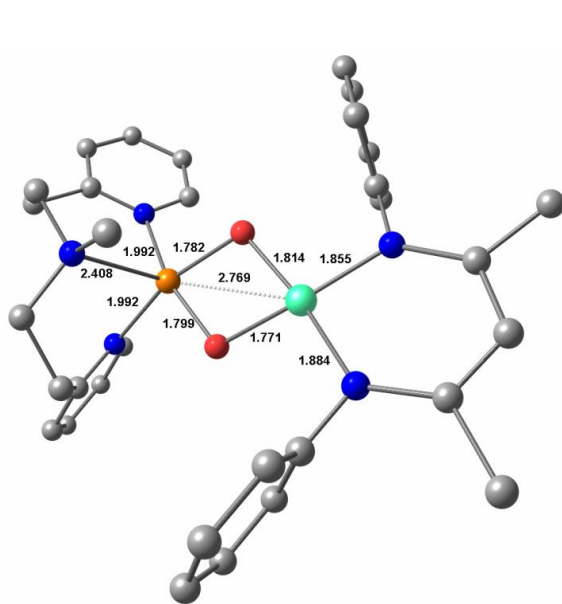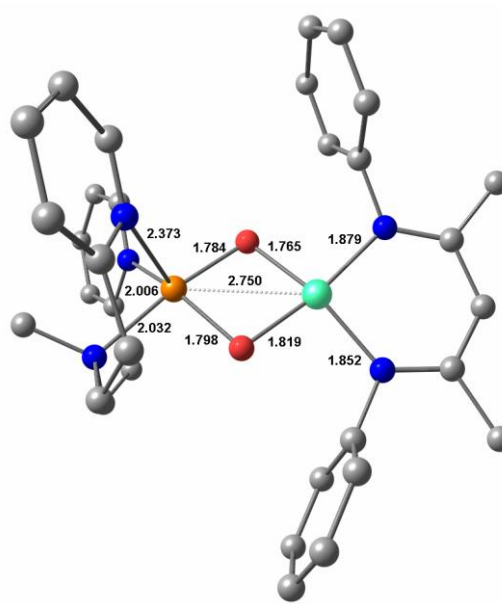
Conformer A   Conformer B

Figure 78 : Optimized molecular structures for **3b**; Conformers A (left) and B (right)

However, energetic analysis conducted on both **3a** and **3b** showed that the minimum free energy is obtained for the conformers (A) which make these structures the most favoured one (Table 10).

Table 10 : Calculated Gibbs free energies for the **3a** and **3b** conformers

Complex	Conformer	Energy (Eh)	Stability (kcal/mol)	Favored species
3a	(A)	-5121.457043	0	Conformer (A)
	(B)	-5121.372839	52.8	
3b	(A)	-4813.04405014	0	Conformer (A)
	(B)	-4813.02925132	9.30	

III.2.2. Singly Occupied Molecular Orbitals

Furthermore, both spin density plots and Singly Occupied Molecular Orbitals (SOMO) reveal that **3a** and **3b** bear one unpaired electron located at the nickel centre (Figure 79-Figure 80).
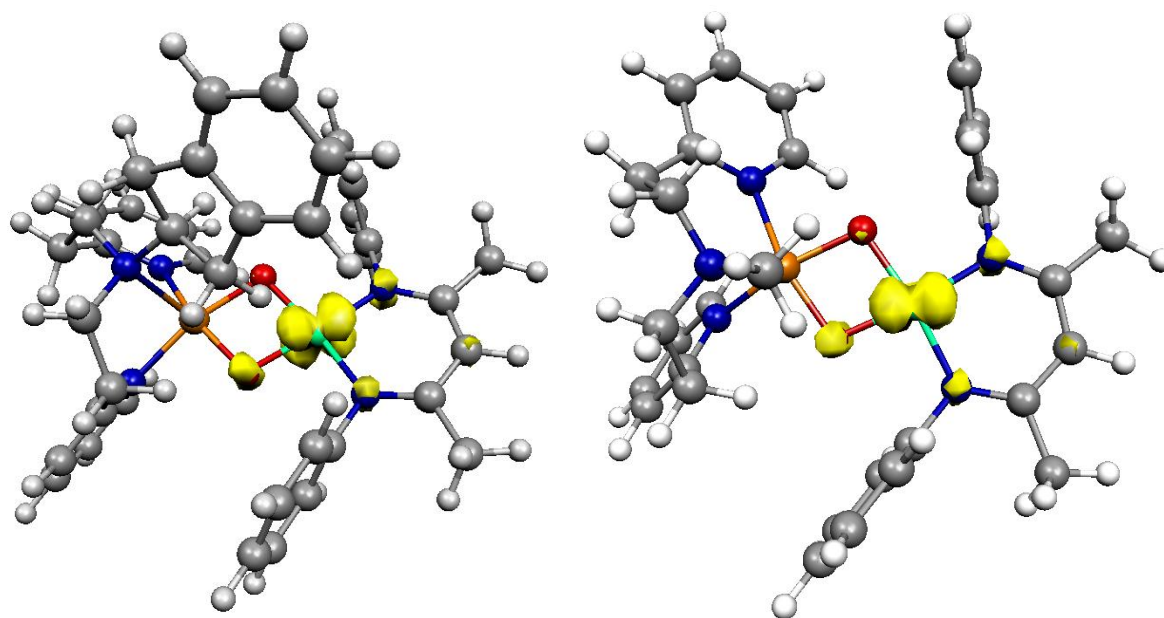
Figure 79 : Spin density plots of **3a** and **3b** conformer (A)
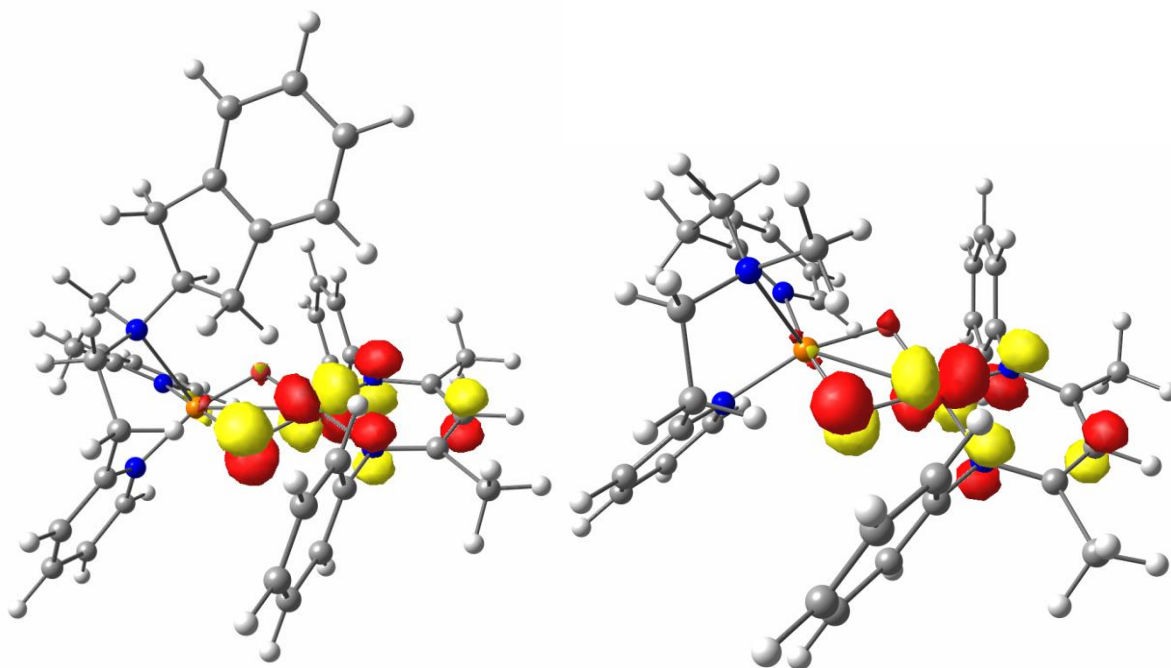
Figure 80 : Singly Occupied Molecular Orbitals of **3a** and **3b** (conformer A)

These results confirm the presence of one low-spin Ni^{III} (S=1/2, $3d^7$) and one low-spin Cu^{III} (S=0, $3d^8$) centres in both **3a** and **3b**. This assignment is further confirmed by the computed EPR parameters, which are in fair agreement with the experimental data (Table 11).

Table 11 : Comparison between calculated and experimental EPR parameters for **3a** and **3b** conformer (A)

g_1; g_2; g_3; (g_{av})	3a	3b
Expt.	2.006; 2.140; 2.410 (2.185)	2.006; 2.130; 2.390 (2.175)
Calc.	2.067; 2.129; 2.282 (2.160)	2.061; 2.124; 2.280 (2.155)

III.2.3. Frequency calculations

Frequency calculations were conducted on the DFT-optimized structures of the two species and Raman spectra were calculated. Tetraatomic vibration modes involving the NiO_2Cu core were predicted at 596 cm^{-1} and 621 cm^{-1} for **3a** and **3b**, respectively, in agreement with the assignment previously proposed for the MeAN-based Cu-Ni analog.[158] A second mode was calculated to be at 553 cm^{-1} and 528 cm^{-1} for **3a** and **3b**, respectively, originating from the coupling of the $Ni(\mu-O_2)Cu$ core and the Ni-coordinated β-diketiminate ligand coordinates (Figure 81-Figure 82).
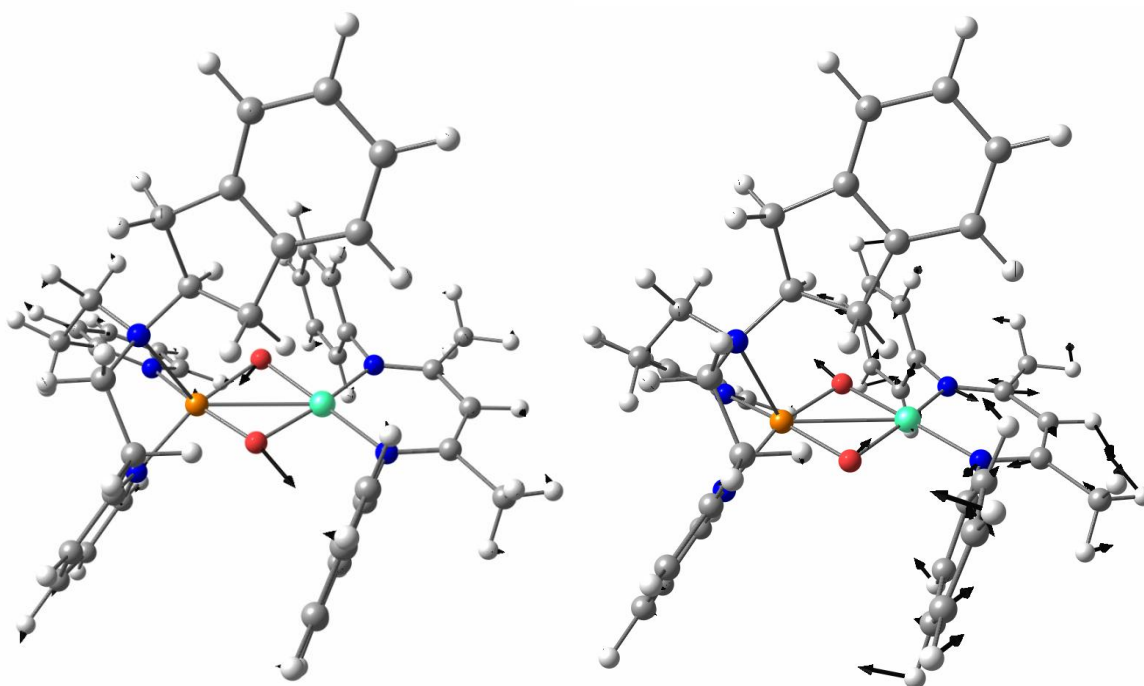
Figure 81 : Normal modes relevant to the 596 cm^{-1} (left) and 553 cm^{-1} (right) Raman shifts of **3a**.
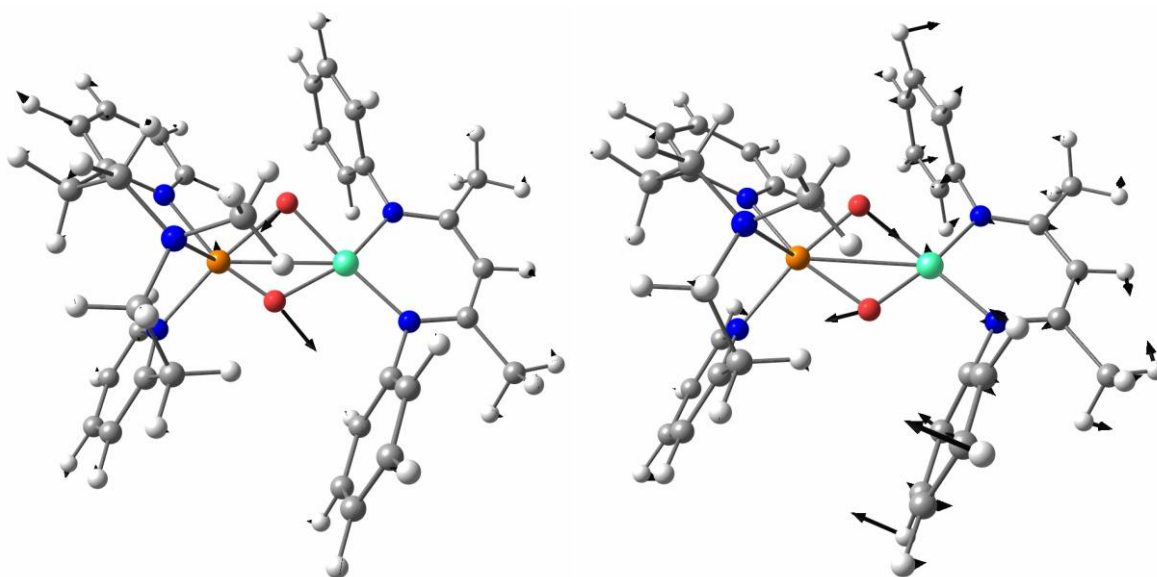
Figure 82 : Normal modes relevant to the 621 cm^{-1} (left) and 528 cm^{-1} (right) Raman shifts of **3b**.

Both sets of calculated results are in good agreement with the observed rRaman bands for each complex. The five-coordination geometry at the Cu ions obtained in the case of RPY$_2$-type ligands is affecting the coordination sphere of the Ni ion in **3a** and **3b** and the geometry around the Ni ion appears to be significantly distorted from planarity (dihedral angle of 11.2 and 16.2°, respectively) while it is perfectly planar in the MeAN-based complex (dihedral angle of 2.3°). This explains the appearance of a

new vibration in the rR spectra of the two species. The spectroscopic data thus support the DFT-calculated structure and validate the formation of both **3a** and **3b**.

III.3. Reactivity studies

The reactivity of the complexes **3a** and **3b** have been investigated in a number of nucleophilic and electrophilic reactions. The nucleophilicity of **3a** and **3b** has been studied in reactions with benzaldehyde, and cyclohexene carboxaldehyde (CCA). The ability of **3a** (**3b**) to undergo electrophilic Hydrogen Atom Transfer (HAT) reactions were also evaluated in reactions with 9,10 dihydroantracene (DHA) and 1,3 cyclohexadiene (CHD) for C-H bonds and with 2,4-di-tert-butylphenol (2,4-DTBP) and 2,6- di-tert-butylphenol (2,6-DTBP) for O-H bonds (Scheme 50).
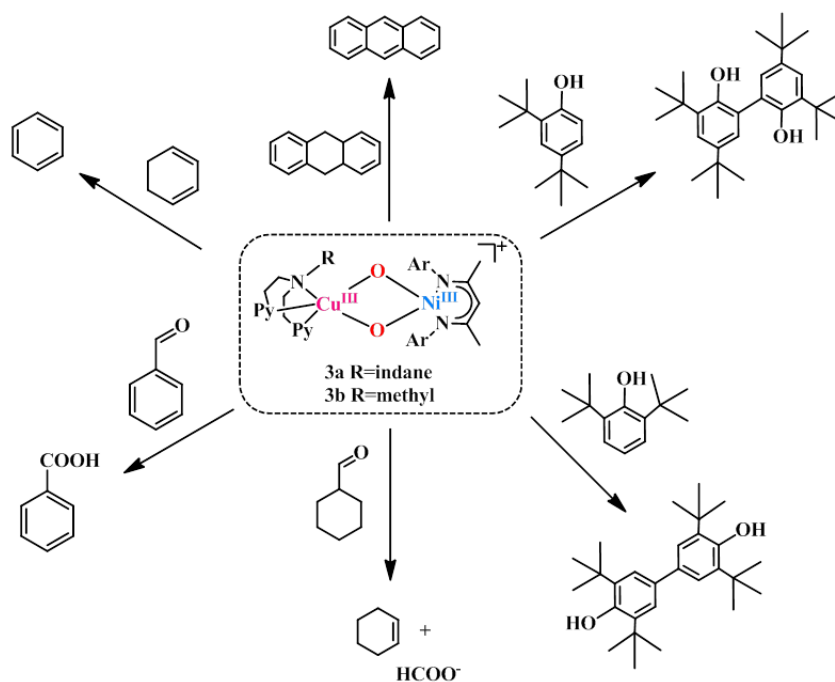
Scheme 50 : Substrates that have been used in this study and products formed.

In a typical reaction preformed, **3a** and **3b** at -60°C was treated with an excess of the above-mentioned substrates under a pseudo first-order condition. The disappearance of the characteristic band at 885 nm in the UV-Vis absorption spectrum was then monitored over time (see Figure 83 for reaction of **3a** with CCA). Rate constants in CH$_2$Cl$_2$ at -60°C (or at -90°C when too fast) were obtained from the pseudo-first order fit of the time trace of the decay of the 885 nm band (Figure 83). The pseudo-first order oxidation rate was then compared to the self decay of **3a** (**3b**) in the absence of substrate. If the rate of oxidation in the presence of substrate was higher than that in the absence of substrate, it was concluded that **3a** (**3b**) reacted with that substrate.
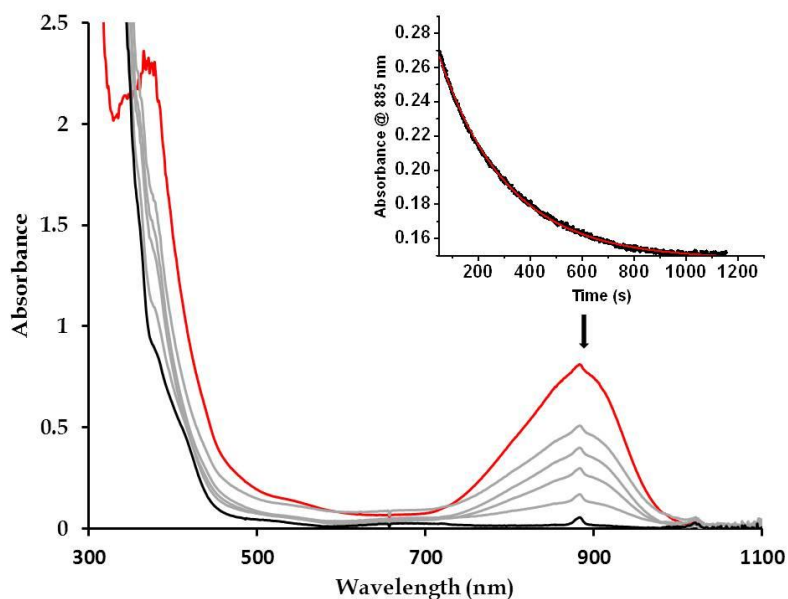
Figure 83 : Spectral changes of **3a** in the presence of 50 mM CCA at -60°C. Inset: Time trace of the decay at 885nm band upon addition of the substrate (black trace) and the first-order fit (inset: red trace).

Second-order rate constants were then determined from the dependence of the first-order rate constants on substrate concentration (Figure 84-Figure 89).

III.3.1. Reaction of 3a with external substrates

$$k_2(-60\ ^{\circ}C)=0.021\ M^{-1}s^{-1}$$

$$k_2(-60\ ^{\circ}C)=0.088M^{-1}s^{-1}$$
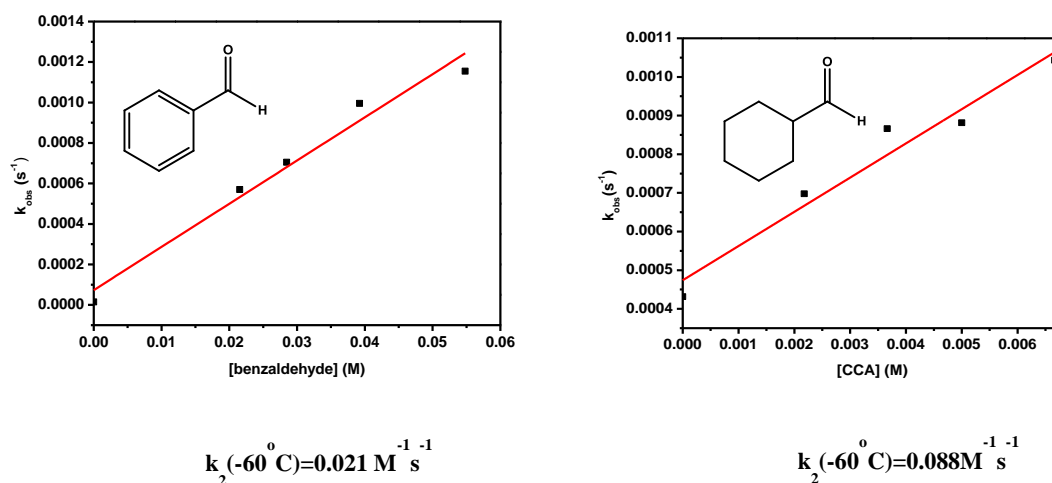
Figure 84 : Pseudo first-order rate constants as a function of substrate concentration the reaction of **3a** with benzaldehyde (left) and cyclohexane carboxaldehyde (right) at -60°C in CH$_2$Cl$_2$.
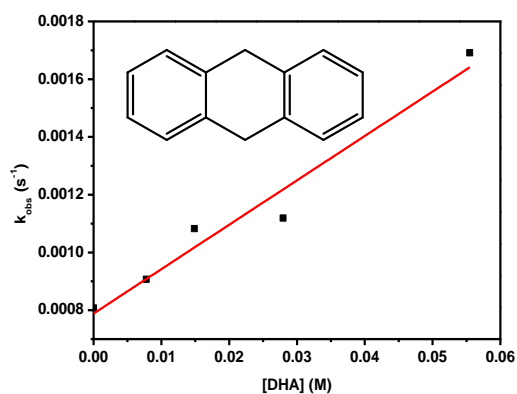
$$k_2(-60^o C)=0.015 \text{ M}^{-1}\text{s}^{-1}$$

$$k_2(-60^o C)=0.053 \text{ M}^{-1}\text{s}^{-1}$$

Figure 85 : Pseudo first-order rate constants as a function of substrate concentration the reaction of **3a** with dihydroanthracene (left) and 1,3 cyclohexadiene (right) at -60°C in CH$_2$Cl$_2$.
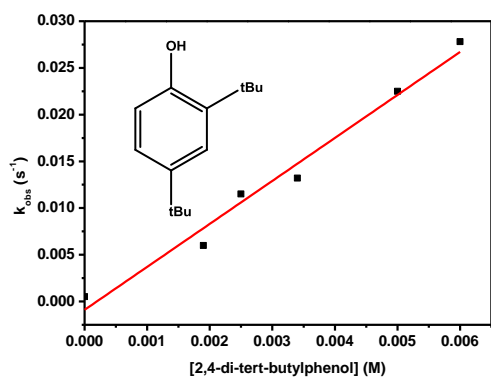
$$k_2(-90^o C)=4.60 \text{ M}^{-1}\text{s}^{-1}$$
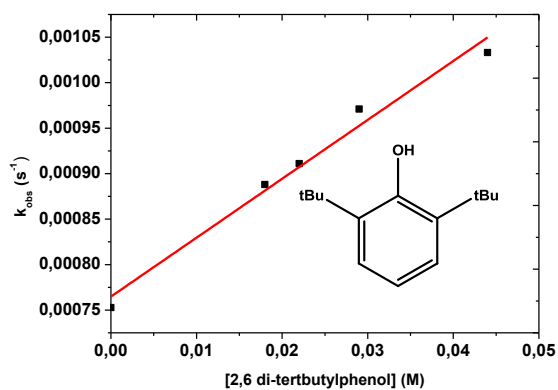
$$k_2(-90^o C)=0.006 \text{ M}^{-1}\text{s}^{-1}$$

Figure 86 : Pseudo first-order rate constants as a function of substrate concentration the reaction of **3a** with 2,4-di-*tert*-butylphenol (left) and 2,6-di-*tert*-butylphenol (right) at -90°C in CH$_2$Cl$_2$.

III.3.2. Reaction of 3b with external substrates
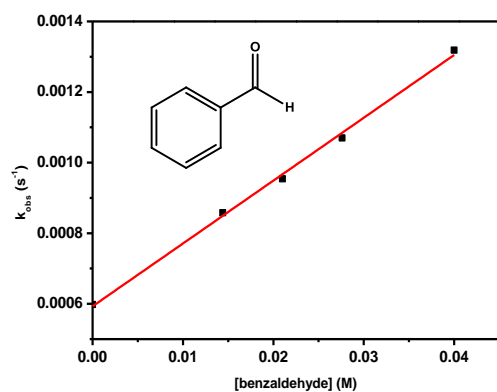
$$k_2(-60^{\circ}C)=0.0178 \; M^{-1} \; s^{-1}$$
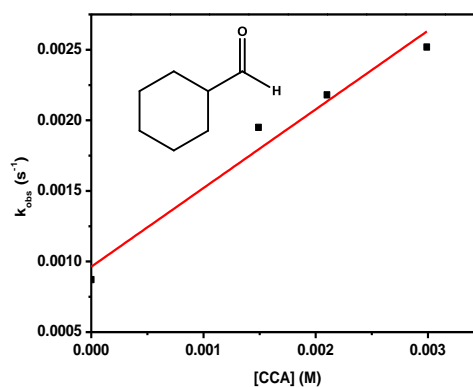
$$k_2(-60^{\circ}C)=0.557 \; M^{-1} \; s^{-1}$$

Figure 87 : Pseudo first-order rate constants as a function of substrate concentration the reaction of **3b** with benzaldehyde (left) and cyclohexane carboxaldehyde (right) at -60°C in CH_2Cl_2.
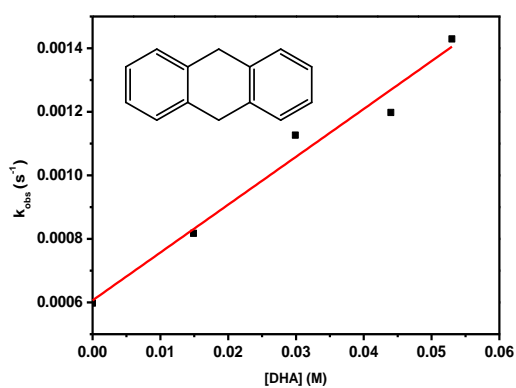
$$k_2(-60^{\circ}C)=0.015 \; M^{-1} \; s^{-1}$$
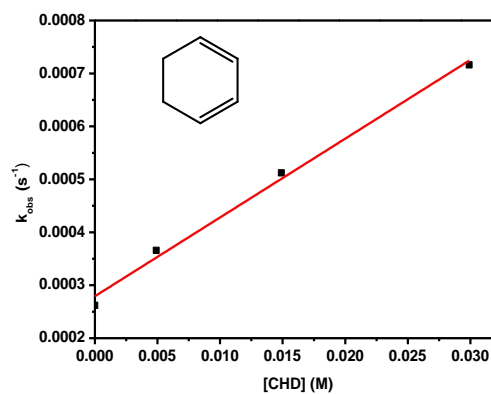
$$k_2(-60^{\circ}C)=0.0148 \; M^{-1} \; s^{-1}$$

Figure 88 : Pseudo first-order rate constants as a function of substrate concentration the reaction of **3b** dihydroanthracene (left) and 1,3 cyclohexadiene (right) at -60°C in CH_2Cl_2.

$$k_2(-90^{\mathrm{o}}\mathrm{C})=0.098\ \mathrm{M}^{-1}\ \mathrm{s}^{-1}$$
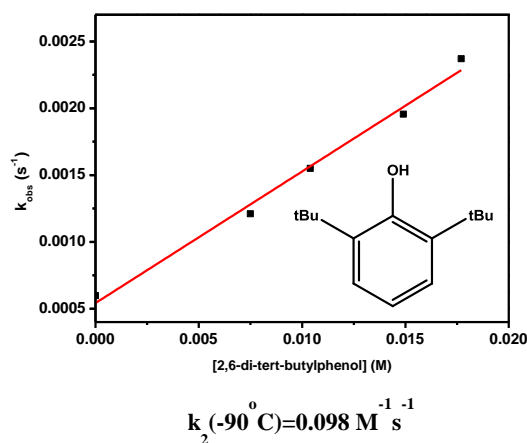
Figure 89 : Pseudo first-order rate constants as a function of substrate concentration the reaction of **3b** 2,6-di-*tert*-butylphenol (right) at -60°C in CH$_2$Cl$_2$.

In summary, second-order rate constants derived from those studies are listed in Table 12 and compared to that previously reported for [LNiO$_2$Cu(MeAN)]$^+$ intermediate.[158]

Table 12 : Second order rate constants determined for different substrates by kinetic studies by UV-Vis spectroscopy.

Substrates	Electrophiles		Nucleophiles			
	Benzaldehyde (-60°C)	CCA (-60°C)	DHA (-60°C)	CHD (-60°C)	2,4 DTBP (-90°C)	2,6 DTBP (-60°C)
3a k_2 / M^{-1} s^{-1}	0.021	0.088	0.015	0.053	4.60	0.0065
3b k_2 / M^{-1} s^{-1}	0.0178	0.557	0.015	0.014	Too fast	0.0985
LNi^{III}(μ-oxo)Cu^{III}(MeAN)]$^+$ k_2 / M^{-1} s^{-1}	0.11 (-50°C)	Too fast (-90°C)	Too Slow (-70°C)	0.0005 (-70°C)	2.44 (-90°C)	0.0001 (-80°C)

Notably, complex **3b** reacts with CCA and benzaldehyde at rates significantly slower than [LNiO$_2$Cu(MeAN)]$^+$. In contrast, in presence of DHA, CHD, 2,4-DTBP, or 2,6-DTBP, complex **3b** is found to be a better oxidant than [LNiO$_2$Cu(MeAN)]$^+$. These studies point to the presence of less nucleophilic oxygen atoms in **3b** relative to [LNiO$_2$Cu(MeAN)]$^+$, which may be attributed to a weaker donation to the Cu centre from the terminal pyridine nitrogens of the MePY$_2$ ligand relative to the tertiary amine nitrogen donors of the MeAN ligand.

Notably, replacement of the methyl group of the MePY$_2$ ligand in **3b** with a bulkier indane group in **3a** did not lead to any significant change in the rate constants for the

reactions with DHA and benzaldehyde. However, for reactions with bulkier substrates like 2,6-DTBP, 2,4-DTBP, or CCA, a significantly reduced rate constant is observed for **3a** relative to **3b**. This may be attributed to the sterically induced hindered access of the substrates in presence of the covalently attached indane group of the IndanePY$_2$ ligand in **3a**.

Interestingly, for reactions with **3a** no hydroxylation of the indane moiety was observed, which is in contrast to the previous report of the intramolecular indane hydroxylation reaction mediated by the homodinuclear copper-oxygen intermediate.

III.4. Natural population analysis

In order to explain the reactivity differences of our new complexes as compared to [LNi^{III}O$_2$Cu^{III}(MeAN)]$^+$, natural population analysis were performed for **3a/3b** and the results were compared to those obtained for [LNi^{III}O$_2$Cu^{III}(MeAN)]$^+$. No significant changes are observed on the Ni side. On the contrary, the charges on the copper ligands in **3a/3b** are more negative than in MeAN. This may be due to π effects or geometrical effects. In consequence, the positive charges on the copper ions decrease in **3a/3b** as compared to MeAN and the natural negative charges found at the O atoms are smaller (by −7% to −8%) in **3a** and **3b** (Figure 90) with respect to those of the corresponding atoms in [LNi^{III}O$_2$Cu^{III}(MeAN)]$^+$ (Figure 91). These data indicate that the oxido cores in **3a** and **3b** are less electron-rich compared to that of [LNi^{III}O$_2$Cu^{III}(MeAN)]$^+$. It thus correlates with the decreased nucleophilicity presently observed.
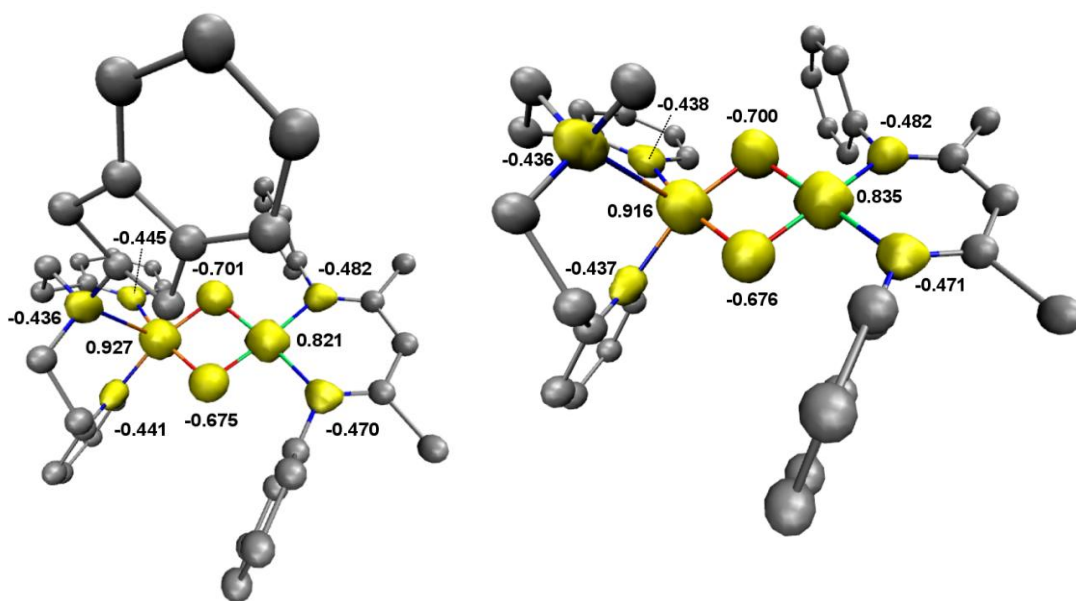
Figure 90 : Total density and individual natural charges for **3a** and **3b**.

127
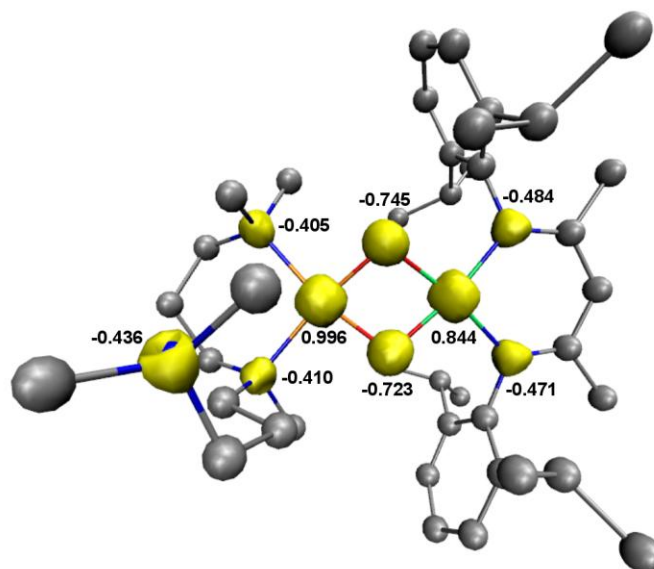
Figure 91 : Total density and individual natural charges for [LNi^{III}O$_2$Cu^{III}(MeAN)]$^+$.

IV. Conclusion

In this chapter we have shown that the nucleophilicity of the oxo groups can be tuned by varying the electron donation and the geometry at the copper center. Thus replacement of the MeAN ligand in the previously reported [(NacNac)Ni(μ-O$_2$)Cu(MeAN)]$^+$ complex by RPY$_2$ ligands in **3a/3b** led to slower nucleophilic and faster electrophilic reactions. Furthermore, for reactions with **3a** no hydroxylation of the indane moiety occurred, in contrast to the previous report of the intramolecular indane hydroxylation reaction mediated by the homodinuclear {L$_{ind}$CuO$_2$CuL$_{ind}$} complex. This emphasizes the initiation of novel reactivity properties in heterodinuclear systems relative to their homobimetallic counterparts. The present results therefore underline the significance of geometric and electronic changes in the physical and chemical properties of this important class of biologically relevant metal–dioxygen intermediates.

Chapter V

General Conclusion and Perspectives

In our studies the regio- and stereoselectivities of O-atom transfer was used to gain more information of the copper-oxygen species involved in different conditions. Indeed, the "substrate ligand binding approach" appeared as a powerfull tool to investigate the reactivity of high valent species, either mononuclear or binuclear (homo- *vs.* heterobimetallic).

In Chapter I, we investigated the formation and reactivity of binuclear or mononuclear copper-oxygen species after the reaction of Cu^I or Cu^{II} complexes with different oxidants in different solvents. It was observed that all the different species formed were able to oxidize activated C-H bonds. On the other hand, only two species were able to oxidize non-activated C-H bonds: mixed-valent species or Cu^{II}-O° (oxyl) species.

Regarding the mixed-valent species, Tolman *et al.* and Belle *et al.* have characterized the first examples of bis (µ-oxo)$Cu^{II}Cu^{III}$ (see **Chapter I**). However, few reactivity data of those complexes have been postulated. This work therefore provides evidence that such species can be involved in strong C-H bond activation.

We now intend to prepare, characterize and study the reactivity of such species starting from dinuclear Cu^{II} complexes. Our approach is to prepare unsymmetrical ligands for two different copper sites with an alkyl spacer to link the copper centers (Scheme 51). The one site will contain amidate groups stabilizing Cu^{III} oxidation state and the second site with pyridine groups to stabilize Cu^{II} oxidation state.
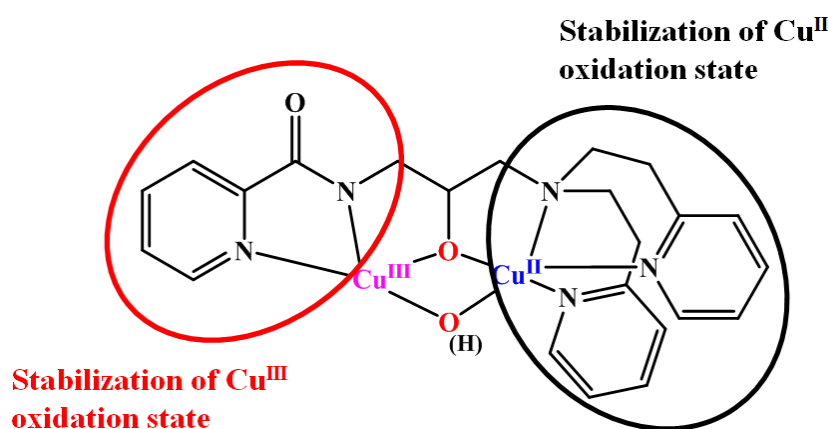
Scheme 51 : Unsymmetrical ligand coordinated to copper in order to stabilize mixed-valent $Cu^{II}Cu^{III}$ species.

This work was initiated and the unsymmetrical ligand (Scheme 51) together with the symmetrical one bearing pyridine groups on both sides were synthesized in order to compare the reactivity and the redox properties of the two systems. This work is still in progress in the laboratory.

In addition, reaction of RPY2-based Cu(II) complexes with sodium hypochlorite as an oxidant has led to very interesting results. Interestingly, copper-oxygen species formed with sodium hypochlorite, possibly through unprecedented Cu(III)-O° species, were able to oxidize activated C-H bonds. It has to be mentioned that those species have been postulated as active species formed in peptidylglycine-α-hydroxylating monooxygenase. Therefore, it would be very interesting to investigate if those highly reactive species are able to oxidize non-activated C-H bonds. In this case, an n-propyl or a cyclopentyl group could be used as an internal substrate. This work is also in progress in the laboratory.

In Chapter II, we have provided the **first example** of stereoselective O-atom transfer towards indane as an internal substrate (activated C-H bond) through dinuclear copper species and water as the oxygen atom source. In perspective, we intend to investigate the reactivity and stereoselectivity of dinuclear species towards non-activated C-H bonds, for example towards cyclopentyl group as internal substrate (Scheme 52).
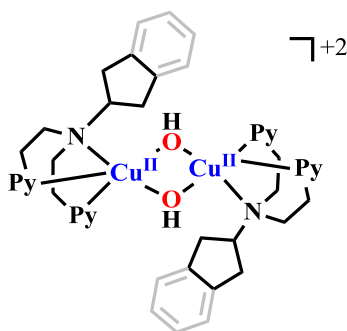
Scheme 52 : Dinuclear (bis-µ-hydroxo) complexes surrounded by cyclopentylPY$_2$.

In chapter III, we have reported the reactivity of the oxo groups of Cu-Ni heterobimetallic (bis-µ-oxo) complexes. The nucleophilicity of the oxo groups of those complexes prevented the O-atom transfer towards the internal substrate (indane), in contrast to the intramolecular O-atom transfer mediated by homobimetallic copper counter-parts. In perspective, it would be interesting to investigate the reactivity of other Cu-M heterobimetallic (bis-µ-oxo) species by changing the second metal ion. Iron and manganese are good candidates, since they can accommodate various oxidation states.

Overall, these studies will help to develop new catalysts that will selectively react either with electrophilic or nucleophilic substrates.

Experimental part

All chemicals used in this study except the ligands and the complexes were commercial products of the highest available purity. Commercial starting materials were used without further purification, except for 2-vinylpyridine which was distilled prior to use. Preparation and handling of air sensitive materials were performed in a N_2 glove box Jacomex or OMNI-Lab 2 (VAC) with O_2 and moisture concentration less than 2 ppm. All aqueous solutions were prepared using Milli-Q Ultrapure water. A Metrohm-605 pH meter was used to adjust the pH values (at 25°C) and was calibrated with standard buffer solutions. ^{18}O 99%, $H_2^{18}O$ 97% and $H_2^{18}O_2$ 90% (2-3% concentration in water) were purchased from Sigma-Aldrich.

Physical methods

Elemental analyses were performed using a Thermo Finnigan EA 1112 instrument. The results were validated by at least two measurements. ESI-MS analyses were performed using a SYNAPT G2 HDMS (Waters) spectrometer equipped with a pneumatically assisted Atmospheric Pressure Ionization source. The ion-spray voltage was 2.8 kV, the orifice lens was 20 V, and the nitrogen flux (nebulization) was 100 L h^{-1}. The HR mass spectrum was obtained with a time-of- flight analyzer. The sample was placed in a dichloromethane/methanol solution.

NMR experiments

^1H, and ^{13}C NMR spectra were recorded at 25°C either on Bruker Avance III nanobay 300 MHz or 400 MHz spectrometers. Chemical shifts were reported in parts per million (ppm) referenced to residual solvent peak. ^{19}F NMR spectra were recorded at 25°C on Bruker Avance III nanobay 500MHz. The spectra were recorded using CDCl$_3$ or D$_2$O as deuterated solvents. The letters following the chemical displacement δ, such as s, d, t, q, qt, and m correspond to singlet, doublet, triplet, quartet, quintet and multiplet.

X-ray diffraction analysis

Suitable crystals were measured on a Rigaku Oxford Diffraction SuperNova diffractometer at 293K using the MoKα radiation (λ= 0.71073 Å). Data collection reduction and multiscan ABSPACK correction were performed with CrysAlisPro (Rigaku Oxford Diffraction). The structures were solved by direct methods with ShelXT[161,162] and ShelXL[163] was used for full matrix least squares refinement. All H-atoms were found experimentally and their coordinates and Uiso parameters were constraint to 1.5Ueq. (parent atoms) for the methyls and to 1.2Ueq. (parent atom) for the other carbons.

Infrared spectroscopy

FT-IR spectra were recorded in FT-IR in attenuated total reflection (ATR) mode on a Bruker TENSOR 27 spectrometer equipped with a single-reflection DuraSamplIR diamond ATR accessory.

UV-Vis spectroscopy

Low temperature UV-Vis spectra were recorded by Agilent 8453 diode array spectrophotometer from 300-1100 nm with samples in 1.0 path length quartz cuvette, connected with a cryostat from Unisoku Scientific Instruments, Japan.

Room temperature electronic absorption spectra were recorded on a Perkin-Elmer Lamda 650 or Cary 50 spectrometer from 250nm – 800nm with samples in 1.0 cm path length quartz cuvette.

EPR spectroscopy

ESR spectra were obtained using a Bruker Elexsys E500-9.5/2.7 spectrometer equipped with a BVT 3000 digital temperature controller (100−400 K). The samples were prepared in H_2O in the presence of electrolyte at pH varying from 5 to 10. The spectra were recorded either in calibrated EPR tubes in the presence of 10% glycerol at 120K or in capillary tubes at 295K. The simulations were performed with automatic parameter fitting.[164] The contribution of naturally abundant ^{63}Cu and ^{65}Cu was considered, but the values given in the text refer to ^{63}Cu. All principal axes were supposed parallel.

Resonance Raman

rRaman spectra were measured in the group of Peter Hildebrandt (TU Berlin). experiments were performed in CH_2Cl_2 at -92°C (Bruker cryostat) using 413 nm excitation with by a Horiba Jobin-Yvon LabRAM HR800 confocal Raman spectrometer. The concentrations of samples were from 3 mM to 8 mM.

General procedure of synthesis of ligands

CH₃PY2. The ligand was synthesized in slightly different way from the already reported procedure.[46] To absolute MeOH (80mL) were added 2-vinylpyridine (11g, 0.210 mol), 2-(2-methylaminoethyl) pyridine (4.2g, 0.030 mol), and glacial acetic acid (1.8g, 0.060 mol). After refluxing for 5 days under Argon, MeOH was evaporated and 15% NaOH was added. The product was extracted with CH_2Cl_2 (x3) and the combined organic layers were dried over Na_2SO_4. Evaporation of CH_2Cl_2 under reduced pressure left the crude product. Flash chromatography (neutral alumina, ethylacetate/MeOH, 98:2) afforded the ligand as a yellow product (yield: 40%). ^{1}H NMR (300 MHz, CDCl₃) δ 8.45 (d, J = 4.7 Hz, 2H), 7.50 (td, J = 7.7, 1.8 Hz, 2H), 7.12 – 6.97 (m, 4H), 2.90 (dt, J = 6.8, 2.2 Hz, 4H), 2.79 (dt, J = 7.2, 2.2 Hz, 4H), 2.34 (s, 3H).

IndanePY₂: The ligand was synthesized in a slightly different way from the already reported procedure.[70] A solution of 2-aminoindane (798 mg, 6 mmol), 2-vinylpyridine (4.2 mL, 3.785 g, 36 mmol) and acetic acid (1mL, 900mg, 15mmol) in absolute MeOH (10mL) was placed in a schlenk flask with a screw cap. Then dioxygen was removed with freeze-pump-thraw technique (x3). After warming it at $55^{\circ}C$ for 3-4 days, methanol was evaporated and 15% NaOH (10mL) was added. The product was extracted with DCM (3x30mL) and the organic layers were collected and dried over Na_2SO_4. Evaporation of dichloromethane under pressure left the crude product. Flash chromatography (SiO_2, CH_2Cl_2/MeOH 90:10) gave the pure product in 30% yield. ^{1}H NMR (300 MHz, $CDCl_3$) δ 8.47 (dd, J = 4.9, 0.8 Hz, 2H), 7.51 (td, J = 7.7, 1.8 Hz, 2H), 7.15 – 6.95 (m, 8H), 3.81 – 3.59 (qt, 1H), 3.14 – 2.87 (m, 10H), 2.79 (dd, J = 15.1, 9.0 Hz, 2H).

IndanePY₂-OH: The *cis*-2-amino-1-indol ligand was synthesized according to the already reported procedure.[70] To a blue solution of **2a** (40mg, 57 mmol) in degassed dichloromethane (4mL), excess of benzoin (21 mg, 98 mmol) and triethylamine (21μL, 98 mmol) were added. After some minutes the color of the solution turned to yellow. After exposure of the solution in the atmosphere for 24h, the color of the solution returned to green. The obtained complex was precipitated after addition of ether and washed several times to remove degradation products of benzoin and triethylamine. Then, the mixture was extracted with 35% NH_4OH and dried over Na_2SO_4. Evaporation of dichloromethane gave the pure product. ^{1}H NMR (400 MHz, CD_3Cl) δ 8.53 (d, *J* = 4.6 Hz, 2H), 7.56 (tt, *J* = 11.2, 5.6 Hz, 2H), 7.45 (d, *J* = 7.3 Hz, 1H), 7.22 (td, *J* = 8.4, 3.4 Hz, 3H), 7.16 – 7.06 (m, 4H), 4.99 (d, *J* = 4.8 Hz, 1H), 3.43 (ddd, *J* = 14.1, 9.5, 5.9 Hz, 1H), 3.28 – 3.13 (m, 4H), 3.12 – 2.94 (m, 6H).

CyclopentylPY₂: The ligand was synthesized according to the already reported procedure.[69]

nPropylPY₂: The ligand was synthesized in a slightly different way from the already reported procedure.[69]

General procedure of the synthesis of Cu^I complexes

The complexes $RPY_2Cu^I(CH_3CN)(PF_6)$, **1a** and **1b**, as well as $cyclopentylPY_2Cu^I(CH_3CN)(PF_6)$ and $npropylPY_2Cu^I(CH_3CN)(PF_6)$ have been synthesized *in situ* by the dropwise addition of solution of 1 eq. $Cu^I(CH_3CN)_4PF_6$ or $Cu^I(CH_3CN)_4OTf$ in anhydrous and degassed dichloromethane in a solution of 1eq. dissolved ligand in the same solvent inside the glove box or under argon.

Synthesis and characterization of Cu^{II} complexes

IndanePY$_2$Cu^{II}(OTf)$_2$: The Cu^{II} complex has been synthesized according to the already reported procedure.[70] To a solution of Cu^{II}(OTf)$_2$ (0.4 mmols) in dry MeOH (10mL), a solution of 1 eq. of IndanePY$_2$ (0.4 mmols) was added dropwise and the mixture was stirred for 30min. Then methanol was evaporated and diethyl ether was added resulting to blue precipitation. Recrystallization with diffusion of ether in DCM gave blue crystals suitable for X-ray diffraction. Elemental analysis: calculated for C$_{25}$H$_{25}$CuN$_3$F$_5$O$_6$S$_2$: C 42.58; H 3.57; N 5.96; S 9.09; Found: C 42.49; H 3.98; N 5.75 S 8.89.

CH$_3$PY$_2$Cu^{II}(OH$_2$)$_2$(OTf)$_2$: To a solution of Cu^{II}(OTf)$_2$ (0.740 g, 0.0021 mol) in MeOH (10mL) was added a solution of deoxygenated CH$_3$PY$_2$ (0.500 g, 0.0021 mol) dropwise and the resulting blue solution was stirring for 1h. The powder precipitated by the addition of ether (70%). Diffusion of ether in a solution of complex in MeOH gave light blue crystals suitable for X-ray diffraction. Elemental analysis: Calculated for C$_{17}$H$_{23}$CuN$_3$O$_8$F$_6$S$_2$: C 31.95; H 3.63; N 6.58 S 10.04; Found: C 32.22; H 3.33; N 6.76 S 9.93.

CyclopentylPY$_2$Cu^{II}(OTf)$_2$: The complex was synthesized according to the already reported procedure.[69]

npropylPY$_2$Cu^{II}(OTf)$_2$: The complex was synthesized according to the already reported procedure.[69]

[(IndPY$_2$)Cu](ClO$_4$)$_2$.(MeOH)(H$_2$O) *Precautions! The perchlorate salts are potentially explosive and should be handled with care!*
To a solution of IndPY$_2$ (55 mg, 0.160 mmol) in 2.5mL MeOH was added dropwise a solution of Cu(ClO$_4$)$_2$·6H$_2$O (60 mg, 0.160 mmol) in 1 mL H$_2$O. The deep blue reaction mixture was stirred for 1h at room temperature. After addition of diethyl ether, the complex was precipitated as a blue solid (85%). Elemental analysis: calculated for C$_{23}$H$_{29}$Cl$_2$CuN$_3$O$_{10}$: C 43.93; H 4.76; N 6.55; Found: C 43.66; H 4.65; N 6.46. FT-IR ν/cm^{-1} 3400 (O−H), 1613 and 1449 (pyridine ring), 775 (C-Hpy), 1046 and 620 (ClO$_4$$^-$).

Preparation of iodosylbenzene (PhIO)
The iodosylbenzene has been prepared according to the already reported procedure.[92] In a round bottom flask, iodobenzene diacetate was mixed with 100mL solution of NaOH (5M) and the final suspension was stirring vigorously for 1h. Then additional 50mL of water were added and the mixture was stirring for 15 min more. The mixture was filtrated, washed several times with water obtaining the crude PhIO. A last

purification step was performed by adding placing the solid in 50 mL chloroform. The yellow PhIO powder was separated by filtration and dried in a desiccator. ^{18}O labeled iodosylbenzene was prepared using the same procedure but starting from $H_2^{18}O$ in presence of NaH. The ^{18}O content of iodosylbenzene in the present labeling study was determined by mass spectral analysis of triphenylphosphine oxide prepared from the labeled iodosylbenzene.

General procedure for the synthesis of $[LNi^{III}(O_2)Cu^{III}(RPY_2)]$

The greenish solution of **2** in anhydrous CH_2Cl_2 (2.5 mL; 0.15 mM) was cooled to -90°C. Then 1 equivalent of **1a** (**1b**) in anhydrous CH_2Cl_2 (0.1mL) was added, to yield deep brown intermediate **3a** (**3b**). The generation of the deep brown species **3a** (**3b**) was monitored by the growth of 885 nm band in the UV/vis spectrum. ^{18}O Labeled samples for rRaman experiments were prepared using the same procedure but starting from ^{18}O labeled Ni precursor **2**.

Potentiometric Studies

The ionic strength of the experimental solutions was kept at 0.1 M with $NaNO_3$, the temperature was controlled at 25.0 ± 0.1 °C and atmospheric CO_2 was excluded from the titration cell during experiments by passing purified nitrogen across the top of the experimental solution. Additionally, the solution was bubbled with nitrogen before starting the titration. Titrant solutions were added through capillary tips at the surface of the experimental solution by means of a Metrohm Dosino 800 automatic burette. Calibration of the electrode and pH meter was performed using standard solutions provided by Metrohm at pH 4.0, 7.0, 9.0. A 0.100 M standard solution of HNO_3 (1000 mL) was prepared from a commercial Merck ampoule and purified water from a Millipore Milli-Q demineralisation system. Carbonate-free solutions of the titrant NaOH were obtained at 0.099M by using freshly prepared solution from a Merck ampoule in water (1000 mL; freshly boiled for about 2 h and allowed to cool under flux of nitrogen). This solution was standardized with HNO_3 standard solution. Measurements during titrations were carried out with L_{ind} (0.0182 mmol) in a total volume of 20 mL, in the absence and presence of Cu^{2+} (0.5, 1 and 1.5 equiv relative to the ligand). The titrations of the free ligand were run between pH 3 and 8 and in the presence of metal between pH 3 till the point of visible precipitation. A back titration was not performed at the end of each direct complexation titration due to precipitation. Each titration curve consisted typically of 140–180 points.

Calculation of equilibrium constants

Calculations of the overall equilibrium constants were performed by fitting the potentiometric data from protonation or complexation titrations with HYPERQUARD program.[137] Species distribution diagrams were plotted from the calculated constants with HYSS program.[165] Differences in log units, between the values of protonated and non-protonated constants provided the stepwise reaction constants.

Electrochemical methods

Electrochemical experiments were recorded on a Bio-logic SP-150 potentiostat eq.uipped with EC-Lab software or on an AUTOLAB PGSTAT 100 (Metrohm) potentiostat monitored by the NOVA software which is available in our collaborator's lab. Cyclic voltammetry experiments were conducted using three-electrode setup (each compartment is separated by a porous bridge), which consists of: *(i)* a glassy carbon (2 mm^2) or PGEE pyrolytic graphite (7 mm^2) working electrode *(ii)* a platinum wire counter electrode and *(iii)* Ag/AgCl reference electrode (3M KCl, 0.210 V *vs.* Normal Hydrogen Electrode, NHE). In organic solvents ferrocene was added at the end of the experiments to determine redox potential values.

All aqueous electrochemical experiments were obtained using different supporting electrolytes, either CH_3COONa, $NaNO_3$ or NaOTf set at 0.1 M. The salts were purchased from commercial sources and were of the highest purity.

The concentration of the complexes was ranged from 0.1 mM to 2.5 mM in 3 mL aqueous electrolyte. In order to increase the solubility of our complex in some cases, 5% of co-solvent (acetone) was added. The final aqueous solutions were adjusted to the desired pH using either 2,6-lutidine as a non-oxygen source base or 1M NaOH solution. Controlled potential electrolysis experiments were conducted with a relatively high surface area Pt electrode or a graphite rod applying at 1.1 V *vs.* AgCl/Ag (unless otherwise mentioned). Electrolysis were performed under inert atmosphere either by degassing with argon at least 20 minutes and maintaining an argon flow during electrolysis or by placing the electrochemical cell inside a JACOMEX glove box (O_2 < 1 ppm). A magnetic stirrer bar was used to stir the solution. The temperature in all cases was 25°C.

Detection of O_2 evolution

The detection of dioxygen produced in solution during electrolysis was performed using a calibrated Oxygen monitoring Kit with probe (NEOFOX-KIT-Probe). A three-neck electrochemical cell is charged with copper complex containing solution, the electrodes and the Oxygen monitoring probe fitted with a septum. Before each experiment the probe was calibrated in oxygen free (sodium sulfite solution) and oxygen saturated (O_2 purged) water. The mixture was purged with argon for 10 min to remove any traces of oxygen. The program NeofoxViewer gave an O_2 reading every 10 sec. Electrolysis experiments were performed under inert atmosphere after degassing with argon but the argon flow was stopped during electrolysis.

DFT Calculations mentioned in Chapter III

All calculations have been performed with the ORCA program package.[139] Full geometry optimizations have been calculated with the hybrid functional B3LYP.[140,166] The RI approximation, in the Split-RI-J variant[167] with the appropriate Coulomb fitting sets,[168] has been applied in conjunction with the Def2-TZV/P[169] basis set for all atoms. Scalar relativistic effects have been taken in account in the form of the ZORA

approximation.[170,171] Increased integration grids (Grid4 in ORCA convention) and tight SCF convergence criteria were used. According to the experimental conditions, solvent effects were accounted for property calculations, energy calculations and geometry optimizations. For that purpose, we used the water ($\varepsilon = 80.4$) solvent within the framework of the conductor like screening (COSMO) dielectric continuum approach.[141] The relative energies were obtained from single-point calculations using the same functional/basis set as employed before. The counterpoise (CP) procedure was used to correct the total energy for the basis set superposition error (BSSE).[172,173] The Heisenberg isotropic exchange coupling constants J were evaluated from additional single point calculations based on the Broken Symmetry (BS) approach[174–176] using the hybrid functional B3LYP and the TZVP basis set. The Yamaguchi formula[142,143] was used to estimate the exchange coupling constants J based on the Heisenberg–Dirac–van Vleck Hamiltonian.[144,145,146,147] Optical properties and EPR parameters were also obtained from single-point calculations using the same criteria as mentioned for geometry optimization. Electronic transition energies and dipole moments for all models were calculated using time-dependent DFT (TD-DFT)[177,178,179] within the Tamm-Dancoff approximation,[180,181] and 30 excited states were calculated in the TD-DFT calculations.

Reactivity studies

General procedure of oxidation of Cu^{I} complex with O$_2$

To a solution of the IndanePY$_2$ in 3mL of dichloromethane, prepared inside the glove box (O$_2$< 2ppm), was added a solution of 1eq. of Cu^{I}(CH$_3$CN)$_4$PF$_6$ prepared in the same solvent. The resulting yellow solution was stirring for 1h. Then, the solution was exposed to air and its color turned from yellow to green. Then, the complex was treated with NH$_4$OH 35%, washed with brine (x2) and dried it with Na$_2$SO$_4$. The conversion yield was estimated by ^{1}H NMR spectroscopy of the crude product. ^{18}O Labeled product was prepared using the same procedure but starting from ^{18}O$_2$ labeled dioxygen (99%).

General procedure of oxidation of Cu^{II} with O$_2$ in presence of benzoin/triethylamine

To a solution of Cu^{II} complex in degassed dichloromethane, prepared under argon, excess of benzoin was added changing the blue color to yellow. After 30 min of stirring, the solution mixture was exposed to air changing the color from yellow to green. Then, the complex was treated with NH$_4$OH 35%, washed with brine (x2) and dried it with Na$_2$SO$_4$. The conversion yield was estimated by ^{1}H NMR spectroscopy of the crude product. ^{18}O Labeled product was prepared using the same procedure but starting from ^{18}O$_2$ labeled dioxygen (99%).

General procedure of oxidation of Cu^I complexes by H₂O₂

General procedure of oxidation of Cu^{I} complexes by H$_2$O$_2$

To a solution of the IndPY$_2$ in 3mL of methanol, prepared inside the glove box (O$_2$< 2ppm), was added a solution of 1eq. of Cu^{I}(CH$_3$CN)$_4$PF$_6$ prepared in the same solvent and it was stirring for 1h. Then, 2 eq. of H$_2$O$_2$ 30%, was added in obtaining yellow solution of Cu^{I} complex which turned to blue and let stirring overnight. The complex was treated with NH$_4$OH 35%, washed with brine (x2) and dried it with Na$_2$SO$_4$. The conversion yield was estimated by ^{1}H NMR spectroscopy of the crude product.

General procedure of oxidation of Cu^{II} complexes by H$_2$O$_2$

To a solution of Cu^{II} complex either in methanol or in water pH 6.0 or at pH 8.5, 1 or 10 eq. of 30% H$_2$O$_2$ was added changing the blue color to yellow. The solution mixture was stirring overnight. Then, the complex was treated with NH$_4$OH 35%, washed with brine (X2) and dried it with Na$_2$SO$_4$. The conversion yield was estimated by ^{1}H NMR spectroscopy of the crude product. ^{18}O Labeled experiments were prepared using the same procedure but starting from ^{18}O labeled hydrogen peroxide H$_2$^{18}O$_2$ (90%).

General prodecure of oxidation of Cu^{I} complexes by Iodosylbenzene

To a solution of the IndPY$_2$ in 3mL of dichloromethane or in acetonitrile, prepared inside the glove box (O$_2$< 2ppm), was added a solution of 1eq. of Cu^{I}(CH$_3$CN)$_4$PF$_6$ prepared in the same solvent. The resulting yellow solution was stirring for 1h. After addition of 2 eq. of PhIO, the yellow color changed to green and it was stirring overnight. The solvent was evaporated in the rotary evaporator and the powder was washed with ether to remove any degradation products of PhIO. The complex was re-solubilized in 3mL DCM and the solution was treated with NH$_4$OH 35%, washed with brine (x2) and dried it with Na$_2$SO$_4$. The conversion yield was estimated by ^{1}H NMR spectroscopy of the crude product. ^{18}O Labeled product was prepared using the same procedure but starting from ^{18}O labeled PhI^{18}O.

General procedure of oxidation of Cu^{I} complexes by NaOCl

To a solution of the IndanePY$_2$ in 3mL of methanol, prepared inside the glove box (O$_2$< 2ppm), was added a solution of 1eq. of Cu^{I}(CH$_3$CN)$_4$PF$_6$ prepared in the same solvent and it was stirring for 1h. Then, 2 or 10 eq. of 10% concentrated NaOCl, was added in obtaining yellow solution of Cu^{I} complex which turned to green and let stirring overnight. The complex was treated with NH$_4$OH 35%, washed with brine (x2) and dried it with Na$_2$SO$_4$. The conversion yield was estimated by ^{1}H NMR spectroscopy of the crude product.

General procedure of oxidation of Cu^{II} complexes by NaOCl

To a solution of Cu^{II} complex in water pH 8.5, 2 or 10 eq. of 10% concentrated NaOCl was added changing the blue color to yellow. The solution mixture was stirring overnight. Then, the complex was treated with NH$_4$OH 35%, washed with brine (X2)

and dried it with Na_2SO_4. The conversion yield was estimated by ^{1}H NMR spectroscopy of the crude product.

Oxidation of p-nitrophenyl-β-D-glucopyranoside

Activity assays were performed in total volume of 300 μL placed in 96-well plates. Complexes **2b** was solubilized at concentration ranging from 0.01 to 0.6 mM in aqueous solutions (carbonate buffer 100 mM at pH 10.5). The substrate p-nitrophenyl-β-D-glucopyranoside was used at 20 mM concentration and hydrogen peroxide at 20 mM concentration. Controls were performed using the same conditions, but in the absence of complexes or hydrogen peroxide or the substrate alone in similar reaction conditions. Reaction mixtures were incubated at 30°C and were monitored by following the absorbance at 400 nm using a BioTek Synergy MX microplate reader. Initial velocities were extracted from the slopes during the first 10 minutes of reaction in carbonate buffer at pH 10.5. Quantification was performed measuring the absorbance at 400 nm (ε=18500 mol^{-1}Lcm^{-1}) and using calibration curves obtained with commercial p-nitrophenol placed at different pHs. When performed in water, the amount of p-nitrophenolate was determined at the end of the reaction after basification of the medium by addition of carbonate buffer at pH 10.5 to reach a final concentration of 100 mM.

Heterobimetallic Cu^{III}-Ni^{III} complexes

Exogenous substrate oxidation

In a typical experiment, 0.15mM to 0.2mM of **3a** (**3b**) was generated at -90°C, as discussed previously. The reactivity studies of **3a** (**3b**) were performed at -60°C under inert atmosphere, by injecting the CH_2Cl_2 solution of substrate (varying from 1mM to 60mM). Spectral changes at 885 nm band were monitored by a UV-Vis spectrum every 1 second. The pseudo-first order oxidation rate was then extracted and compared to the self-decay of **3a** (**3b**) in the absence of substrate. If the rate of oxidation in the presence of substrate was higher than that in the absence of substrate, it was concluded that **3a** (**3b**) reacted with that substrate. The pseudo-first order fitting of the decay curves yielded the rate constants (k_{obs}), which follow linear dependence with the concentration of the substrate. The slope of the rate constant (k_{obs}) versus substrate concentration fitting plot provided the second order rate constants (k_2).

Determination and quantitative analysis of oxidation of internal substrate.

The brownish solution of **3a** was warmed up at room temperature. The solution wastreated with 35% ammonia solution and after extraction with dichloromethane (×2) the organic phases were washed with brine (×2); the organic phases were collected, dried over $MgSO_4$ and the solvent was removed under vacuum. The resulting solid was

analysed by ^{1}H NMR spectroscopy and mass spectrometry which showed the absence of the hydroxylated product.

DFT Calculations mentioned in Chapter IV

All theoretical calculations were performed with the ORCA program package.[139] Full geometry optimizations were carried out for all complexes using the GGA functional BP86[182,183] in combination with the TZV/P[184] basis set for all atoms and by taking advantage of the resolution of the identity (RI) approximation in the Split-RI-J variant[167] with the appropriate Coulomb fitting sets.[168] Increased integration grids (Grid4 in ORCA convention) and tight SCF convergence criteria were used. Solvent effects were accounted within the framework of the conductor like screening (COSMO) dielectric continuum approach.[141] Vibrational frequency calculations were performed to ensure that each geometry optimization converged to a real minimum. IR and rRaman spectra were obtained from numerical frequency calculations performed on optimized structures using the B3LYP[140,166] functional together with the TZV/P[23] basis set. The relative energies were obtained from single-point calculations using the same combination of functional and basis sets. They were computed from the gas-phase optimized structures as a sum of electronic energy, thermal corrections to free energy, and free energy of solvation. g-tensors[185–188] were evaluated from additional single point calculations using the B3LYP functional. Scalar relativistic effects were included with ZORA paired using the SARC def2-TZVP(-f) basis sets[189,190] and the decontracted def2-TZVP/J Coulomb fitting basis sets for all atoms. Increased integration grids (Grid4 and GridX4 in ORCA convention) and tight SCF convergence criteria were used. Picture change effects were applied and the integration grids were increased to an integration accuracy of 11 (ORCA convention) for the metal centre. Natural charges were obtained from additional single-point calculations using the Natural Population Analysis (NPA) and the B3LYP functional together with the TZV/P basis set.[191] Molecular orbitals, spin density plots and vibrational normal modes were visualized with Chemcraft software.

Annex: Articles

PAPER

CrossMark
click for updates

Changing the chemical and physical properties of high valent heterobimetallic bis-(μ-oxido) Cu–Ni complexes by ligand effects†

Maria-Chrysanthi Kafentzi,[a] Maylis Orio,[a] Marius Réglier,[a] Shenglai Yao,[b] Uwe Kuhlmann,[b] Peter Hildebrandt,[b] Matthias Driess,*[b] A. Jalila Simaan*[a] and Kallol Ray*[c]

Two new heterobimetallic $[LNiO_2Cu(RPY2)]^+$ (RPY2 = N-substituted bis 2-pyridyl(ethylamine) ligands with R = indane, **3a** or R = Me, **3b**) complexes have been spectroscopically trapped at low temperatures. They were prepared by reacting the mononuclear side-on LNi^{II} superoxo precursor bearing a β-diketiminate ligand (L = $[HC-(CMeNC_6H_3(iPr)_2)_2]$) with the Cu(I) complexes. In contrast to the oxo groups in known high-valent $[M_2(μ-O)_2]^{n+}$ (M = Fe, Co, Ni, Cu) cores that display electrophilic reactivities, **3a** and **3b** display rather nucleophilic oxo cores active in aldehyde deformylation reactions. However, the spectroscopic and reactivity properties of **3a**/**3b** are found to be distinct relative to that of the previously reported $[LNiO_2$-$Cu(MeAN)]^+$ complex containing a more basic (nucleophilic) N,N,N′,N′,N′-pentamethyl-dipropylenetriamine (MeAN) ligand at the copper centre. The geometry and electronic properties of the copper ligands affect the electron density of the oxygen atoms of the heterodinuclear {Ni(μ-O)₂} core and **3a**/**3b** undergo slower nucleophilic and faster electrophilic reactions than the previously reported $[LNiO_2Cu(MeAN)]^+$ intermediate. The present study therefore demonstrates the tuning of the electrophilicity/nucleophilicity of the oxygen atoms of the heterobimetallic $[Ni(μ-O)_2Cu]^{2+}$ cores by controlling the electron donation from the ancillary ligands, and underlines the significance of subtle electronic changes in the physical and chemical properties of the biologically relevant heterobimetallic metal–dioxygen intermediates.

aAix Marseille Univ, CNRS, Centrale Marseille, iSm2, Marseille, France.
E-mail: jalila.simaan@univ-amu.fr
bDepartment of Chemistry, Technische Universität Berlin, Straße des 17. Juni 135, 10623 Berlin, Germany. E-mail: matthias.driess@tu-berlin.de
cDepartment of Chemistry, Humboldt-Universität zu Berlin, Brook-Taylor-Straße 2, 12489 Berlin, Germany. E-mail: kallol.ray@chemie.hu-berlin.de
†Electronic supplementary information (ESI) available. See DOI: 10.1039/c6dt02391f

Introduction

The synthesis and characterisation of metal–oxygen intermediates are very important for understanding the mechanisms of transition metal mediated dioxygen activation reactions taking place in chemical and biological systems. In this context homobimetallic bis(μ-oxido) complexes with $[M_2(μ-O)_2]^{n+}$ cores have attracted much attention and they have been extensively studied for systems involving Cu,[1] Mn,[2] Ni,[3] Co,[4] Fe,[5] and Pt centres.[6] In particular, homobimetallic copper dioxygen cores have been the subject of extensive investigations due to their possible involvement in biological oxidation reactions as key intermediates in phenol hydroxylation by tyrosinase,[7] as well

as in methane oxidation by particulate methane monooxygenase.[8]

In contrast to the homobimetallic systems, the properties of mixed-metal dioxygen species have been less explored. These types of intermediates are probably involved in various catalytic processes in metalloenzymes; for example, in cytochrome c oxidase, where a Cu^I ion cooperates with an Fe^{II}(heme) to activate dioxygen or in Cu–Zn superoxide dismutase, in which the superoxido ligand disproportionation is mediated through a mixed Cu–Zn metal site. The generation and the study of such mixed metal species are therefore of significant interest due to the unique properties obtained by the combination of two different metal ions. The synthesis of heterodinuclear complexes, however, presents a special challenge because of the possibility of disproportionation and selectivity problems resulting in the formation of mixtures of homo- and hetero-dinuclear complexes, as well as metal-site isomers. In order to overcome these problems two main strategies were previously used in the literature (Fig. 1).[9]

The first one involves the synthesis of ligands providing different coordination environments that are specific for each of the two metal ions. An alternative route is the reaction of a

Fig. 1 Two main strategies for the development of heterobimetallic metal–dioxygen complexes.

Scheme 1 A: Generation of the $[LNi^{III}O_2Cu^{III}(MeAN)]^+$ complex which is already reported.[17] B: Generation of $[LNi^{III}O_2Cu^{III}(RPY_2)]^+$ species **3a** (**3b**) upon mixing a solution of the LNi^{II} superoxo complex **2** with the (RPY$_2$) Cu^I complexes **1a** (or **1b**).

well-defined dioxygen metal subunit L_nM-O_2 with a low-valent metal complex fragment L'_mM'. This last strategy has been successfully used to generate heterobimetallic oxygen-containing species with PdMo,[10] CuNi,[11] CuGe,[12] PtCu[13] and CuPd[13] combinations, starting from well-defined metal–dioxygen precursors. Our contribution in the field involves the synthesis of a novel family of NiO$_2$M complexes generated by using a mononuclear *side-on* LNi^{II} superoxo precursor bearing a β-diketiminate (Nacnac) ligand (L = $[HC\text{-}(CMeNC_6H_3(iPr)_2)_2]$) system.[14] Notably, this precursor is remarkably stable and can be handled at room temperature, which made it a suitable precursor for the synthesis of heterobimetallic metal–dioxygen complexes. Interestingly, in our previous studies, the electronic structure of the $[NiO_2M]^{n+}$ core in such complexes was found to be dependent on the nature of the second metal ion, M; whereas a peroxido species[15] $[Ni(\mu\text{-}O_2)K]^{2+}$ was stabilized in the presence of potassium, replacement of the monovalent potassium ion by LZn$^+$ [15] (L = Nacnac) or LFe$^+$ [16] ions initiated peroxido O–O bond scission and subsequent H-atom abstraction to generate the heterobimetallic bis(μ-hydroxo) Ni–Zn or alkoxo hydroxido Ni–Fe species, respectively. Although the fleeting [LNiO$_2$ML] (M = Fe, Zn) could not be isolated, in a subsequent study a related $[LNiO_2Cu(MeAN)]^+$ species was stabilized at low temperature by reacting the [LNi^{II}O$_2$] precursor with a copper triamine $[Cu(MeAN)]^+$ reductant (Scheme 1A). Interestingly, the presence of Cu in the second metal binding site was shown to result in nucleophilic oxo groups in the high-valent bis-μ-oxido Ni–Cu species, and it was able to react towards aldehyde substrates, in contrast to the reported electrophilic properties of the homobimetallic NiO$_2$Ni, CuO$_2$Cu and heterobimetallic NiO$_2$Fe counterparts.[17] In the present manuscript we now try to systematically explore how the nature of the ancillary ligand can modulate the formation, structure, electronic properties and reactivity of such high-valent heterobimetallic dioxygen species. For this purpose, we report on the synthesis, spectroscopy, DFT derived description, and reactivity studies of two new bis-μ-oxido CuNi intermediates, where the triamine MeAN ligand at Cu is replaced by relatively weaker bases/nucleophiles in the bis 2-pyridyl(ethylamine) (RPY$_2$; R = methyl or indane) ligand systems. Notably, the RPY$_2$-type ligands have been previously utilised in the formation of binuclear Cu$_2^{II}$-peroxido complexes, which were shown to exist in equilibrium with the isomeric Cu$_2^{III}$(μ-oxido) species depending on the reaction con-

ditions.[1a] The side-on peroxido dicopper(II) intermediates exhibited electrophilic character towards C–H bond oxygenation of substrates.[1f,h,i] For example, on using an "indane" substrate covalently attached to the ligand (IndanePY$_2$, Scheme 1), intramolecular oxygen atom transfer was shown to take place in a highly regio- and stereo-selective manner leading to the *cis*-hydroxylated diastereoisomers of the ligand.[18] The successful generation of the $[LNiO_2Cu(RPY_2)]^+$ complexes now offers the opportunity to compare and contrast the reactivity of the present complexes with that of the previously reported heterodinuclear $[LNiO_2Cu(MeAN)]^+$ and homodinuclear $[\{Cu(RPY_2)\}_2O_2]^{2+}$ complexes.
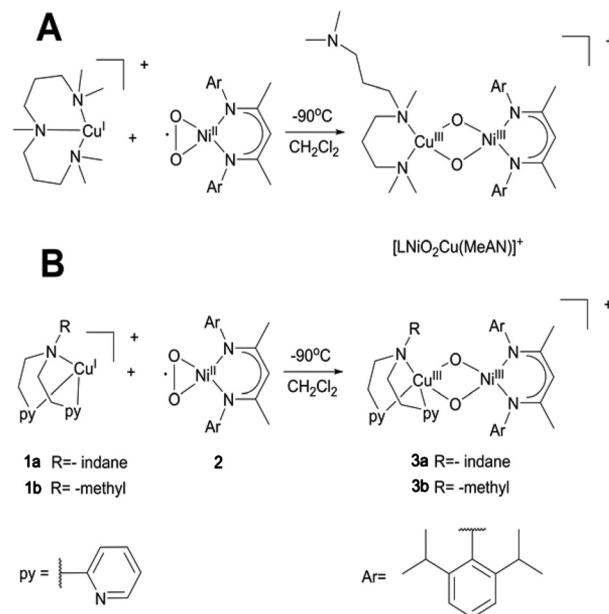
Results and discussion

Synthesis and UV-Vis spectroscopy

The complexes **1a** and **1b** were prepared by mixing one molar eq. of Cu^I(CH$_3$CN)$_4$(OTf) with one molar eq. of ligand in dichloromethane. Equimolar amounts of **1a** {(IndanePY$_2$) Cu^I(OTf)} or **1b** {(CH$_3$PY$_2$)Cu^I(OTf)} and **2** were then mixed at −90 °C in dry dichloromethane leading to the immediate formation of the brownish intermediates **3a** {[IndanePY$_2$]Cu(O$_2$) Ni[C-(CMeNC$_6$H$_3$(iPr)$_2$)$_2$](OTf)} and **3b** {[CH$_3$PY$_2$]Cu(O$_2$)Ni[C-(CMeNC$_6$H$_3$(iPr)$_2$)$_2$](OTf)}, respectively (Scheme 1B). The generation of these species was monitored by UV-Vis spectroscopy following the appearance of a characteristic absorption band centred at 885 nm for **3a** and 870 nm for **3b** (Fig. 2). The intermediates are stable at −90 °C, but they are thermally sensitive, as indicated by bleaching of their UV-Vis absorption features
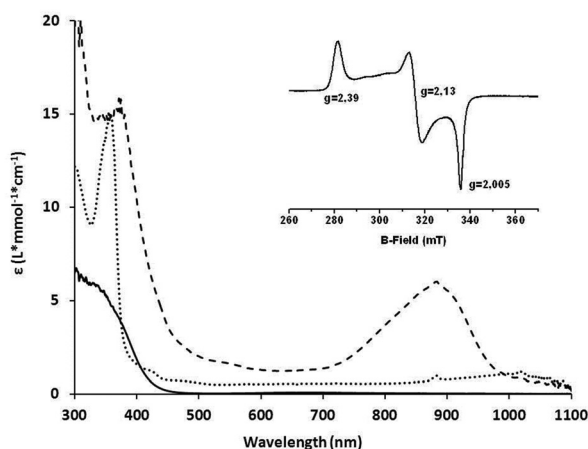
Fig. 2 Absorption spectra of the Cu^I complex (solid trace) **1a**, Ni^{II} superoxo complex **2** (dotted trace) and the 0.15 mM $[Ni^{III}(\mu\text{-}O_2)Cu^{III}]^+$ species **3a** (dashed trace) in dichloromethane at −90 °C. Inset: X-band EPR spectrum of **3a** in dichloromethane at 77 K.

Fig. 3 Raman shifts obtained using a 413 excitation laser for **3a** involving ^{16}O (top) and ^{18}O (bottom) atoms. Bands originated from the solvent are marked by asterisks.

upon warming to higher temperatures (see the ESI†) with $t_{1/2}$ = 2000 s at −60 °C.

EPR spectroscopy

The EPR spectra were recorded in frozen CH_2Cl_2 solutions (77 K) for **3a** and **3b** and are very similar for both complexes. The EPR spectrum obtained in the case of **3a** is presented in Fig. 2. The spectra are composed of typical S = 1/2 rhombic signals with g_1 = 2.39, g_2 = 2.13, and g_3 = 2.005 for **3a** and g_1 = 2.39, g_2 = 2.13, and g_3 = 2.006 for **3b**. These EPR signals are very similar to the one reported previously for the $[LNiO_2Cu(MeAN)]^+$ complex.[17] Notably, no interaction of the electron spin with the nuclear spin of copper is observed for both **3a**/**3b**, consistent with their $Ni^{III}(\mu\text{-}O)_2Cu^{III}$ assignment, in agreement with the data previously reported in the literature for the Cu–Ni analog.[17]

Resonance Raman spectroscopy

The resonance Raman (rRaman) spectra of **3a** and **3b** were recorded using 413 nm laser excitation. rRaman bands are detected at 605 cm^{-1} and 612 cm^{-1} for **3a** and **3b**, respectively (Fig. 3, ESI†), which are sensitive to ^{18}O substitution (performed by using $Ni^{18}O_2$ as a starting reagent) and downshift ($\Delta^{18}O$) by 31 cm^{-1} and 29 cm^{-1}, respectively. Notably, these bands are shifted to lower energies relative to the tetra-atomic vibrational mode of the $[LNi(\mu\text{-}O_2)Cu(MeAN)]^+$ complex observed at 625 cm^{-1}.[17] Furthermore, as previously observed, the absence of any isotope sensitive bands in the 700–1200 cm^{-1} region excludes the possibility of the presence of peroxo or superoxo units in **3a** or **3b**. Interestingly, a second ^{18}O sensitive band is also detected at 556 cm^{-1} ($\Delta^{18}O$ = −21 cm^{-1}) and 579 cm^{-1} ($\Delta^{18}O$ = −19 cm^{-1}) for **3a** and **3b** respectively, which was not observed in the previously reported spectrum of the $[LNiO_2Cu(MeAN)]^+$ complex.

DFT calculations

DFT calculations were performed on **3a** and **3b** in an effort to understand their structural and electronic properties as well as the origin of the additional ^{18}O sensitive band in the rRaman spectra. DFT-optimised structures revealed a four-coordinate distorted square-planar geometry around the nickel centre. Two conformations around the copper ion were computed for each system (conformers A and B). In all cases, the copper site is in a five-coordinate square pyramidal geometry but with either the amine group (conformer A) or one pyridine group (conformer B) weakly bonded to the metal ion in the axial position. Energetic analysis conducted on both **3a** and **3b** showed that the minimum free energy is obtained for the conformers (A) which make these structures the most favoured one (see Table S3; ESI†). The computed structures for **3a** and **3b** (conformers A and B) are presented in Fig. 4, S11 and S12.†

Both spin density plots and Singly Occupied Molecular Orbitals (SOMO) reveal that **3a** and **3b** bear one unpaired electron located at the nickel centre (see Fig. S13 and S14; ESI†). These results confirm the presence of one low-spin Ni^{III} centre (S = 1/2, $3d^7$) and one low-spin Cu^{III} (S = 0, $3d^8$) centre in both **3a** and **3b**. This assignment is further confirmed by the computed EPR parameters, which are in fair agreement with the experimental data (see Table S4; ESI†). Frequency calculations were conducted on the DFT-optimised structures of the two species and Raman spectra were calculated. Vibration modes involving the oxygen ligands were predicted at 596 cm^{-1} and 621 cm^{-1} for **3a** and **3b** (Fig. S15 and S16; Table S5†), respectively, in agreement with the assignment previously proposed for the MeAN-based Cu–Ni analog.[17] A second mode was calculated to be at 553 cm^{-1} and 528 cm^{-1} for **3a** and **3b**, respectively, originating from the coupling of the $Ni(\mu\text{-}O_2)Cu$ core and the Ni-coordinated β-diketiminate ligand coordinates (see Fig. S17 and S18; ESI†). Both sets of the calculated results are in good agreement with the observed rRaman bands for each complex (Table S5; ESI†). The five-coordination geometry at the Cu ions obtained in the case of RPY_2-type ligands is
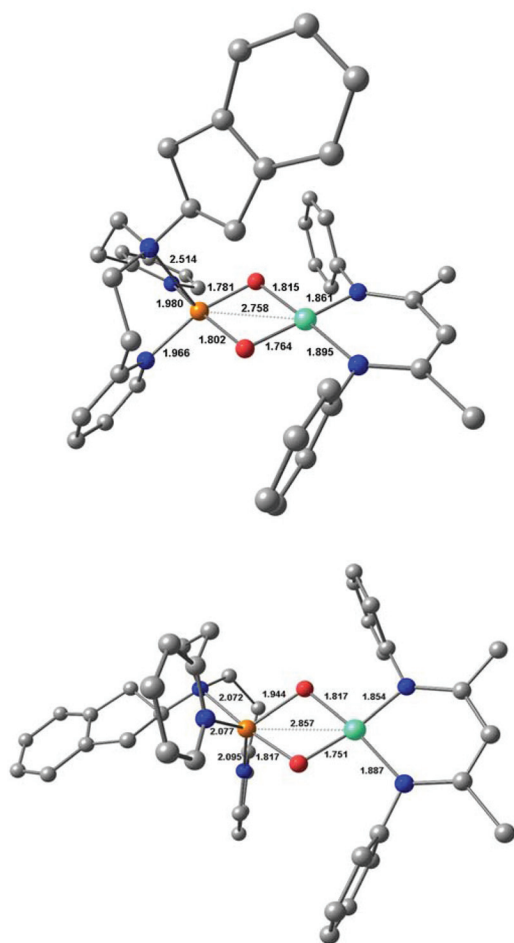
Fig. 4 Optimised molecular structures for **3a**; conformers A (top) and B (bottom).

affecting the coordination sphere of the Ni ion in **3a** and **3b** and the geometry around the Ni ion appears to be significantly distorted from planarity (dihedral angle of 11.2 and 16.2°, respectively) while it is perfectly planar in the MeAN-based complex (dihedral angle of 2.3°). This explains the appearance of a new vibration in the rR spectra of **3a/3b**. The spectroscopic data thus support the DFT-calculated structure and validate the formation of both **3a** and **3b**.

Reactivity studies

The reactivity of the complexes **3a** and **3b** has been investigated in a number of nucleophilic and electrophilic reactions. The nucleophilicity of **3a** and **3b** has been studied in reactions with benzaldehyde, and cyclohexane carboxaldehyde (CCA). The ability of **3a** (**3b**) to undergo electrophilic Hydrogen Atom Transfer (HAT) reactions was also evaluated in reactions with 9,10-dihydroanthracene (DHA) and 1,3-cyclohexadiene (CHD) for C–H bonds and with 2,4-di-*tert*-butylphenol (2,4-DTBP) and 2,6-di-*tert*-butylphenol (2,6-DTBP) for O–H bonds. In a typical reaction preformed **3a** and **3b** at −60 °C were treated with an

excess of the above-mentioned substrates under a pseudo first-order condition.

The disappearance of the characteristic band at 885 nm in the UV-Vis absorption spectrum was then monitored over time (Fig. 5 for reaction of **3a** with CCA). Rate constants in CH_2Cl_2 at −60 °C or at −90 °C were obtained from the pseudo-first order fit of the time trace of the decay of the 885 nm band (Fig. 5). Second-order rate constants were then determined from the dependence of the first-order rate constants on the substrate concentration (Fig. 6). Second-order rate constants derived from those studies are listed in Table 1 and compared with that of the results obtained for the previously reported $[LNiO_2Cu(MeAN)]^+$ intermediate. Notably, complex **3b** reacts with CCA and benzaldehyde at rates significantly slower than $[LNiO_2Cu(MeAN)]^+$.

In contrast, in the presence of DHA, CHD, 2,4-DTBP, or 2,6-DTBP, complex **3b** is found to be a better oxidant than $[LNiO_2Cu(MeAN)]^+$. These studies point to the presence of less nucleophilic oxygen atoms in **3b** relative to $[LNiO_2Cu(MeAN)]^+$. Notably, replacement of the methyl group of the $MePy_2$ ligand in **3b** with a bulkier indane group in **3a** did not lead to any significant change in the rate constants for the reactions with
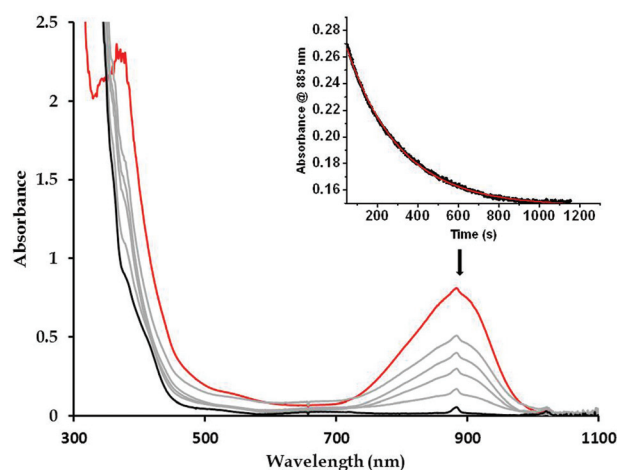
Fig. 5 Spectral changes of **3a** in the presence of 50 mM CCA at −60 °C. Inset: Time trace of the decay at 885 nm band upon addition of the substrate (black trace) and the first-order fit (inset: red trace).
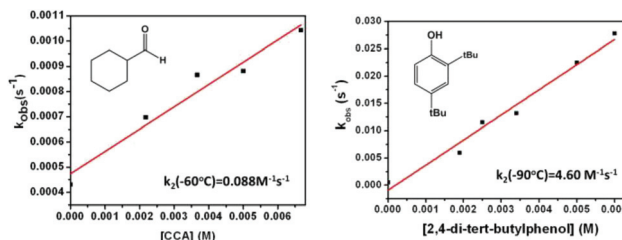
Fig. 6 Pseudo first-order rate constants as a function of substrate concentration; the reaction of **3a** with cyclohexane carboxaldehyde (left) and 2,4 di-*tert*-butylphenol (right) in CH_2Cl_2.

Table 1 Second order rate constants determined for different substrates by kinetic studies by UV-Vis spectroscopy

Substrates	Benzaldehyde (−60 °C)	CCA (−60 °C)	DHA (−60 °C)	CHD (−60 °C)	2,4 DTBP (−90 °C)	2,6 DTBP (−60 °C)
3a k_2/M^{-1} s^{-1}	0.021	0.088	0.015	0.053	4.60	0.0065
3b k_2/M^{-1} s^{-1}	0.0178	0.557	0.015	0.014	Too fast	0.0985
LNi^{III}[(μ-oxo)Cu^{III}(MeAN)]$^+$ k_2/M^{-1} s^{-1}	0.11 (−50 °C)	Too fast (−90 °C)	Too slow (−70 °C)	0.0005 (−70 °C)	2.44 (−90 °C)	0.0001 (−80 °C)

DHA and benzaldehyde. However, for reactions with bulkier substrates like 2,6-DTBP, 2,4-DTBP, or CCA, a significantly reduced rate constant is observed for **3a** relative to **3b**. This may be attributed to the sterically induced hindered access of the substrates in the presence of the covalently attached indane group of the IndanePY₂ ligand in **3a**. Analysis of the resultant solution after reactions of **3a** or **3b** with various substrates showed the formation of the oxidised products in 45–70% yields (Table S1; ESI†). Interestingly, for reactions with **3a** no evidence of the hydroxylation of the indane moiety was observed, which is in contrast to the previous report of the intramolecular indane hydroxylation reaction mediated by the homodinuclear copper–oxygen intermediate.[18]

Additional DFT calculations were performed in order to further characterise the reactivity differences. Natural population analysis was performed for **3a**/**3b** and the results were compared with those obtained for [LNi^{III}O₂Cu^{III}(MeAN)]$^+$ (see the ESI†). The natural negative charges found at the O atoms are smaller (by −7% to −8%) in **3a** and **3b** with respect to those of the corresponding atoms in [LNi^{III}O₂Cu^{III}(MeAN)]$^+$. These data indicate that the oxido cores in **3a** and **3b** are less electron-rich compared to that of [LNi^{III}O₂Cu^{III}(MeAN)]$^+$. It thus correlates with the decreased nucleophilicity presently observed.

Conclusions

Examples of heterobimetallic dioxygen intermediates are extremely rare in the literature and hence, very little is known about their reactivity. This is unfortunate, as metal dioxygen cores involving non-equivalent metal-sites have been proposed as the active species in a number of biological and chemical oxidation processes, and a detailed knowledge about their reactivity can provide vital mechanistic insights. In our continuous effort to uncover structure–reactivity relationships of unprecedented dinuclear metal–dioxygen intermediates we now investigate the role of ancillary ligands in controlling the spectroscopic and reactivity properties of a heterobimetallic [Ni(μ-O)₂Cu]$^+$ core. The first (and only example before this study of such a core) has been spectroscopically identified in our groups and previously shown to possess a nucleophilic oxo group that led to the deformylation of aldehydes. We now show that the nucleophilicity of the oxo groups can be tuned by varying the electron donation of the ancillary ligand at the copper centre. Thus replacement of the MeAN ligand in the

previously reported [LNi(μ-O₂)Cu(MeAN)]$^+$ complex by less basic/nucleophilic RPY₂ ligands in **3a**/**3b** led to slower nucleophilic and faster electrophilic reactions in the latter. Based on the DFT calculations, the difference in reactivity has been attributed to the presence of a five coordinate copper centre and a significant distortion of the nickel centre from planarity in **3a**/**3b**. These result in the development of lower negative charges at the oxygen atoms of **3a**/**3b** relative to the [LNi(μ-O₂)Cu(MeAN)]$^+$ complex, where a four coordinate square planar structure has been reported to be prevalent at both the Cu and Ni centres. Furthermore, for reactions with **3a** no hydroxylation of the indane moiety occurred, in contrast to the previous report of the intramolecular indane hydroxylation reaction mediated by the homodinuclear {(indane-py₂)CuO₂Cu(indane-py₂)} complex. This again emphasizes the initiation of novel reactivity properties in heterodinuclear systems relative to their homobimetallic counterparts. The present results therefore underline the significance of subtle geometric and electronic changes in the physical and chemical properties of this important class of biologically relevant metal–dioxygen intermediates.

Experimental

All chemicals used in this study except for the ligands and the complexes were commercial products of the highest available purity. Commercial starting materials were used without further purification, except for 2-vinylpyridine which was distilled prior to use. Preparation and handling of air sensitive materials were performed in a N₂ glove box OMNI-Lab 2 (VAC) with O₂ and moisture concentrations less than 2 ppm. ^{1}H NMR spectra were recorded on a Bruker Avance III 300 MHz NMR spectrometer. UV-Vis spectra were recorded by using an Agilent 8453 diode array spectrophotometer from 300–1100 nm with samples in a 1.0 path length quartz cuvette, connected with a cryostat from Unisoku Scientific Instruments, Japan.

Synthetic procedures

General procedure of synthesis of ligands

CH₃PY2. The ligand has been synthesized in a slightly different way from the already reported procedure.[1g] To absolute MeOH (80 mL) were added 2-vinylpyridine (11 g, 0.210 mol), 2-(2-methylaminoethyl) pyridine (4.2 g, 0.030 mol), and glacial acetic acid (1.8 g, 0.060 mol). After refluxing for 5 days under argon, MeOH was evaporated and 15% NaOH was

added. The product was extracted with CH_2Cl_2 (×3) and the combined organic layers were dried over Na_2SO_4. Evaporation of CH_2Cl_2 under reduced pressure left the crude product. Flash chromatography (neutral alumina, ethylacetate/MeOH, 98 : 2) afforded the ligand as a yellow product (yield: 40%).

IndanePY2. The ligand has been synthesized according to the already reported procedure.[18a]

General procedure of the synthesis of complexes

The complexes **1a** and **1b** have been synthesized *in situ* by the dropwise addition of a solution of 1 eq. $Cu^I(CH_3CN)_4OTf$ in anhydrous dichloromethane in a solution of 1 eq. dissolved ligand in the same solvent.

General procedure for the synthesis of [LNi^{III}(O$_2$)Cu^{III}(RPY2)]

The greenish solution of **2** in anhydrous CH_2Cl_2 (2.5 mL; 0.15 mM) was cooled to −90 °C. Then 1 equivalent of **1a** (**1b**) in anhydrous CH_2Cl_2 (0.1 mL) was added to yield the deep brown intermediate **3a** (**3b**). The generation of the deep brown species **3a** (**3b**) was monitored by the growth of the 885 nm band in the UV/vis spectrum. ^{18}O labelled samples for rRaman experiments were prepared using the same procedure but starting from ^{18}O labelled Ni precursor **2**.

EPR spectroscopy

EPR measurements were performed on a Bruker ESP 300 X-band EPR spectrometer equipped with a fused quartz Dewar for measurements at liquid nitrogen temperature.

Resonance Raman

rRaman spectra were recorded in CH_2Cl_2 at −92 °C (Bruker cryostat) using 413 nm excitation with a Horiba Jobin-Yvon LabRAM HR800 confocal Raman spectrometer. The concentrations of samples were from 3 mM to 8 mM.

DFT calculations

All theoretical calculations were performed with the ORCA program package.[19] Full geometry optimizations were carried out for all complexes using the GGA functional BP86[20–22] in combination with the TZV/P[23] basis set for all atoms and by taking advantage of the resolution of the identity (RI) approximation in the Split-RI-J variant[24] with the appropriate Coulomb fitting sets.[25] Increased integration grids (Grid4 in ORCA convention) and tight SCF convergence criteria were used. Solvent effects were accounted within the framework of the conductor like screening model (COSMO) which is a dielectric continuum approach.[26] Vibrational frequency calculations were performed to ensure that each geometry optimization converged to a real minimum. IR and rRaman spectra were obtained from numerical frequency calculations performed on the optimised structures using the B3LYP[27,28] functional together with the TZV/P[23] basis set. The relative energies were obtained from single-point calculations using the same combination of functional and basis sets. They were computed from the gas-phase optimised structures as a sum of electronic energy, thermal corrections to free energy, and free energy of solvation. *g*-Tensors[29–32] were evaluated from additional single point calculations using the B3LYP functional. Scalar relativistic effects were included with ZORA paired using the SARC def2-TZVP(-f) basis sets[33,34] and the decontracted def2-TZVP/J Coulomb fitting basis sets for all atoms. Increased integration grids (Grid4 and GridX4 in ORCA convention) and tight SCF convergence criteria were used. Picture change effects were applied and the integration grids were increased to an integration accuracy of 11 (ORCA convention) for the metal centre. Natural charges were obtained from additional single-point calculations using the Natural Population Analysis (NPA) and the B3LYP functional together with the TZV/P basis set.[35] Molecular orbitals, spin density plots and vibrational normal modes were visualized with Chemcraft software.[36]

Reactivity studies

Exogenous substrate oxidation. In a typical experiment, 0.15 mM to 0.2 mM of **3a** (**3b**) was generated at −90 °C, as discussed previously. The reactivity studies of **3a** (**3b**) were performed at −60 °C under an inert atmosphere, by injecting the CH_2Cl_2 solution of the substrate (varying from 1 mM to 60 mM). Spectral changes at the 885 nm band were monitored by using a UV-Vis spectrum every 1 second. The pseudo-first order oxidation rate was then extracted and compared with the self decay of **3a** (**3b**) in the absence of the substrate. If the rate of oxidation in the presence of the substrate was higher than that in the absence of the substrate, it was concluded that **3a** (**3b**) reacted with that substrate. The pseudo-first order fitting of the decay curves yielded the rate constants (k_{obs}), which follow linear dependence with the concentration of the substrate. The slope of the rate constant (k_{obs}) *versus* substrate concentration fitting plot provided the second order rate constants (k_2).

Intramolecular ligand oxidation. The brownish solution of **3a** was warmed up at room temperature. The solution was treated with 35% ammonia solution and after extraction with dichloromethane (×2) the organic phases were washed with brine (×2); the organic phases were collected, dried over $MgSO_4$ and the solvent was removed under vacuum. The resulting solid was analysed by ^1H NMR spectroscopy and mass spectrometry which showed the absence of the hydroxylated product.

Acknowledgements

Notes and references

1 (a) L. M. Mirica, X. Ottenwaelder and T. D. P. Stack, *Chem. Rev.*, 2004, **104**, 1013–1046; (b) E. A. Lewis and W. B. Tolman, *Chem. Rev.*, 2004, **104**, 1047–1076; (c) T. Osako, S. Terada, T. Tosha, S. Nagatomo, H. Furutachi, S. Fujinami, T. Kitagawa, M. Suzukib and S. Itoh, *Dalton Trans.*, 2005, 3514–3521; (d) L. Hatcher and K. D. Karlin, *J. Biol. Inorg. Chem.*, 2004, **9**, 669–683; (e) M. Schatz, M. Becker, F. Thaler, F. Hampel, S. Schindler, R. R. Jacobson, Z. Tyeklár, N. N. Murthy, P. Ghosh, Q. Chen, J. Zubieta and K. D. Karlin, *Inorg. Chem.*, 2001, **40**, 2312–2322; (f) H. V. Obias, Y. Lin, N. N. Murthy, E. Pidcock, E. I. Solomon, M. Ralle, N. J. Blackburn, Y.-M. Neuhold, A. D. Zuberbühler and K. D. Karlin, *J. Am. Chem. Soc.*, 1998, **120**, 12960–12961; (g) I. Sanyal, M. Mahroof-Tahir, M. S. Nasir, P. Ghosh, B. I. Cohen, Y. Gultneh, R. W. Cruse, A. Farooq and K. D. Karlin, *Inorg. Chem.*, 1992, **31**, 4322–4332; (h) C. Xin Zhang, H.-C. Liang, E.-i. Kim, J. Shearer, M. E. Helton, E. Kim, S. Kaderli, C. D. Incarvito, A. D. Zuberbühler, A. L. Rheingold and K. D. Karlin, *J. Am. Chem. Soc.*, 2003, **125**, 634–635; (i) J. Shearer, C. Xin Zhang, L. N. Zakharov, A. L. Rheingold and K. D. Karlin, *J. Am. Chem. Soc.*, 2005, **127**, 5469–5483.

2 (a) R. Manchanda, G. W. Brudvig and R. H. Crabtree, *Coord. Chem. Rev.*, 1995, **144**, 1–38; (b) A. J. Wu, J. E. Penner-Hahn and V. L. Pecoraro, *Chem. Rev.*, 2004, **104**, 903–938.

3 (a) R. Schenker, B. S. Mandimutsira, C. G. Riordan and T. C. Brunold, *J. Am. Chem. Soc.*, 2002, **124**, 13842–13855; (b) K. Shiren, S. Ogo, S. Fujinami, H. Hayashi, M. Suzuki, A. Uehara, Y. Watanabe and Y. Moro-oka, *J. Am. Chem. Soc.*, 2000, **122**, 254–262; (c) S. Itoh, H. Bandoh, M. Nakagawa, S. Nagatomo, T. Kitagawa, K. D. Karlin and S. Fukuzumi, *J. Am. Chem. Soc.*, 2001, **123**, 11168–11178.

4 (a) S. Hikichi, M. Yoshizawa, Y. Sasakura, M. Akita and Y. Moro-oka, *J. Am. Chem. Soc.*, 1998, **120**, 10567–10568; (b) S. Hikichi, M. Yoshizawa, Y. Sasakura, H. Komatsuzaki, Y. Moro-oka and M. Akita, *Chem. – Eur. J.*, 2001, **7**, 5011–5028.

5 A. J. Skulan, M. A. Hanson, H. Hsu, L. Que Jr. and E. I. Solomon, *J. Am. Chem. Soc.*, 2003, **125**, 7344–7356.

6 (a) P. R. Sharp, *J. Chem. Soc., Dalton Trans.*, 2000, 2647–2657; (b) J. J. Li, W. Li and P. R. Sharp, *Inorg. Chem.*, 1996, **35**, 604–613.

7 H. Decker, R. Dillinger and F. Tuczek, *Angew. Chem., Int. Ed.*, 2000, **39**, 1591–1595.

8 R. L. Lieberman and A. C. Rosenzweig, *Dalton Trans.*, 2005, 3390–3396.

9 I. Garcia-Bosch, X. Ribas and M. Costas, *Eur. J. Inorg. Chem.*, 2012, 179–187.

10 P. L. Alsters, J. Boersma and G. van Koten, *Organometallics*, 1993, **12**, 1629–1638.

11 N. W. Aboelella, J. T. York, A. M. Reynolds, K. Fujita, C. R. Kinsinger, C. J. Cramer, C. G. Riordan and W. B. Tolman, *Chem. Commun.*, 2004, 1716–1717.

12 J. T. York, V. G. Young Jr. and W. B. Tolman, *Inorg. Chem.*, 2006, **45**, 4191–4198.

13 J. T. York, A. Llobet, C. J. Cramer and W. B. Tolman, *J. Am. Chem. Soc.*, 2007, **129**, 7990–7999.

14 S. Yao, E. Bill, C. Milsmann, K. Wieghardt and M. Driess, *Angew. Chem., Int. Ed.*, 2008, **47**, 7110–7113.

15 S. Yao, Y. Xiong, M. Vogt, H. Grützmacher, C. Herwig, M. C. Limberg and M. Driess, *Angew. Chem., Int. Ed.*, 2009, **48**, 8107–8110.

16 S. Yao, C. Herwig, Y. Xiong, A. Company, E. Bill, C. Limberg and M. Driess, *Angew. Chem., Int. Ed.*, 2010, **39**, 7208–7212.

17 S. Kundu, F. F. Pfaff, E. Miceli, I. Zaharieva, C. Herwig, S. Yao, E. R. Farquhar, U. Kuhlmann, E. Bill, P. Hildebrandt, H. Dau, M. Driess, C. Limberg and K. Ray, *Angew. Chem., Int. Ed.*, 2013, **52**, 5622–5626.

18 (a) I. Blain, P. Bruno, M. Giorgi, E. Lojou, D. Lexa and M. Réglier, *Eur. J. Inorg. Chem.*, 1998, 1297–1304; (b) I. Blain, M. Giorgi, I. De Riggi and M. Réglier, *Eur. J. Inorg. Chem.*, 2000, 393–398; (c) I. Blain, M. Giorgi, I. De Riggi and M. Réglier, *Eur. J. Inorg. Chem.*, 2001, 205–211.

19 F. Neese, *Wiley Interdiscip. Rev.: Comput. Mol. Sci.*, 2012, **2**, 73–78.

20 J. P. Perdew, *Phys. Rev. B: Condens. Matter*, 1986, **33**, 8822.

21 J. P. Perdew, *Phys. Rev. B: Condens. Matter*, 1986, **34**, 7406.

22 A. D. Becke, *Phys. Rev. A*, 1988, **38**, 3098–3100.

23 A. Schäfer, C. Huber and R. J. Ahlrichs, *J. Chem. Phys.*, 1994, **100**, 5829–5835.

24 F. Neese, *J. Comput. Chem.*, 2003, **24**, 1740–1747.

25 F. Weigend, *Phys. Chem. Chem. Phys.*, 2006, **8**, 1057–1065.

26 A. Klamt and G. Schüürmann, *J. Chem. Soc., Perkin Trans. 2*, 1993, 799–805.

27 A. D. Becke, *J. Chem. Phys.*, 1993, **98**, 1372.

28 C. T. Lee, W. T. Yang and R. G. Parr, *Phys. Rev. B: Condens. Matter*, 1988, **37**, 785–789.

29 F. Neese, *J. Chem. Phys.*, 2001, **115**, 11080–11096.

30 S. Koseki, M. W. Schmidt and M. S. Gordon, *J. Chem. Phys.*, 1992, **96**, 10768–10772.

31 S. Koseki, M. S. Gordon, M. W. Schmidt and N. J. Matsunaga, *J. Chem. Phys.*, 1995, **99**, 12764–12772.

32 F. Neese, *J. Chem. Phys.*, 2003, **118**, 3939.

33 D. A. Pantazis, X.-Y. Chen, C. R. Landis and F. Neese, *J. Chem. Theory Comput.*, 2008, **4**, 908–919.

34 D. A. Pantazis and F. Neese, *J. Chem. Theory Comput.*, 2009, **5**, 2229–2238.

35 A. E. Reed, R. B. Weinstock and F. Weinhold, *J. Chem. Phys.*, 1985, **83**, 735–746.

36 Chemcraft, http://chemcraftprog.com.

List of Figures

153

List of Schemes

List of Tables

References

1. Festa, R. A. & Thiele, D. J. Copper: An essential metal in biology. *Curr. Biol.* **21,** R877–R883 (2011).
2. Solomon, E. I., Sundaram, U. M. & Machonkin, T. E. Multicopper oxidases and oxygenases. *Chem. Rev.* **96,** 2563–2606 (1996).
3. Mirica, L. M., Ottenwaelder, X. & Stack, T. D. P. Structure and Spectroscopy of Copper−Dioxygen Complexes. *Chem. Rev.* **104,** 1013–1046 (2004).
4. Solomon, E. I. *et al.* Copper Active Sites in Biology. *Chem. Rev.* **114,** 3659–3853 (2014).
5. *Bioinorganic Chemistry of Copper*. (Springer Netherlands, 1993).
6. Kitajima, N. *et al.* A new model for dioxygen binding in hemocyanin. Synthesis, characterization, and molecular structure of the. mu.-. eta. 2:. eta. 2 peroxo dinuclear copper (II) complexes,[Cu (HB (3, 5-R2pz) 3)] 2 (O2)(R= isopropyl and Ph). *J. Am. Chem. Soc.* **114,** 1277–1291 (1992).
7. Kitajima, N., Fujisawa, K., Morooka, Y. & Toriumi, K. . mu.-. eta. 2:. eta. 2-Peroxo binuclear copper complex,[Cu (HB (3, 5-(Me2CH) 2pz) 3)] 2 (O2). *J. Am. Chem. Soc.* **111,** 8975–8976 (1989).
8. Itoh, S. *et al.* Oxygenation of phenols to catechols by a (μ-η2: η2-peroxo) dicopper (II) complex: mechanistic insight into the phenolase activity of tyrosinase. *J. Am. Chem. Soc.* **123,** 6708–6709 (2001).
9. Matoba, Y., Kumagai, T., Yamamoto, A., Yoshitsu, H. & Sugiyama, M. Crystallographic Evidence That the Dinuclear Copper Center of Tyrosinase Is Flexible during Catalysis. *J. Biol. Chem.* **281,** 8981–8990 (2006).
10. Klinman, J. P. The Copper-Enzyme Family of Dopamine -Monooxygenase and Peptidylglycine -Hydroxylating Monooxygenase: Resolving the Chemical Pathway for Substrate Hydroxylation. *J. Biol. Chem.* **281,** 3013–3016 (2006).
11. *Copper-oxygen chemistry*. (Wiley, 2011).
12. Skotland, T. & Ljones, T. Direct spectrophotometric detection of ascorbate free radical formed by dopamine β-monooxygenase and by ascorbate oxidase. *Biochim. Biophys. Acta BBA-Gen. Subj.* **630,** 30–35 (1980).
13. Ljones, T. & Flatmark, T. Dophamine β-Hhydroxylase: Evidence against a ping-pong mechanism. *FEBS Lett.* **49,** 49–52 (1974).
14. Stewart, L. C. & Klinman, J. P. Characterization of alternate reductant binding and electron transfer in the dopamine. beta.-monooxygenase reaction. *Biochemistry (Mosc.)* **26,** 5302–5309 (1987).
15. Ash, D. E., Papadopoulos, N. J., Colombo, G. & Villafranca, J. J. Kinetic and spectroscopic studies of the interaction of copper with dopamine beta-hydroxylase. *J. Biol. Chem.* **259,** 3395–3398 (1984).
16. McCracken, J., Desai, P. R., Papadopoulos, N. J., Villafranca, J. J. & Peisach, J. Electron spin-echo studies of the copper(II) binding sites in dopamine .beta.-hydroxylase. *Biochemistry (Mosc.)* **27,** 4133–4137 (1988).
17. Brenner, M. C. & Klinman, J. P. Correlation of copper valency with product formation in single turnovers of dopamine .beta.-monooxygenase. *Biochemistry (Mosc.)* **28,** 4664–4670 (1989).
18. Blackburn, N. J., Pettingill, T. M., Seagraves, K. S. & Shigeta, R. T. Characterization of a carbon monoxide complex of reduced dopamine beta-hydroxylase. Evidence for inequivalence of the Cu (I) centers. *J. Biol. Chem.* **265,** 15383–15386 (1990).
19. Prigge, S. T. Amidation of Bioactive Peptides: The Structure of Peptidylglycine -Hydroxylating Monooxygenase. *Science* **278,** 1300–1305 (1997).
20. Prigge, S. T., Kolhekar, A. S., Eipper, B. A., Mains, R. E. & Amzel, L. M. Substrate-mediated electron transfer in peptidylglycine α-hydroxylating monooxygenase. *Nat. Struct. Mol. Biol.* **6,** 976–983 (1999).
21. Rosenzweig, A. C. & Sazinsky, M. H. Structural insights into dioxygen-activating copper enzymes. *Curr. Opin. Struct. Biol.* **16,** 729–735 (2006).
22. Prigge, S. T. Dioxygen Binds End-On to Mononuclear Copper in a Precatalytic Enzyme Complex. *Science* **304,** 864–867 (2004).

23. Evans, J. P., Ahn, K. & Klinman, J. P. Evidence That Dioxygen and Substrate Activation Are Tightly Coupled in Dopamine -Monooxygenase: IMPLICATIONS FOR THE REACTIVE OXYGEN SPECIES. *J. Biol. Chem.* **278,** 49691–49698 (2003).

24. Vendelboe, T. V. *et al.* The crystal structure of human dopamine -hydroxylase at 2.9 A resolution. *Sci. Adv.* **2,** e1500980–e1500980 (2016).

25. Hanson, R. S. & Hanson, T. E. Methanotrophic bacteria. *Microbiol. Rev.* **60,** 439–471 (1996).

26. Sirajuddin, S. & Rosenzweig, A. C. Enzymatic Oxidation of Methane. *Biochemistry (Mosc.)* **54,** 2283–2294 (2015).

27. Phelps, P. A., Agarwal, S. K., Speitel, G. E. & Georgiou, G. Methylosinus trichosporium OB3b mutants having constitutive expression of soluble methane monooxygenase in the presence of high levels of copper. *Appl. Environ. Microbiol.* **58,** 3701–3708 (1992).

28. Culpepper, M. A. & Rosenzweig, A. C. Architecture and active site of particulate methane monooxygenase. *Crit. Rev. Biochem. Mol. Biol.* **47,** 483–492 (2012).

29. Higgins, I. J., Best, D. J. & Hammond, R. C. New findings in methane-utilizing bacteria highlight their importance in the biosphere and their commercial potential. *Nature* **286,** 561–564 (1980).

30. Green, J. & Dalton, H. Substrate specificity of soluble methane monooxygenase. Mechanistic implications. *J. Biol. Chem.* **264,** 17698–17703 (1989).

31. Fox, B. G., Borneman, J. G., Wackett, L. P. & Lipscomb, J. D. Haloalkene oxidation by the soluble methane monooxygenase from Methylosinus trichosporium OB3b: mechanistic and environmental implications. *Biochemistry (Mosc.)* **29,** 6419–6427 (1990).

32. Merkx, M. *et al.* Dioxygen activation and methane hydroxylation by soluble methane monooxygenase: a tale of two irons and three proteins. *Angew. Chem. Int. Ed.* **40,** 2782–2807 (2001).

33. Hakemian, A. S. & Rosenzweig, A. C. The Biochemistry of Methane Oxidation. *Annu. Rev. Biochem.* **76,** 223–241 (2007).

34. Chan, S. I. *et al.* Efficient Oxidation of Methane to Methanol by Dioxygen Mediated by Tricopper Clusters. *Angew. Chem. Int. Ed.* **52,** 3731–3735 (2013).

35. Culpepper, M. A., Cutsail III, G. E., Gunderson, W. A., Hoffman, B. M. & Rosenzweig, A. C. Identification of the Valence and Coordination Environment of the Particulate Methane Monooxygenase Copper Centers by Advanced EPR Characterization. *J. Am. Chem. Soc.* **136,** 11767–11775 (2014).

36. Balasubramanian, R. & Rosenzweig, A. C. Structural and Mechanistic Insights into Methane Oxidation by Particulate Methane Monooxygenase. *Acc. Chem. Res.* **40,** 573–580 (2007).

37. Lieberman, R. L. & Rosenzweig, A. C. Crystal structure of a membrane-bound metalloenzyme that catalyses the biological oxidation of methane. *Nature* **434,** 177–182 (2005).

38. Woertink, J. S. *et al.* A [Cu2O]2+ core in Cu-ZSM-5, the active site in the oxidation of methane to methanol. *Proc. Natl. Acad. Sci.* **106,** 18908–18913 (2009).

39. Haack, P. & Limberg, C. Molecular Cu [II] -O-Cu [II] Complexes: Still Waters Run Deep. *Angew. Chem. Int. Ed.* **53,** 4282–4293 (2014).

40. Itoyama, S., Doitomi, K., Kamachi, T., Shiota, Y. & Yoshizawa, K. Possible Peroxo State of the Dicopper Site of Particulate Methane Monooxygenase from Combined Quantum Mechanics and Molecular Mechanics Calculations. *Inorg. Chem.* **55,** 2771–2775 (2016).

41. Citek, C., Lin, B.-L., Phelps, T. E., Wasinger, E. C. & Stack, T. D. P. Primary Amine Stabilization of a Dicopper(III) Bis(μ-oxo) Species: Modeling the Ligation in pMMO. *J. Am. Chem. Soc.* **136,** 14405–14408 (2014).

42. Shiota, Y., Juhász, G. & Yoshizawa, K. Role of Tyrosine Residue in Methane Activation at the Dicopper Site of Particulate Methane Monooxygenase: A Density Functional Theory Study. *Inorg. Chem.* **52,** 7907–7917 (2013).

43. Hemsworth, G. R., Henrissat, B., Davies, G. J. & Walton, P. H. Discovery and characterization of a new family of lytic polysaccharide monooxygenases. *Nat. Chem. Biol.* **10,** 122–126 (2013).

44. Quinlan, R. J. *et al.* Insights into the oxidative degradation of cellulose by a copper metalloenzyme that exploits biomass components. *Proc. Natl. Acad. Sci.* **108,** 15079–15084 (2011).

45. Kjaergaard, C. H. *et al.* Spectroscopic and computational insight into the activation of O2 by the mononuclear Cu center in polysaccharide monooxygenases. *Proc. Natl. Acad. Sci.* **111,** 8797–8802 (2014).

46.   Kim, S., Stahlberg, J., Sandgren, M., Paton, R. S. & Beckham, G. T. Quantum mechanical calculations suggest that lytic polysaccharide monooxygenases use a copper-oxyl, oxygen-rebound mechanism. *Proc. Natl. Acad. Sci.* **111,** 149–154 (2014).

47.   Beeson, W. T., Vu, V. V., Span, E. A., Phillips, C. M. & Marletta, M. A. Cellulose Degradation by Polysaccharide Monooxygenases. *Annu. Rev. Biochem.* **84,** 923–946 (2015).

48.   Hemsworth, G. R., Johnston, E. M., Davies, G. J. & Walton, P. H. Lytic Polysaccharide Monooxygenases in Biomass Conversion. *Trends Biotechnol.* **33,** 747–761 (2015).

49.   Phillips, C. M., Beeson, W. T., Cate, J. H. & Marletta, M. A. Cellobiose Dehydrogenase and a Copper-Dependent Polysaccharide Monooxygenase Potentiate Cellulose Degradation by *Neurospora crassa. ACS Chem. Biol.* **6,** 1399–1406 (2011).

50.   Itoh, S. Developing Mononuclear Copper–Active-Oxygen Complexes Relevant to Reactive Intermediates of Biological Oxidation Reactions. *Acc. Chem. Res.* **48,** 2066–2074 (2015).

51.   Cramer, C. J., Smith, B. A. & Tolman, W. B. Ab Initio Characterization of the Isomerism between the μ-η ^{2} :η ^{2} -Peroxo- and Bis(μ-oxo)dicopper Cores. *J. Am. Chem. Soc.* **118,** 11283–11287 (1996).

52.   Lee, J. Y. & Karlin, K. D. Elaboration of copper–oxygen mediated C–H activation chemistry in consideration of future fuel and feedstock generation. *Curr. Opin. Chem. Biol.* **25,** 184–193 (2015).

53.   Kitajima, N. & Moro-oka, Y. Copper-dioxygen complexes. Inorganic and bioinorganic perspectives. *Chem. Rev.* **94,** 737–757 (1994).

54.   Schindler, S. Reactivity of Copper(I) Complexes Towards Dioxygen. *Eur. J. Inorg. Chem.* **2000,** 2311–2326 (2000).

55.   Hatcher, L. Q., Vance, M. A., Narducci Sarjeant, A. A., Solomon, E. I. & Karlin, K. D. Copper−Dioxygen Adducts and the Side-on Peroxo Dicopper(II)/Bis(μ-oxo) Dicopper(III) Equilibrium: Significant Ligand Electronic Effects. *Inorg. Chem.* **45,** 3004–3013 (2006).

56.   Mahadevan, V., Henson, M. J., Solomon, E. I. & Stack, T. D. P. Differential Reactivity between Interconvertible Side-On Peroxo and Bis- *μ* -oxodicopper Isomers Using Peralkylated Diamine Ligands. *J. Am. Chem. Soc.* **122,** 10249–10250 (2000).

57.   Itoh, S. Mononuclear copper active-oxygen complexes. *Curr. Opin. Chem. Biol.* **10,** 115–122 (2006).

58.   Sanyal, I. *et al.* Reactions of dioxygen (O2) with mononuclear copper (I) complexes: temperature-dependent formation of peroxo-or oxo-(and dihydroxo-) bridged dicopper (II) complexes. *Inorg. Chem.* **31,** 4322–4332 (1992).

59.   Zhang, C. X. *et al.* Tuning Copper−Dioxygen Reactivity and Exogenous Substrate Oxidations via Alterations in Ligand Electronics. *J. Am. Chem. Soc.* **125,** 634–635 (2003).

60.   Karlin, K. D., Gultneh, Y., Hayes, J. C. & Zubieta, J. Copper(I)-dioxygen reactivity. 2. Reaction of a three-coordinate copper(I) complex with dioxygen, with evidence for a binuclear oxo-copper(II) species: structural characterization of a parallel-planar dihydroxo-bridged dimer. *Inorg. Chem.* **23,** 519–521 (1984).

61.   Obias, H. V. *et al.* Peroxo-, Oxo-, and Hydroxo-Bridged Dicopper Complexes: Observation of Exogenous Hydrocarbon Substrate Oxidation. *J. Am. Chem. Soc.* **120,** 12960–12961 (1998).

62.   Henson, M. J. *et al.* Resonance Raman Investigation of Equatorial Ligand Donor Effects on the Cu $_2$ O $_2$ $^{2+}$ Core in End-On and Side-On μ-Peroxo-Dicopper(II) and Bis-μ-oxo-Dicopper(III) Complexes. *J. Am. Chem. Soc.* **125,** 5186–5192 (2003).

63.   Shearer, J., Zhang, C. X., Hatcher, L. Q. & Karlin, K. D. Distinguishing Rate-Limiting Electron versus H-Atom Transfers in Cu $_2$ (O $_2$)-Mediated Oxidative *N* -Dealkylations: Application of Inter- versus Intramolecular Kinetic Isotope Effects. *J. Am. Chem. Soc.* **125,** 12670–12671 (2003).

64.   Lewis, E. A. & Tolman, W. B. Reactivity of Dioxygen−Copper Systems. *Chem. Rev.* **104,** 1047–1076 (2004).

65.   Nasir, M. S., Cohen, B. I. & Karlin, K. D. Mechanism of aromatic hydroxylation in a copper monooxygenase model system. 1,2-Methyl migrations and the NIH shift in copper chemistry. *J. Am. Chem. Soc.* **114,** 2482–2494 (1992).

66.   Holland, P. L., Rodgers, K. R. & Tolman, W. B. Is the Bis(m-oxo)dicopper Core Capable of Hydroxylating an Arene? *Angew. Chem.* **38,** 1139–1142 (1999).

67.   Mahapatra, S., Halfen, J. A. & Tolman, W. B. Mechanistic Study of the Oxidative N-Dealkylation Reactions of Bis(μ-oxo)dicopper Complexes. *J. Am. Chem. Soc.* **118,** 11575–11586 (1996).

68.   Itoh, S. *et al.* Functional Model of Dopamine .beta.-Hydroxylase. Quantitative Ligand Hydroxylation at the Benzylic Position of a Copper Complex by Dioxygen. *J. Am. Chem. Soc.* **117,** 4714–4715 (1995).

69.   Blain, I., Giorgi, M., De Riggi, I. & Réglier, M. Substrate-Binding Ligand Approach in Chemical Modeling of Copper-Containing Monooxygenases, 1 Intramolecular Stereoselective Oxygen Atom Insertion into a Non-Activated C–H Bond. *Eur. J. Inorg. Chem.* **2000,** 393–398 (2000).

70.   Blain, I. *et al.* Copper Complexes as Functional Models for Dopamine β-Hydroxylase – Stereospecific Oxygen Atom Transfer. *Eur. J. Inorg. Chem.* **1998,** 1297–1304 (1998).

71.   Anson, F. C. *et al.* Highly stabilized copper(III) complexes. *J. Am. Chem. Soc.* **109,** 2974–2979 (1987).

72.   Dhar, D. *et al.* Perturbing the Copper(III)–Hydroxide Unit through Ligand Structural Variation. *J. Am. Chem. Soc.* **138,** 356–368 (2016).

73.   Dhar, D. & Tolman, W. B. Hydrogen Atom Abstraction from Hydrocarbons by a Copper(III)-Hydroxide Complex. *J. Am. Chem. Soc.* **137,** 1322–1329 (2015).

74.   Gagnon, N. & Tolman, W. B. [CuO]$^+$ and [CuOH]$^{2+}$ Complexes: Intermediates in Oxidation Catalysis? *Acc. Chem. Res.* **48,** 2126–2131 (2015).

75.   Shiota, Y. & Yoshizawa, K. Comparison of the Reactivity of Bis(μ-oxo)Cu^{II}Cu^{III} and Cu^{III}Cu^{III} Species to Methane. *Inorg. Chem.* **48,** 838–845 (2009).

76.   Halvagar, M. R. *et al.* Hydroxo-Bridged Dicopper(II,III) and -(III,III) Complexes: Models for Putative Intermediates in Oxidation Catalysis. *J. Am. Chem. Soc.* **136,** 7269–7272 (2014).

77.   Isaac, J. A. *et al.* Room-Temperature Characterization of a Mixed-Valent μ-Hydroxodicopper(II,III) Complex. *Inorg. Chem.* (2016). doi:10.1021/acs.inorgchem.6b01504

78.   Blain, I., Giorgi, M., De Riggi, I. & Réglier, M. Copper Complexes as Functional Models for Dopamine β-Hydroxylase–Mechanistic Study of Oxygen Atom Transfer from Cu/O Species to Benzylic C- H Bonds. *Eur. J. Inorg. Chem.* **2001,** 205–211 (2001).

79.   Addison, A. W., Rao, T. N., Reedijk, J., van Rijn, J. & Verschoor, G. C. Synthesis, structure, and spectroscopic properties of copper (II) compounds containing nitrogen–sulphur donor ligands; the crystal and molecular structure of aqua [1, 7-bis (N-methylbenzimidazol-2′-yl)-2, 6-dithiaheptane] copper (II) perchlorate. *J. Chem. Soc. Dalton Trans.* 1349–1356 (1984).

80.   Maiti, D., Narducci Sarjeant, A. A. & Karlin, K. D. Copper−Hydroperoxo-Mediated N-Debenzylation Chemistry Mimicking Aspects of Copper Monooxygenases. *Inorg. Chem.* **47,** 8736–8747 (2008).

81.   Wada, A. *et al.* Structural and Spectroscopic Characterization of a Mononuclear Hydroperoxo ± Copper(ii) Complex with Tripodal Pyridylamine Ligands. *Angew. Chem. Int. Ed Engl.* **37,** 798–799 (1998).

82.   Shimokawa, C., Teraoka, J., Tachi, Y. & Itoh, S. A functional model for pMMO (particulate methane monooxygenase): Hydroxylation of alkanes with H2O2 catalyzed by β-diketiminatocopper(II) complexes. *J. Inorg. Biochem.* **100,** 1118–1127 (2006).

83.   Osako, T., Nagatomo, S., Tachi, Y., Kitagawa, T. & Itoh, S. Low-Temperature Stopped-Flow Studies on the Reactions of Copper(ii) Complexes and H2O2 : The First Detection of a Mononuclear Copper(ii)±Peroxo Intermediate. *Angew. Chem. Int. Ed.* **41,** 4325–4328 (2002).

84.   Zhu, Q. *et al.* Hydrogen Peroxide and Dioxygen Activation by Dinuclear Copper Complexes in Aqueous Solution: Hydroxyl Radical Production Initiated by Internal Electron Transfer. *J. Am. Chem. Soc.* **130,** 6304–6305 (2008).

85.   Kunishita, A. *et al.* Reactions of Copper(II)-H$_2$O$_2$ Adducts Supported by Tridentate Bis(2-pyridylmethyl)amine Ligands: Sensitivity to Solvent and Variations in Ligand Substitution. *Inorg. Chem.* **47,** 8222–8232 (2008).

86.   Itoh, S. *et al.* Mechanistic Studies of Aliphatic Ligand Hydroxylation of a Copper Complex by Dioxygen: A Model Reaction for Copper Monooxygenases. *J. Am. Chem. Soc.* **120,** 2890–2899 (1998).

87.   *Metal-oxo and metal-peroxo species in catalytic oxidations*. (Springer, 2000).

88.   Groves, J. T., Nemo, T. E. & Myers, R. S. Hydroxylation and epoxidation catalyzed by iron-porphine complexes. Oxygen transfer from iodosylbenzene. *J. Am. Chem. Soc.* **101,** 1032–1033 (1979).

89.   Company, A. *et al.* Triggering the Generation of an Iron(IV)-Oxo Compound and Its Reactivity toward Sulfides by Ru^{II} Photocatalysis. *J. Am. Chem. Soc.* **136,** 4624–4633 (2014).

90.   Réglier, M., Amadeï, E., Tadayoni, R. & Waegell, B. Pyridine nucleus hydroxylation with copper oxygenase models. *J. Chem. Soc. Chem. Commun.* 447–450 (1989).

91. Schardt, B. C. & Hill, C. L. Preparation of iodobenzene dimethoxide. A new synthesis of [18O] iodosylbenzene and a reexamination of its infrared spectrum. *Inorg. Chem.* **22,** 1563–1565 (1983).

92. Chen, G.-Q., Xu, Z.-J., Zhou, C.-Y. & Che, C.-M. Selective oxidation of terminal aryl and aliphatic alkenes to aldehydes catalyzed by iron(iii) porphyrins with triflate as a counter anion. *Chem. Commun.* **47,** 10963 (2011).

93. Nam, W. *et al.* Reversible formation of iodosylbenzene-iron porphyrin intermediates in the reaction of oxoiron(IV) porphyrin pi-cation radicals and iodobenzene. *Angew. Chem. Int. Ed Engl.* **42,** 109–111 (2003).

94. Karlin, K. D., Gultneh, Y., Hayes, J. C. & Zubieta, J. Copper(I)-dioxygen reactivity. 2. Reaction of a three-coordinate copper(I) complex with dioxygen, with evidence for a binuclear oxo-copper(II) species: structural characterization of a parallel-planar dihydroxo-bridged dimer. *Inorg. Chem.* **23,** 519–521 (1984).

95. Tai, A. F., Margerum, L. D. & Valentine, J. S. Epoxidation of olefins by iodosylbenzene catalyzed by binuclear copper(II) complexes. *J. Am. Chem. Soc.* **108,** 5006–5008 (1986).

96. Meunier, B. Metalloporphyrins as versatile catalysts for oxidation reactions and oxidative DNA cleavage. *Chem. Rev.* **92,** 1411–1456 (1992).

97. Singh, K. K., Tiwari, M. k., Dhar, B. B., Vanka, K. & Sen Gupta, S. Mechanism of Oxygen Atom Transfer from Fe $^{\mathrm{V}}$ (O) to Olefins at Room Temperature. *Inorg. Chem.* **54,** 6112–6121 (2015).

98. Limburg, J. A Functional Model for O-O Bond Formation by the O2-Evolving Complex in Photosystem II. *Science* **283,** 1524–1527 (1999).

99. McEvoy, J. P. & Brudvig, G. W. Water-Splitting Chemistry of Photosystem II. *Chem. Rev.* **106,** 4455–4483 (2006).

100. Umena, Y., Kawakami, K., Shen, J.-R. & Kamiya, N. Crystal structure of oxygen-evolving photosystem II at a resolution of 1.9 Å. *Nature* **473,** 55–60 (2011).

101. Armstrong, F. A. Why did Nature choose manganese to make oxygen? *Philos. Trans. R. Soc. B Biol. Sci.* **363,** 1263–1270 (2008).

102. Vrettos, J. S. & Brudvig, G. W. Water oxidation chemistry of photosystem II. *Philos. Trans. R. Soc. B Biol. Sci.* **357,** 1395–1405 (2002).

103. Fillol, J. L. *et al.* Efficient water oxidation catalysts based on readily available iron coordination complexes. *Nat. Chem.* **3,** 807–813 (2011).

104. Roeser, S. *et al.* Chemical, Electrochemical, and Photochemical Catalytic Oxidation of Water to Dioxygen with Mononuclear Ruthenium Complexes. *ChemSusChem* n/a-n/a (2011). doi:10.1002/cssc.201000358

105. Cady, C., Crabtree, R. & Brudvig, G. Functional models for the oxygen-evolving complex of photosystem II. *Coord. Chem. Rev.* **252,** 444–455 (2008).

106. Yin, Q. *et al.* A Fast Soluble Carbon-Free Molecular Water Oxidation Catalyst Based on Abundant Metals. *Science* **328,** 342–345 (2010).

107. Surendranath, Y., Kanan, M. W. & Nocera, D. G. Mechanistic Studies of the Oxygen Evolution Reaction by a Cobalt-Phosphate Catalyst at Neutral pH. *J. Am. Chem. Soc.* **132,** 16501–16509 (2010).

108. Ray, K., Heims, F., Schwalbe, M. & Nam, W. High-valent metal-oxo intermediates in energy demanding processes: from dioxygen reduction to water splitting. *Curr. Opin. Chem. Biol.* **25,** 159–171 (2015).

109. Kundu, S., Schwalbe, M. & Ray, K. Metal-oxo-mediated O-O bond formation reactions in chemistry and biology. *Bioinorg. React. Mech.* **8,** (2012).

110. Yagi, M. & Kaneko, M. Molecular Catalysts for Water Oxidation. *Chem. Rev.* **101,** 21–36 (2001).

111. Parent, A. R., Crabtree, R. H. & Brudvig, G. W. Comparison of primary oxidants for water-oxidation catalysis. *Chem Soc Rev* **42,** 2247–2252 (2013).

112. Hetterscheid, D. G. H. & Reek, J. N. H. Periodate as an Oxidant for Catalytic Water Oxidation: Oxidation via Electron Transfer or O-Atom Transfer?: Mechanism of Catalytic Water Oxidation by Periodate. *Eur. J. Inorg. Chem.* **2014,** 742–749 (2014).

113. Parent, A. R., Brewster, T. P., De Wolf, W., Crabtree, R. H. & Brudvig, G. W. Sodium Periodate as a Primary Oxidant for Water-Oxidation Catalysts. *Inorg. Chem.* **51,** 6147–6152 (2012).

114. Savéant, J.-M. Molecular Catalysis of Electrochemical Reactions. Mechanistic Aspects. *Chem. Rev.* **108,** 2348–2378 (2008).

115. Fukuzumi, S. & Hong, D. Homogeneous versus Heterogeneous Catalysts in Water Oxidation: Homogeneous versus Heterogeneous Catalysts in Water Oxidation. Eur. J. Inorg. Chem. 2014, 645–659 (2014).

116. Barnett, S. M., Goldberg, K. I. & Mayer, J. M. A soluble copper–bipyridine water-oxidation electrocatalyst. *Nat. Chem.* **4,** 498–502 (2012).

117. Zhang, T., Wang, C., Liu, S., Wang, J.-L. & Lin, W. A Biomimetic Copper Water Oxidation Catalyst with Low Overpotential. *J. Am. Chem. Soc.* **136,** 273–281 (2014).

118. Zhang, M.-T., Chen, Z., Kang, P. & Meyer, T. J. Electrocatalytic Water Oxidation with a Copper(II) Polypeptide Complex. *J. Am. Chem. Soc.* **135,** 2048–2051 (2013).

119. Pap, J. S. *et al.* Electrocatalytic water oxidation by Cu^{II} complexes with branched peptides. *Chem Commun* **51,** 6322–6324 (2015).

120. Lu, C., Wang, J. & Chen, Z. Water Oxidation by Copper-Amino Acid Catalysts at Low Overpotentials. *ChemCatChem* **8,** 2165–2170 (2016).

121. Garrido-Barros, P. *et al.* Redox Non-innocent Ligand Controls Water Oxidation Overpotential in a New Family of Mononuclear Cu-Based Efficient Catalysts. *J. Am. Chem. Soc.* **137,** 6758–6761 (2015).

122. Fu, L.-Z., Fang, T., Zhou, L.-L. & Zhan, S.-Z. A mononuclear copper electrocatalyst for both water reduction and oxidation. *RSC Adv* **4,** 53674–53680 (2014).

123. Coggins, M. K., Zhang, M.-T., Chen, Z., Song, N. & Meyer, T. J. Single-Site Copper(II) Water Oxidation Electrocatalysis: Rate Enhancements with HPO$_4{}^{2-}$ as a Proton Acceptor at pH 8. *Angew. Chem. Int. Ed.* **53,** 12226–12230 (2014).

124. Du, J., Chen, Z., Ye, S., Wiley, B. J. & Meyer, T. J. Copper as a Robust and Transparent Electrocatalyst for Water Oxidation. *Angew. Chem. Int. Ed.* **54,** 2073–2078 (2015).

125. Chen, Z. & Meyer, T. J. Copper(II) Catalysis of Water Oxidation. *Angew. Chem. Int. Ed.* **52,** 700–703 (2013).

126. Winikoff, S. G. & Cramer, C. J. Mechanistic analysis of water oxidation catalyzed by mononuclear copper in aqueous bicarbonate solutions. *Catal Sci Technol* **4,** 2484–2489 (2014).

127. Su, X.-J. *et al.* Electrocatalytic Water Oxidation by a Dinuclear Copper Complex in a Neutral Aqueous Solution. *Angew. Chem. Int. Ed.* **54,** 4909–4914 (2015).

128. Yu, W.-B., He, Q.-Y., Ma, X.-F., Shi, H.-T. & Wei, X. A new copper species based on an azo-compound utilized as a homogeneous catalyst for water oxidation. *Dalton Trans* **44,** 351–358 (2015).

129. Xiang, R.-J. *et al.* A Water-Soluble Copper-Polypyridine Complex as a Homogeneous Catalyst for both Photo-Induced and Electrocatalytic O$_2$ Evolution. *Chem. - Eur. J.* **22,** 1602–1607 (2016).

130. Hirai, Y. *et al.* Ruthenium-Catalyzed Selective and Efficient Oxygenation of Hydrocarbons with Water as an Oxygen Source. *Angew. Chem. Int. Ed.* **47,** 5772–5776 (2008).

131. Lee, Y.-M. *et al.* Water as an Oxygen Source in the Generation of Mononuclear Nonheme Iron(IV) Oxo Complexes. *Angew. Chem. Int. Ed.* **48,** 1803–1806 (2009).

132. Herrero, C. *et al.* Oxidation catalysis via visible-light water activation of a [Ru(bpy)$_3$]$^{2+}$ chromophore BSA–metallocorrole couple. *Dalton Trans* **45,** 706–710 (2016).

133. Guillo, P. *et al.* Photocatalyzed Sulfide Oxygenation with Water as the Unique Oxygen Atom Source. *Inorg. Chem.* **51,** 2222–2230 (2012).

134. Hamelin, O., Guillo, P., Loiseau, F., Boissonnet, M.-F. & Ménage, S. A Dyad as Photocatalyst for Light-Driven Sulfide Oxygenation with Water As the Unique Oxygen Atom Source. *Inorg. Chem.* **50,** 7952–7954 (2011).

135. Artero, V. & Fontecave, M. Solar fuels generation and molecular systems: is it homogeneous or heterogeneous catalysis? *Chem Soc Rev* **42,** 2338–2356 (2013).

144. Liu, X., Zheng, H., Sun, Z., Han, A. & Du, P. Earth-Abundant Copper-Based Bifunctional Electrocatalyst for Both Catalytic Hydrogen Production and Water Oxidation. ACS Catal. 5, 1530–1538 (2015).

137. Gans, P., Sabatini, A. & Vacca, A. Investigation of equilibria in solution. Determination of equilibrium constants with the HYPERQUAD suite of programs. *Talanta* **43,** 1739–1753 (1996).

138. Selmeczi, K., Giorgi, M., Speier, G., Farkas, E. & Réglier, M. Mono- versus Binuclear Copper(II) Complexes in Phosphodiester Hydrolysis. *Eur. J. Inorg. Chem.* **2006,** 1022–1031 (2006).

139. Neese, F. The ORCA program system. *Wiley Interdiscip. Rev. Comput. Mol. Sci.* **2,** 73–78 (2012).

140. Lee, C., Yang, W. & Parr, R. G. Development of the Colle-Salvetti correlation-energy formula into a functional of the electron density. *Phys. Rev. B* **37,** 785–789 (1988).

141. Klamt, A. & Schüürmann, G. COSMO: a new approach to dielectric screening in solvents with explicit expressions for the screening energy and its gradient. *J Chem Soc Perkin Trans 2* 799–805 (1993). doi:10.1039/P29930000799

142. Soda, T. *et al.* Ab initio computations of effective exchange integrals for H–H, H–He–H and Mn2O2 complex: comparison of broken-symmetry approaches. *Chem. Phys. Lett.* **319,** 223–230 (2000).

143. Yamaguchi, K., Takahara, Y. & Fueno, T. in *Applied quantum chemistry* 155–184 (Springer, 1986).

144. Heisenberg, W. Zur Theorie des Ferromagnetismus. *Z. F�r Phys.* **49,** 619–636 (1928).

145. Heisenberg, W. Mehrk�rperproblem und Resonanz in der Quantenmechanik. *Z. F�r Phys.* **38,** 411–426 (1926).

146. Dirac, P. A. M. Quantum Mechanics of Many-Electron Systems. *Proc. R. Soc. Math. Phys. Eng. Sci.* **123,** 714–733 (1929).

147. Van Vleck, J. H. *The theory of electric and magnetic susceptibilities.* (Oxford University Press, 1965).

148. Kim, E. *et al.* Superoxo, μ-peroxo, and μ-oxo complexes from heme/O2 and heme-Cu/O2 reactivity: Copper ligand influences in cytochrome c oxidase models. *Proc. Natl. Acad. Sci.* **100,** 3623–3628 (2003).

149. Tainer, J. A., Getzoff, E. D., Beem, K. M., Richardson, J. S. & Richardson, D. C. Determination and analysis of the 2 Å structure of copper, zinc superoxide dismutase. *J. Mol. Biol.* **160,** 181–217 (1982).

150. Garcia-Bosch, I., Ribas, X. & Costas, M. Well-Defined Heterometallic and Unsymmetric M2O2 Complexes Arising from Binding and Activation of O2. *Eur. J. Inorg. Chem.* **2012,** 179–187 (2012).

151. Alsters, P. L., Boersma, J. & van Koten, G. Reactivity of organopalladium compounds toward molybdenum peroxides: oxygen insertion versus carbon-chlorine and carbon-oxygen coupling. Evidence for palladium(IV) molybdate intermediates. *Organometallics* **12,** 1629–1638 (1993).

152. Aboelella, N. W. *et al.* Mixed metal bis(μ-oxo) complexes with [CuM(μ-O) $_2$] $^{n+}$ (M = Ni(III) or Pd(II)) cores. *Chem Commun* 1716–1717 (2004). doi:10.1039/B404640D

153. York, J. T., Young, V. G. & Tolman, W. B. Heterobimetallic Activation of Dioxygen: Characterization and Reactivity of Novel Cu(I)−Ge(II) Complexes. *Inorg. Chem.* **45,** 4191–4198 (2006).

154. York, J. T., Llobet, A., Cramer, C. J. & Tolman, W. B. Heterobimetallic Dioxygen Activation: Synthesis and Reactivity of Mixed Cu−Pd and Cu−Pt Bis(μ-oxo) Complexes. *J. Am. Chem. Soc.* **129,** 7990–7999 (2007).

155. Yao, S., Bill, E., Milsmann, C., Wieghardt, K. & Driess, M. A 'Side-on' Superoxonickel Complex [LNi(O $_2$)] with a Square-Planar Tetracoordinate Nickel(II) Center and Its Conversion into [LNi(μ-OH) $_2$ NiL]. *Angew. Chem. Int. Ed.* **47,** 7110–7113 (2008).

156. Yao, S. *et al.* O□O Bond Activation in Heterobimetallic Peroxides: Synthesis of the Peroxide [LNi(μ,η ^{2} :η ^{2} -O $_2$)K] and its Conversion into a Bis(μ-Hydroxo) Nickel Zinc Complex. *Angew. Chem. Int. Ed.* **48,** 8107–8110 (2009).

157. Yao, S. *et al.* Monooxygenase-Like Reactivity of an Unprecedented Heterobimetallic {FeO2Ni} Moiety. *Angew. Chem. Int. Ed.* **49,** 7054–7058 (2010).

158. Kundu, S. *et al.* A High-Valent Heterobimetallic [Cu ^{III} (μ-O) $_2$ Ni ^{III}] $^{2+}$ Core with Nucleophilic Oxo Groups. *Angew. Chem. Int. Ed.* **52,** 5622–5626 (2013).

159. Shiren, K. *et al.* Synthesis, Structures, and Properties of Bis(μ -oxo)nickel(III) and Bis(μ -superoxo)nickel(II) Complexes: An Unusual Conversion of a Ni ^{II} $_2$ (μ -O) $_2$ Core into a Ni ^{II} $_2$ (μ -OO) $_2$ Core by H $_2$ O $_2$ and Oxygenation of Ligand. *J. Am. Chem. Soc.* **122,** 254–262 (2000).

160. Schenker, R., Mandimutsira, B. S., Riordan, C. G. & Brunold, T. C. Spectroscopic and Computational Studies on [(PhTt <sup/> ^{t} ^{Bu}) $_2$ Ni $_2$ (μ-O) $_2$]: Nature of the Bis-μ-oxo (Ni $^{3+}$) $_2$ 'Diamond' Core. *J. Am. Chem. Soc.* **124,** 13842–13855 (2002).

161. Palatinus, L. & van der Lee, A. Symmetry determination following structure solution in *P* 1. *J. Appl. Crystallogr.* **41,** 975–984 (2008).

162. Palatinus, L., Prathapa, S. J. & van Smaalen, S. *EDMA* : a computer program for topological analysis of discrete electron densities. *J. Appl. Crystallogr.* **45,** 575–580 (2012).

163. Sheldrick, G. M. Crystal structure refinement with *SHELXL. Acta Crystallogr. Sect. C Struct. Chem.* **71,** 3–8 (2015).

164. Rockenbauer, A. & Korecz, L. Automatic computer simulations of ESR spectra. *Appl. Magn. Reson.* **10,** 29–43 (1996).

165. Alderighi, L. *et al.* Hyperquad simulation and speciation (HySS): a utility program for the investigation of equilibria involving soluble and partially soluble species. *Coord. Chem. Rev.* **184,** 311–318 (1999).

166. Becke, A. D. A new mixing of Hartree–Fock and local density-functional theories. *J. Chem. Phys.* **98,** 1372 (1993).

167. Neese, F. An improvement of the resolution of the identity approximation for the formation of the Coulomb matrix. *J. Comput. Chem.* **24,** 1740–1747 (2003).

168. Weigend, F. Accurate Coulomb-fitting basis sets for H to Rn. *Phys. Chem. Chem. Phys.* **8,** 1057 (2006).

169. Weigend, F. & Ahlrichs, R. Balanced basis sets of split valence, triple zeta valence and quadruple zeta valence quality for H to Rn: Design and assessment of accuracy. *Phys. Chem. Chem. Phys.* **7,** 3297 (2005).

170. van Lenthe, E., Snijders, J. G. & Baerends, E. J. The zero-order regular approximation for relativistic effects: The effect of spin–orbit coupling in closed shell molecules. *J. Chem. Phys.* **105,** 6505 (1996).

171. van Lenthe, E., van der Avoird, A. & Wormer, P. E. S. Density functional calculations of molecular hyperfine interactions in the zero order regular approximation for relativistic effects. *J. Chem. Phys.* **108,** 4783 (1998).

172. Boys, S. F. & Bernardi, F. The calculation of small molecular interactions by the differences of separate total energies. Some procedures with reduced errors. *Mol. Phys.* **19,** 553–566 (1970).

173. Simon, S., Duran, M. & Dannenberg, J. J. How does basis set superposition error change the potential surfaces for hydrogen-bonded dimers? *J. Chem. Phys.* **105,** 11024 (1996).

174. Noodleman, L. Valence bond description of antiferromagnetic coupling in transition metal dimers. *J. Chem. Phys.* **74,** 5737 (1981).

175. Noodleman, L. & Case, D. A. in *Advances in Inorganic Chemistry* **38,** 423–470 (Elsevier, 1992).

176. Noodleman, L. & Davidson, E. R. Ligand spin polarization and antiferromagnetic coupling in transition metal dimers. *Chem. Phys.* **109,** 131–143 (1986).

177. *Recent advances in density functional methods*. (World Scientific, 1995).

178. Bauernschmitt, R. & Ahlrichs, R. Treatment of electronic excitations within the adiabatic approximation of time dependent density functional theory. *Chem. Phys. Lett.* **256,** 454–464 (1996).

179. Stratmann, R. E., Scuseria, G. E. & Frisch, M. J. An efficient implementation of time-dependent density-functional theory for the calculation of excitation energies of large molecules. *J. Chem. Phys.* **109,** 8218 (1998).

180. Hirata, S. & Head-Gordon, M. Time-dependent density functional theory within the Tamm–Dancoff approximation. *Chem. Phys. Lett.* **314,** 291–299 (1999).

181. Hirata, S. & Head-Gordon, M. Time-dependent density functional theory for radicals. *Chem. Phys. Lett.* **302,** 375–382 (1999).

182. Perdew, J. P. Erratum: Density-functional approximation for the correlation energy of the inhomogeneous electron gas. *Phys. Rev. B* **34,** 7406–7406 (1986).

183. Becke, A. D. Density-functional exchange-energy approximation with correct asymptotic behavior. *Phys. Rev. A* **38,** 3098–3100 (1988).

184. Schäfer, A., Huber, C. & Ahlrichs, R. Fully optimized contracted Gaussian basis sets of triple zeta valence quality for atoms Li to Kr. *J. Chem. Phys.* **100,** 5829 (1994).

185. Neese, F. Prediction of electron paramagnetic resonance g values using coupled perturbed Hartree–Fock and Kohn–Sham theory. *J. Chem. Phys.* **115,** 11080 (2001).

186. Koseki, S., Schmidt, M. W. & Gordon, M. S. MCSCF/6-31G(d,p) calculations of one-electron spin-orbit coupling constants in diatomic molecules. *J. Phys. Chem.* **96,** 10768–10772 (1992).

187. Koseki, S., Gordon, M. S., Schmidt, M. W. & Matsunaga, N. Main Group Effective Nuclear Charges for Spin-Orbit Calculations. *J. Phys. Chem.* **99,** 12764–12772 (1995).

188. Neese, F. Metal and ligand hyperfine couplings in transition metal complexes: The effect of spin–orbit coupling as studied by coupled perturbed Kohn–Sham theory. *J. Chem. Phys.* **118,** 3939 (2003).

189. Pantazis, D. A., Chen, X.-Y., Landis, C. R. & Neese, F. All-Electron Scalar Relativistic Basis Sets for Third-Row Transition Metal Atoms. *J. Chem. Theory Comput.* **4,** 908–919 (2008).

190. Pantazis, D. A. & Neese, F. All-Electron Scalar Relativistic Basis Sets for the Lanthanides. *J. Chem. Theory Comput.* **5,** 2229–2238 (2009).

191. Reed, A. E., Weinstock, R. B. & Weinhold, F. Natural population analysisa). *J. Chem. Phys.* **83,** 735 (1985).

Abstract

Copper-containing monooxygenases are enzymatic systems capable of transferring an oxygen atom to their subtrates in highly regio or stereo-specific modes. Model complexes for copper-containing monooxygenases have provided valuable information on the structure and reactivity of several copper-dioxygen adducts. However, the recent discovery of two new enzymatic systems (LPMO and pMMO) able to perform activation of very strong C-H bonds has re-opened the debate on the catalytically relevant copper-dioxygen species.

The use of model systems that mimic an enzyme is a simple approach to obtain a better knowledge of how nature works. For this study, Cu(I) and Cu(II) complexes containing ligand-substrate were prepared. After reaction with different oxidants or O-atom donors, we investigated the regio- and stereo-selectivity of the oxidation of the internal substrate. Based on the relatively well-known chemistry of Cu(I) with dioxygen, we, were also interested in investigating the water as an O-atom donor in C-H bond activation reactions. We have therefore investigated electrochemical water oxidation or activation to generate dioxygen and selective oxygen-insertion into the substrate-bound moiety. Finally, we explored the properties of mixed-metal dioxygen species as compared to their homometalic counter-parts. Indeed heterobimetallic active sites are found in various metalloenzymes such as cytochrome c oxidase. Therefore, two new high-valent Cu-Ni heterobimetallic complexes were synthesized. We investigated their electronic properties using various spectroscopic methods and their reactivity was evaluated towards external and internal substrates (indane).

Keywords : copper-oxygen species, C-H activation, intramolecular, water activation, metalloenzymes, mixed-valent, ligand RPY2

Résumé

Les monooxygénases à cuivre sont des systèmes enzymatiques capables de transférer un atome d'oxygène à leur substrat de manière hautement régio et stéréo-spécifique. Les complexes modèles de monooxygénases à cuivre ont fourni de précieuses informations sur la structure et la réactivité des espèces «cuivre-dioxygène» impliquées dans une telle réactivité. Cependant, la découverte récente de deux nouveaux systèmes enzymatiques (LPMO et pMMO) capables d'effectuer l'activation des liaisons C-H très énergétiques a réouvert le débat sur les espèces cuivre--oxygène capables d'une telle réactivité. L'utilisation de complexes modèles d'une métalloenzyme est une approche simple pour obtenir des informations sur façon dont fonctionne la nature. Dans ce travail, nous avons choisi de préparer des complexes bio-inspirés de Cu(I) et Cu(II) avec un ligand contenant un substrat interne. Ces complexes ont été exposés à différents oxydants ou donneurs d'atome d'oxygène et nous avons étudié la régio- et stéréo-sélectivité de la réaction d'oxydation du substrat interne. De plus, nous avons évalue la capacité de ces systèmes à utiliser l'eau comme donneur d'atome d'oxygène. Pour cela, nous avons l'oxydation ou l'activation de l'eau par voie électrochimique afin de générer des intermédiaires cuivre-oxygène conduisant éventuellement à la production de dioxygène ou à l'oxydation sélective du ligand. Enfin, nous nous sommes intéressés aux propriétés d'espèces hétérobimétalliques à haute valence. Des centres hétérobimétalliques sont en effet impliqués dans divers processus catalytiques de métalloenzymes telles que le cytochrome c oxydase. Par conséquent, deux nouveaux complexes hétérobimétalliques à haute valence contenant du nickel et du cuivre ont été synthétisés. Nous avons étudié leurs propriétés électroniques en utilisant diverses méthodes spectroscopiques et leur réactivité envers des substrats externes et internes (ligands) a été évaluée et comparée à la réactivité de leurs homologues homobimétalliques.

Mots clefs : espèces de cuivre-oxygène, C-H activation, intermoléculaires, activation de l'eau, métalloenzymes, mixte-valent